UNIVERSITY OF MESSINA

Department of Engineering

Research Doctorate Course:

"Engineering and Chemistry of Materials and Constructions"

XXXIV Cycle

ICAR/08: Structural mechanics

Generation of time and frequency dependent random processes compatible with recorded seismic accelerograms

PhD Candidate:

Federica GENOVESE

PhD Coordinator:

Prof. Giovanni NERI

Tutor:

Prof. Eng. Giuseppe MUSCOLINO

Co-Tutor:

Prof. Eng. Giovanni BIONDI

2020-2021

"Strong motion accelerograms properly interpreted are the nearest thing to scientific truth in earthquake engineering" [Trifunac 2009]

Index

Introduction

Strong earthquakes, caused by a sudden release of stress along faults in the earth's crust, are among the most damaging and deadly natural phenomena. The energy released by an earthquake travels in the form of waves, known as seismic waves. When the seismic waves reach the ground surface, the produced shaking induces dynamic effects on structural and geotechnical systems that can severely compromise their safety level and stability. The induced dynamic action at a given site depends on several factors such as: the strength, and duration of shaking and the mechanical properties of the soil layers crossed by the seismic waves.

The knowledge of ground motion attributable to earthquakes is essential for the design of earthquake-resistant structures, and the evaluation of the seismic vulnerability of existing ones. Among all possible sources of uncertainty stemming from the structural and soil material properties, the selection of the earthquake-induced ground motions has the highest effect on the variability observed in the response history analysis of structures and geotechnical systems.

The characteristics of the design ground motion, representing the level of shaking for which satisfactory performance is expected, are influenced by the characteristics of seismic source, the rupture process, the source-site travel path, the local site conditions, and the importance of the structure or facility for which the ground motion is to be used.

When the local, geologic and tectonic conditions of the site of interest is similar to those of sites where actual strong motions have previously been detected, the recorded time histories can be used directly as input motions in the dynamic analyses. Otherwise, the use of artificial accelerograms, having characteristics consistent with those of actual earthquakes, could represent a valid alternative. However, the generation of artificial accelerograms might not be easy: many motions that appear reasonable in the time domain may not be so when examined in the frequency domain, and vice versa. Furthermore, many reasonable-looking time histories of acceleration produce, after integration, unreasonable time histories of velocity and/or displacement.

The main aim of this Ph.D. thesis is to propose two novel procedures for the generation of artificial accelerograms having the same time and frequency contents of recorded time histories.

The purpose of the Chapter 1 is to illustrate the basic concepts of seismic engineering that may be useful in reading this thesis. Specifically, this Chapter describes the recording instruments used to detect strong ground motion and the signals processing techniques by which measured motions are corrected. Finally, a brief overview of the main intensity measures that can be used to characterize the amplitude, frequency content and duration of strong ground motions, is presented.

Chapter 2 highlights the limitations of the classical *Fourier analysis* in describing non-stationary signals whose statistical parameters vary with time. Therefore, an introduction to joint time-frequency signal representation through the *short time Fourier transform* and the *wavelet transform*, is presented. More details will be given about a particular kind of harmonic wavelet, called *"circular"*, and the related theory.

In Chapter 3, after a brief introduction on stochastic variables and processes, the *discrete circular wavelet transform* is proposed to randomly generate an arbitrary number of records with the same non-stationary characteristics of the target accelerogram. The influence of a novel correlation structure for the definition of the wavelet random phases and a different subdivision of the earthquake record in frequency bands are highlighted and discussed. Through the proposed stochastic generation method, an effective trade-off is identified between localisation in the frequency domain and in the time domain of the generated signals.

In Chapter 4, a novel method for generating samples of a fully non-stationary zero-mean Gaussian process, having a target acceleration time-history as one of its own samples, is described. The *evolutionary power spectral density* (*EPSD*) function of the proposed fully non-stationary model is evaluated as the sum of uniformly modulated processes. These are defined in each time interval, as the product of deterministic modulating functions per stationary zero-mean Gaussian sub-processes, whose unimodal *power spectral density* (*PSD*) functions are filtered by high pass and low pass Butterworth filters. In each time interval the parameters of the *modulating functions* are estimated by least-square fitting the expected energy of the proposed model to the energy of the target accelerogram, while the parameters of the *PSD* functions of stationary sub-processes are estimated once both occurrences of *peaks* and *zero-level up-crossings* of the target accelerogram, in the various intervals, are counted.

Chapter 4 concludes with the application of an iterative procedure aimed to obtain the compatibility between the mean spectrum of the generated samples and a target one. Depending on the aim to be achieved, it is possible to obtain the spectrum-compatibility in terms of *response spectrum* or *Fourier spectrum*, using two different corrective *PSD* function terms.

In Chapter 5, a new approach which takes into account the inherent random nature of the ground motion acceleration as well as epistemic uncertainties affecting the definition of its power spectrum, is presented. Specifically, seismic excitation is modelled as a zero-mean stationary Gaussian random process fully characterized by an imprecise *PSD* function, i.e. with interval parameters. The ranges of such interval parameters are determined by analysing a large set of accelerograms recorded on rigid soil deposits. To discard outliers, the *Chauvenet's Criterion* is applied iteratively. The proposed imprecise *PSD* function may be viewed as representative of the actual accelerograms recorded on rigid soil deposits. Due to imprecision of the excitation, the fractile of order p of the structural response turn out to have an interval nature. The bounds of the fractile order p are here used to define the range of structural performance.

In this Ph.D. thesis, several numerical applications will be done in order to test the effectiveness of the proposed procedures.

Chapter 1

Characterization of earthquake ground motions

1.1 Introduction

The analysis of *strong ground motions* (i.e., motions of sufficient strength to affect people and their environment) produced by earthquakes, plays a key role in the field of seismic engineering. The ground movement can be completely described by three components of translation and three components of rotation. However, in most seismological studies it is assumed that the rotational components of earthquake ground motion are small enough to be neglected, consequently only the three orthogonal components of translational motion (two horizontals and one vertical) are usually measured [Kramer 1996].

Detection of ground motion at a particular site requires specialized measurement equipment: *seismographs* are used to measure relatively *weak ground motions* while *accelerographs* are employed to detect the *strong ground motions*.

The first record obtained with an analog strong motion accelerograph dates back to 1933 and was triggered by the Long Beach, California earthquake. Since that time a considerable amount of ground motions has been acquired thanks to the worldwide installation of an ever-denser accelerograph network. Nowadays, the analog instruments have been surpassed by the digital ones that, being technologically superior, allow to obtain an accurate time stamping of the ground movements.

Nonetheless, digitized signals need to be processed because they usually contain “errors” and background noises that alter the frequency content of the detected ground motions. The noise present in the record is caused by various factors and can be removed by the application of different post processing techniques such as the *baseline adjustment* and *frequencies filtering*.

Generally, it is not possible to identify the "ideal" processing for a given record, any correction scheme must necessarily be approximate and empirically based.

Nowadays, the main sources of strong motion data for engineering application are organized in databases available online. For many scientific applications, rather than using the entire waveform, it is more useful both to describe and to classify the ground motion in terms of several parameters that reflect the characteristics of the signals that are of engineering significance. For an adequate characterization of a ground motion, it is usually necessary to use more than one of these parameters, also called *intensity measures*.

This Chapter describes the instruments used to detect strong ground motions (including the issues related to devices characteristics) and the techniques by which measured signals are corrected. It concludes with a brief description of the main intensity measures that can be computed to characterize the amplitude, frequency content and duration of strong ground motions.

1.2 A brief historical review of strong motion observation

The modern Seismic Engineering was born in the early 1930s with the first installation of instruments able to detect the ground motions associated with devastating earthquakes.

The strong motion instrumentation program, started in America in 1931, was a result of the personal efforts of John Ripley Freeman (1855–1932) and a few other engineers and businessmen who were impressed with the advances in the design of earthquake-resistant structures in Japan and who recognized that further progress could not be made without recording the destructive earthquake shaking. With the lectures of Kyoji Suyehiro (1877–932) providing technical background and ideas, and with Freeman's vision and persistence, Federal aid was enlisted, and United States Congress approved funds for the "US Coast and Geodetic Survey" (USC&GS) to start the program [Trifunac 2009]. After the installation of the USC&GS instruments in Long Beach, Vernon, El Centro and San Diego, the first detecting ground motion having a magnitude of 7.3 occurred in Western Nevada on December 20, 1932. It was detected by the Long Beach instrument, but because the earthquake was about 350 miles away from it, the record amplitudes were very small.

In the history of earthquake engineering, the first *strong* motion was recorded on March 10, 1933 during the main event of the Long Beach Earthquake (local Magnitude M_L=6.3) by

three accelerograph stations at (1) the Long Beach Public Utilities Building, (2) the Vernon CMD Building, and (3) the Los Angeles Subway Terminal.

The strong motion accelerogram recorded at the Long Beach Public Utilities Building is shown in Figure 1.1.

Thanks to the installation of an increasingly dense network of accelerographs around the world, a large number of ground movement records is now collected in many databases available on-line.

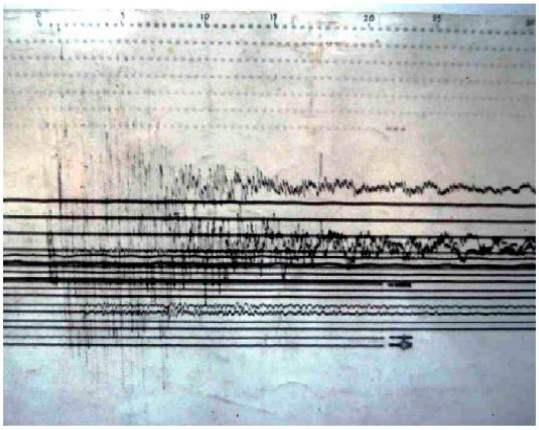

Figure 1.1 First strong motion recording: Long Beach Public Utilities Building.

1.3 Recording seismic signals

Seismic waves are detected by two types of seismic sensors: *seismometers* and *accelerometers*. These instruments give out electrical signals proportional to the ground motion in terms of velocity and acceleration, respectively. For the analysis and the interpretation of the ground motion, the detected seismic signals must be recorded in *analog* or *digital* form.

1.3.1 Analog recording

Analog accelerographs are optical-mechanical devices that produce the traces of the signal on film or paper. These instruments were in use since the early 1930s to the end of twentieth century, although the 2004 Parkfield earthquake was recorded principally on such instruments [Pacord and Luzi 2014]. A recording in analog form on paper is called *seismogram*. All *analog* paper recorders are based on a rotating drum with a pen which moves along an axis

parallel to the rotating axis to provide a continuous trace for the whole recording period, usually 24 hours [Alguacil and Havskov 2014].

An example of seismogram representing the earthquake activity during a dome-building of Mount St. Helens is shown in Figure 1.2.

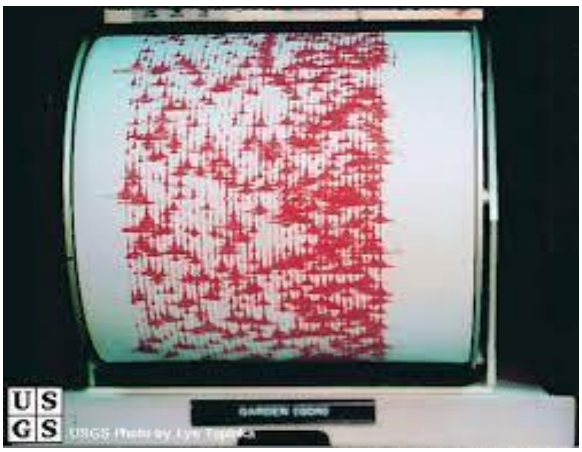

Figure 1.2 Example of an analog recording.

Analog accelerographs have three main drawbacks. First, they operate in "trigger mode" so as not to waste any data recording medium. This means that the accelerographs are triggered by a specific acceleration threshold and generally employ a very short memory buffer. So, these instruments do not preserve the pre- and post-event time series or even in the worst case, part of the waveform. Second, the natural frequency of transducers is generally limited to about 25 Hz or even less, limiting the usable frequency band. Third, in order to be able to use the recording in engineering applications, it is necessary to processing the film and then digitize the traces. This process is one of the main sources of errors and noise in the signal. [Pacord and Luzi 2014].

1.3.2 Digital recording

From the 1980s to nowadays, the most common way of recording ground motion is by digital accelerographs. These instruments provide a solution for all three drawbacks of analog records: *i*) they record signals in continuous mode on re-usable digital media (e.g., cassettes or solid-state memory) and preserve the pre- and post-event portions of the time series by use of memories able to retain wave arrivals, regardless of how weak these are, *ii*) the transducers have a much wider natural frequency range (50–100 Hz or even higher), *iii*) the digitization

process is performed automatically [Boore and Bommer 2005]. The precision of the recorded ground motion depends on the instrument settings, such as the digitizer's dynamic range, sampling rate and sensor full scale [Pacord and Luzi 2014].

A requirement for recording data digitally is to convert a continuous signal from analog to digital form. The process of converting a continuous analog signal into a series of numbers representing the signal at discrete intervals is called *analog-to-digital conversion* (*ADC*). The *ADC* process consists of two steps: first the signal is sampled at discrete time intervals, and then each sample is evaluated in terms of a number which then corresponds to the amplitude at the time of sampling [Alguacil and Havskov 2014].

In Figure 1.3 are reported two horizontal acceleration components $a(t)$ of the Aftershock of the Umbria-Marche seismic sequence occurred on 1997-10-07 05:09:56 UTC, recorded by co-located instruments (NCR-analog and NCR2-digital), installed at the Nocera Umbra (Central Italy) station.

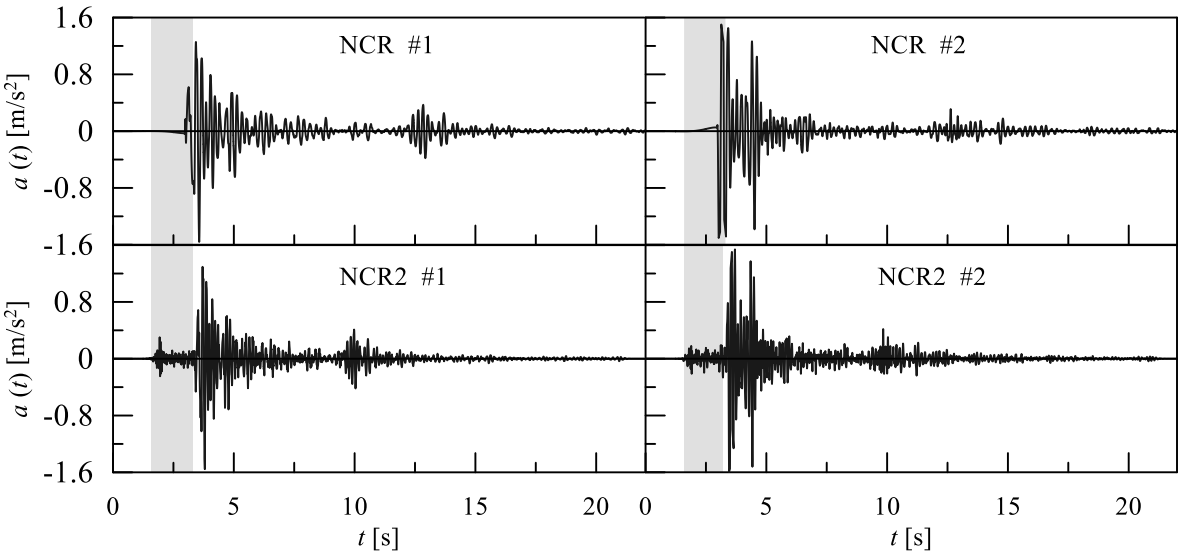

Figure 1.3 Acceleration time series of the same event recorded by the analog NCR (top) and the digital NCR2 (bottom) instruments, located in the same place.

This example shows that the Primary-waves (P-waves), occurred in the first instants of the ground movement, have been detected only by the NCR2 digital instrument (see horizontal components #1 and #2 of $a(t)$ in the shaded grey areas). The NCR analog instruments are not able to record the P-waves because analog devices are typically triggered by the Secondary-waves (S-waves). Thus, the use of digital instruments is preferred to also overcome this disadvantage.

1.4 Strong motion data processing

Signals obtained from accelerographs are not the exact reproduction of the ground motions as they may include background noises from several sources, each of which must be carefully evaluated and corrected. Different types of noise of various origins, at both high and low frequencies, may be caused from ocean waves, traffic, construction activity, wind (transmitted to the ground by vibration of trees), atmospheric pressure changes, etc.

Another source of error can be associated with the triggering of analog seismographs: if an instrument does not start until some triggering level of motion is reached, the entire accelerogram is in error by the level of motion at the time of triggering. Errors due to the analog recording process and the often hand-made analog-to-digital conversion have been overcome by the spread of digital recordings.

Nowadays, high-dynamic-range, broadband, high-resolution digital recordings of ground accelerations from earthquakes have the potential to yield ground displacements over a wide range of frequencies, including those so low that the displacements give the residual static deformation following an earthquake (also called “residual displacement”) [Boore et al. 2002]. The long-period information is of interest to seismologists for unravelling the dynamic process of fault rupture and may be of interest to engineers for designing large structures with very-long-period response [Wang et al. 2003]. Unfortunately, the digital recordings are often plagued by the baseline offsets: small steps or distortions in the reference level of motion [Iwan et al. 1985, Chiu 1997, Boore 1999, Boore 2001]; these offsets are caused by: mechanical or electrical hysteresis in the sensor, static buildup in the Analog/Digital converter, ground tilt and rotation due either to elastic deformation close to large ruptures or to inelastic deformation from slumping or cracking of the earth beneath the recording site.

The influence of noises and errors in ground motion records are more evident in the velocity $v(t)$ and displacement $d(t)$ traces rather than in acceleration $a(t)$ ones. Specifically, drifts in velocity and displacement are caused by the accumulation of the random errors in the accelerogram resulting from single and double integration of the random noise [Boore et al. 2002]. Integration of an uncorrected acceleration time history, for example, will produce a linear error in velocity and a quadratic error in displacement (see Figure 1.4).

An acceleration error as small as 0.001 g at the beginning of a 30-sec long accelerogram would erroneously predict a permanent displacement of 441 cm at the end of the motion [Kramer 1996].

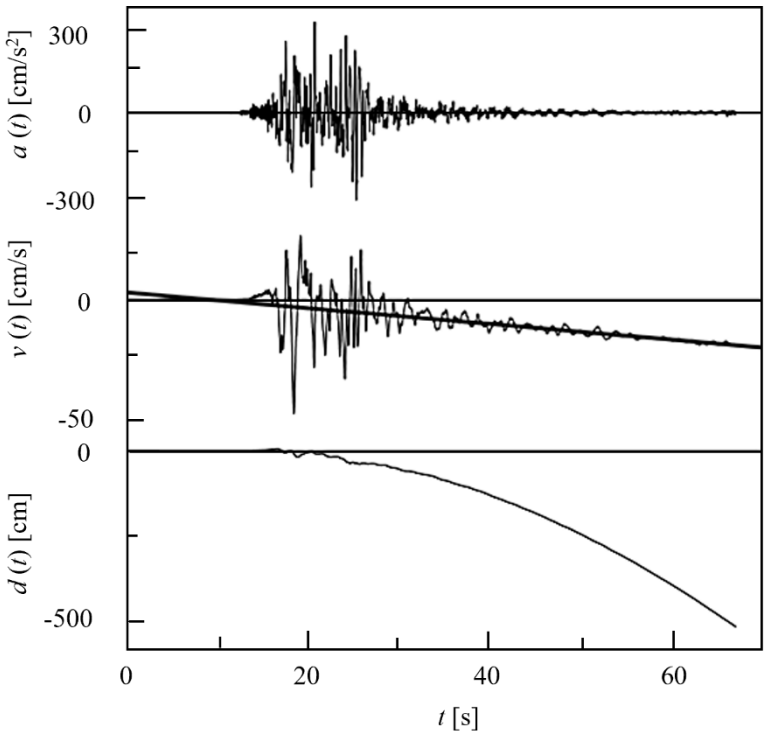

Figure 1.4 Velocity (middle) and displacement (bottom) time histories obtained by successive integration of the acceleration trace (top) without the baseline correction [Boore et al. 2002].

Due to the numerous sources of noises and errors there is no universal correction scheme that can be applied blindly to the records, but a degree of subjectivity is always involved during the processing of a record. Hence, the need of a processing procedure arises to evaluate reliable ground motion and to retrieve the maximum amount of reliable information from the analysis of the recorded signals. In order to correct the aforementioned errors and noises two correction methods can be applied*: baseline adjustment* and *low frequency filtering*.

1.4.1 Baseline correction

Strong motion recordings contain baseline offsets that need to be removed as they can produce unrealistic velocity and displacement time histories.

After one earthquake, there is slow down on ground motion with time: the acceleration decreases becoming small, the velocity tends to zero, and the displacement tends to a steady value (zero or permanent displacement value). Therefore, the result of correct baseline should satisfy the following: *i*) the end of amplitude velocity time history value is zero; *ii*) the

displacement time history curve tends to be parallel to the abscissa [Guorui and Tao 2015]. The displacement time history curve ending value determine whether there is permanent displacement.

According to Peizhen et al. [2008] and Xiaojun et al. [2008], one way to assess the reliability of the baseline correction result consists in the comparison between the final value of the displacement time history and the actual ground deformation measured by the Global Position System (GPS). However, not all of the station's ground deformations are recorded by GPS in real time so this might not be an option for all stations around the world.

Different baseline correction schemes have been proposed in the literature. The simplest way to obtain a zero-value at the end of the velocity time history consists in subtracting from the accelerogram its mean value. In case of strong motion records having a pre-event, it's possible to subtract to the whole record, the mean value calculated only on the prior part of the event [Zhang et al. 2010, Wang and Zhou 2004]. In their studies, [Boore 1999, Haiying et al. 2009, Decai and Xianguo 2001] suggest adopting the baseline initialization subtracting the mean values between 0 ~20 s.

The baseline correction, based on the use of the least square method, was originally accomplished by *i*) determining, through regression analysis the second-order polynomial curve (parabola) that best fits the time-acceleration pairs of values and then *ii*) subtracting from the actual acceleration values their corresponding counterparts as obtained with the regression-derived equation [Kramer 1996]. Nowadays, polynomials of up to the 3rd degree are employed for the baseline correction. The choice of the order curve should be made on an individual basis with some level of subjectivity, and this is the drawback of the approach.

1.4.2 Frequency filtering

Filtering is employed to remove unwanted frequency components from a given signal. *Lowpass filtering* suppresses frequencies that are higher than a defined cut-off frequency; *highpass filtering* allows frequencies that are higher than the cut-off frequency to pass through, *bandpass filtering* allows signals within a given frequency range bandwidth to pass through and *bandstop filtering* suppresses signals within the given frequency range. The Butterworth, Chebyshev and Bessel filters are typically used for this operation.

1.5 Ground-motion intensity measures

For different engineering purposes can be convenient to represent the seismic ground motion in terms of simple parameters instead of the entire time-history. The ground motion parameters can be essential for describing the salient features of the recorded accelerograms in compact form. They can be evaluated both in time and frequency domains.

1.5.1 Time-domain parameters

The most common way of representing a ground motion is through a time history expressed in terms of acceleration $a(t)$, velocity $v(t)$, or displacement $d(t)$. Typically, only the first of these quantities is measured directly while the others are computed from it by integration and/or differentiation [Kramer 1996].

Acceleration, velocity, and displacement time histories of the two horizontal components of the Loma Prieta earthquake recorded in 1989 by the station Gilroy #1 (rock), are shown in Figure 1.5. A large amount of information can be extracted by examining a time history.

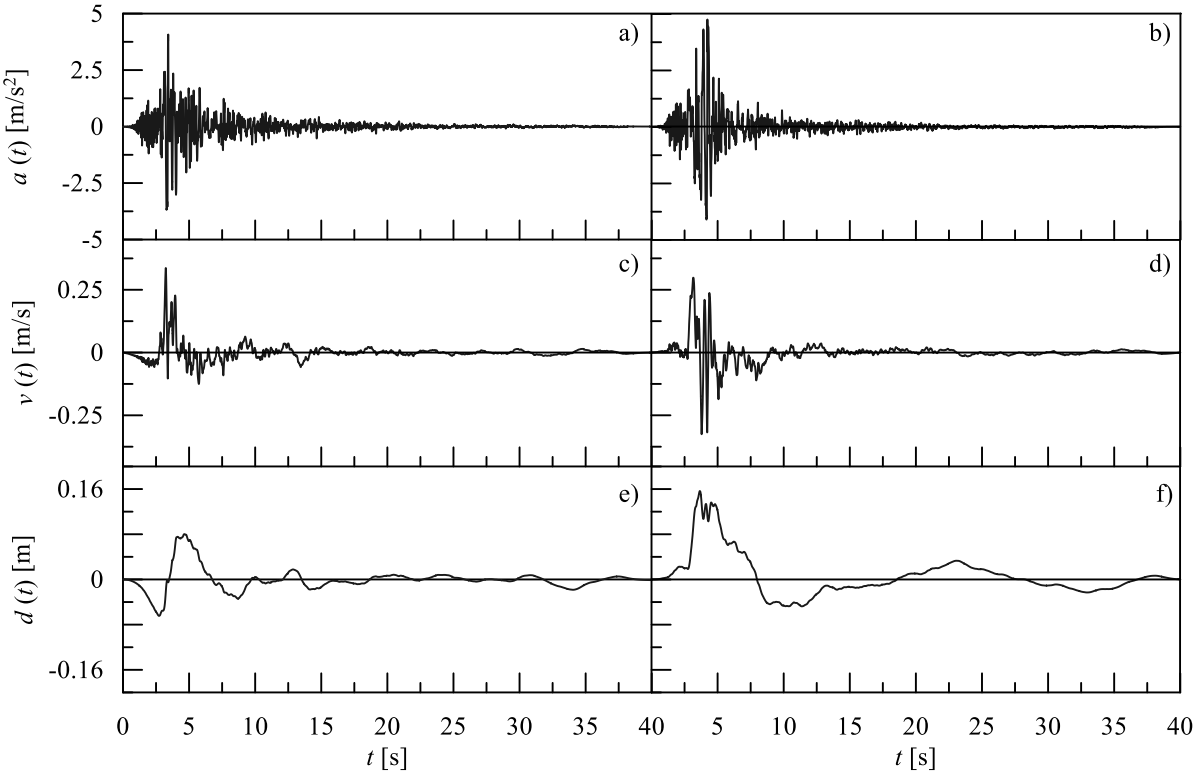

Figure 1.5 Horizontal components of the Loma Prieta 1989 earthquake (Gilroy #1 station): a), b) accelerations, c), d) velocities, e), f) displacements. Left column: 000 component, right column: 090 component.

➢ PGA, PGV, PGD

The most commonly parameter used for the characterization of ground motion amplitude is the *peak ground acceleration*, $PGA=\max|a(t)|$, which denotes the largest absolute acceleration observed on the accelerometric time history. Since the acceleration record undergoes few changes after the application of the processing procedure, it is possible to calculate the *PGA* value either from raw or corrected signal. The *peak ground velocity* $PGV=\max|v(t)|$ and the *peak ground displacement* $PGD=\max|d(t)|$ are others useful parameter for characterization of ground motion amplitude. These two parameters can be estimated only after processing the accelerometric record, since the time histories in terms of velocity and displacement are strongly influenced by the correction made through the processing procedure. In Figure 1.6 is shown a comparison between the peak ground values of acceleration (*PGA*), velocity (*PGV*) and displacement (*PGD*) evaluated for both raw and corrected time-histories of the Est-West Aquila earthquake occurred on 2016-08-24 at 17:46:09 in Central Italy and recorded at AQV station.

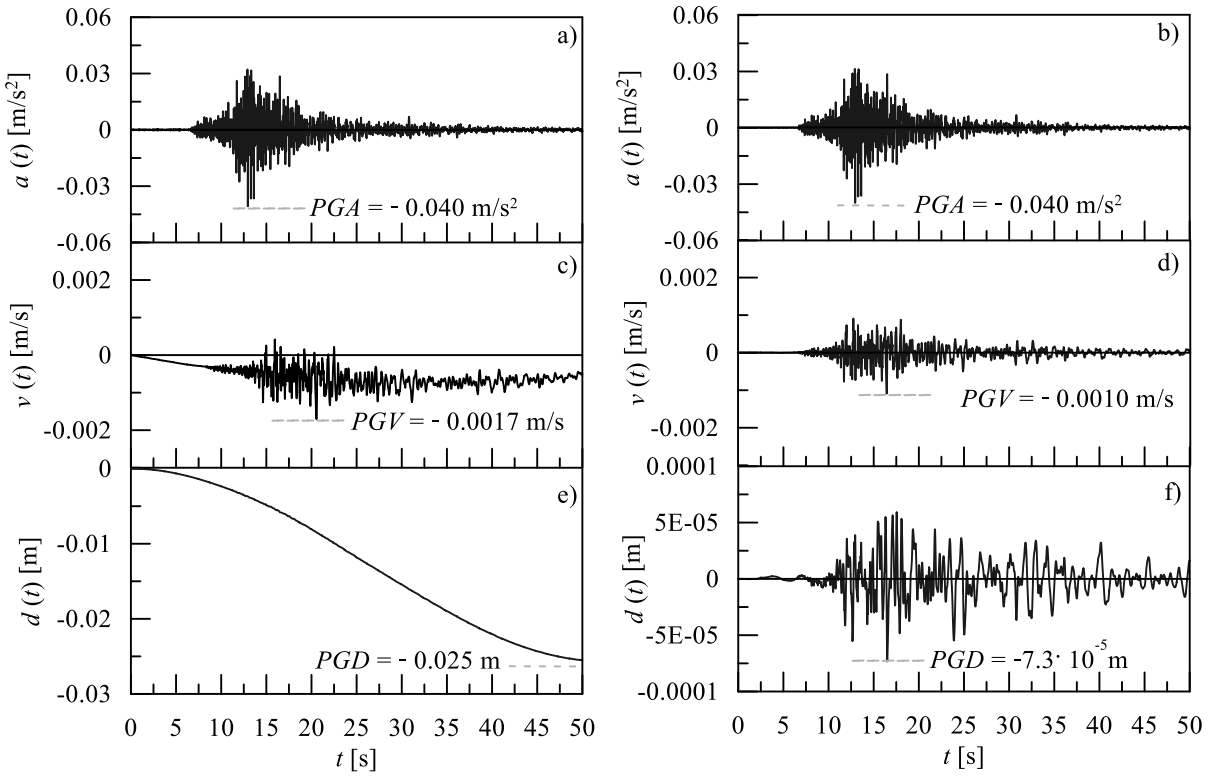

Figure 1.6 Est-West component of the 2016 Aquila earthquake (AQV station): a), b) accelerations, c), d) velocities, e), f) displacements. Left column: raw signal, right column: processed signal.

It can be noticed that: the value of PGA = -0.040 m/s^2 is the same for both cases, the PGV assumes slightly different values that are equal to -0.0017 m/s and -0.0010 m/s respectively while the PGD value differs a lot decreasing from $-2.5 \cdot 10^{-2}$ m (uncorrected time-history) to $-7.3 \cdot 10^{-2}$ m (processed signal).

The three aforementioned parameters (*PGA*, *PGV* and *PGD*) provide information only on the peak amplitudes of single cycles that occur within the ground motion record. In some cases, damage may be closely related to peak amplitudes, but in others, it may be associated with repeated cycles of high amplitude.

In Figure 1.7 is shown a comparison between the first horizontal component of the 1972 Stone Canyon Earthquake recorded by: the Bear Valley #1 and the Stone Canyon Geophys Obs stations. The two accelerograms, characterized by the same values of magnitude M=4.81 and PGA=1.6 m/s^2, have completely different features in time. In the first case the maximum amplitude of the time history is concentrated around 1.7 s while, in the second case, there are several instants in which the acceleration reaches values close to the peak one. Therefore, to characterize the earthquake ground motion it is necessary to calculate different seismic parameters able to reflect other important waveform features.

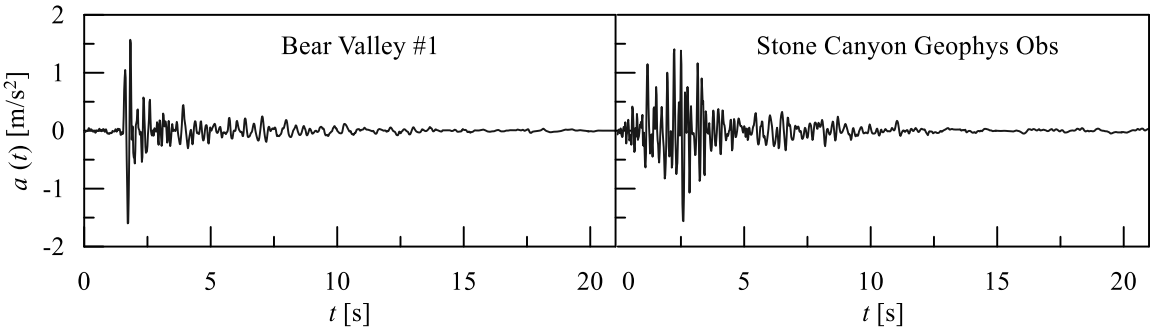

Figure 1.7 Acceleration time histories of the 1972 Stone Canyon Earthquake recorded by the Bear Valley #1 and the Stone Canyon Geophys Obs stations.

➢ Total intensity and Arias intensity

Other parameters of fundamental importance in defining the variation in time of the accelerogram are the *total intensity*, I_0, and its variation in time, usually referred as *cumulative total intensity* $I_0(t)$. The *total intensity* I_0, of a recorded accelerogram $a(t)$ of duration t_F, is given in the time domain by the area under the time history of squared acceleration [Kramer 1996].

It can be easily recognized that the *total intensity* is dimensionally proportional to the energy of the accelerogram. The *cumulative variation in time of total intensity* $I_0(t)$, is defined in the time-domain as:

$$I_0(t) = \int_0^t a^2(\tau)\,\mathrm{d}\tau; \quad 0 \le t \le t_F\,. \tag{1.1}$$

A parameter related to the *total intensity* I_0 is the *Arias intensity* I_A [Arias, 1970] defined as:

$$I_A = \frac{\pi}{2g}\int_0^{t_F} a^2(\tau)\,\mathrm{d}\tau; \tag{1.2}$$

being g the gravity acceleration. The *Arias intensity*, that is a time-integral parameter adopted to measure the strength of a ground motion, has the dimension of a velocity.

The *cumulative Arias intensity* $I_A(t)$ of the seismic signal, normalized with respect to the *Arias intensity* I_A, is referred in the literature as *Husid function*, and can be expressed as:

$$H(t) = \frac{I_A(t)}{I_A} \equiv \frac{\int_0^t a^2(\tau)\,\mathrm{d}\tau}{\int_0^{t_F} a^2(\tau)\,\mathrm{d}\tau}; \quad 0 \le t \le t_F \Rightarrow 0 \le H(t) \le 1 \tag{1.3}$$

It can be used to determine the portion of the accelerogram which is more likely to cause damage to the built environment.

For illustrative purposes, Figure 1.8 shows the time histories of the ground acceleration (horizontal components azimuth equal to 0) recorded during the 1989 Loma Prieta Earthquake, at Gilroy #1 and Gilroy #6 stations, respectively.

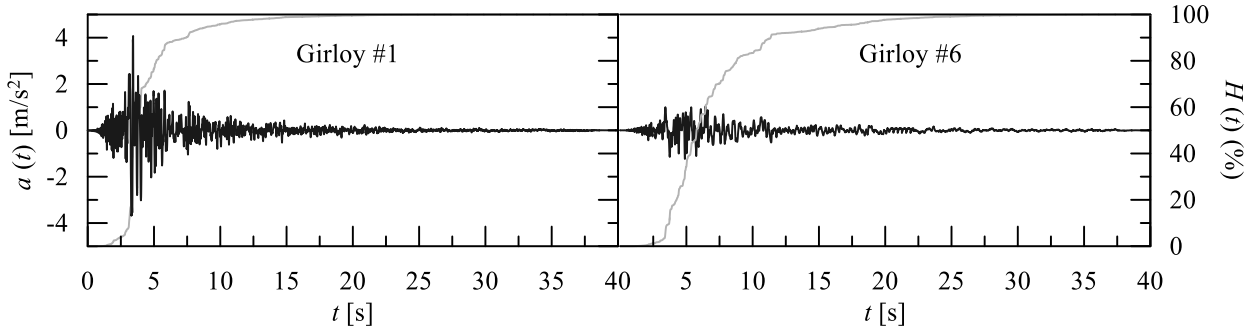

Figure 1.8 Time histories and percentage of *Husid function* $H(t)$ (%) of the 1989 Loma Prieta earthquake (Gilroy #1 and Gilroy #6 stations).

➢ A_{95} parameter

For a given acceleration record $a(t)$ and for a given acceleration level A, it's possible to determine the area E_x bounded by the curve $a(t)^2$ and the horizontal line at A^2 level, as shown in Figure 1.9. The acceleration level A which gives the ratio I_A/E_x equal to 0.05 is defined as the parameter A_{95}, being E_x a fraction of *Arias intensity* above the acceleration level A. This parameter, related to the *Arias intensity*, is widely used to describe the damage potential of the earthquake at a site [Sarma and Yang 1987].

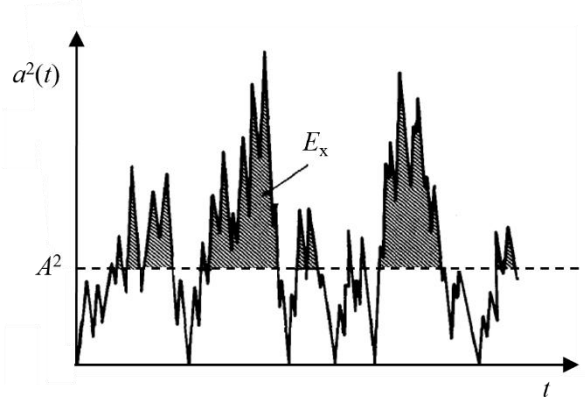

Figure 1.9 Schematic diagram for the definition of E_x [Sarma and Yang 1987].

➢ Strong motion duration

The *strong motion duration* (*SMD*) of an accelerogram rather than the duration of the entire time history is a more useful parameter for identifying the portion of the record where the amplitude of ground motion can potentially cause damage to engineering structures. Several definitions of the *strong motion duration* of an acceleration record have been proposed in the literature [Bommer and Martinez-Pereira 1999]. The most commonly used are the *bracketed duration* [Ambraseys 1967, Bolt 1973] and the *significant duration* [Trifunac and Brady 1975].

In 1969, Bolt proposed the *bracketed duration*, which is the elapsed time between the first and the last excursions of a specified level of acceleration (usually 0.05g).

An example of the definition of *bracketed duration* for the E-W acceleration components of the 1989 Loma Prieta earthquake recorded by a) Gilroy #1 (rock) and b) Gilroy #2 stations, are reported in Figure 1.10.

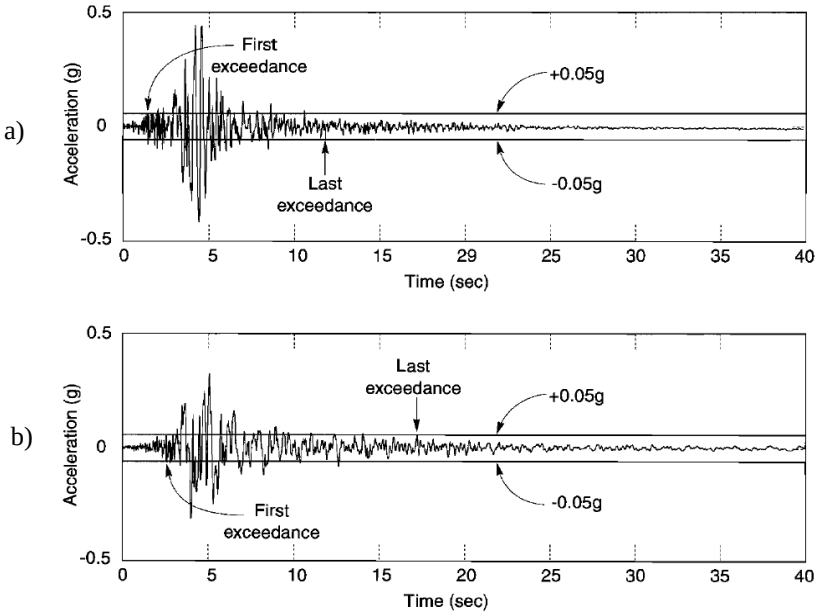

Figure 1.10 *Bracketed durations* of the E-W components of the: a) Gilroy #1 (rock) and b) Gilroy #2 (soil) ground motions [Kramer 1996].

In 1975, Trifunac and Brady defined the *significant duration* as the interval of time over which a percentage of *Arias intensity* is accumulated. Usually, this range is between 5% and 95% ($t_{5\text{-}95}$) or between 5% and 75% ($t_{5\text{-}75}$) of the *cumulative normalized Aria intensity* $I_A(t)$, that is coincident with the *Husid function*. An example of the definition of the *significant duration* is shown in Figure 1.11.

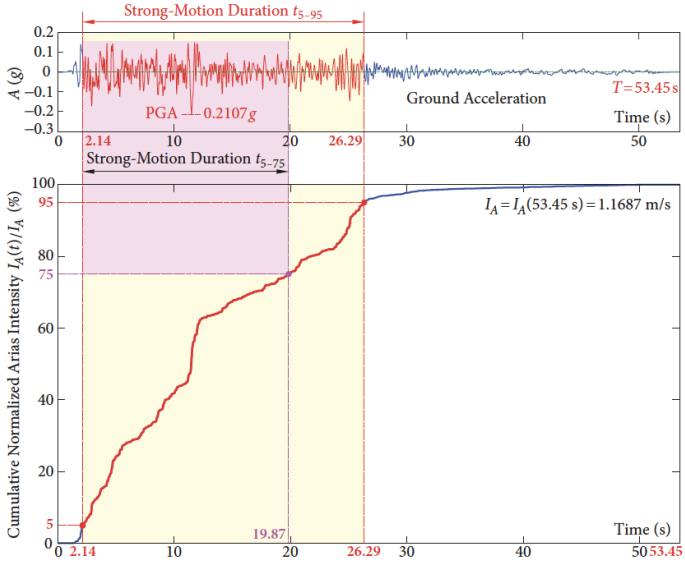

Figure 1.11 *Cumulative normalized Arias intensity* and *strong-motion duration* of the El Centro earthquake [Xie et al. 2019].

1.5.2 Frequency-content Parameters

The dynamic response of compliant objects, be they buildings, bridges, slopes, or soil deposits, is very sensitive to the frequency at which they are loaded. Earthquakes produce complicated loading with components of motion that span a broad range of frequencies. The analysis of frequency content describes how the amplitude of a ground motion is distributed among different frequencies. Since the frequency content of an earthquake motion will strongly influence the effects of that motion, characterization of the motion cannot be complete without consideration of its frequency content [Kramer 1996]. In the following the most common parameters or functions able to characterize the frequency content of the accelerograms are briefly described.

➢ PGV/PGA

A preliminary estimation of the frequency content of the ground motion may be evaluated by the *PGV*/*PGA* ratio. For a simple harmonic wave of period *T*, the ratio $PGV/PGA=\omega$. For earthquake motion that includes many frequencies, the quantity $T=2\pi/(PGV/PGA)$ can be interpreted as the period of vibration of an equivalent harmonic wave thus, this ratio parameter provides an indication of which period of the ground motion is most significant.

➢ Fourier amplitude spectrum and power spectral density function

The representation of a function of time in the frequency domain can bring up some of the signal salient characteristics and can be obtained through the application of the *Fourier transform* $\mathbb{F}\langle\cdot\rangle$.

The *Fourier transform* of an accelerogram $a(t)$ with total duration t_F is defined as follow:

$$A(\omega)=\mathbb{F}\langle a(t)\rangle=\int_{-\infty}^{\infty}a(t)\,\mathrm{e}^{-i\omega t}\mathrm{d}t\equiv\int_{0}^{t_F}a(t)\,e^{-i\omega t}\mathrm{d}t \tag{1.4}$$

being $i=\sqrt{-1}$ the imaginary unity.

Since $A(\omega)$ is a complex-values function, it can be expressed as:

$$A(\omega) = \mathrm{Re}[A(\omega)] - i\,\mathrm{Im}\left[A(\omega)\right] \tag{1.5}$$

where:

$$\mathrm{Re}[A(\omega)] = \int_0^{t_F} a(t)\,\cos\left(\omega t\right)\mathrm{d}t; \quad \mathrm{Im}[A(\omega)] = \int_0^{t_F} a(t)\sin\left(\omega t\right)\mathrm{d}t; \tag{1.6}$$

A quantity of particular significance is the *Fourier amplitude spectrum* $FAS_A(\omega)$ defined as:

$$FAS_A\left(\omega\right) = |\,A(\omega)\,| = \sqrt{\mathrm{Re}\left[A(\omega)\right]^2 + \mathrm{Im}\left[A(\omega)\right]^2} \tag{1.7}$$

The FAS_A (ω) shows the harmonic functions present in the original signal while the *argument spectrum* (*Fourier phase spectrum*) θ_A (ω) indicates the phase offset of each sine wave:

$$\theta_A(\omega) = \mathrm{arct}\,\frac{\mathrm{Im}\left[A(\omega)\right]}{\mathrm{Re}\left[A(\omega)\right]} \tag{1.8}$$

The *Fourier amplitude spectrum*, often called *Fourier spectrum*, of a ground motion portrays the ground motion in the frequency domain and serves to analyse the composition of the ground motion in terms of harmonic components. In particular, the *Fourier spectrum* is used to identify the harmonic components of the ground motion that possess the largest amplitudes. As these harmonic components are in general identified in terms of their frequencies, this type of analysis is referred to as a frequency analysis. By the same token, the description of the frequency composition of a ground motion is known as the analysis of its frequency content. *Fourier spectrum* is the quantity most frequently studied by seismologists in their investigations of earthquake mechanisms, as the frequency content of a ground motion is a function of source mechanism, focal depth, epicentral distance, travel path, site-soil conditions, and earthquake magnitude.

The *Fourier amplitude spectrum* may be narrow or broad. A narrow spectrum implies that the motion has dominant frequency (or period), which can produce a smooth, almost sinusoidal time history. A broad spectrum corresponds to a motion that contains a variety of frequencies that produce a more jagged, irregular time history [Kramer 1996].

Strictly related to the *Fourier spectrum* is the *power spectrum*, often improperly referred in the literature as *power spectral density* (*PSD*) function. For a recorded accelerogram, $a(t)$, of duration t_F, it is defined as [Kramer 1996]:

$$G(\omega) = \frac{A(\omega)^2}{\pi t_F} \tag{1.9}$$

Notice that by applying the Parseval's theorem the energy of a signal, also called *total intensity* of an accelerogram, can be evaluated in both time and frequency domain, as:

$$I_0 = \int_0^{t_F} a^2(\tau)\,\mathrm{d}\tau = \frac{1}{\pi}\int_0^{\infty} \left|A(\omega)\right|^2 \mathrm{d}\omega \cong \frac{1}{\pi}\int_0^{\omega_N} \left|A(\omega)\right|^2 \mathrm{d}\omega \tag{1.10}$$

where $\omega_N = \pi/\Delta t$ is the Nyquist frequency [Kramer 1996].

➢ Cumulative Fourier energy function and strong circular frequency

The *cumulative Fourier energy* function $E_A(\omega)$ gives information about the distribution of the frequencies in the *Fourier amplitude spectrum* FAS_A. This parameter is very useful in the applications concerning the *wavelet analysis* in which, the way to divide the frequency range of interest into many bands represents a fundamental step [Genovese et al. 2021 a].

The *cumulative Fourier energy* function is given by:

$$E_A(\omega) = E\left\langle FAS_A \right\rangle = \frac{1}{\pi}\int_0^{\infty} |\,A(\omega)\,|^2\,\mathrm{d}\omega \tag{1.11}$$

The range between 5% and 95% of the *cumulative Fourier energy* function can be defined as *strong* (*circular*) *frequency* $\omega_{5\text{-}95} \equiv \upsilon_{5\text{-}95}$.

➢ Predominant period

The *predominant period* T_p is defined as the period of vibration corresponding to the maximum value of the *Fourier amplitude spectrum*. To avoid undue influence of individual spikes of the *Fourier amplitude spectrum*, the *predominant period* is often obtained from a smoothed spectrum. While the *predominant period* provides some information regarding the

frequency content, it is easy to see (Figure 1.12) that motions with radically different frequency contents can have the same predominant period [Kramer 1996].

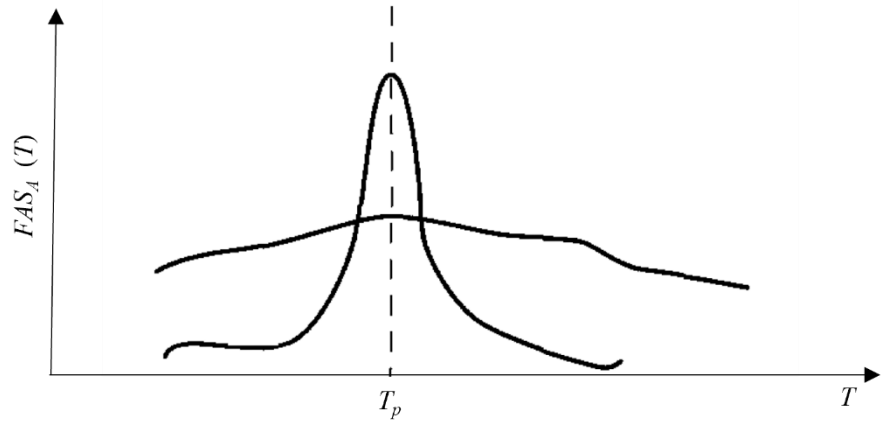

Figure 1.12 Two hypothetical *Fourier amplitude spectra* with the same predominant period but very different frequency contents. The upper curve describes a wideband motion and the lower a narrowband motion [Kramer 1996].

➢ Bandwidth

The *predominant period* can be used to locate the peak of the *Fourier amplitude spectrum*. However, it provides no information on the dispersion of spectral amplitudes about the *predominant period*. The *bandwidth* of the *Fourier amplitude spectrum* is the range of frequency over which some level of *Fourier* amplitude is exceeded. Specifically, *bandwidth* is usually measured at the level where the power of the spectrum is half its maximum value; this corresponds to a level of $1/\sqrt{2}$ times the maximum *Fourier* amplitude. The irregular shape of individual *Fourier amplitude spectra* often renders bandwidth difficult to evaluate. It is determined more easily for smoothed spectra [Kramer 1996].

➢ Central frequency

The *central frequency* Ω [Vanmarke 1976] is a measure of the frequency where the power spectral density is concentrated:

$$\Omega = \frac{\lambda_2}{\lambda_0} \tag{1.12}$$

being λ_0 and λ_2 respectively the zero-order and second-order spectral moments of a ground motion. The *i*-th spectral moment can be defined as follows:

$$\lambda_i = \int_0^{\omega_N} \omega^i G(\omega) d\omega. \tag{1.13}$$

➢ Shape factor

The *shape factor* [Vanmarcke 1976] indicates the dispersion of the power spectral density function about the central frequency:

$$\delta = \sqrt{1 - \frac{\lambda_1^2}{\lambda_0 \lambda_2}} \tag{1.14}$$

The *shape factor* always lies between 0 and 1, with higher values corresponding to larger bandwidths.

➢ Zero-level up-crossings and peaks

It is well known that the frequency content of a recorded accelerogram is related to the frequency of occurrences of: a) both positive and negative maxima, also called *peaks P*; b) crossings of the time-axis with positive slope, commonly called *zero-level up-crossings* N_0^+.

The counting of *zero-level crossings N* of the time axis and *peaks P* of an accelerogram, are widely used to evaluate some spectral parameters or to characterize the *power spectral density* (*PSD*) function [Muscolino et al. 2021] of a recorded accelerogram.

Zero-level crossing is a point where the sign of a mathematical function changes from positive to negative (*zero-level up-crossing* $N_0^+ \cong N/2$) or from negative to positive *(zero-level down-crossing* $N_0^- \cong N/2$). *Peaks* are the sum of the positive P^+ and negative P^- maxima inside a function.

A representation of *zero-level crossings N*, maxima and minima *P* (positive and negative) of a function are reported in Figure 1.13. An example of the cumulative variation in time of *zero level up crossing* $N_0^+(t)$ for the 1989 Loma Prieta earthquake (0 component), recorded by the Girloy #6 station, is reported in Figure 1.14.

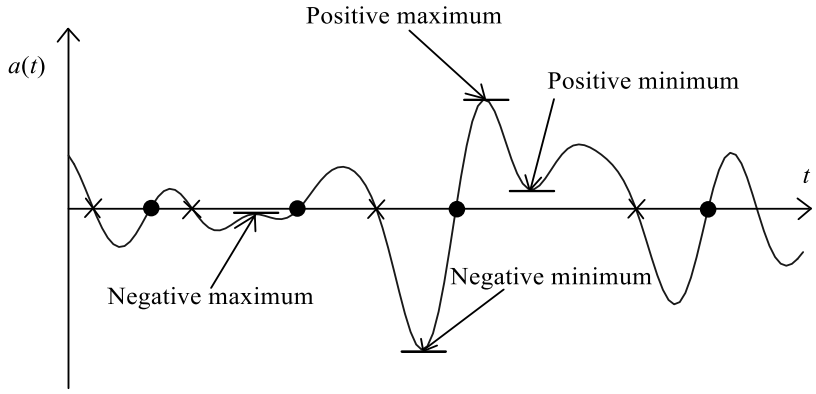

Figure 1.13 Maxima and minima of the function together with the *zero-level up-crossing* (●) and *zero-level down-crossing* (×) rate of the time axis of the signal $a(t)$.

The relationship between *zero-crossings* and spectral content of a signal has been investigated extensively in the literature [Kedem 1986, Kay and Sudhaker 1986, Sreenivas and Niederjohn 1992].

The counting of *zero-level crossings* N of the time axis is used to evaluate the *destructiveness potential factor* P_D that allows to separate among accelerograms that produce real damage from the ones that are only ground vibration without produce damage to structures at the site of recording [Saragoni and Díaz 1999]. It is expressed as follows:

$$P_D = \frac{I_A}{\upsilon_0^2} \tag{1.15}$$

being $\upsilon_0 = N/t_F$ the *intensity of zero crossings* (value of the zero crossing per second).

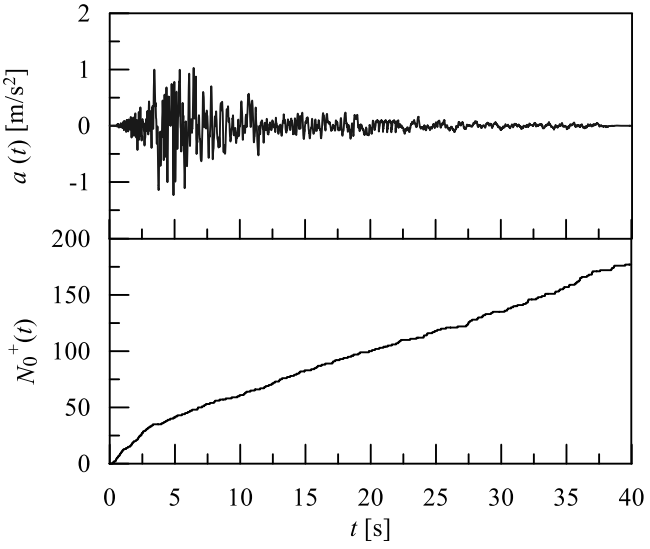

Figure 1.14 Accelerogram, $a(t)$, and *cumulative zero-level up crossings*, $N_0^+(t)$, of the 1989 Loma Prieta earthquake.

The ratio of the *zero-level up-crossings frequency* to the *peak frequency*, the so-called *irregularity factor* I_F [Lutes and Sarkani 2004], gives a measure of the bandwidth of the process, i.e. how much the examined stochastic process differs from the narrow band one. It is defined as:

$$I_F = \frac{\upsilon_0^+}{\upsilon_P} = \frac{N_0^+}{P}; \quad 0 < I_F \leq 1 \tag{1.16}$$

being $\upsilon_0^+ = N_0^+ / t_F$ the *intensity of zero-level up crossings* and $\upsilon_P = P/t_F$ the *intensity of peaks*. Indeed, for ideal very narrow-band zero-mean stationary stochastic processes, the *zero-level up-crossings* frequency and *peaks* frequency are exactly the same, and the *irregularity factor* is unitary; for wider bandwidths, more than one peak occurs between two *zero-level up-crossings*, and the *irregularity factor* is less than one (see Figure 1.15).

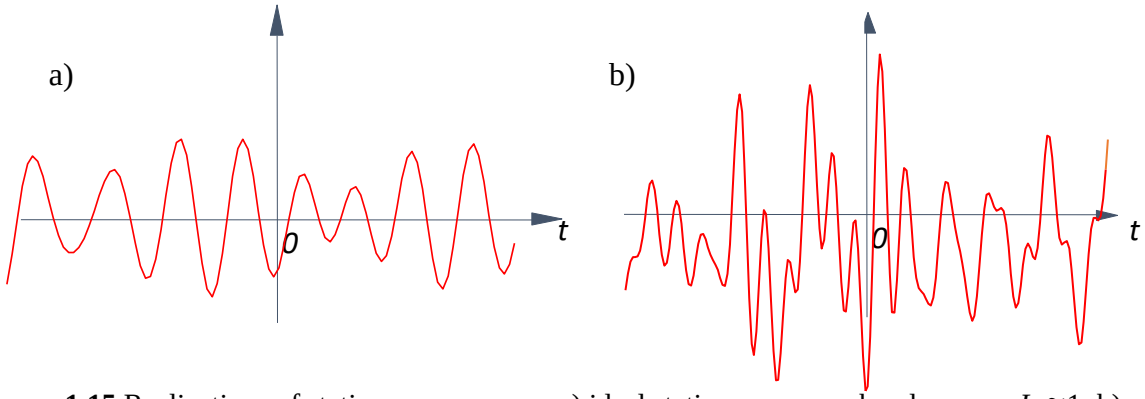

Figure 1.15 Realizations of stationary processes: a) ideal stationary narrowband process $I_F \cong 1$; b) stationary broadband process $I_F < 1$.

The bandwidth parameter can be approximately evaluated by the following alternative formula [Solnes 1997]:

$$\varepsilon = \sqrt{4r(1-r)} \tag{1.17}$$

being $r = P^- / P$.

The evaluation of spectral parameters by analysing the frequency of *zero-level up-crossings* and *peaks* of recorded accelerograms emphasizes the usefulness of the time-history also to identify the frequency content of an accelerogram.

➢ Response spectra

For many engineering and scientific applications, *response spectra* are used extensively to represent the seismic action in terms of maxima of relative displacement, relative velocity or absolute acceleration at selected frequencies or periods. In particular, the *response spectrum* is defined as the maximum response amplitude of a single degree-of-freedom (*SDOF*) system, subject to an acceleration time history, as a function of the system natural frequency ω (or natural period T) and damping ratio ξ (usually assumed equal to 5%).

The maximum amplitude of the response is obtained by integrating the equation of the motion of the *SDOF* system with unitary mass, the so-called canonical oscillator:

$$\ddot{y}(t) + 2\,\xi\,\omega\,\dot{y}(t) + \omega^2\,y(t) = a(t) \tag{1.18}$$

where $\ddot{y}(t)$, $\dot{y}(t)$, $y(t)$ are respectively the relative acceleration, velocity, and displacement of the oscillator with respect to the ground while $\omega=2\pi/T$ is the circular frequency of the oscillator. When acceleration, velocity or displacement is considered, the following functions are introduced:

displacement response spectrum:

$$SD(T,\xi) = \max_{0\le t\le t_F} |\,y(t)\,| \tag{1.19}$$

velocity response spectrum:

$$SV(T,\xi) = \max_{0\le t\le t_F} |\,\dot{y}(t)\,| \tag{1.20}$$

acceleration spectrum (absolute):

$$SA(T,\xi) = \max_{0\le t\le t_F} |\,\ddot{y}(t) + a(t)\,| = \max_{0\le t\le t_F} |\,2\xi\,\omega\,\dot{y}(t) + \omega^2\,y(t)\,| \tag{1.21}$$

The *pseudo-velocity* and *pseudo-acceleration response spectra* are also widely used in practice and can be defined as a function of the displacement as follows:

pseudo-acceleration response spectrum:

$$PSA(T,\xi) = \left(\frac{2\pi}{T}\right)^2 SD(T,\xi) \tag{1.22}$$

pseudo-velocity response spectrum:

$$PSV(T,\xi)=\left(\frac{2\pi}{T}\right)SD(T,\xi) \tag{1.23}$$

The *acceleration response spectrum* is used extensively in earthquake engineering practice for the representation of the maximum force imposed on the structure which can be evaluated as the product of the maximum absolute value of the acceleration times the mass *m* of the system. Computed *response spectra* for the 1989 Loma Prieta earthquake (Girloy #6 station – 0 component) are illustrated in Figure 1.16.

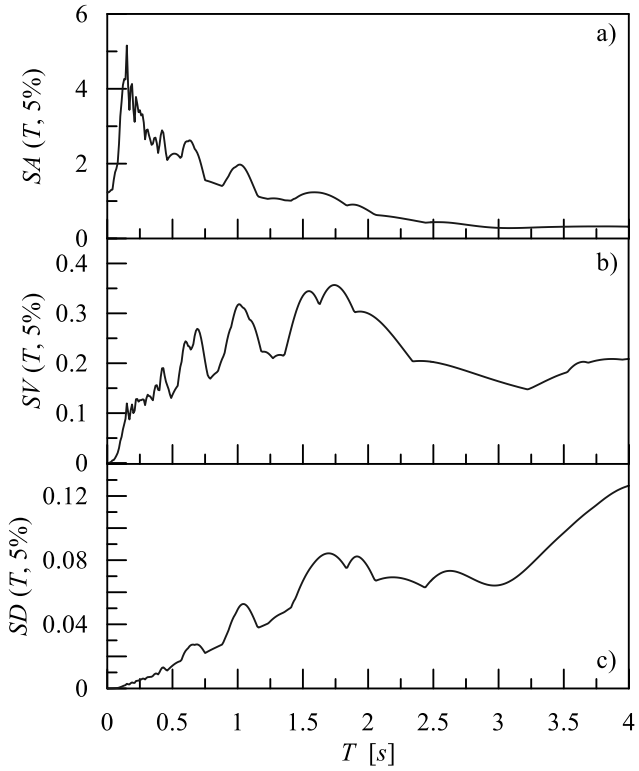

Figure 1.16 *Response spectra* computed for the 1989 Loma Prieta earthquake in terms of: a) absolute acceleration, b) velocity, c) displacement.

1.5.3 Other parameters

The aforementioned parameters describing the amplitude, the frequency content or the time duration of an accelerogram are the main adopted parameters in the framework of seismic engineering. However, in the literature, other parameters have been introduced that combine

more than one effect. In this paragraph, parameters that reflect important characteristics of ground motions, have been summarized.

A single parameter that includes the effects of the amplitude and frequency content of a strong motion record is the root mean square (*rms*) acceleration, *arms*, defined as:

$$arms = \sqrt{\frac{1}{t_F}\int_0^{t_F} a(t)^2 dt} = \sqrt{\lambda_0} \tag{1.24}$$

Similar to *arms* definition, can be evaluated the *rms* velocity and displacement:

$$vrms = \sqrt{\frac{1}{t_F}\int_0^{t_F} v(t)^2 dt}; \qquad drms = \sqrt{\frac{1}{t_F}\int_0^{t_F} d(t)^2 dt} \tag{1.25}$$

The *characteristic intensity Ic* is related linearly to an index of structural damage due to maximum deformations and absorbed hysteretic energy [Ang 1990].

$$Ic = arms^{1.5}\sqrt{t_F} \tag{1.26}$$

The *cumulative absolute velocity* is the area under the absolute accelerogram:

$$CAV = \int_0^{t_F} \left|a(t)\right| dt \tag{1.27}$$

while the *specific energy density SED* is the integral of the square of the velocity time history. It is a measure of the overall energy of the record (larger *SED*, larger energy and expected damage).

$$SED = \int_0^{t_F} \left|v(t)^2\right| dt \tag{1.28}$$

The *acceleration spectrum intensity* (*ASI*) is the area under the *acceleration response spectrum* between periods of 0.1 sec and 0.5 sec.

$$ASI = \int_{0.1}^{0.5} SA\left(T,\xi\right) \mathrm{d}t \tag{1.29}$$

Similar to *ASI* definition, can be evaluated the *velocity spectrum intensity* (*VSI*):

$$VSI = \int_{0.1}^{0.5} SV\left(T,\xi\right) \mathrm{d}t \tag{1.30}$$

The *response spectrum intensity* (*SI*) [Housner 1959] is the area under the *pseudovelocity response spectrum* between periods of 0.1 sec and 2.5 sec.

$$SI(\xi) = \int_{0.1}^{2.5} PSV\left(T,\xi\right) \mathrm{d}t \tag{1.31}$$

Chapter 2

Joint time-frequency signal representation

2.1 Introduction

This Chapter provides a brief overview to some key aspects of *Signal Analysis and Processing Theory* starting from a description of the main methods used for characterizing and manipulating signals.

A signal is a time function, but its frequency domain representation can bring up some of its salient features. Signals can be classified into different types depending on their characteristics: a signal is called “stationary” if its statistics do not change over time while it is defined “non-stationary” if its statistical characteristics change with time.

The classical *Fourier transform* is a powerful technique for the spectral analysis of stationary time-histories whose characteristics do not change with time. Since the signals encountered in earthquake engineering are typically non-stationary thus, the time-averaged amplitude spectrum, found by using *Fourier transform*, is not appropriate to track their changes in time of both frequency magnitude and phase. For the spectral analysis of these types of signals, having a spectral content that varies over time, there is a need for methods implementing a joint analysis in time and frequency domains.

A technique used for the time-frequency representations of non-stationary signals is the *windowed Fourier transform,* also called *Gabor transform* or *short time Fourier transform* (*STFT*), that consists firstly in the subdivision of a temporal signal into pieces with an appropriate window function and then in the evaluation of the *Fourier spectrum* for each windowed segment. The *STFT* assumes local stationarity of signal within short temporal windows. The main disadvantage of this method is about the choice of the window size that is not so straightforward. A wide window leads to a good frequency resolution with a reduced

time localization while, a narrower window leads to a good time resolution but a poor localization in frequency.

The trade-off between time and frequency resolution is related to the "Heisenberg's uncertainty principle" also called "Heisenberg–Gabor limit" which states that "for a given signal, one cannot achieve high temporal resolution and frequency resolution at the same time".

The disadvantages of the traditional *STFT* can be overcome by the *wavelet analysis* to which the last part of this Chapter is extensively dedicated.

2.2 Harmonic signals representation

The Harmonic analysis is a branch of mathematics that deals with the representation of a function as the superposition of basic waves.

The simplest time-varying signal $a(t)$ is the harmonic wave that varies sinusoidally with time. It can be expressed using trigonometric notation:

$$a(t) = A_{\mathrm{M}} \sin(\omega t + \phi) \tag{2.1}$$

being A_{M} the harmonic Amplitude, ω the circular frequency (rad/sec) and ϕ the angle phase (amount of time by which the peaks of the signal are shifted from those of the reference sinusoid having ϕ=0).

The geometric representation of a harmonic signal can be obtained by means of a phasor of radius A_{M} that rotates in the counter-clockwise direction at an angular speed of ω rad/sec and a ϕ starting angular position respect to the horizontal axis.

The interval of time taken for the phasor to make one full revolution is called "Period of vibration" T which is related to the circular frequency ω by:

$$T = \frac{\text{angular distance for one revolution}}{\text{angular speed}} = \frac{2\pi}{\omega} \tag{2.2}$$

being T, the time required for one cycle of the motion, its inverse, the frequency ν, represents the number of cycles per unit time, that is:

$$\nu = \frac{1}{T} = \frac{\omega}{2\pi} \tag{2.3}$$

2.3 Fourier analysis

Fourier analysis is the key to frequency analysis of vibration signals and represents a useful tool in many branches of science and engineering. It grew from the study of *Fourier series* made by the French mathematician Jean-Baptiste Joseph Fourier (1768-1830), who, in the early nineteenth century, showed that any periodic function that meets certain conditions can be expressed as the sum of a series of sinusoids of different amplitude, frequency, and phase.

Depending on the type of signal to be represented in frequency domain, three different versions of *Fourier transform* are used. The *Fourier series expansion* (*FSE*) is applicable only to periodic signals, the *Fourier transform* (*FT*), also called *Fourier integral transform*, can be applied to any general signal and the *discrete Fourier transform* (*DFT*) is used for discrete signals.

The coefficients deriving from the *Fourier analysis* can be expressed in terms of their real and imaginary parts or in terms of modulus and phase angle. In particular, the latter representation completely separates the frequency information which is apparent in the coefficients amplitudes and the time information hidden in their phases.

2.3.1 Fourier series

The *Fourier series expansion* represents any periodic function $f(t)$ of period T as a sum of n sinusoidal harmonic waves $e^{-i\omega_n t}$ of frequency $\omega_n = 2\pi n/T$. Since a *Fourier series* is simply a summation of simple harmonic functions, it can be expressed using either trigonometric notation or complex notation. The general exponential form of the *Fourier series* for a function $f(t)$ of period T can be expressed as follows:

$$f(t) = \sum_{k=-\infty}^{\infty} c_n^* \, \mathrm{e}^{i\omega_n t} \tag{2.4}$$

where the asterisk * indicates complex conjugate quantity. The *Fourier* coefficients c_n^* can be determined as:

$$c_n^* = \frac{1}{T}\int_0^T f(t)\,\mathrm{e}^{-i\omega_n t}\mathrm{d}t \tag{2.5}$$

being $i = \sqrt{-1}$ the imaginary unit.

The projection of the signal $f(t)$ on a basis of harmonic functions gives a measure on how a signal is similar to a sinusoidal wave of a given frequency. An example of the decomposition of a periodic signal into its harmonic wave functions is reported in Figure 2.1 .

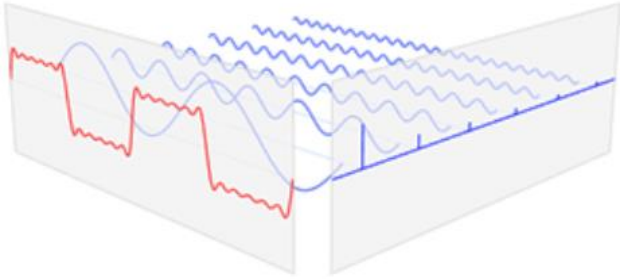

Figure 2.1 Decomposition of a signal into its harmonic components.

2.3.2 Fourier transform

Starting from the complex *Fourier series* it is possible to derive the *Fourier transform*, which is able to represent non-periodic functions in the frequency domain. It is well known that the sufficient condition for a representation of a function to be unique and reversible is that it comes from the projection on an orthogonal basis. Since harmonic components $e^{-i\omega_n t}$ constitute an *orthonormal basis*, the *Fourier transform* $\mathbb{F}\langle\cdot\rangle$

$$\mathbb{F}\langle f(t)\rangle = F(\omega) = \int_{-\infty}^{\infty} f(t)\,\mathrm{e}^{-i\omega t}\mathrm{d}t \Leftrightarrow F(\nu) = \int_{-\infty}^{\infty} f(t)\mathrm{e}^{-i2\pi\nu t}\mathrm{d}t \tag{2.6}$$

gives a unique representation of the signal in frequency domain. A perfect reconstruction of the signal $f(t)$ into time domain is given by the *Inverse Fourier transform*:

$$f(t) = \frac{1}{2\pi}\int_{-\infty}^{\infty} F(\omega)\,\mathrm{e}^{i\omega t}\mathrm{d}\omega \Leftrightarrow f(t) = \int_{-\infty}^{\infty} F(\nu)\,\mathrm{e}^{i2\pi\nu t}\mathrm{d}\nu \tag{2.7}$$

Notice that the more regular $f(t)$, the faster the decay of the sinusoidal wave amplitude $|F(\nu)|$ when frequency ν increases [Mallat 1999].

Some examples are described below to show how the *Fourier transform* measures whether or not a frequency is present in a given function. In particular, in the first case, the *FT* is evaluated in correspondence of a frequency equal to that of oscillation of the test signal while, in the second case, the *FT* is calculated for a frequency not present into analysed signal.

Let's consider the test signal of Figure 2.2, defined as:

$$f(t) = \cos(2\pi 3t)\mathrm{e}^{-\pi t^2} \tag{2.8}$$

The function *f*(*t*) oscillates at 3 Hz (if t measures seconds) and tends quickly to 0. The second factor of Eq. (2.8) $\mathrm{e}^{-\pi t^2}$ is an envelope function that shapes the continuous sinusoid into a short pulse.

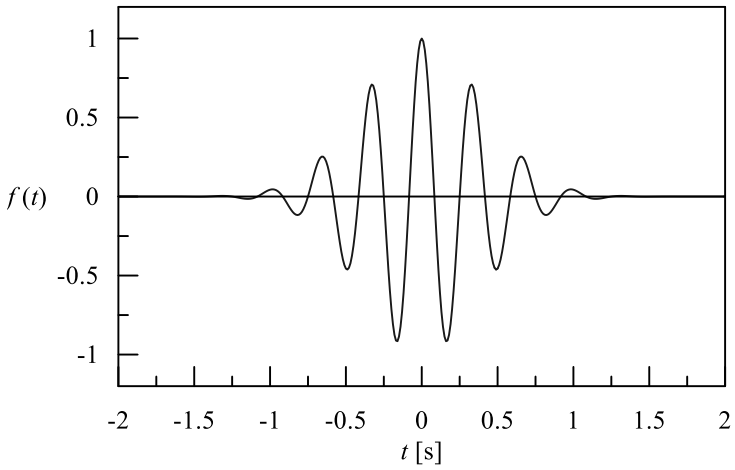

Figure 2.2 Test signal $f(t) = \cos(2\pi 3t)\mathrm{e}^{-\pi t^2}$.

The value of the *Fourier transform* at 3 Hz is evaluated as follow:

$$F(3) = \int_{-\infty}^{\infty} f(t) \cdot e^{-i(2\pi 3)t} \mathrm{d}t = 0.5 \text{ Hz} \tag{2.9}$$

As shown in Figure 2.3, in this case the function *f*(*t*) and the exponential term $e^{-i(2\pi 3)t}$ oscillate at the same rate consequently, real part of the integrand $f(t) \cdot e^{-i(2\pi 3)t}$ is almost always positive because when $f(t)$ is negative, the real part of $e^{-i(2\pi 3)t}$ is negative as well and when $f(t)$ is positive, so is the real part of $e^{-i(2\pi 3)t}$. Real and imaginary parts of integrand $f(t) \cdot e^{-i(2\pi 3)t}$ for *Fourier transform* at 3 Hz are reported in Figures 2.4 a) and b) respectively.

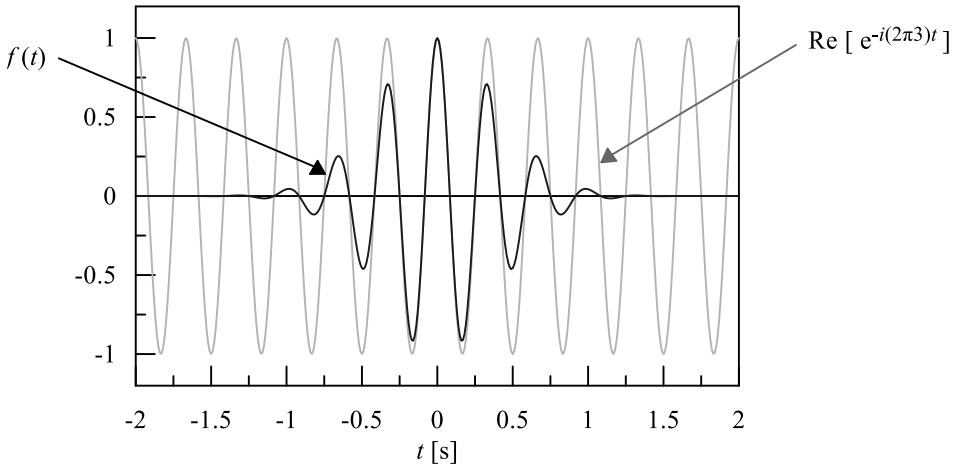

Figure 2.3 Original function (black line) and real part of the exponential term (grey line) of the *Fourier transform.*

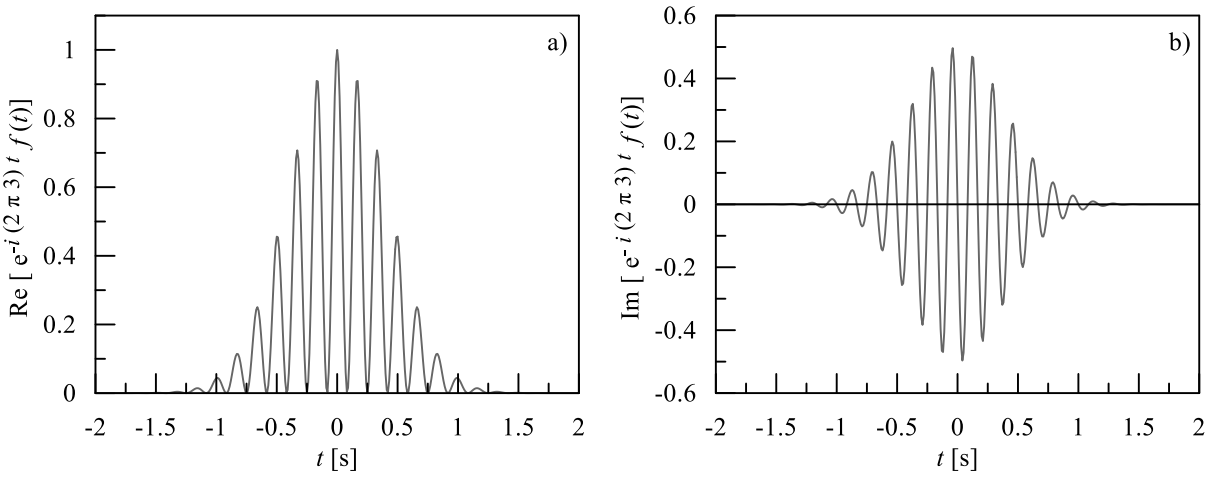

Figure 2.4 Real a) and imaginary b) parts of integrand for *Fourier transform* at 3 Hz.

The case of the *Fourier transform* evaluated in correspondence of the frequency of $\nu = 5\,\mathrm{Hz}$, not present into the time-domain signal, is investigated below:

$$F(5) = \int_{-\infty}^{\infty} f(t) \cdot e^{-i(2\pi 5)t} \mathrm{d}t \cong 0 \ \ \mathrm{Hz} \tag{2.10}$$

The original function $f(t)$ and the exponential term $e^{-i(2\pi 5)t}$ of the integrand function of the *Fourier transform* are shown in Figure 2.5.

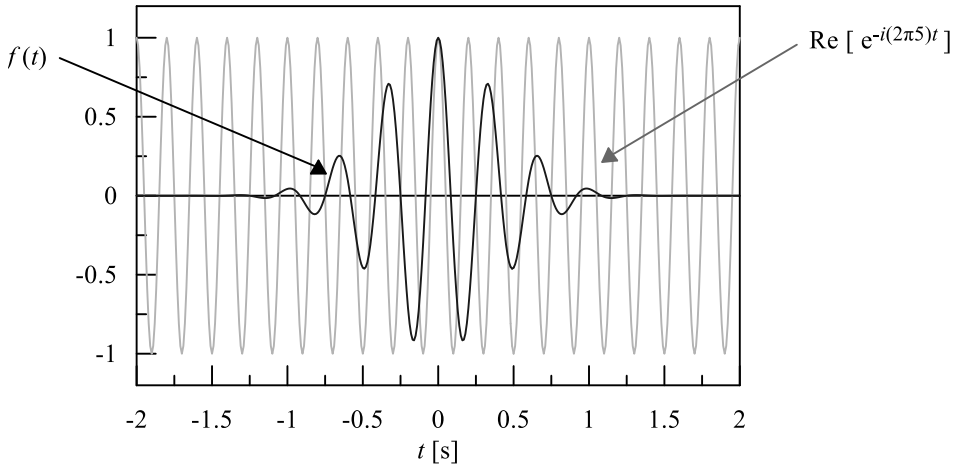

Figure 2.5 Terms of the integrand function of the *Fourier transform* at 5 Hz: original signal (black line), exponential function (grey line).

As plotted in Figures 2.6 a) and b) both real and imaginary components of the integrand function vary rapidly between positive and negative values, therefore, in this case, the integrand oscillates fast enough so that the integral is very small, and the value of the *Fourier transform* for that frequency is nearly zero.

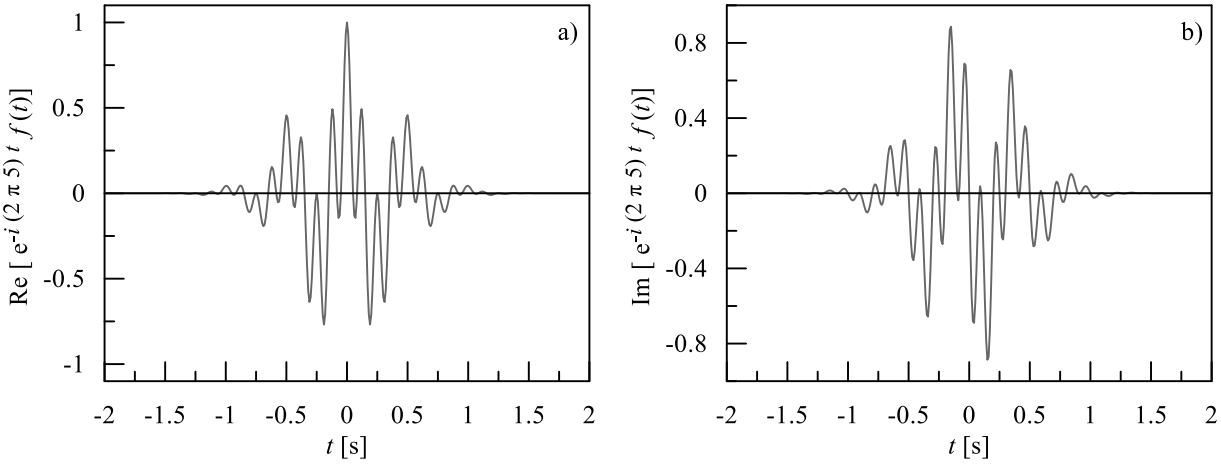

Figure 2.6 Real a) and imaginary b) parts of integrand for *Fourier transform* at 5 Hz.

The magnitude of the *Fourier transform* of the function *f* (*t*) is reported in Figure 2.7. The two points refer to the *Fourier transform* in correspondence of the two analysed cases.

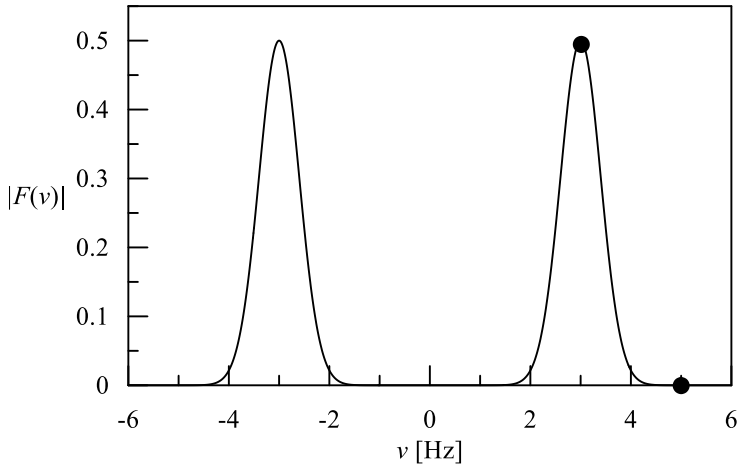

Figure 2.7 Magnitude of *Fourier transform*, with 3 and 5 Hz labelled.

A remarkable property of the *Fourier transform* is related to *the Plancherel theorem* (also called the *Parseval–Plancherel identity* [Plancherel and Mittag-Leffler 1910, Cohen-Tannoudji et al. 1997]). It states that the integral of a function's squared modulus is equal to the integral of the squared modulus of its frequency spectrum:

$$E = \int_{-\infty}^{\infty} \left| f(t) \right|^2 \mathrm{d}t = \frac{1}{2\pi} \int_{-\infty}^{\infty} \left| F(\omega) \right|^2 \mathrm{d}\omega = \int_{-\infty}^{\infty} \left| F(\nu) \right|^2 \mathrm{d}\nu \tag{2.11}$$

which implies that in mapping $f(t)$ in frequency domain, via the *Fourier transform*, the energy E of the time-signal is preserved. The quantity $\left|F(\nu)\right|^2$ plotted versus the frequency ν shows how the energy of the signal $f(t)$ is distributed among the various frequencies.

The *Fourier transform* of a sin function in the time domain is a Dirac delta function in frequency domain, however since sinusoid is a not-decaying function in time domain, the *Fourier transform* achieves the sharpest possible frequency resolution but has no temporal localization capabilities.

2.3.3 Discrete Fourier transform

In many engineering applications, the time domain functions, representing real data as the recorded accelerograms, are sampled into a finite number of points equally spaced in time. It follows that the integrals of equations (2.6) and (2.7) must be replaced by a summation. This approach is referred in the literature as the *discrete Fourier transform* (*DFT*).

To show this, let's consider the discrete, real-valued signal $f_\ell = f(t_\ell) = f\left(t = \ell\,\Delta t\right)$ of Figure 2.8, with $\ell = 0, 1, \cdots, 2N$, where $t_\ell = \ell\,\Delta t$ is the generic time instant in which the continuous time signal $f(t)$ has been sampled over the time interval [0, t_{2N}]; v_0=1/Δt is the sampling frequency; and t_{2N}=2$N\Delta t$ is the time duration of the signal, known at p=2N+1 points.

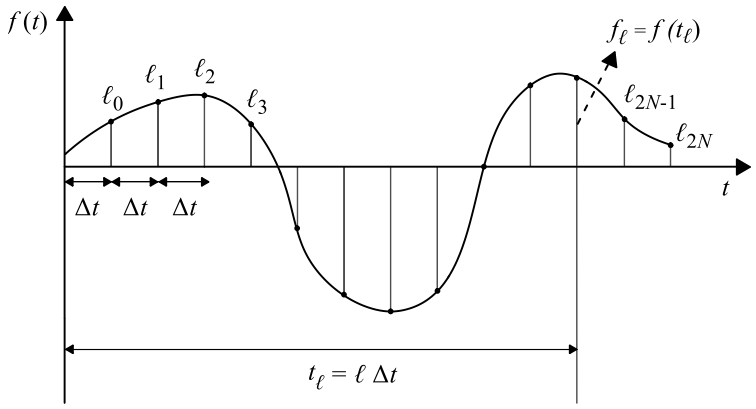

Figure 2.8 Sampling continuous function of time $f(t)$ at regular intervals Δt.

Let assume $\omega_n = 2\pi n / \left(2N\Delta t\right) = n\,\Delta\omega$, being $\Delta\omega = 2\pi / t_{2N}$ the discretization step in the frequency domain, then from Equation (2.6), the *DFT*<·> of the discretized signal f_ℓ is given by:

$$DFT\left\langle f_\ell \right\rangle = F_n = F\left(\omega_n\right) = \int_{-\infty}^{\infty} f(t)\,\mathrm{e}^{-i\omega_n t}\mathrm{d}t = \Delta t \sum_{\ell=0}^{2N} f_\ell\,\mathrm{e}^{-i\omega_n t_\ell} \Leftrightarrow F\left(\nu_n\right) = \Delta t \sum_{\ell=0}^{2N} f_\ell\,\mathrm{e}^{-i\pi n\ell/N} \quad (2.12)$$

where F_n is the *DFT* value at the nth discrete circular frequency ω_n.

By applying the *DFT* algorithm, the following relationship can be used to represent the discrete signal in the frequency domain:

$$\left\{F_0, F_1, F_2, \cdots, F_n, \cdots, F_{2N}\right\}^{\mathrm{T}} = DFT\left[\left\{f_0, f_1, f_2, \cdots, f_\ell, \cdots, f_{2N}\right\}^{\mathrm{T}}\right], \quad (2.13)$$

where the superscripted T means transpose.

A quantity of particular significance is the *discrete Fourier amplitude spectrum* defined as:

$$\left|F\left(\omega_n\right)\right| = |\,F_n\,| \;\Leftrightarrow\; \left|F\left(\nu_n\right)\right| \quad (2.14)$$

2.3.4 Fourier analysis limits

The *Fourier spectrum* obtained by the *FT* or *DFT* is averaged over the entire time consequently, it is not appropriate to track the changes in time of both frequency magnitude and phase of non-stationary signals.

In order to illustrate the main limitations of the *Fourier analysis*, some examples are described below.

Let's consider a test signal of Figure 2.9 a), defined as:

$$f(t) = 5\cos\left[2\pi t\right] + 4\cos\left[2\pi 5t\right] + 6\cos\left[2\pi 5t\right] \tag{2.15}$$

having a time duration t_{2N} =2 s and a discretized time step Δt=0.001 s. The modulus of the *DFT* of the discretised signal $f_\ell = f\left(t_\ell\right)$ is shown in Figure 2.9 b).

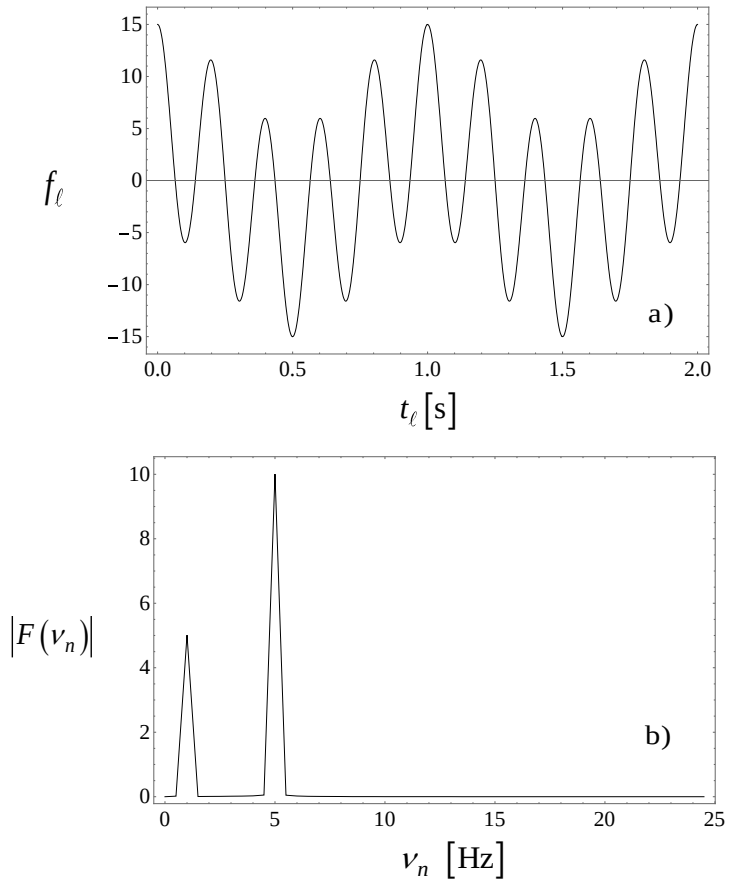

Figure 2.9 Discretized signal consisting of the superposition of different harmonics a); *discrete Fourier amplitude spectrum* b).

In the above example, the *DFT* provides good frequency and amplitude information (see Figure 2.9 b); what it lacks is the time information, i.e., the knowledge of the time in which these frequencies occur (see Figure 2.9 a).

To better appreciate the properties of the *Fourier transform*, let's consider a second test signal defined as:

$$f(t)=\begin{cases}5\cos\left[2\pi t\right] & 0\le t<2\\ 4\cos\left[2\pi 5t\right] & 2\le t<4\\ 6\cos\left[2\pi 5t\right] & 4\le t\le 6\end{cases} \tag{2.16}$$

having a time duration t_{2N} =6 s and a discretized time step Δt=0.001 s.

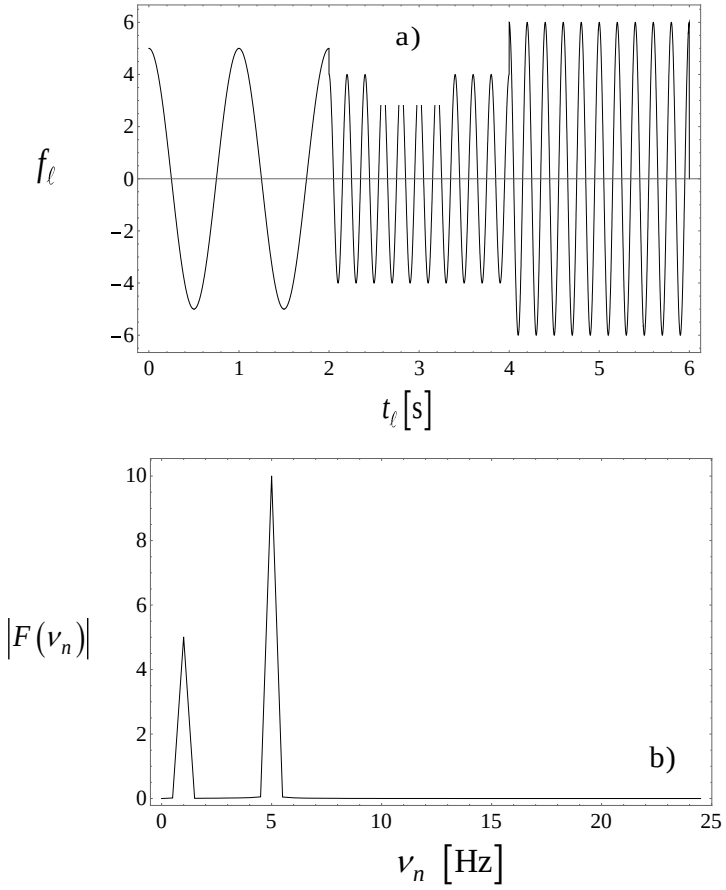

Figure 2.10 Test signal consisting of three different harmonics arranged one after the other a); *discrete Fourier amplitude spectrum* b).

It can be noticed that the signal of Eq.(2.16) consists of the same harmonics of that of Eq. (2.15). Nevertheless the two signals differ in the time domain: in the first case (see Eq. (2.15)) the three harmonics are added while in the second one (see Eq.(2.16)) they are located one

behind the other. It can be observed that the *discrete Fourier amplitude spectrum* $\left|F\left(\nu_n\right)\right|$ of the discretized test signal of Eq. (2.16), represented in Figure 2.10 b), is the same as that of the signal of Eq.(2.15), shown in Figure 2.9 a). This is due to the fact that the two signals are made up of three harmonics having the same frequencies but arranged in a different position. Therefore, signal frequency content is hidden in time domain while the frequency domain representation hides the temporal localization of the signal features. Time localization and frequency content are always present even if hidden, because, since perfect reconstruction of the signal is doable, no information is lost. Two signals may possess the same discrete *Fourier amplitude spectrum*, while what distinguishes them is the *Fourier phase spectrum*.

2.3.5 Windowed Fourier transform

First attempt to overcome classical *Fourier analysis* limitations was done by Gabor in 1946, who applied in signal analysis fundamental concepts developed in quantum mechanics a decade earlier [Gabor 1946]. The *Gabor transform*, also called *short time Fourier transform* (*STFT*) [Mallat 1999] is a sequence of *Fourier transforms* of a windowed signal. Unlike the standard *Fourier transform* that provides the frequency information averaged over the entire signal time interval, the *STFT* provides the time-localized frequency information for situations in which frequency components of a signal vary over time.

In order to illustrate the different results obtained by the application of the two aforementioned frequency transformations (*FT* and *STFT*), the *STFT* is applied to the same non-stationary signal of Eq. (2.16).

It can be noted that, in Figure 2.11 it's possible to distinguish the three harmonics of the signal: one located in υ_n=1 and two in υ_n=5 while in Figure 2.10 b) the contributions related to the second and third harmonic of the signal, located in correspondence of υ_n=5 appear superimposed and consequently, not distinguishable.

Since the time support governed by the window function (in this case rectangular) is equal for all the window functions, the *STFT* exhibit considerable limitations. The main complexity of the *STFT* regards the choice of the shape (i.e. Gaussian, rectangular) and of the size of the window function. Window should be narrow enough to ensure that the portion of the signal falling within the window is stationary.

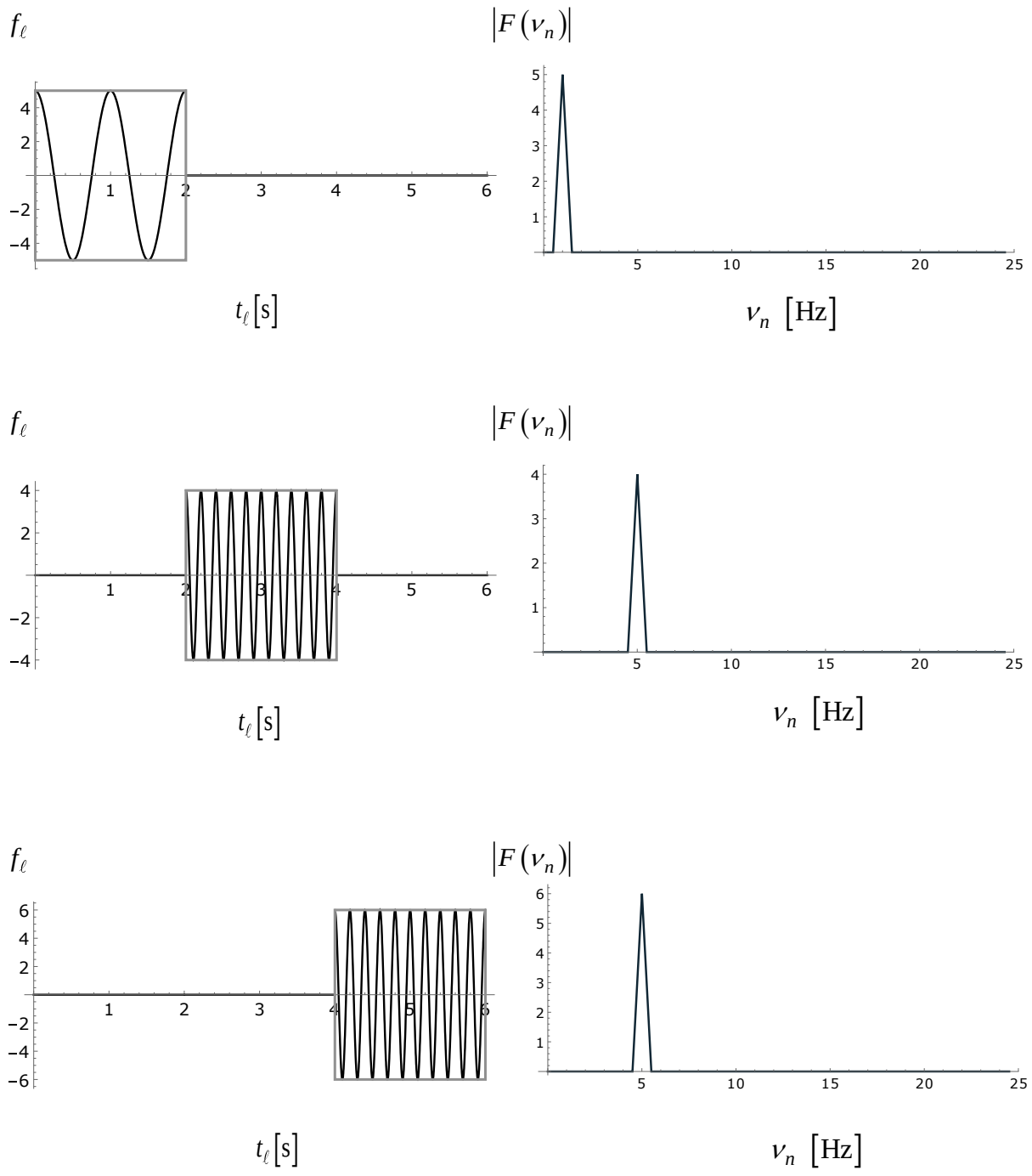

Figure 2.11 Example of *short time Fourier transform* application: three components of the windowed signal in time domain (left column); corresponding amplitude spectra (right column).

2.3.6 Uncertainty principle

Most signals recorded in nature, such as earthquake motions, are non-stationary due to their time-varying characteristics. In signal processing, time–frequency analysis encloses those methods used to study a signal in both the time and frequency domains simultaneously. However, the representation of a signal having jointly the best resolution in both domains represents an ideal situation that, according to the well-known *Heisenberg uncertainty principle* [Choen 1995], is not possible to obtain. The meaning of the uncertainty principle and its importance for signal analysis have been clearly stated often enough by different authors. In particular, in [Skolnik 1980] the author stated that "a narrow waveform yields a wide spectrum and a wide waveform yields a narrow spectrum and both the time waveform and frequency spectrum cannot be made arbitrarily small simultaneously"; in [Choen 1995], it is pointed out that the density in time and in the frequency are related in such that if one density is narrow then the other is broad consequently, it is not that both time and frequency cannot arbitrarily be made narrow, but that the densities of time and frequency cannot both be made narrow. A measure of the resolution in time or frequency domain may be obtained by evaluating the average $\mu\langle t\rangle$ and the standard deviation $\sigma^2\langle t\rangle$ of the density $|g(t)|^2$ in the time domain, that is:

$$\mu\langle t\rangle = \int_{-\infty}^{\infty} t\,|g(t)|^2\,\mathrm{d}t \tag{2.17}$$

$$\sigma^2\langle t\rangle = \int_{-\infty}^{\infty} \left(t-\langle t\rangle\right)^2 |g(t)|^2\,\mathrm{d}t \tag{2.18}$$

The counterparts of Eq. (2.17) and Eq. (2.18) in the frequency domain are:

$$\mu\langle \omega\rangle = \int_{-\infty}^{\infty} \omega\left|G(\omega)\right|^2\,\mathrm{d}\omega \tag{2.19}$$

$$\sigma^2\langle \omega\rangle = \int_{-\infty}^{\infty} \left(\omega-\langle \omega\rangle\right)^2 \left|G(\omega)\right|^2\,\mathrm{d}\omega \tag{2.20}$$

where $\left|G(\omega)\right|$ denotes the *Fourier transform* of $g(t)$ given by the equation:

$$G(\omega) = \frac{1}{\sqrt{2\pi}} \int_{-\infty}^{\infty} g(t) e^{-\mathrm{i}\omega t}\,\mathrm{d}t \tag{2.21}$$

The well-known *Heisenberg uncertainty principle* is a mathematically proven property and states that the values $\sigma\langle t\rangle$ and $\sigma\langle\omega\rangle$ cannot be independently small. Specifically, for an arbitrary window normalized so that:

$$\| g(x) \|^2 = \int_{-\infty}^{\infty} | g(x) |^2 \mathrm{d}x = 1 \tag{2.22}$$

can be demonstrated that:

$$\sigma\langle t\rangle \sigma\langle\omega\rangle \geq \frac{1}{2} \tag{2.23}$$

thus, high resolution in the time domain (small value of $\sigma\langle t\rangle$) may be generally achieved only at the expense of a poor resolution (bigger than a minimum value $\sigma\langle\omega\rangle$) in the frequency domain and vice versa. Note that the optimal *time – frequency* resolution, that is $\sigma\langle t\rangle \sigma\langle\omega\rangle = 1/2$, may be obtained when the Gaussian window is selected:

$$g(t) = \frac{1}{\sqrt[4]{2\pi\sigma^2\langle t\rangle}} \exp\left(-\frac{t^2}{4\sigma^2\langle t\rangle}\right) \tag{2.24}$$

In order to achieve good signal localization of high frequency components, narrow windows are required; as a result of that, low-frequency components are poorly represented. Thus, a more flexible representation with non-constant windowing is quite desirable to enhance the time resolution for short-lived high-frequency phenomena and frequency resolution for long-lasting low-frequency phenomena [Spanos et al. 2005].

2.4 Wavelet harmonic analysis

The mainly shortcomings of the *Fourier analysis* (capable of detecting only the frequency components of signals) and the *windowed Fourier transform* (related to the choice of the type and fixed size window function) have been overcome with significant effectiveness and efficiency by wavelets-based signal representation. *Wavelet analysis* reveals the frequency components of signals just like the *Fourier transform*, but it also identifies where a certain frequency exists in the temporal or spatial domain. This is possible because, unlike a

harmonic wave which is an ever-lasting periodic function, a wavelet is a decaying function, and this feature gives to the *wavelet analysis* a time localisation capability.

The concept of *wavelet transform*, introduced first by Goupillaud et al. in 1984, for seismic records analysis, consists of projecting a given signal on a convenient set of function, called wavelets, which can be generated by scaling and shifting a fixed function called mother wavelet [Mallat 1999]. Families of wavelets can be generated in way to form an orthogonal basis, so that the *wavelet transform* is bijective, giving a unique representation for any signal [Cecini and Palmeri 2015]. This is the case, for instance, of the harmonic wavelets $\psi(t)$ proposed by Newland [1993], which are complex-valued functions in time domain with a rectangular box-shaped in the frequency domain:

$$\psi(\omega) = \mathbb{F}\langle \psi(t) \rangle = \begin{cases} 1/2\pi & \text{for} \quad 2\pi \le |\omega| < 4\pi \\ 0 & \text{elsewhere} \end{cases} \tag{2.25}$$

The corresponding complex valued harmonic mother wavelet in time domain is:

$$\psi(t) = \frac{e^{i4\pi t} - e^{i2\pi t}}{i2\pi t} \tag{2.26}$$

The real and imaginary parts of $\psi(t)$ are shown in Figure 2.12. It should be noted that Eq. (2.25) and Eq. (2.26) refer to the case of signal of unitary time length, i.e. $0 \le t \le 1$ and energy content for $\omega > 2\pi$. The first scheme proposed by Newland [1993] to generate the whole family of orthogonal wavelets from the mother one is called dyadic, and can be derived by changing the argument in (2.26) from t to $\left(2^j t - k\right)$, being j and k integers numbers that define the scale (or compression) of the wavelet and its position on the t-axis, respectively. By doing this, the shape of the wavelet is not changed but its horizontal scale is compressed by the factor 2^j, being $j \ge 0$ the level of the wavelet, while its position is translated by k units at the news scale:

$$\hat{\psi}_{j,k}(t) = \psi\left(2^j t - k\right) \tag{2.27}$$

The real part of $\hat{\psi}_{j,k}(t)$, for three different values of j and two fixed values of k, are shown in Figure 2.13 (k=0) and Figure 2.14 (k=1), respectively.

Figure 2.15 shows that, following Newland's dyadic scheme, the *Fourier transform* of the generic wavelet at jth level occupies the frequency band from $2\pi 2^j$ to $4\pi 2^j$.

The scheme proposed by Newland [1994] leads to the generalised harmonic *wavelet transform* by the introduction of the musical wavelet $\hat{\psi}_{\{m,n\}}(t)$. Instead of splitting the frequency axis into bands of increasing width $B = \pi\ 2^{\,j+1}$, the whole set of band wavelets is generated by:

$$\hat{\psi}_{\{m,n\}}(t) = \frac{e^{i2n\pi t} - e^{i2m\pi t}}{i2(n-m)\pi t} \tag{2.28}$$

which in the frequency domain corresponds to a real-valued rectangular box function with a height of 1/[2 (*n*-*m*) π] over the interval [2 π *m*, 2 π *n*]:

$$\psi_{\{m,n\}}(\omega) = \mathbb{F}\left\langle \psi_{\{m,n\}}(t)\right\rangle = \frac{\operatorname{sgn}\left(2n\pi\text{-}\omega\right) - \operatorname{sgn}\left(2m\pi\text{-}\omega\right)}{4(n-m)\pi} \tag{2.29}.$$

where sgn (·) is the signum function.

The translation of the wavelet by a time step *k* / (*n*-*m*) is then achieved by:

$$\hat{\psi}_{\{m,n\},k}(t) = \frac{e^{i2n\pi\left(t-\frac{k}{n-m}\right)} - e^{i2m\pi\left(t-\frac{k}{n-m}\right)}}{i2\left(n-m\right)\pi\left(t-\frac{k}{n-m}\right)} = \hat{\psi}_{\{m,n\}}\left(t-\frac{k}{n-m}\right) \tag{2.30}$$

that in the frequency domain correspond to:

$$\hat{\psi}_{\{m,n\},k}(\omega) = \mathbb{F}\left\langle \hat{\psi}_{\{m,n\}}(t)\right\rangle e^{\left(-i\frac{k}{n-m}\omega\right)} \tag{2.31}$$

The notation {*m*,*n*} denotes a wavelet occupying the band of circular frequencies from 2π*m* to 2π*n*, where *n*>*m*, as shown within Figure 2.15 b) [Cecini and Palmeri 2015].

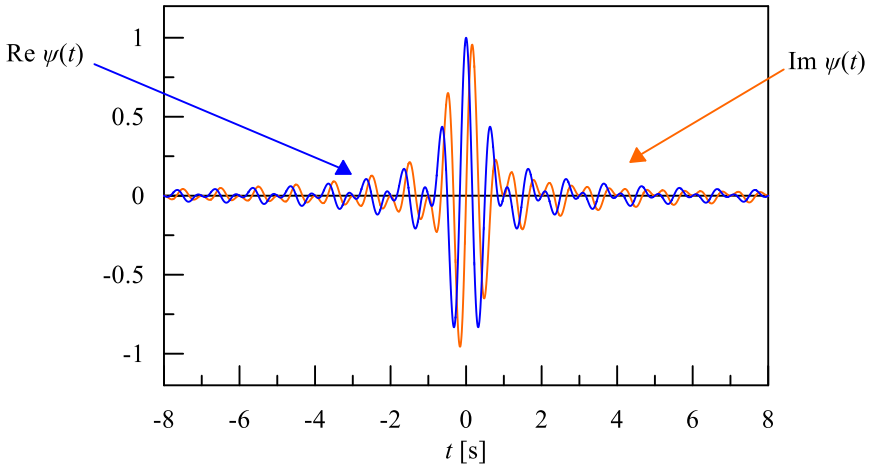

Figure 2.12 Real part (blue line), and imaginary part (orange line) of the harmonic mother wavelet of Eq. (2.26).

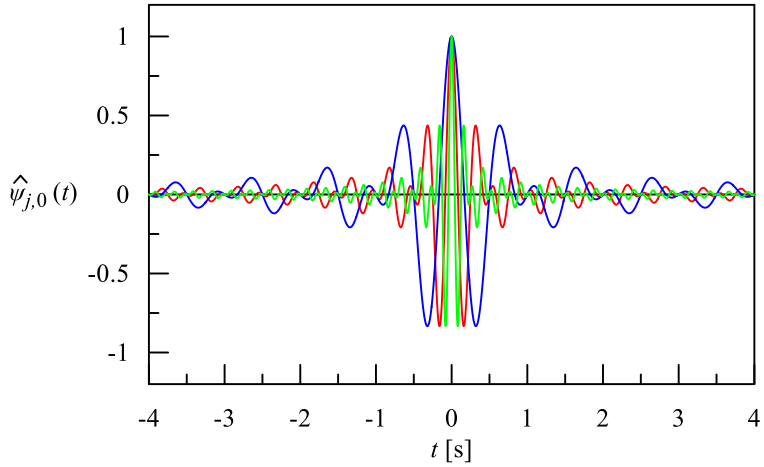

Figure 2.13 Real part of the harmonic wavelet (Eq.(2.27)) for k=0 and different values of j: j=0 blue line; j=1 red line; j=2 green line.

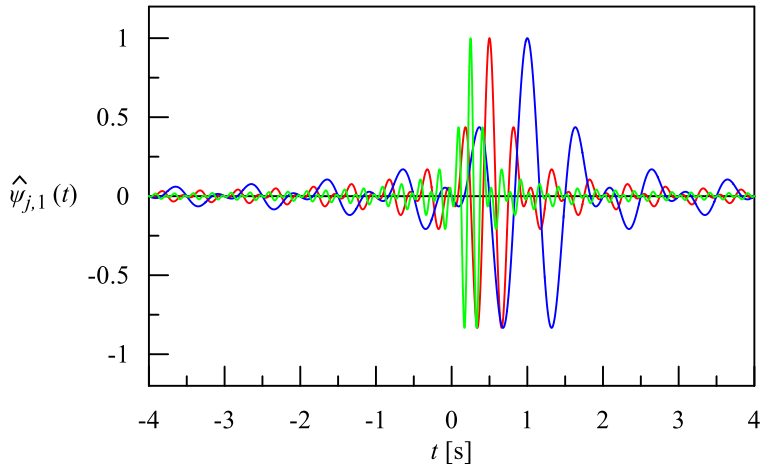

Figure 2.14 Real part of the harmonic wavelet (Eq.(2.27)) for k=1 and different values of j: j=0 blue line; j=1 red line; j=2 green line.

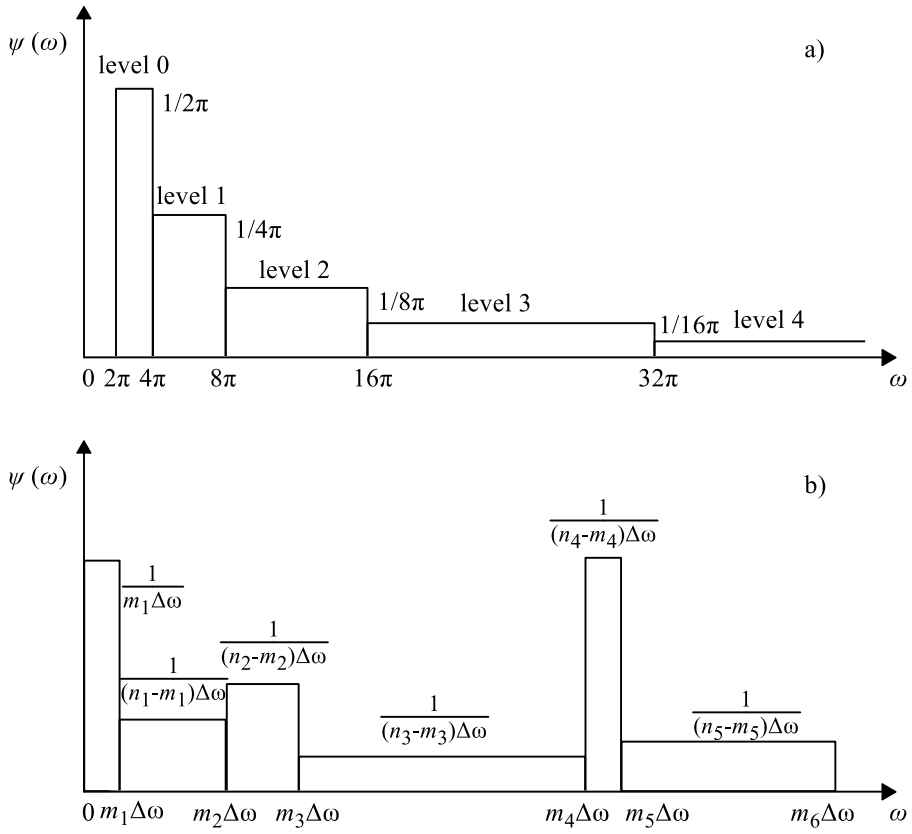

Figure 2.15 Representation in the frequency domain: a) dyadic scheme; b) an example of generalised scheme for harmonic wavelet base with non-overlapping intervals ($n_j = m_{j-1}$) of arbitrary bandwidth.

2.5 Circular-wavelet-based representation of discretized signals

For the application of *wavelet analysis*, the frequency range $[0, \omega_N]$ of a given discretized signal f_ℓ, with $\ell = 0, 1, \cdots, 2N$, where $t_\ell = \ell \Delta t$, can be arbitrary portioned in M frequency bands $\left[\omega_{m_j} = m_j \Delta\omega, \omega_{n_j} = n_j \Delta\omega\right]$, with $j \le M$ and $1 \le M \le N$; furthermore, m_1=0, n_M=M and for $1 \le j \le M$, $n_j = m_{j+1}$, so that jth and (j+1)th frequency bands are adjacent to each other.

Bandwidth and central circular frequency of the jth band are given by:

$$B_j = b_j \Delta\omega \tag{2.32}$$

$$\bar{\omega}_j = \left(\frac{m_j + n_j}{2}\right)\Delta\omega \tag{2.33}$$

in which $b_j = n_j - m_j$.

Another approach to decompose a real-valued signal into the superposition of complex-valued wavelets consists in the use of the circular wavelet as mother wavelet.

The *j*th complex-valued circular wavelet $\Psi_{j,k,\ell}$, in the discretized time domain, can be defined as:

$$\Psi_{j,k,\ell} = \frac{1}{b_j} \sum_{s=m_j}^{n_j-1} \exp\left[i\pi(2s+1)\left(\frac{\ell}{2N} - \frac{k}{b_j} \right) \right]; \quad \ell = 0,1,\cdots,2N; \quad k = 0,1,\cdots,b_j - 1 \tag{2.34}$$

where *k* and ℓ are two time indexed, defining the time instants at which the generic wavelet $\Psi_{j,k,\ell}$, belonging to the b_j frequency band, is centered $\tau_{j,k} = k\, t_{2N} / b_j$ and evaluated (t_ℓ), respectively.

Importantly, the larger b_j, i.e. the wider the *j*th frequency band, the larger the number of wavelets belonging to it, the more precise the time localisation of the energy that can be achieved in that frequency band.

The expansion of a given discrete signal f_ℓ, using circular wavelets as the basis functions, can be performed by applying the following reconstruction formula:

$$f_\ell \cong \hat{f}_\ell = \overline{f}_\ell + 2\,\mathrm{Re}\left[\sum_{j=1}^{M} \sum_{k=0}^{b_j-1} \hat{a}_{j,k} \Psi_{j,k,\ell} \right] \tag{2.35}$$

where Re[·] returns the real part of the complex-valued expression within square brackets and $\overline{f}_\ell$ is the linear-trend value in the time, so defined:

$$\overline{f}_\ell = f_0 + \frac{f_{2N} - f_0}{2N} \ell; \tag{2.36}$$

while $\hat{a}_{j,k}$ is the generic complex-valued coefficient associated to the discrete signal f_ℓ that can be calculated as:

$$\hat{a}_{j,k} = \frac{b_j}{2N} \sum_{\ell=0}^{2N} \left(f_\ell - \overline{f}_\ell \right) \Psi^*_{j,k,\ell} \tag{2.37}$$

where the superscripted asterisk * means complex conjugate quantity.

Because circular wavelets are complex functions, the decomposition of any arbitrary signal involves coefficients $\hat{a}_{j,k}$ which are also complex. Independently of the band-partitioning of the frequency domain, $\hat{a}_{j,k}$ is the number of wavelets contributing to the double summation in the *right-hand side* (*rhs*) of Eq. (2.35).

An alternative reconstruction formula of Eq. (2.35), for the expansion of a given signal in terms of complex wavelets, can be expressed as:

$$\hat{f}_\ell = \overline{f}_\ell + 2\sum_{j=1}^{M}\frac{1}{b_j}\sum_{k=0}^{b_j-1}\left|\hat{a}_{j,k}\right|\sum_{s=m_j}^{n_j-1}\cos\left[\pi\left(2s+1\right)\left(\frac{\ell}{2N}-\frac{k}{b_j}\right)+\hat{\theta}_{j,k}\right] \tag{2.38}$$

where $\left|\hat{a}_{j,k}\right|$ and $\hat{\theta}_{j,k}$ are respectively the modulus and the phase angle of the generic complex-valued coefficient $\hat{a}_{j,k}$ expressed in exponential form:

$$\hat{a}_{j,k} = \left|\hat{a}_{j,k}\right| \mathrm{e}^{i\hat{\theta}_{j,k}} \tag{2.39}$$

A special case occurs for M=N, i.e., when there are N frequency bands $\left[\omega_j,\ \omega_{j+1}\right]$, all with the same bandwidth $B_j = \Delta\omega$, i.e., $b_1 = b_2 = \cdots = b_N = 1$. Accordingly, there is only one wavelet $\psi_{j,0,\ell}$ and one wavelet coefficient $\hat{a}_{j,0}$ for each frequency band (i.e., no time localisation occurs in any of the M frequency band), and Eq. (2.38) can be rewritten as:

$$\hat{f}_\ell = \overline{f} + 2\sum_{j=1}^{N}\left|\hat{a}_{j,0}\right|\cos\left[\overline{\omega}_j t_\ell + \hat{\theta}_{j,0}\right] \tag{2.40}$$

with $\overline{\omega}_j = \frac{1}{2}\left(\omega_j + \omega_{j+1}\right)$, which particularises Eq. (2.33).

Notice that the $DFT\left\langle \Psi_{j,k,\ell} \right\rangle$ will be indicated as $\psi_{j,k,n}$ in the following.

2.5.1 Numerical illustration of the *circular wavelets*

To better appreciate some of the properties of the circular wavelets and their implications in the representation of discrete signals, let's consider the test signal of Figure 2.16 a) defined as:

$$f(t) = \underbrace{3 - t^{3/2}}_{\text{NLT}} + \underbrace{2\sin^2\left(\pi t\right)\cos\left[7\pi\left(t+t^3\right)\right]}_{\text{AMC}} \tag{2.41}$$

consisting of a *non-linear trend* (*NLT*) superimposed with an *amplitude-modulated chirp* (*AMC*). The time duration and sampling frequency are respectively t_{2N}=2 s and υ_0=100 Hz meaning that the discretised signal consists of $2N$+1= $\upsilon_0\ t_{2N}$ +1=201 points. The modulus of the *DFT* of the discretised signal, is reported in Figure 2.16 b).

In Table 2-I: are listed the main characteristics of the discretized signal: time duration t_{2N}, sampling step Δt, sampling frequency υ_0, number of the discrete non-zero frequencies N, number of points p, Nyquist frequency ω_N and frequency step $\Delta\omega$.

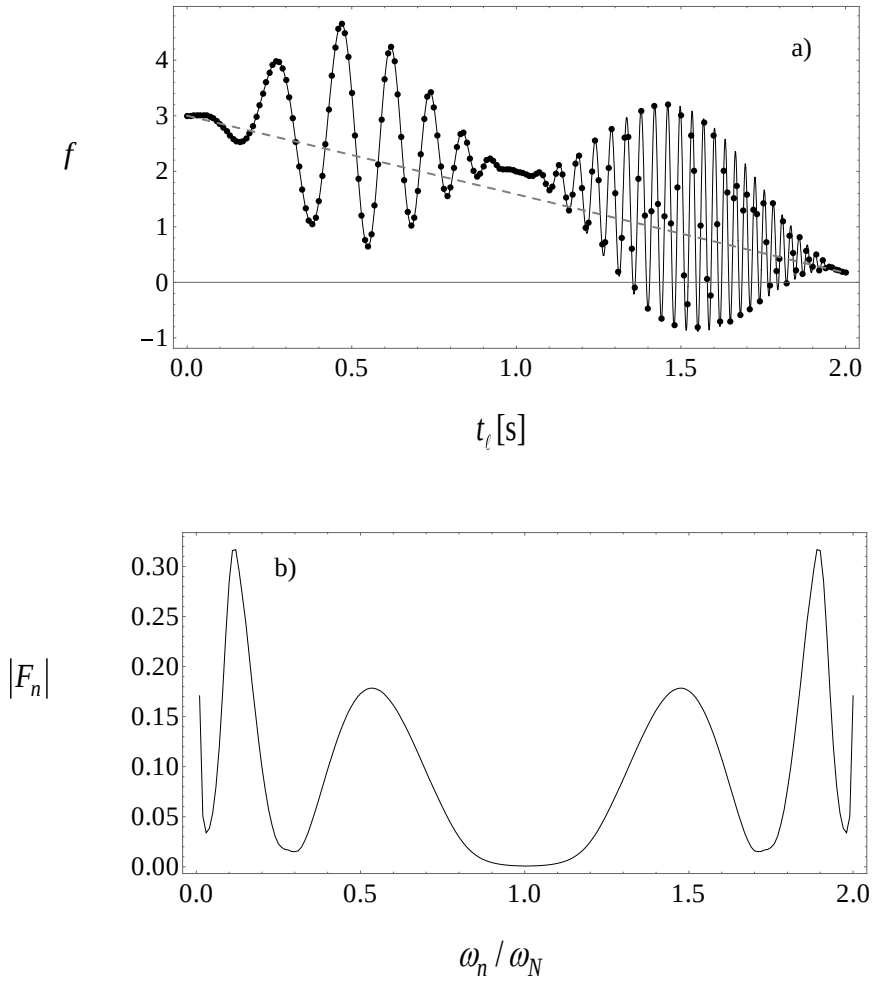

Figure 2.16 Continuous signal $f(t)$ (solid line), discretised signal f_ℓ (dots) and trend line $\overline{f}$ (dashed grey line), in the time domain a); modulus of the *DFT* function in the frequency domain b).

Table 2-I: Main characteristics of the discretized signal.

t_{2N} [s]	Δt [s]	$\upsilon_0 = 1/\Delta t$ [Hz]	$N = t_{2N}/(2\Delta t)$ [-]	$p = 2N+1$ [-]	$\omega_N = N\Delta\omega$ [rad/s]	$\Delta\omega = 2\pi/t_{2N}$ [rad/s]
2	0.01	100	100	201	314.16	3.142

To demonstrate the wavelet representation of the signal, six alternative partitions of the frequency range of interest $[0, \omega_N]$ are considered in this section, with division in M=1,3,7,10,50,100 frequency bands. In each case, the upper bound of the jth band is defined by rounding the corresponding index to the nearest integer, i.e.:

$$n_j = \text{round}\left[\frac{j\,N}{M}\right] \tag{2.42}$$

Since N is not a multiple of any of the values of M that have been chosen, in all six cases, the partition is not perfectly uniform, e.g., for M=7, b_2=b_6=15 and b_j=14 for all the other values of $j \leq M$.

The quantities that characterize the frequency bands belonging to the six investigated schemes, are summarized in Table 2-II a) for M=1,3,7,10 and b) M=50,100.

Figure 2.17 shows the moduli of the N wavelets coefficients $|\hat{a}_{j,k}|$ as calculated through Eq.(2.37). The coordinates of each point in three-dimensional plots represent the centre $C_{j,k} \equiv \{\tau_{j,k}, \bar{\omega}_j\}$ of the generic wavelet $\Psi_{j,k,\ell}$ in the orthogonal partition of the time-frequency plane and the magnitude $|\hat{a}_{j,k}|$ of the generic wavelet contribution to the reconstruction of discrete signal f_ℓ. The modulus of the *Fourier spectrum* of the signal $|F(\omega_n)|$ together with the indication of the central circular frequency $\bar{\omega}_j$ of each band j (black vertical lines), are also reported in Figure 2.17.

It can be noted that for:

- $M = 1$ there is a high resolution in the time domain $(k = 0, \cdots, 99)$ and a poor resolution into frequency domain $(j = 1)$;
- $M = N = 100$ there is a high resolution in the frequency domain $(j = 1, \cdots, 100)$ and a poor resolution into time domain $(k = 0)$;

The comparison of the six plots reveals that increasing the number M of frequency bands results in an improved resolution in the frequency domain, i.e. a more detailed representation of the frequency content with more line plots parallel to the time axis; however, the larger M, the less detailed is the representation of the signal in the time domain, i.e., less points in each line plot parallel to the time axis (see vertical grey lines in Figure 2.17).

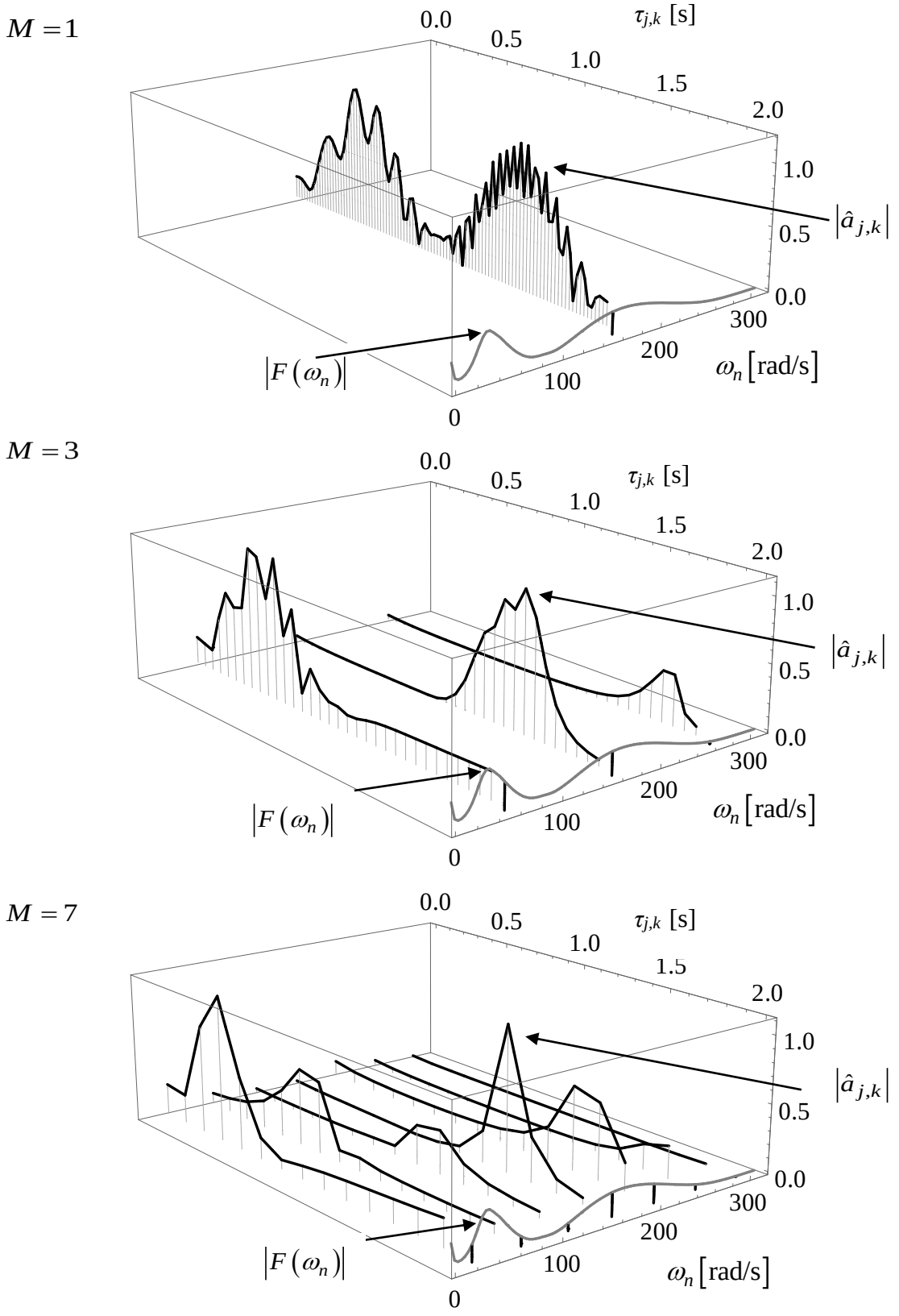

Figure 2.17 Discrete 3D plot of the wavelets coefficients $|\hat{a}_{j,k}|$ with increasing resolution in the frequency domain (M=1,3,7,10,50,100) together with the amplitude *DFT* spectrum $|F(\omega_n)|$.

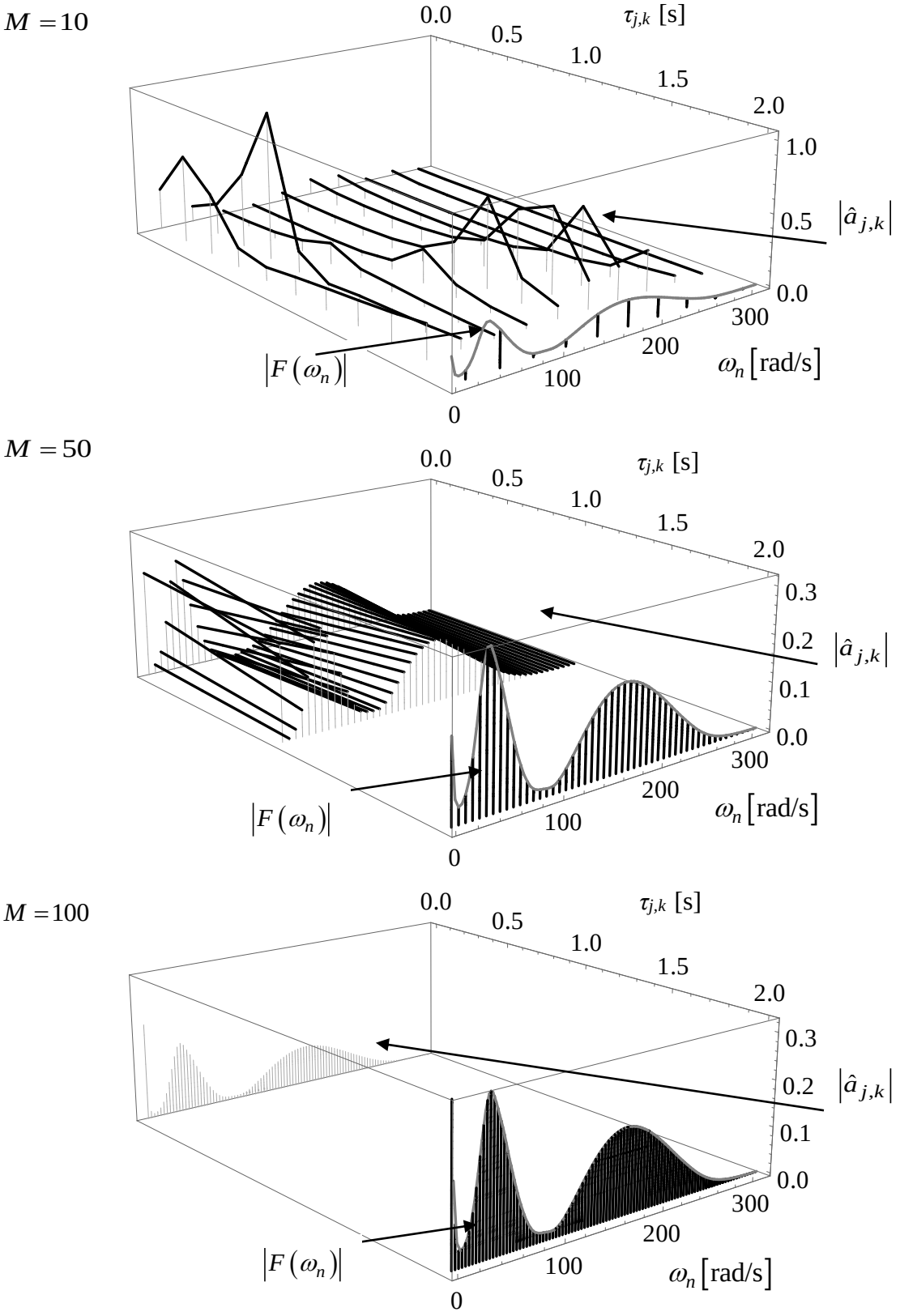

Figure 2.17 (*Continued*).

Table 2-II a) Main characteristics of each frequency band belonging to the M th partition: M=1,3,7,10.

M	j	m_j	n_j	b_j	ω_{m_j} [rad/s]	ω_{n_j} [rad/s]	$\bar{\omega}_j$ [rad/s]
1	1	0	100	100	0	314.16	157.08
3	1	0	33	33	0	103.67	51.84
	2	33	67	34	103.67	210.49	157.08
	3	67	100	33	210.49	314.16	262.32
7	1	0	14	14	0	43.98	21.99
	2	14	29	15	43.98	91.11	67.54
	3	29	43	14	91.11	135.09	113.09
	4	43	57	14	135.09	179.07	157.08
	5	57	71	14	179.07	223.05	201.06
	6	71	86	15	223.05	270.18	246.62
	7	86	100	14	270.18	314.16	292.17
10	1	0	10	10	0	31.42	15.71
	2	10	20	10	31.42	62.83	47.12
	3	20	30	10	62.83	94.25	78.54
	4	30	40	10	94.25	125.67	109.96
	5	40	50	10	125.67	157.08	141.37
	6	50	60	10	157.08	188.50	172.79
	7	60	70	10	188.50	219.91	204.20
	8	70	80	10	219.91	251.33	235.62
	9	80	90	10	251.33	282.74	267.04
	10	90	100	10	282.74	314.16	298.45

Table 2-II b) Main characteristics of each frequency band belonging to the *M*-th partition: *M*=50,100.

M	j	m_j	n_j	b_j	ω_{m_j} [rad/s]	ω_{n_j} [rad/s]	$\bar{\omega}_j$ [rad/s]
50	1	0	2	2	0	6.283	3.141
	2	2	4	2	6.283	12.566	9.424
	⋮	⋮	⋮	⋮	⋮	⋮	⋮
	M/2	48	50	2	150.796	157.08	153.938
	⋮	⋮	⋮	⋮	⋮	⋮	⋮
	M-1	96	98	2	301.593	307.876	304.734
	M	98	100	2	307.876	314.159	311.018
100	1	0	1	1	0	3.141	1.570
	2	1	2	1	3.142	6.283	4.712
	⋮	⋮	⋮	⋮	⋮	⋮	⋮
	M/2	49	50	1	153.938	157.08	155.509
	⋮	⋮	⋮	⋮	⋮	⋮	⋮
	M-1	98	99	1	307.876	311.018	309.447
	M	99	100	1	311.018	314.159	312.588

With reference to six analysed cases, Figure 2.18 shows a three-dimensional plot of the complex-valued circular wavelet $\Psi_{j,k,\ell}$, centered at time $\tau_{j,k} = \left(k \cdot t_{2N}\right)/b_j$. Real and imaginary parts of the wavelet $\Psi_{j,k,\ell}$ are projected on the vertical and horizontal planes, respectively. The phase angle $\hat{\theta}_{j,k}$ of the associated wavelet coefficient $\hat{a}_{j,k}$, determines a rigid rotation on the wavelet plot around the longitudinal, time-proportional axis. According to Eqs. (2.35) and (2.38), only the real part of the rotated wavelet contributes to the reconstruction of the discrete signal f_ℓ, proportionally to the modulus $\left|\hat{a}_{j,k}\right|$.

The parameters of the wavelets represented in Figure 2.18 are summarised into Table 2-III.

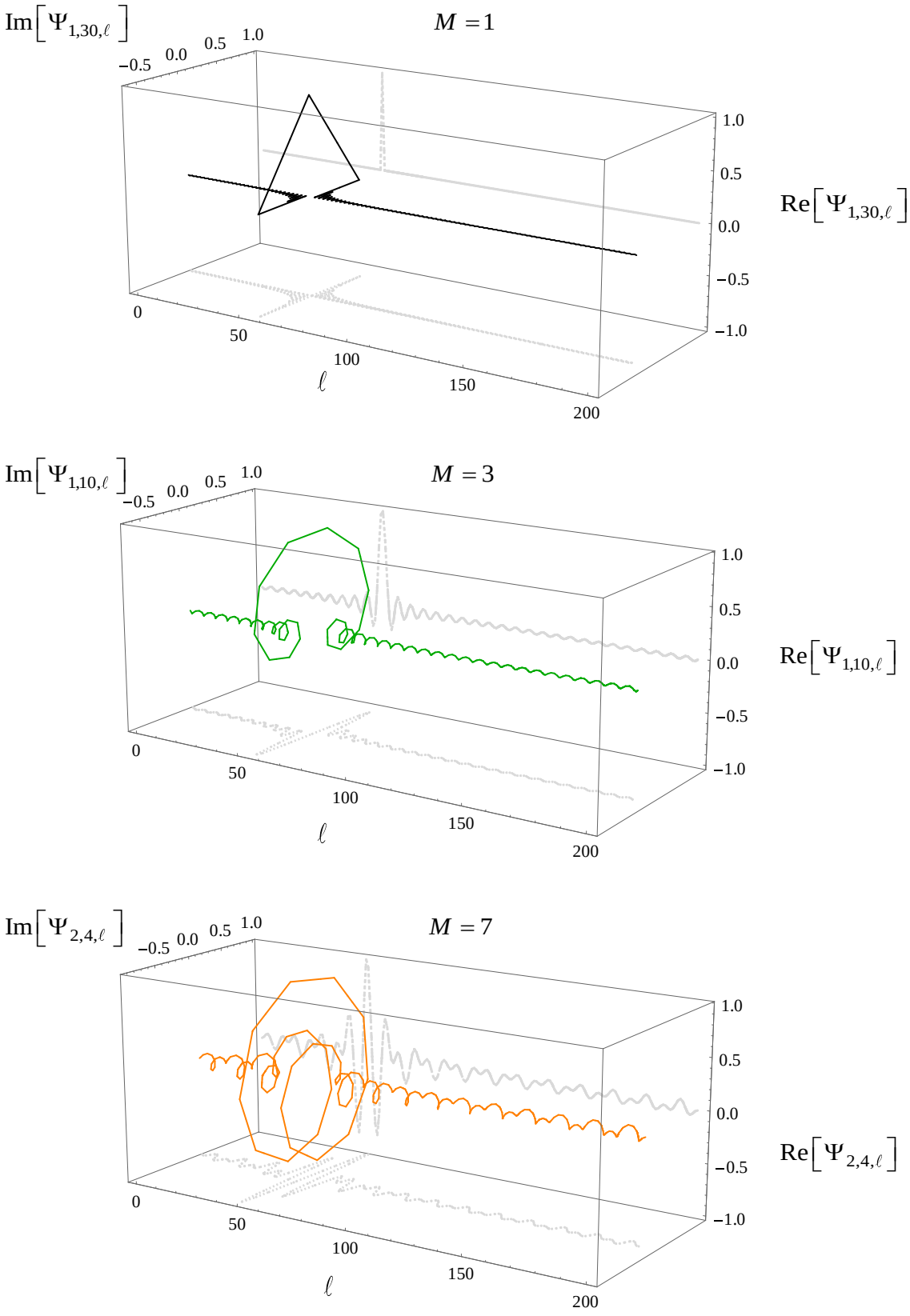

Figure 2.18 Three-dimensional plot (coloured solid line) of the circular wavelet together with the projections of the real part (grey line in vertical plane), and imaginary part (grey line in horizontal plane) with increasing resolution in the frequency domain: *M*=1,3,7,10,50,100.

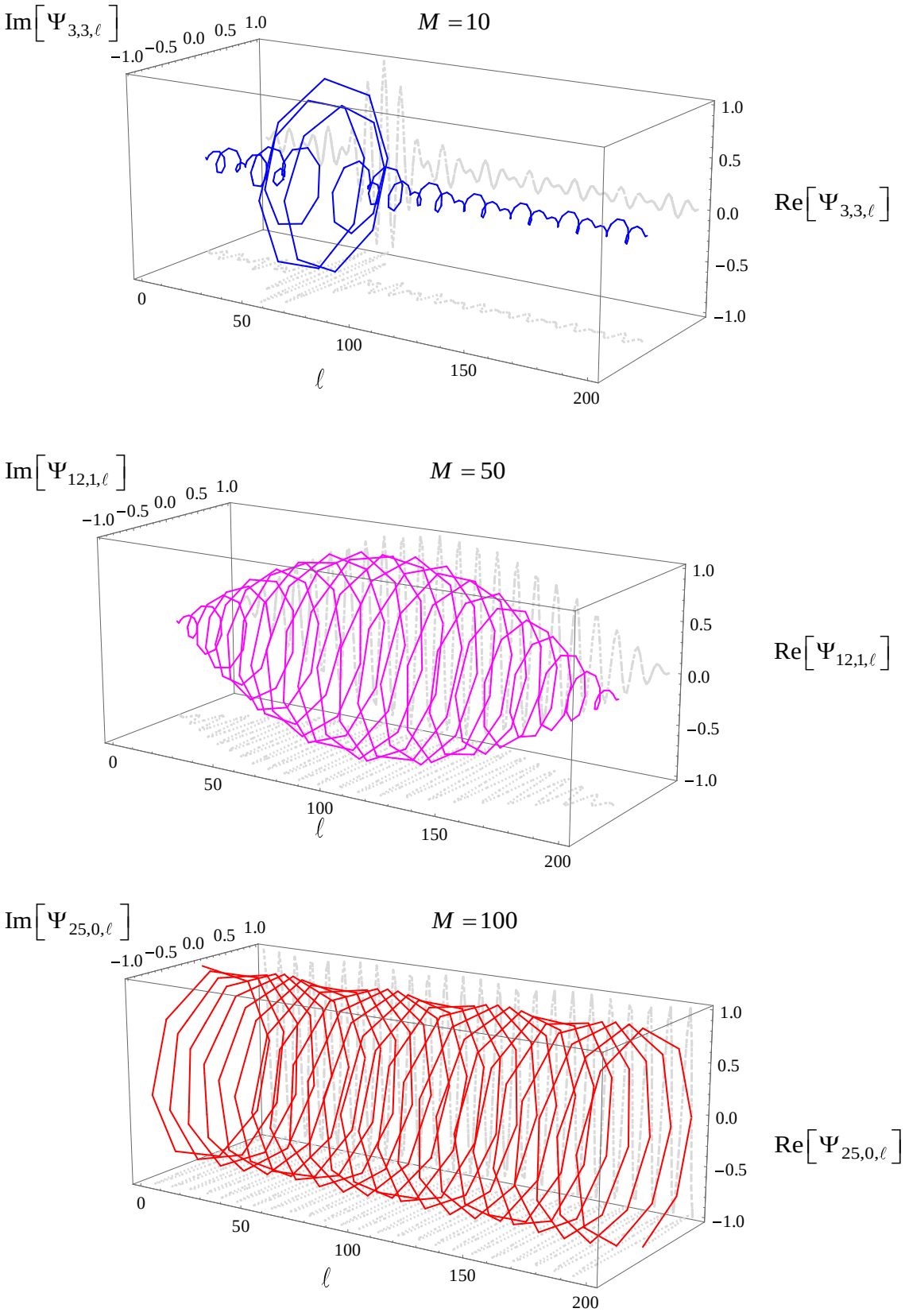

Figure 2.18 (*Continued*).

For the cases of M=3 and M=10, the representation of the signal (black line) obtained by Eq. (2.38) broken down into its components (grey lines) belonging to the generic jth band is shown in Figure 2.19.

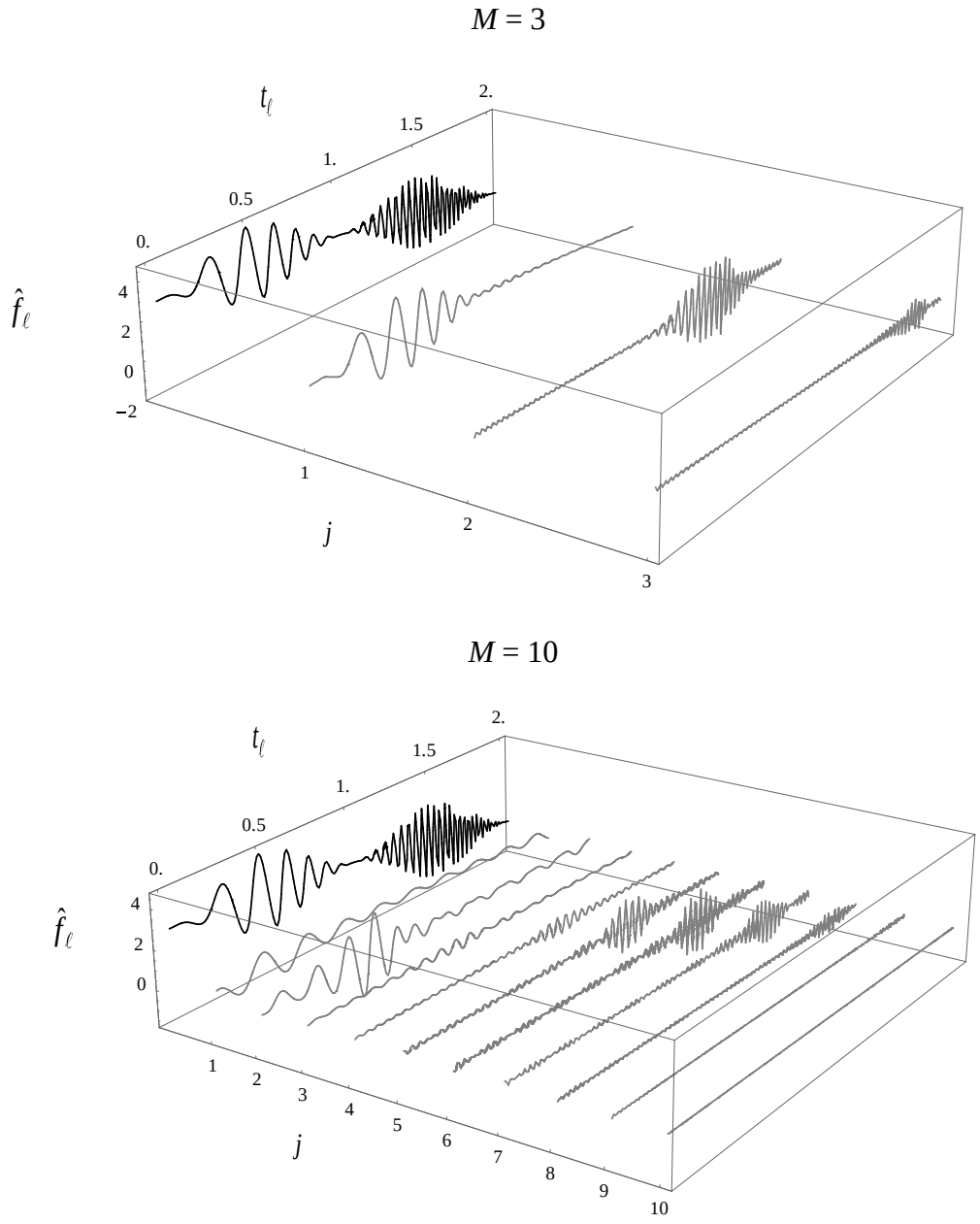

Figure 2.19 Representation of the signal (black line), and its components (grey lines): M =1 and M =3.

Table 2-III Parameters of the wavelets represented in Figure 2.18.

M	j	k	$b_j=n_j - m_j$	$\tau_{1,4} = (k\, t_{2N})/\, b_j$ [s]
1	1	30	100	0.6
3	1	10	33	0.6
7	2	4	15	0.53
10	3	3	10	0.6
50	12	1	2	1
100	25	0	1	0

2.5.2 Effect of the bandwidth parameter

In this subsection, the effect of the bandwidth parameter b_j on the generic circular wavelet $\Psi_{j,k,\ell}$, is investigated.

For M=1 there is only one frequency band $\left(b_j = b_1 = N\right)$ and the real part of the resulting wavelets can be expresses as:

$$\mathrm{Re}\left[\Psi_{j,k,\ell}\right] = \mathrm{Re}\left[\Psi_{1,k,\ell}\right] = \delta_{k,2\ell} = \begin{cases} 0 & \text{if } \ell \neq 2k; \\ 1 & \text{if } \ell = 2k, \end{cases} \tag{2.43}$$

meaning that:

1) a perfect localisation is achieved in the time domain (see Figures 2.18 and 2.20 a) where k=30 and the wavelet is centered at time $\tau_{1,30} = \left(k \cdot t_{2N}\right) / b_1 = \left(30 \cdot 2\right)/100 = 0.6\,\mathrm{s}$);
2) no localization is possible in the frequency domain, where the energy of the wavelet is spread nearly uniformly over the frequency range $\left[0, \omega_N\right]$ (see the nearly flat plot in Figure. 2.20 b) for $N \leq n \leq 2N$).

The opposite situation occurs for $M = N$: in this case b_j=1 and the frequency content of the wavelet is concentrated around a single discrete frequency $\bar{\omega}_j$, as shown by the red, dashed line in the frequency-domain plot in Figure 2.20.

In the numerical example used in this plot, j=25 and $\bar{\omega}_j = \left(j - 0.5\right)\Delta\omega = 77$ rad/s. Interestingly: *i*) due to the "circularity" of the wavelet, energy "bleeds" outside the nominal

bandwidth $\Delta\omega$; *ii*) no localisation is possible in the time domain as only one wavelet is associated with the discrete frequency $\bar{\omega}_j$.

The blue, thin solid line in Figures 2.20 a) and b) are representative of an intermediate situation between those considered before. In this case, for b_j=N/10, the circular wavelets simultaneously provide some localisation in both time and frequency, around $\tau_{j,k} = 0.6\,\text{s}$ and $\bar{\omega}_j = 78.6\,\text{rad/s},$ respectively.

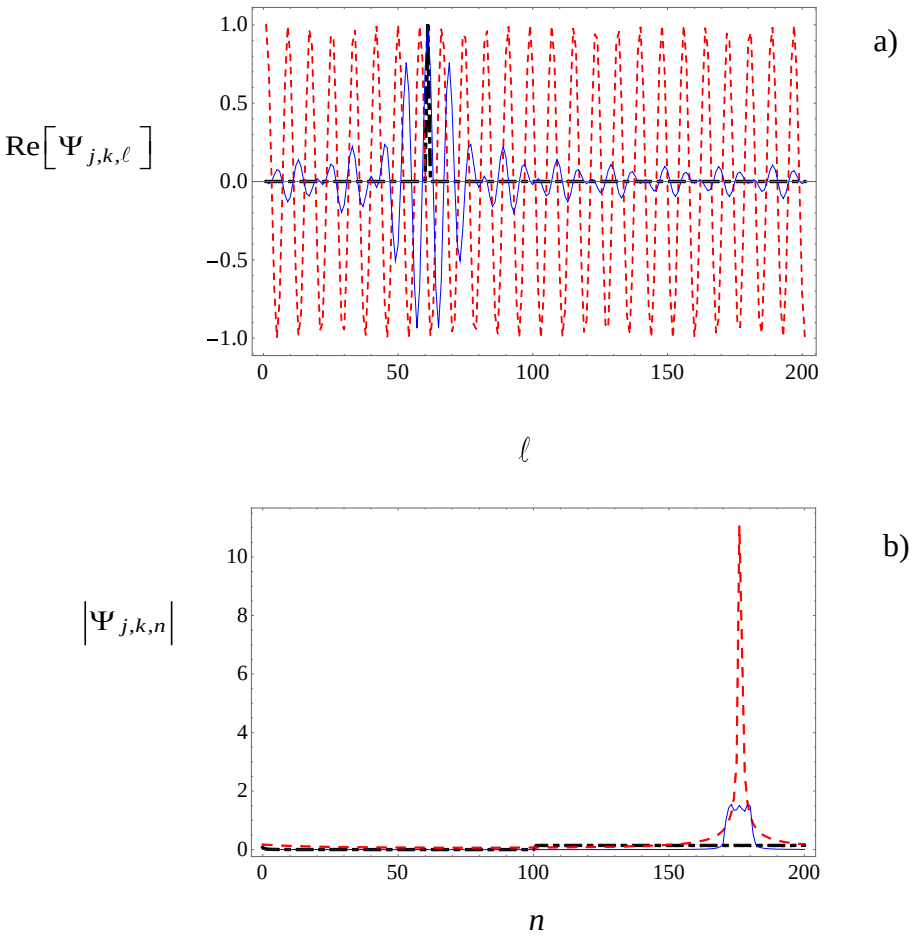

Figure 2.20: Circular wavelets with different bandwidth in the time a) and frequency b) domain: M=1, b_j=100=N and {j,k}={1,30}, black, dot-dashed line; M=10, b_j=10=N/10 and {j,k}={3,3}, blue, solid line; M=100, b_j=1 and {j,k}={25,0}, red , dashed line.

Chapter 3

Wavelet-based generation of non-stationary accelerograms

3.1 Introduction

The worldwide increasing availability of strong motion records makes the use of natural accelerograms an attractive option to properly define the input motions for dynamic analysis of both structural and geotechnical systems [Bommer and Acevedo 2004, Katsanos et al. 2010]. In nature there are no two identical recorded ground motions, consequently it's almost sure that the coming earthquake will be different from the ones used as input motions in the structural design.

Due to the uncertain nature of earthquakes, the rational way to assess the performance of earthquake-resistant structures consists in the use of the *stochastic approach* for modelling the dynamic action. The *stochastic approach* needs gaining a sufficient level of abstraction from the expected seismic event in a way that the generated records are considered realization of a stochastic process. Due to their non-stationary characteristics, the seismic ground motions are not suitable to be represented by a stationary process.

Joint time-frequency signal representation can be considered as a powerful strategy to analyse the time-varying amplitude and the evolutionary frequency content of accelerograms. Since the wavelets possess joint time-frequency localisation capabilities, wavelets analysis has been successfully exploited for different applications involving: simulation of earthquake ground motions [Iyama and Kuwamura 1999], analysis of dynamic systems with time-varying characteristics [Newland 1994, Carmona et al. 1998], analysis of linear structural responses to seismic excitations [Basu and Gupta 1997, 1998, 2000], modelling non-stationary dynamic loads for structural analysis and design [Spanos and Failla 2005, Cecini and Palmeri 2015], etc. In particular, Iyama and Kuwamura [1999], proposed a technique for simulating artificial

accelerograms based on the inverse *wavelet transform* of a random sequence of wavelet coefficients satisfying some constrains in terms of instantaneous energy for each frequency component. Then years later, Giaralis and Spanos [2009] proposed a stochastic approach for simulating non-stationary strong ground motion records compatible with a given design displacement spectrum in combination with a harmonic wavelet-based iterative procedure. Cecini and Palmeri [2015] proposed a deterministic modification method based on the harmonic *wavelet transform*, aimed matching the elastic *response spectrum* of a given accelerogram to a target elastic *response spectrum*; Basu and Gupta [1997, 1998] derived in explicit closed form solutions for the stochastic response of linear structural systems subjected to a non-stationary ground shaking, whose time dependent amplitude and frequency content are modelled through a generalisation of the Littlewood-Paly (L-P) basis of orthogonal wavelets.

Whitin the theoretical framework of Priestley's non stationary random processes [Priestly 1981], Spanos and co-workers have used different families of wavelets (including Newland's harmonic wavelet [Newland 1993, Newland 1994]) to compute the evolutionary power spectral density (*PSD*) function of stochastic signals [Spanos and Failla 2004, Spanos et al. 2005], and to determine the response statistics of linear and non-linear oscillators driven by non-stationary excitations [Spanos 2012]. These researches clearly show the great potential of wavelet-based approaches when non-stationary plays a key role in in the dynamic analysis of structural and geotechnical systems.

In the first part of this Chapter, the basic concept of random variables and random stationary and non-stationary processes are introduced. In the last part of the present Chapter, a novel stochastic model is presented, and numerically validated to generate an arbitrary number of seismic records having the same characteristics of the target accelerogram. The stochastic generation of artificial accelerograms is pursed through the Circular wavelets, deriving to the harmonic ones, whose key concepts and fundamental equations can be found in [Newland 1993]. The introduction of a new correlation structure for the random phases allows an arbitrary translation and rotation of the complex-valued wavelets that leads to the generation of samples having different variability with respect to a target accelerogram. The choice of the amplitude and of the number of bands in which is partitioned the frequency domain, is a key source of variability to consider for the generation of samples with the desired time-varying amplitude and frequency content [Genovese et al. 2021 a].

3.2 Basic definitions of stochastic variables and processes

A *random* or *stochastic variable X* is a variable whose value depends on outcomes of a random phenomenon. A *random variable* mathematically describes the results of experiments associated to a given event, whose domain is a numeric ensemble. If x_1 and x_2 are the bounds of this domain, any *random variable X* takes values: $x_1 \le X \le x_2$. The probability of occurring is denoted in the following by $\Pr\langle x_1 \le X \le x_2 \rangle$.

The *Cumulative Distribution Function* (*CDF*) and the *Probability Density Function* (*PDF*) of a *random variable X* are defined, respectively, by the following expressions:

$$L_X(x) = \Pr\langle X \le x \rangle; \quad p_X(x) = \frac{\mathrm{d}}{\mathrm{d}x} L_X(x). \tag{3.1}$$

A s*tochastic* or *random process X*(*t*) is defined as a family of *n* random variables related to a phenomenon, which are functions of one or more independent variables, like the time.

In order to obtain a complete probabilistic description of a *stochastic process X*(*t*), it's necessary the knowledge of the *probability distribution* or alternatively the knowledge of the *moment functions* of every order, which are defined as:

$$\begin{aligned} \mathrm{E}\langle X(t_1) \rangle &= \int_{-\infty}^{+\infty} x_1 \, p_{X(t_1)}(x_1) \, \mathrm{d}x_1 \\ \mathrm{E}\langle X(t_1) X(t_2) \rangle &= \int_{-\infty}^{+\infty} \int_{-\infty}^{+\infty} x_1 x_2 \, p_{X(t_1)}(x_1) \, p_{X(t_2)}(x_2) \, \mathrm{d}x_1 \mathrm{d}x_2 \end{aligned} \tag{3.2}$$

where the operator E<·> represents the stochastic average.

In particular, the *first-order moment* of the *random process X*(*t*) coincides with its *mean value* (also called *expected value*) $\mu_X(t)$, defined as:

$$\mu_X(t) = \mathrm{E}\langle X(t) \rangle = \int_{-\infty}^{+\infty} x \, p_{X(t)}(x) \, \mathrm{d}x. \tag{3.3}$$

The *autocorrelation function* represents a measure of correlation of the process with itself at two different times: $X(t_1)$ and $X(t_2)$. It can be defined as:

$$R_X(t_1, t_2) = \mathrm{E}\langle X(t_1) X(t_2) \rangle - \mathrm{E}\langle X(t_1) \rangle \mathrm{E}\langle X(t_2) \rangle. \tag{3.4}$$

The *second-order* moment of the *random process X*(*t*) is represented by the *variance* function, $\sigma^2_X(t)$ that depends on the mean value function $\mu_X(t)$ and on the *mean square value* function $\varphi^2_X(t)$:

$$\sigma_X^2(t) \equiv R_X(t,t) = \varphi_X^2(t) - \mu_X^2(t) = \int_{-\infty}^{+\infty} x^2 \, p_{X(t)}(x)\,\mathrm{d}x - \mu_X^2(t). \tag{3.5}$$

A *random process X* (*t*) is said to be *stationary* or *strict-sense stationary* if the *PDF* of any set of samples does not vary with time. Thus, in this case, the joint *PDF* or *CDF* of $\{X(t_1), X(t_2), X(t_3), \ldots, X(t_n)\}$ is identical to the joint distribution of the same variables displaced an arbitrary amount of time τ: $\{X(t_1+\tau), X(t_2+\tau), X(t_3+\tau), \ldots, X(t_n+\tau)\}$.

A process is defined *weakly stationary* (or stationary in wide sense) if the *mean* and the *variance* of the process are constant (i.e., independent of time), and its *autocorrelation function* depends only on the time difference $\tau = t_2 - t_1$ and not on t_1 and t_2 individually:

$$\begin{aligned} &\mu_X(t) = \mu_X, \\ &\sigma_X^2(t) = \sigma_X^2, \\ &R_X(t_1,t_2) = R_X(t,t+\tau) \equiv R_X(\tau) = \mathrm{E}\langle X(t)\,X(t+\tau)\rangle - \mu_X^2. \end{aligned} \tag{3.6}$$

In other words, in a *wide-sense stationary process*, the *mean* and *autocorrelation* functions do not depend on the choice of the time origin. A *non-stationary* process is characterized by a joint *PDF* or *CDF* that depends on time instants $\{t_1, t_2, t_3, \ldots, t_n\}$. In the theory of probability, a *Gaussian process* is a *stochastic process* such that every finite collection of the *random variables* $\{X(t_1), X(t_2), X(t_3), \ldots, X(t_n)\}$ has a multivariate normal distribution, i.e. every finite linear combination of them is normally distributed. A *stationary Gaussian process* is completely characterized by the knowledge of its *mean function* μ_X and its *autocorrelation function* $R_X(\tau)$ in the time domain; or its *mean* function μ_X and its *Power Spectral Density* (*PSD)* function $S_X(\omega)$ in the frequency domain. The *PSD* function of the *stationary Gaussian random process* is defined analytically by the *Fourier Transform* of the *autocorrelation function*:

$$S_X(\omega) = \frac{1}{2\pi} \int_{-\infty}^{+\infty} R_X(\tau)\,\mathrm{e}^{-i\omega\tau}\,\mathrm{d}\tau \tag{3.7}$$

where $i = \sqrt{-1}$ is the imaginary unity. The inverse *Fourier transform* of the *PSD* function gives the autocorrelation function:

$$R_X(\tau) = \int_{-\infty}^{+\infty} S_X(\omega)\,\mathrm{e}^{i\omega\tau}\,\mathrm{d}\omega. \tag{3.8}$$

The Eqs. (3.7) and (3.8) are the *Wiener-Khinchine relations*, that play a fundamental role in the random vibration analysis. The *PSD* function is not able to give the distribution of frequency content in time domain, but only in the frequency domain. To take into account both the frequency and time variations two approaches (*Wigner-Ville method* and *the evolutionary spectral analysis*) could be used. By applying the *Wigner-Ville* method [Newland 1975], the instantaneous *PSD* function is a time dependent function defined as:

$$S_X(\omega,t)=\frac{1}{2\pi}\int_{-\infty}^{\infty} R_X(\tau,t)\,\mathrm{e}^{i\omega\tau}\,\mathrm{d}\tau \tag{3.9}$$

where $S_X(\omega, t)$ is a measure of the frequency content of *non-stationary random process X* (t) at time *t*.

The *evolutionary spectral analysis* was introduced by Priestley in 1987. Priestley considered a class of non-stationary processes defined by means of the following *Fourier-Stieltjes integral*:

$$X(t)=\int_{-\infty}^{\infty}\mathrm{e}^{\mathrm{i}\omega t}\,a(\omega,t)\,\mathrm{d}N(\omega) \tag{3.10}$$

where $a(\omega, t)$ is a slowly varying complex deterministic time-frequency *modulating function*, which has to satisfy the conditions: $a(\omega, t) \equiv a^*(-\omega, t)$, with $\mathrm{Re}\{a(\omega, t)\} \geq 0$; $N(\omega)$ is a zero-mean process with orthogonal increments satisfying the condition:

$$\mathrm{E}\left\langle \mathrm{d}N(\omega_1)\,\mathrm{d}N^*(\omega_2)\right\rangle=\frac{1}{2}\delta(\omega_1-\omega_2)\,S_0(\omega_1)\,\mathrm{d}\omega_1\,\mathrm{d}\omega_2 \tag{3.11}$$

where $\delta(\cdot)$ is the Dirac delta, and $S_0(\omega)$ is the *PSD* function of the so-called *embedded stationary counterpart process* $\tilde{N}(t)$ [Michealov et al 1999]. The Priestley *evolutionary process X* (t) possesses autocorrelation function:

$$R_X(t_1,t_2)=\int_{-\infty}^{\infty}\mathrm{e}^{\mathrm{i}\omega(t_1-t_2)}\,S_X(\omega,t_1,t_2)\mathrm{d}\omega\,. \tag{3.12}$$

where:

$$S_X(\omega,t_1,t_2)=a(\omega,t_1)\,a^*(\omega,t_2)S_0(\omega) \tag{3.13}$$

In the Priestley evolutionary process model, the function:

$$S_X(\omega,t)=\left|a(\omega,t)\right|^2 S_0(\omega) \tag{3.14}$$

is referred as the *Evolutionary PSD* (*EPSD*) function of the non-stationary process X (t). In the previous equation the symbol $|\cdot|$ denotes the modulus of the function in brackets. The

processes characterized by the *EPSD* function, $S_X(\omega,t)$, given in Eq.(3.14), are called *fully non-stationary random processes*, since both time and frequency content change. If the modulating function is a real time-dependent function, $a(\omega, t) \equiv a(t)$, the *non-stationary* process is called *quasi-stationary* (or *uniformly modulated*) random process. In this case the *EPSD* function assumes the expression: $S_X(\omega,t) = a(t)^2 S_0(\omega)$.

In Figure 3.1 are shown samples of *stationary* a), *quasi stationary* b) and *non-stationary* c) processes. In the Figure 3.1, the red line represents the modulating function $a(t)$.

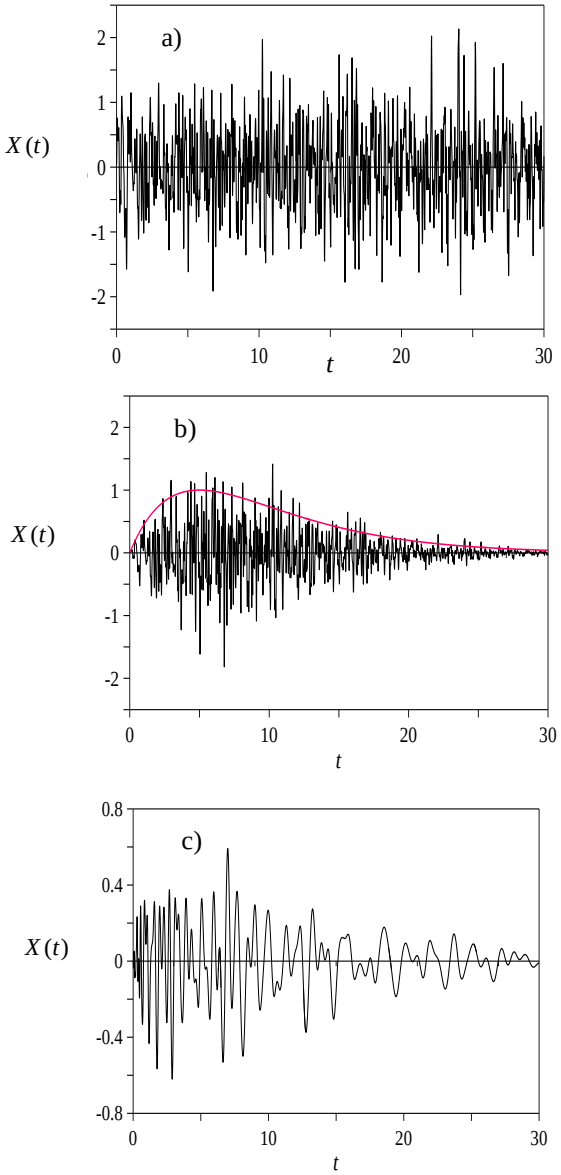

Figure 3.1 Samples of *stationary* a), *quasi stationary* b) and *non-stationary* c) processes. The red line represents the modulating function $a(t)$.

3.3 Proposed randomisation procedure

When the generation of random time histories is required for the analysis and design of structures subjected to dynamic loads, a typical approach requires the following steps: *i*) to define a function of time t and circular frequency ω capable of describing the features of interest about the phenomenon being simulated (e.g. ground acceleration, wind velocity, etcetera), in terms of time evolving frequency content and amplitude [Spanos and Failla 2004, Spanos et al. 2005]; *ii*) to use a generation procedure to obtain the needed samples [Liang et al. 2007, Shinozuka and Deodatis 1988, Shinozuka and Deodatis 1991].

Let $f(t)$ be a zero-mean, stationary Gaussian process, fully defined in the frequency domain by the power spectral density (*PSD*) function $S_F(\omega)$. A popular method for generating the generic realisation of the rando process $f^{(r)}(t)$ consists in the use of the so-called *Shinozuka's formula*, which requires the following steps:

1) choose a "cut-off" frequency ω_N such that (for the purposes of the analyses being carried out) the energy of the random process can be neglected for $\omega > \omega_N$;
2) divide the frequency range of interest [0, ω_N] into a "large number" N of intervals of equal width $\Delta\omega = \omega_N / N$;
3) calculate the value of the *PSD* function at the central frequency of each interval $\Delta\omega$, that is $S_j = S_F(\bar{\omega}_j)$, with $\bar{\omega}_j = \left(j - \frac{1}{2}\right)\Delta\omega$ and $j = 1, 2, \cdots, N$;
4) generate a set of N statistically independent random variables, $\left\{\phi_1^{(r)}, \phi_2^{(r)}, \cdots, \phi_N^{(r)}\right\}$, uniformly distributed over the range $[-\pi, \pi]$;
5) generate the rth sample of the random process through a superposition of N harmonic functions with random phases:

$$f_\ell^{(r)} = f^{(r)}(t_\ell) = 2\sum_{j=1}^{N}\sqrt{S_j\,\Delta\omega}\cos\left(\bar{\omega}_j\,t_\ell + \phi_j^{(r)}\right) \tag{3.15}$$

   where t_ℓ is the generic time instant at which the sample is evaluated;
6) repeat step 4 and 5 until enough samples of the random process have been obtained.

It should be noted that using Euler's formula, Eq. (3.15) is equivalent to:

$$f^{(r)}(t_\ell) = 2\,\mathrm{Re}\sum_{j=1}^{N} C_{j,\ell}\exp\left(i\,\phi_j^{(r)}\right) \tag{3.16}$$

where the complex-valued coefficients $C_{j,\ell} = \sqrt{S_j\,\Delta\omega}\exp\left(i\;\bar{\omega}_j\,t_\ell\right)$ are sample independent, so they need to be calculated only once, while the sample-to-sample variability is achieved through the generation of the random phases $\phi_j^{(r)}$.

Shinozuka's formula of Eq. (3.15) is remarkably similar to Eq. (2.40) which particularises the wavelet-based reconstruction of a discrete signal when the number of frequency bands *M* is the same as the number of points in the frequency-domain representation of the discrete signal *N*. This suggests the possibility of using random phases to randomise the contributions of the harmonic functions appearing in the circular wavelets used to reconstruct a discrete signal. Accordingly, Eq. (2.38), can be randomised as:

$$f_\ell^{(r)} = f^{(r)}(t_\ell) = \bar{f}_\ell + 2\sum_{j=1}^{M}\frac{1}{b_j}\sum_{k=0}^{b_j-1}\left|\hat{a}_{j,k}\right|\sum_{s=m_j}^{n_j-1}\cos\left[\pi(2s+1)\left(\frac{\ell}{2N}-\frac{k}{b_j}\right)+\hat{\theta}_{j,k}+\phi_{j,k}^{(r)}\right] \tag{3.17}$$

in which $\boldsymbol{\phi}^{(r)} = \left\{\phi_{1,0}^{(r)},\cdots,\phi_{j,k}^{(r)},\cdots,\phi_{M,b_{M-1}}^{(r)}\right\}^{\mathrm{T}}$ is the $N-$dimensional array collecting the rth realisation of random phases uniformly distributed over the range $[-\pi,\pi]$. Notice that for a zero-mean process $\bar{f}_\ell = 0$.

Noteworthily: i) if all the random phases are set to zero, i.e., if $\boldsymbol{\phi}^{(r)} = \{0,\cdots,0,\cdots,0\}^{\mathrm{T}}$, the rth realisation of the random signal $f_\ell^{(r)}$ of Eq. (3.17) coincides with the discrete signal $\hat{f}_\ell$, deterministically reconstructed via Eq. (2.38); the generic element $\phi_{j,k}^{(r)}$ of the random vector $\boldsymbol{\phi}^{(r)}$ represents the random rotation of the circular wavelets $\Psi_{j,k,\ell}$ of Eq. (2.34), whose real part is the (j,k)th contribution to the random realisation $f_\ell^{(r)}$. It follows that the generation formula of Eq. (3.17) can be expressed in the equivalent form:

$$f_\ell^{(r)} = \bar{f}_\ell + 2\,\mathrm{Re}\left[\sum_{j=1}^{M}\sum_{k=0}^{b_j-1}\hat{C}_{j,k,\ell}\exp\left(i\,\phi_{j,k}^{(r)}\right)\right] \tag{3.18}$$

in which the generic coefficient $\hat{C}_{j,k,\ell}$ is sample-independent and defined as:

$$\hat{C}_{j,k,\ell} = \hat{a}_{j,k}\,\psi_{j,k,\ell} = \frac{\hat{a}_{j,k}}{b_j}\sum_{s=m_j}^{n_j-1}\exp\left[\,i\,\pi(2s+1)\left(\frac{\ell}{2N}-\frac{k}{b_j}\right)\right] = \hat{C}'_{j,k,\ell} + i\,\hat{C}''_{j,k,\ell} \tag{3.19}$$

where $\hat{C}'_{j,k,\ell}$ = Re $|\hat{C}_{j,k,\ell}|$ and $\hat{C}''_{j,k,\ell}$ = Im $|\hat{C}_{j,k,\ell}|$ are its real and imaginary part respectively. The comparison of Eq. (3.16) and (3.18) reveals that the proposed wavelet-based generation formula coincides with the conventional *Shinozuka's formula* in the special case of $M=N$ (therefore, $b_1=b_2=\cdots=b_M=1$), and the sample independent coefficients are given by:

$$\hat{C}_{j,0,\ell} = \hat{C}_{j,\ell} = \sqrt{S_j\,\Delta\omega}\exp\left[\,i\,\pi\frac{(2j-1)\,\ell}{2N}\right]. \tag{3.20}$$

The application of the expectation operator E<·> to both sides of the proposed generation formula of Eqs. (3.18) yields:

$$\mu_{f_\ell} = \mathrm{E}\langle f_\ell\rangle = 2\sum_{j=1}^{M}\sum_{k=0}^{b_j-1}\mathrm{E}\left[\,\hat{C}'_{j,k,\ell}\cos\left(\phi_{j,k}\right) - \hat{C}''_{j,k,\ell}\sin\left(\phi_{j,k}\right)\right] = 0 \tag{3.21}$$

as $\mathrm{E}\left\langle\cos\left(\phi_{j,k}\right)\right\rangle = 0$ and $\mathrm{E}\left\langle\sin\left(\phi_{j,k}\right)\right\rangle = 0$. It follows that, similarly to *Shinozuka's formula* the generated random process $F_\ell = F\left(t_\ell\right)$ has zero mean.

Importantly, in the *Shinozuka's formula*, the random phases ϕ_j are assumed to be statistically independent; that is, for $j \neq J$ and any pair of exponents a and b:

$$\mathrm{E}\left\langle\phi_j^a\,\phi_J^b\right\rangle = \mathrm{E}\left\langle\phi_j^a\right\rangle\,\mathrm{E}\left\langle\phi_J^b\right\rangle \tag{3.22}$$

on the contrary, in the proposed randomization formula of Eq. (3.18) an arbitrary correlation structure can be adopted for the random phases $\phi_{j,k}$.

3.3.1 Proposed correlation structure

The generated samples by Eq.(3.17) can achieve a different statistical similarity with the target signal f_ℓ at time t_ℓ. Since the random phases are the only non-deterministic quantities in the proposed generation formula of Eq.(3.17), a different variability of the generated samples can be obtained by the introduction of a linear correlation coefficient ρ for the random phases $\phi_{j,k}$ and $\phi_{J,K}$. The proposed correlation structure can be expressed as:

$$\rho_{\phi\phi(j,k,J,K)} = \rho_{\phi(j,k)\,\phi(J,K)} = \frac{\mathrm{E}\left\langle \phi_{j,k}\,\phi_{J,K} \right\rangle}{\sigma_{j,k}\,\sigma_{J,K}} = \\ = \exp\left[-\sqrt{\left(\frac{\left(\omega_{m_j} + \omega_{n_j}\right) - \left(\omega_{m_J} + \omega_{n_J}\right)}{2\,\lambda_\omega} \right)^2 + \left(\frac{\left(k / b_j\right) - \left(K / b_J\right)}{\lambda_\tau} \right)^2} \right] \tag{3.23}$$

where the generic random phases ($\phi_{j,k}$ and $\phi_{J,K}$) are uniformly distributed in the interval $[-\pi, \pi]$, such that the standard deviations of the random phases are equal to: $\sigma_{\phi(i,k)} = \sigma_{\phi(J,K)} = \pi/\sqrt{3}$. In Eq. (3.23) $\lambda\omega$ and $\lambda\tau$ are correlation measures in the frequency domain and in the time domain, respectively. These two quantities can be related to seismic parameters of the target signal: for instance, $\lambda\tau$ can be associated to the *strong motion duration* $t_{5\text{-}95}$ and $\lambda\omega$ to the strong frequency interval $\omega_{5\text{-}95}$ of the target signal $f(t)$. Notice that it is useful to set $\lambda\tau$ and $\lambda\omega$ in terms of seismic ground motion parameters instead of the values associated to the entire waveform (i.e. the total duration of the signal t_{2N} could take very large values if the zeros-padding of the recorded signal have not been appropriately removed in the signal post-processing phase).

The limiting condition $\lambda\omega \to 0$ and $\lambda\tau \to 0$ corresponds to the case where all the random phases are statistically independent or "uncorrelated" (*UC*); conversely, the case of fully correlated (*FC*) phases occurs when simultaneously $\lambda\omega \to +\infty$ and $\lambda\tau \to +\infty$. In the intermediate configurations between the two limit conditions, the correlation structure is called "partially correlated" (*PC*).

3.3.2 Generation of random phases

The evaluation of correlated random phases requires the following steps:

1) define a vector colleting the random phases, through the following transformation of variables:

$$\boldsymbol{\phi} = \Phi\left\{\boldsymbol{u}\right\} \tag{3.24}$$

where $\boldsymbol{u} = \left\{u_1, \cdots, u_i, \cdots, u_N\right\}^{\mathrm{T}}$ is a $N-$dimensional vector of zero-mean, Gaussian variables with unitary variance, i.e. $\sigma_{u_i} = \mathrm{E}\left\langle u_i^2 \right\rangle = 1$. In this case, the Gaussian

distribution in the variate u_i is known as "*standard normal distribution*" having a *probability density function PDF* and a cumulative distribution function *CDF* given by:

$$PDF_{u_i}(u) = \frac{1}{\sqrt{2\pi}} \exp\left(-\frac{u^2}{2}\right) \tag{3.25}$$

$$CDF_{u_i}(u) = \int_{-\infty}^{u} \frac{1}{\sqrt{2\pi}} \exp\left(-\frac{x^2}{2}\right) \mathrm{d}x = \frac{1}{2}\left(1 + \mathrm{erf}\left[-\frac{u}{\sqrt{2}}\right]\right) \tag{3.26}$$

in which erf(·) is the error function:

$$\mathrm{erf}(u) = \frac{2}{\sqrt{\pi}} \int_{0}^{u} \exp\left(-u^2\right) \mathrm{d}u \tag{3.27}$$

The transformation function Φ is assumed as:

$$\Phi(u) = 2\pi\left(CDF_{u(i)}(u) - 0.5\right) = \pi\,\mathrm{erf}\left(\frac{u}{\sqrt{2}}\right) \tag{3.28}$$

2) define a symmetric and defined positive correlation structure $\rho_{\phi\phi(j,k,J,K)}$ of dimension $N \times N$ for the random phases in the $N-$dimensional vector $\boldsymbol{\phi}$;
3) evaluate the auxiliary correlation coefficient $\rho_{uu(j,k,J,K)}$ that is a function of the linear correlation coefficient between the corresponding random phases $\rho_{\phi\phi(j,k,J,K)}$;

$$\rho_{uu(j,k,J,K)} = 2\sin\left(\frac{\pi}{6}\rho_{\phi\phi(j,k,J,K)}\right) \tag{3.29}$$

4) generate random variates of the multinormal distribution having a $N-$dimensional mean vector $\boldsymbol{\mu} = \{0,\cdots,0,\cdots,0\}^{\mathrm{T}}$ and a covariance matrix $\boldsymbol{\Sigma} = \rho_{\phi\phi(j,k,J,K)}$ of the random phases;
5) evaluate the elements of the random variables, through the application of the transformation function, defined in Eq. (3.28), to the multinormal distribution.

3.4 Numerical applications to seismic signals

In order to validate the formulae derived in the previous section, the "090" component of the ground motion recorded at Vasquez Rocks Park during the 1994 Northridge earthquake has been used in the following as target accelerogram $f(t)$.

The selected ground motion, downloaded from the Peer database [Ancheta et al. 2013], having a moment magnitude M_W = 6.7 and a site-source distance R_{JB}=23.1 km [Joyner and Boore 1981], has been recorded with a sampling time Δt=0.02 s at a station having an average shear wave velocity in the upper 30 m equal to $V_{s,30}$=996 m/s (EC8 2004, soil class "A"). The total intensity of the target accelerogram, having an overall duration t_{2N} =39.98 s, is equal to $I_0 = 1.99\ \mathrm{m}^2/\mathrm{s}^3$.

In Figure 3.2 are reported: a) the acceleration time-history $f(t)$, b) the *cumulative energy* function $I_0(t)$ and c) the cumulative *zero-level up-crossing* function $N_0^+(t)$ of the target accelerogram. The shaded grey areas, delimited by the dashed black lines, indicate the strong motion duration $t_{5\text{-}95}$ of the target signal. The corresponding acceleration *response spectrum* $SA(T,\xi)$**,** for a damping ratio equal to ξ =5%, is shown in Figure 3.3.

Figure 3.4 show: a) the modulus of the *Fourier spectrum* $\mathbb{F}\langle f(t)\rangle$ and b) the *cumulative Fourier energy* function $E_A(\omega)$; the shaded grey areas, delimited by the dashed black lines, indicate the *strong circular frequency* $\omega_{5\text{-}95}$ of the target signal.

In Table 3-I: are listed the main characteristics of 1994 Northridge earthquake: time duration t_{2N}, sampling step Δt, sampling frequency υ_0, number of the discrete non-zero frequencies N, number of points p, Nyquist frequency ω_N and frequency step $\Delta\omega$.

For the target signal, the values of the main seismic parameters detailed in the Chapter 1, are summarised in Table 3-II.

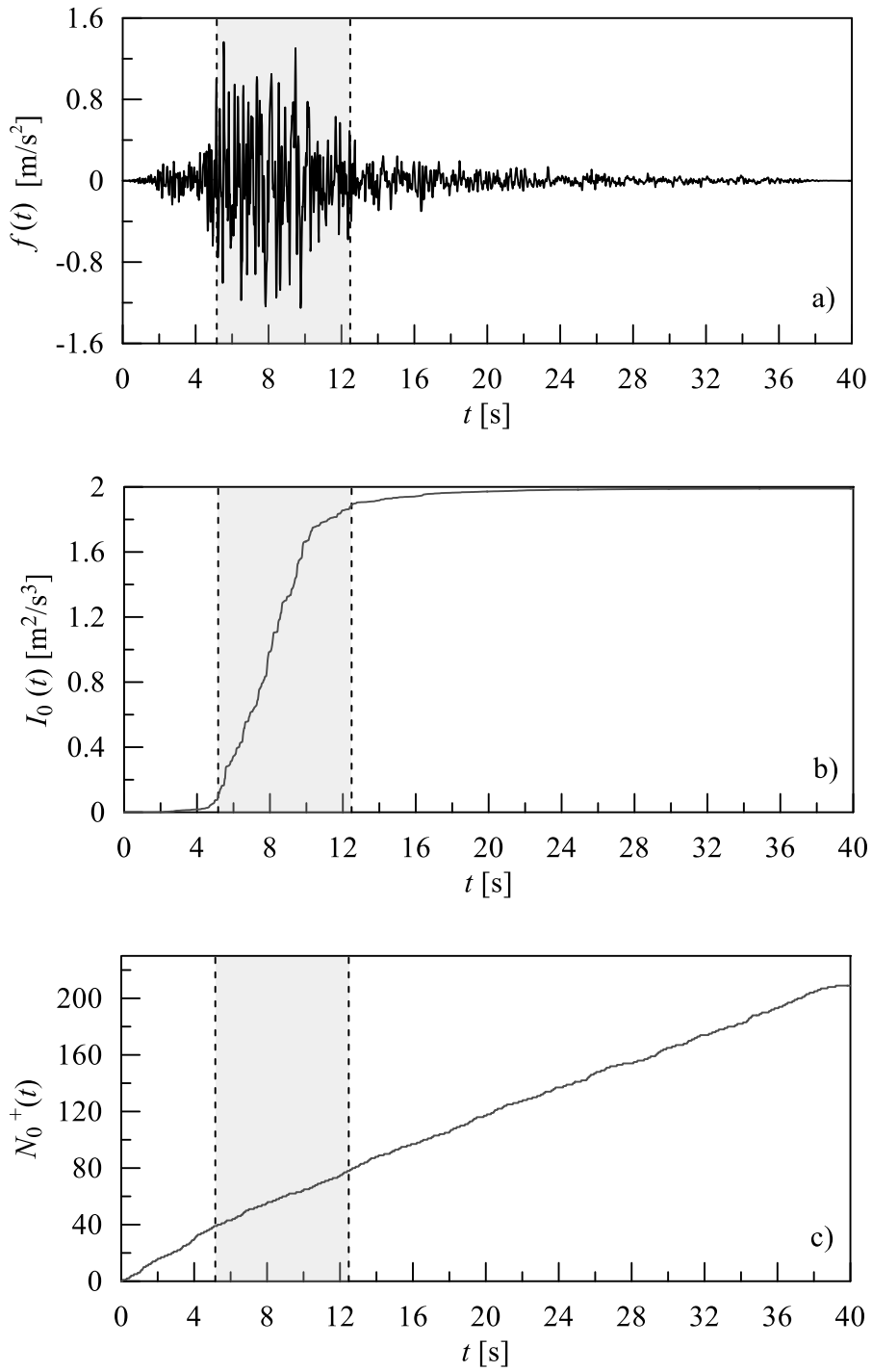

Figure 3.2 Time history a); *cumulative energy* function b); *zero-level up-crossing* function c), of the target 1994 Northridge earthquake accelerogram (solid line) together with the indication of the strong motion duration (grey shaded area) delimited by the two vertical dashed black lines.

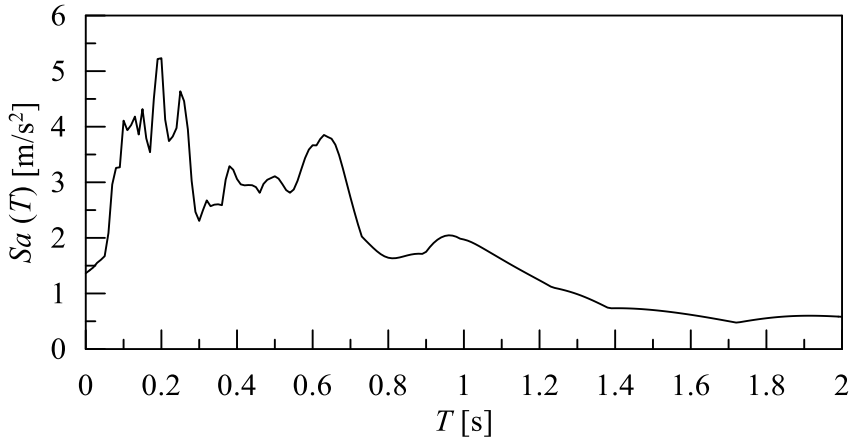

Figure 3.3 *Acceleration response spectrum* of the target 1994 Northridge earthquake accelerogram, for a damping ratio equal to 5%.

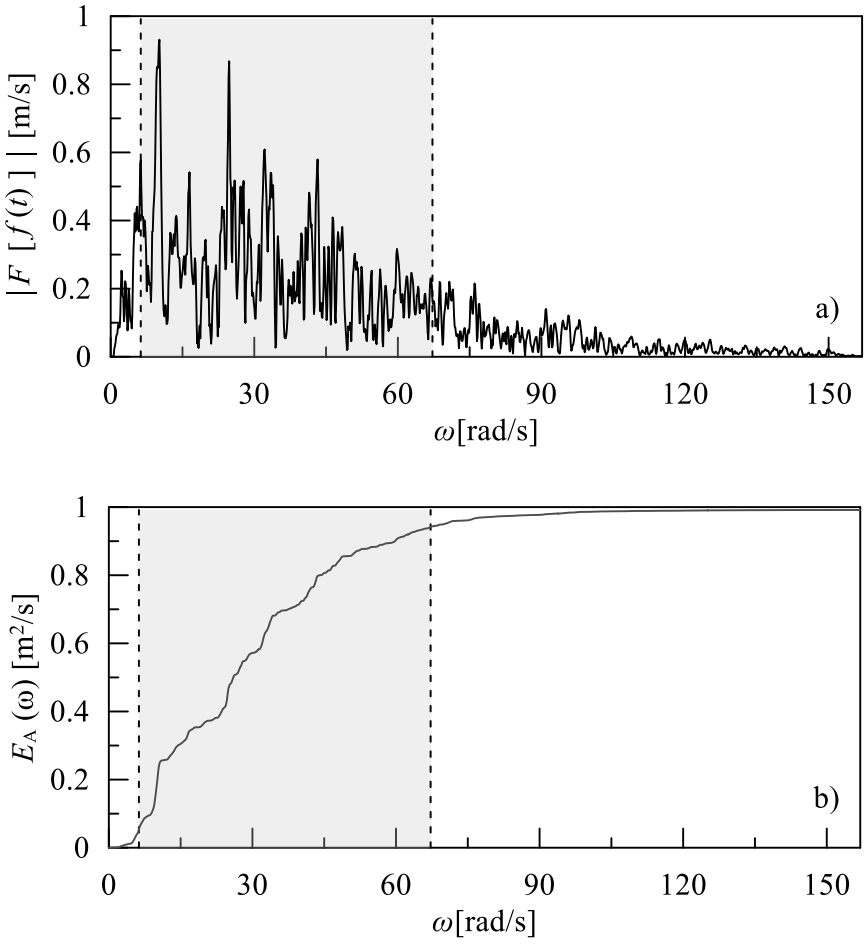

Figure 3.4 Modulus of the *Fourier spectrum* a) and *cumulative Fourier energy* function b) of the target 1994 Northridge earthquake accelerogram (solid line) together with the indication of the *strong circular frequency* (grey shaded area) delimited by the two vertical dashed black lines.

Table 3-I Main characteristics of the 1994 Northridge earthquake.

t_{2N} [s]	Δt [s]	$\upsilon_0 = 1/\Delta t$ [Hz]	$N = t_{2N}/(2\Delta t)$ [-]	$P=2N+1$ [-]	$\omega_N = N\,\Delta\omega$ [rad/s]	$\Delta\omega=2\pi/t_{2N}$ [rad/s]
39.98	0.02	50	1000	2001	157.158	0.157

Table 3-II Seismic parameters of the 1994 Northridge earthquake.

PGA [m/s^2]	*PGV* [m/s]	*PGD* [m]	*PGV/ PGA* [s]	I_0 [m^2/s^3]	I_A [m/s]	N_0^+ [-]	P [-]	I_F [-]	$t_{5\text{-}95}$ [s]
1.364	0.112	0.028	0.0821	1.98	0.318	209	228	0.916	7.32

3.5 Partition of the frequency domain

To validate the formulae derived in the previous section, a set of one hundred accelerograms have been generated by Eq.(3.17).

Three alternative partitions of the frequency range of interest $[0,\omega_N]$ are considered, with a subdivision in M =1, 100, 1000 frequency bands, respectively.

In order to investigate the effect of the correlation structure $\rho_{\phi\phi(j,k,J,K)}$ of Eq.(3.23) on the characteristics of the samples, generated by the proposed randomization procedure, three different cases have been analysed for each of the three M partition of the frequency domain.

In the first case, called "uncorrelated" (*UC*), the random phases $\phi_{j,k}$ and $\phi_{J,K}$ are assumed different from each other consequently $\rho_{\phi\phi(j,k,J,K)}=1$ only for $\{j,k\}=\{J,K\}$ and $\rho_{\phi\phi(j,k,J,K)}=0$ for all the other cases $\{j,k\}\neq\{J,K\}$. This condition is obtained by setting equal to zero the values of the correlation measures of Eq.(3.23), in both time and frequency domain; that is: $\lambda_\omega=\lambda_\tau=0$.

In the second case, called "partially correlated" (*PC*) an intermediary condition is investigated, relating the correlation measures to the seismic parameters of the signal. Specifically: $\lambda_\omega=\omega_{5\text{-}95}$ and $\lambda_\tau=t_{5\text{-}95}$ are considered, being $\omega_{5\text{-}95}$ and $t_{5\text{-}95}$ the *strong circular frequency* and the *strong motion duration* of the target signal, respectively.

In the third case, called "fully correlated" (*FC*), $\rho_{\phi\phi(j,k,J,K)}$=1 for any pair of random phases $\phi_{j,k}$ and $\phi_{J,K}$, therefore their *r*th realizations coincide to each other, i.e. $\phi_{j,k}^{(r)} = \phi_{J,K}^{(r)}$.

In Figures 3.5-7 are reported the results obtained through the subdivision of the frequency range of interest $[0,\omega_N]$ in M =1,100,1000 parts, respectively.

Specifically in Figures 3.5-7 are shown: a) three generic samples (coloured lines) together with the target accelerogram (black line); b) three mean *Fourier spectra* moduli (coloured lines) together with the target *Fourier spectrum* modulus (black line), for *UC*, *PC* and *FC* random phases and considering a partition of the frequency domain in *M*=1,100,1000 parts, respectively.

Figures 3.5-7 show a comparison among the: c) *acceleration response spectrum*; d) *cumulative energy* function*;* e) *cumulative zero level up crossing* function of the target accelerogram (red solid line) with statistics of the artificial ones: mean value function (black line); mean value plus/minus standard deviation functions (black dashed lines); envelope of the maximum and minimum values of all samples (shaded area), considering M =1,100,1000, respectively. The aforementioned functions have been evaluated considering *UC*, *PC* and *FC* random phases in the correlation structure.

It can be noticed that:

1) in Figure 3.5 a) (*M*=1) the variation in amplitude of the generated signals appears to be preserved for all three random phases correlations adopted;
2) in Figure 3.6 a) (*M*=100) the variation in amplitude of the generated samples appears to be preserved only for the fully correlated (*FC*) case. Indeed, a particular situation happens for the uncorrelated (*UC*) and partially correlated cases (*PC*) where the generated samples tend to have a periodic behaviour and they appear as "slowly modulated" signals (Figure 3.6 a);
3) in Figure 3.7 a) (*M*=*N*=1000), for the case *UC*, the generated samples tend to lose the fidelity in terms of non-stationary characteristics, until they become realizations of a stationary random process while, for the *PC* and *FC* cases the variation in amplitude of the generated signals appears to be preserved;
4) the mean *amplitude Fourier spectrum* and the *zero-level up crossing function* of the generated samples are very close to the target one in all the analysed situations except for the uncorrelated case (*UC*) in correspondence of a subdivision of the frequency range into only one part *M*=1 (see Figures 3.5-7 b, e).

5) for the uncorrelated case (*UC*) of the M=1 and M=1000 frequency partitions (see Figure 3.5 c) and Figure 3.7 c)), the mean *acceleration response spectrum* of the generated samples (black line) is very far to that of the target one (red line). In all the other investigated configurations the mean *acceleration response spectrum* is in a good agreement with the trend of the target one.
6) the mean *cumulative energy* function of the generated samples is in a good agreement with the target one in all the analysed situations except for the *UC* case in correspondence of a subdivision of the frequency range into M=N=1000 parts (see Figures 3.5-7 d).

From the analysis of the results obtained it is clear that by varying the parameters present in the correlation structure, it is possible to generate samples having the desired characteristics.

M=1

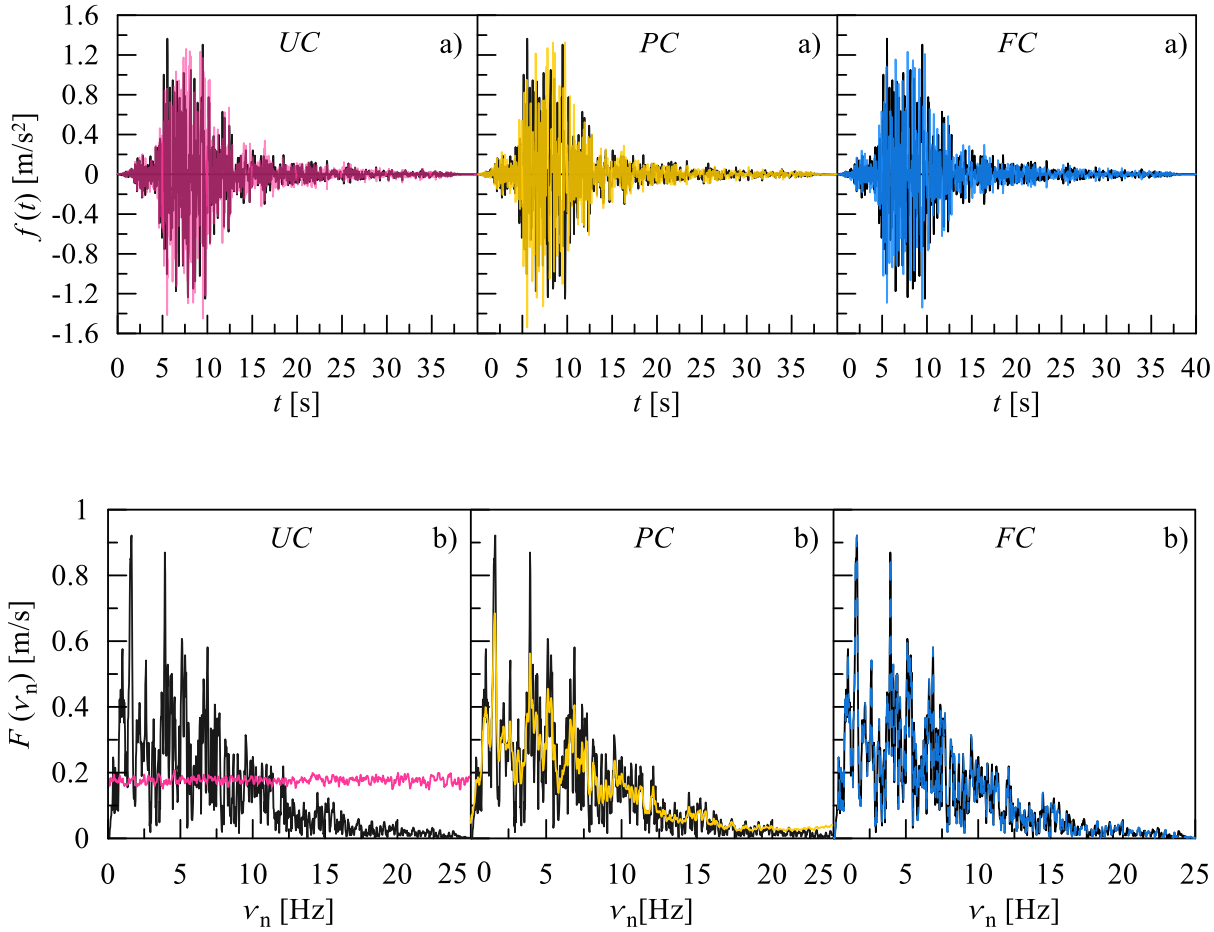

Figure 3.5 Result of the circular *wavelet transform* method, considering a subdivision of the frequency domain into *M*=1 part, for random phases: "uncorrelated" (*UC*), "partially correlated" (*PC*) and "fully correlated" (*FC*). Comparison among the: a) target accelerogram (black line) and the *i*th generated sample (coloured line); b) mean *Fourier spectrum modulus* of the generated samples (coloured line) and the target one (black line); c-e) *response spectrum* c), *cumulative total intensity* d), and *cumulative zero level up crossings* e) functions associated to the target accelerogram (red solid line) with statistics of the artificial ones: mean value function (black line); mean value plus/minus standard deviation functions (black dashed lines); envelope of the maximum and minimum values of all samples (shaded area);

M=1

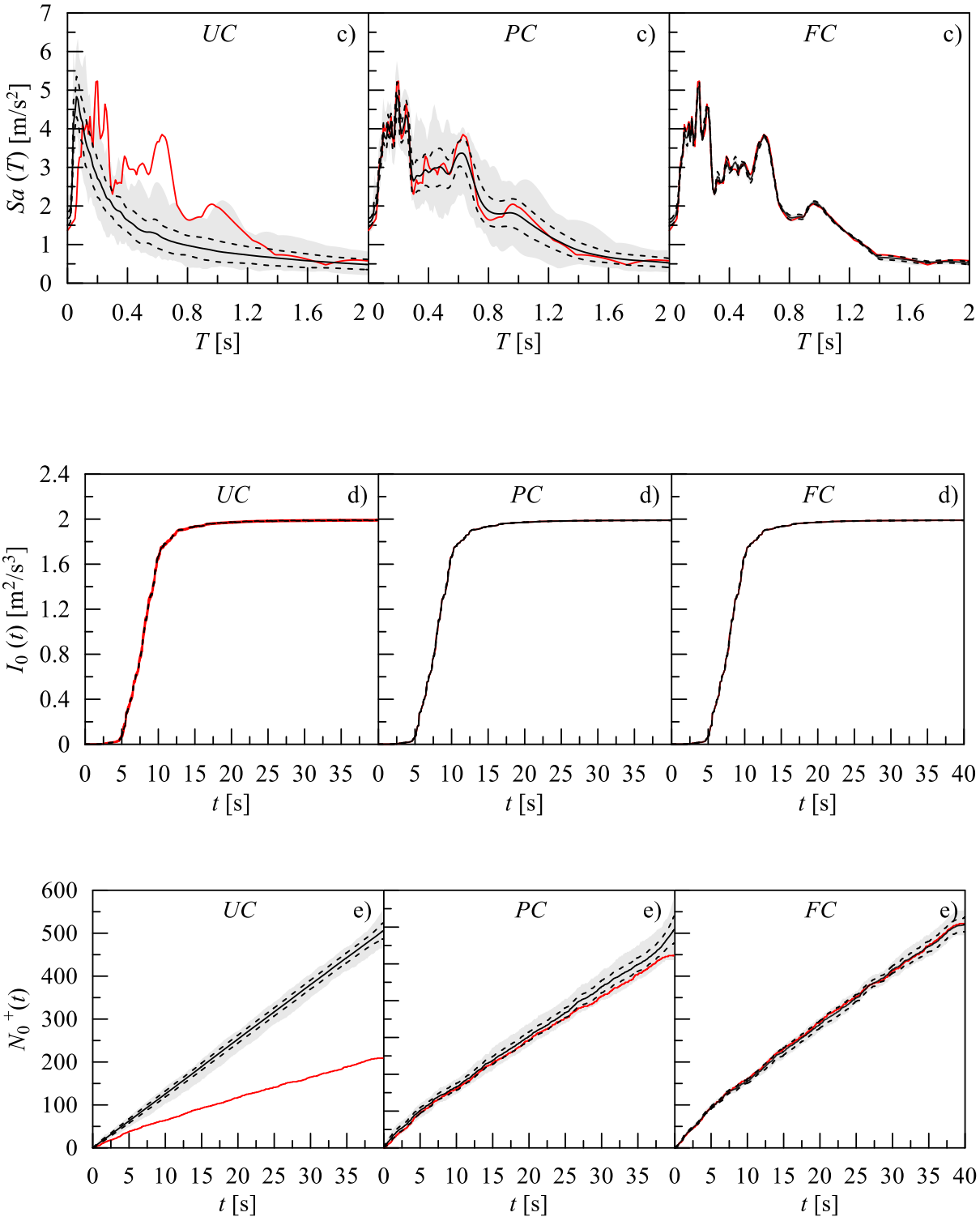

Figure 3.5 (*Continued*)**.**

M=100

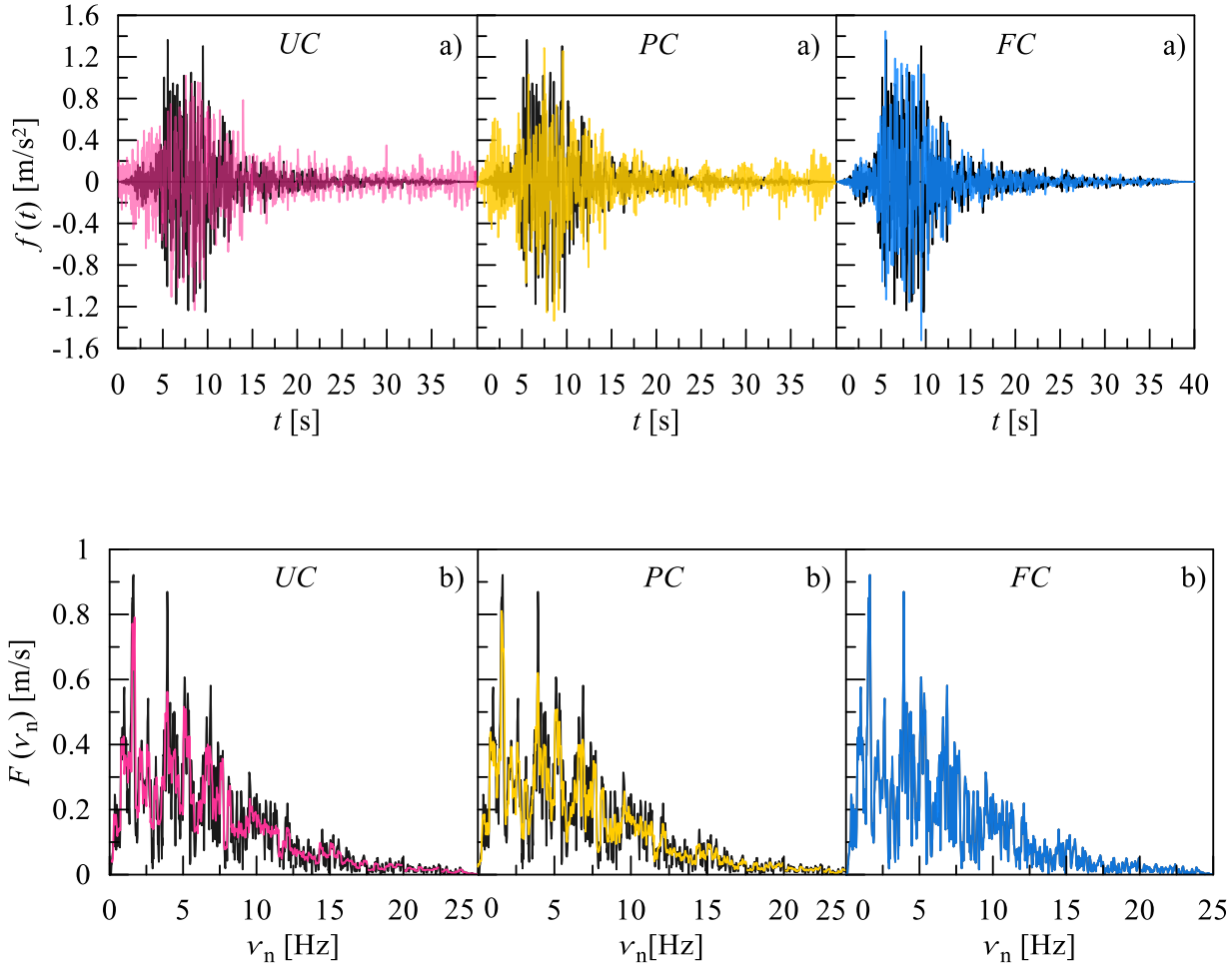

Figure 3.6 Result of the circular *wavelet transform* method, considering a subdivision of the frequency domain into *M*=100 parts, for random phases: "uncorrelated" (*UC*), "partially correlated" (*PC*) and "fully correlated" (*FC*). Comparison among the: a) target accelerogram (black line) and the *i*th generated sample (coloured line); b) mean *Fourier spectrum modulus* of the generated samples (coloured line) and the target one (black line); c-e) *response spectrum* c), *cumulative total intensity* d), and *cumulative zero level up crossings* e) functions associated to the target accelerogram (red solid line) with statistics of the artificial ones: mean value function (black line); mean value plus/minus standard deviation functions (black dashed lines); envelope of the maximum and minimum values of all samples (shaded area);

M=100

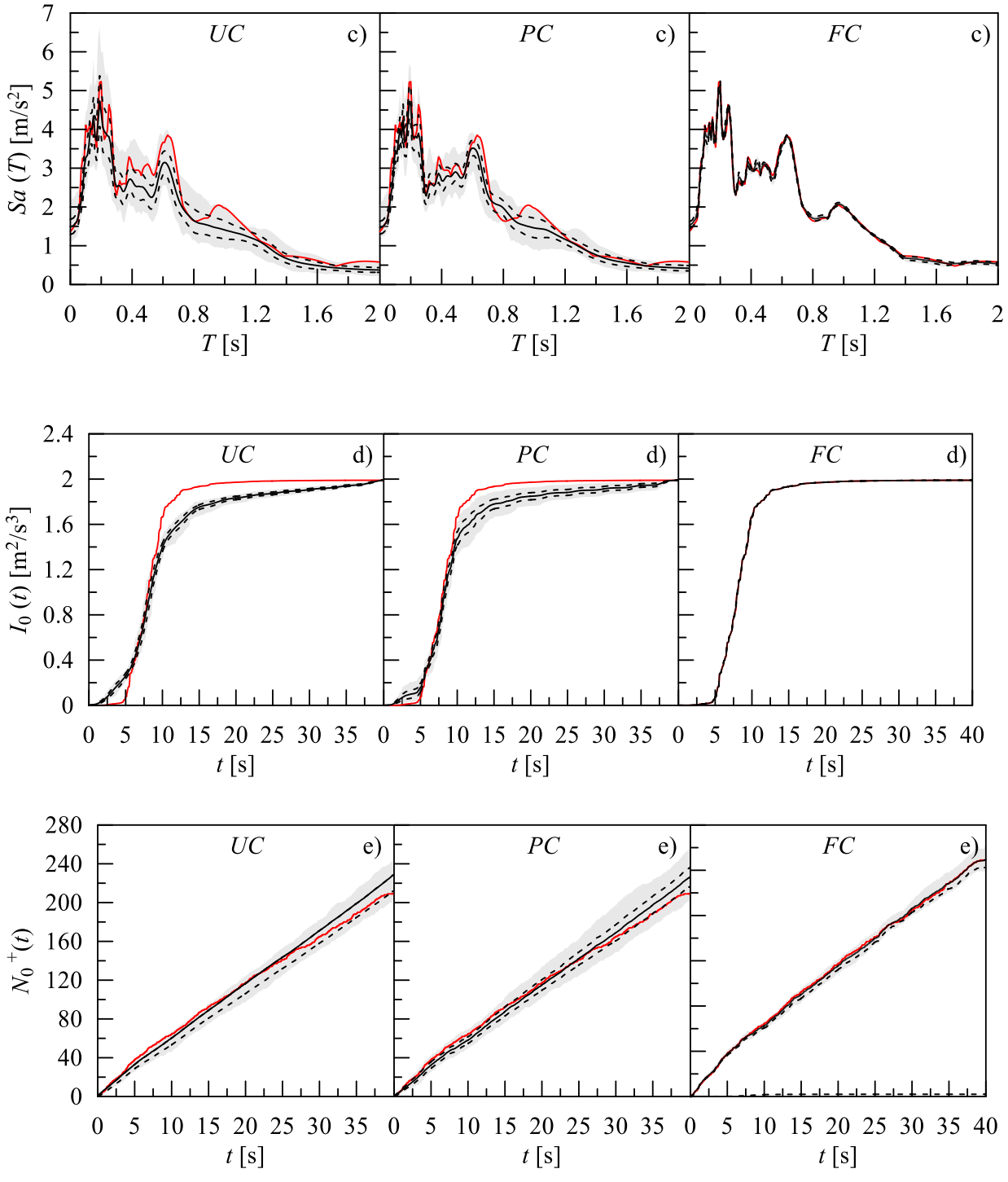

Figure 3.6 (*Continued*).

M=1000

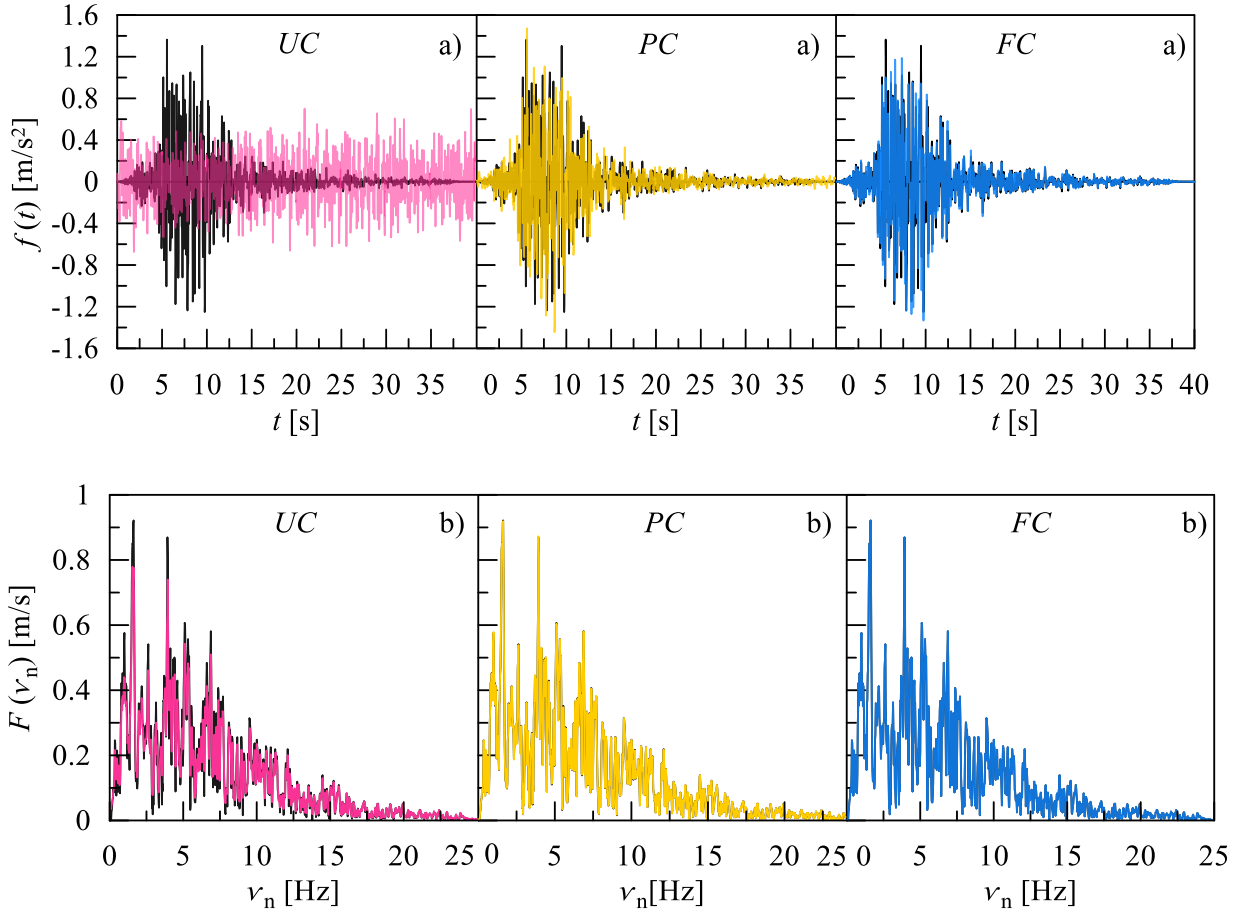

Figure 3.7 Result of the circular *wavelet transform* method, considering a subdivision of the frequency domain into *M*=1000 parts, for random phases: "uncorrelated" (*UC*), "partially correlated" (*PC*) and "fully correlated" (*FC*). Comparison among the: a) target accelerogram (black line) and the *i*th generated sample (coloured line); b) mean *Fourier spectrum modulus* of the generated samples (coloured line) and the target one (black line); c-e) *response spectrum* c), *cumulative total intensity* d), and *cumulative zero level up crossings* e) functions associated to the target accelerogram (red solid line) with statistics of the artificial ones: mean value function (black line); mean value plus/minus standard deviation functions (black dashed lines); envelope of the maximum and minimum values of all samples (shaded area);

M=1000

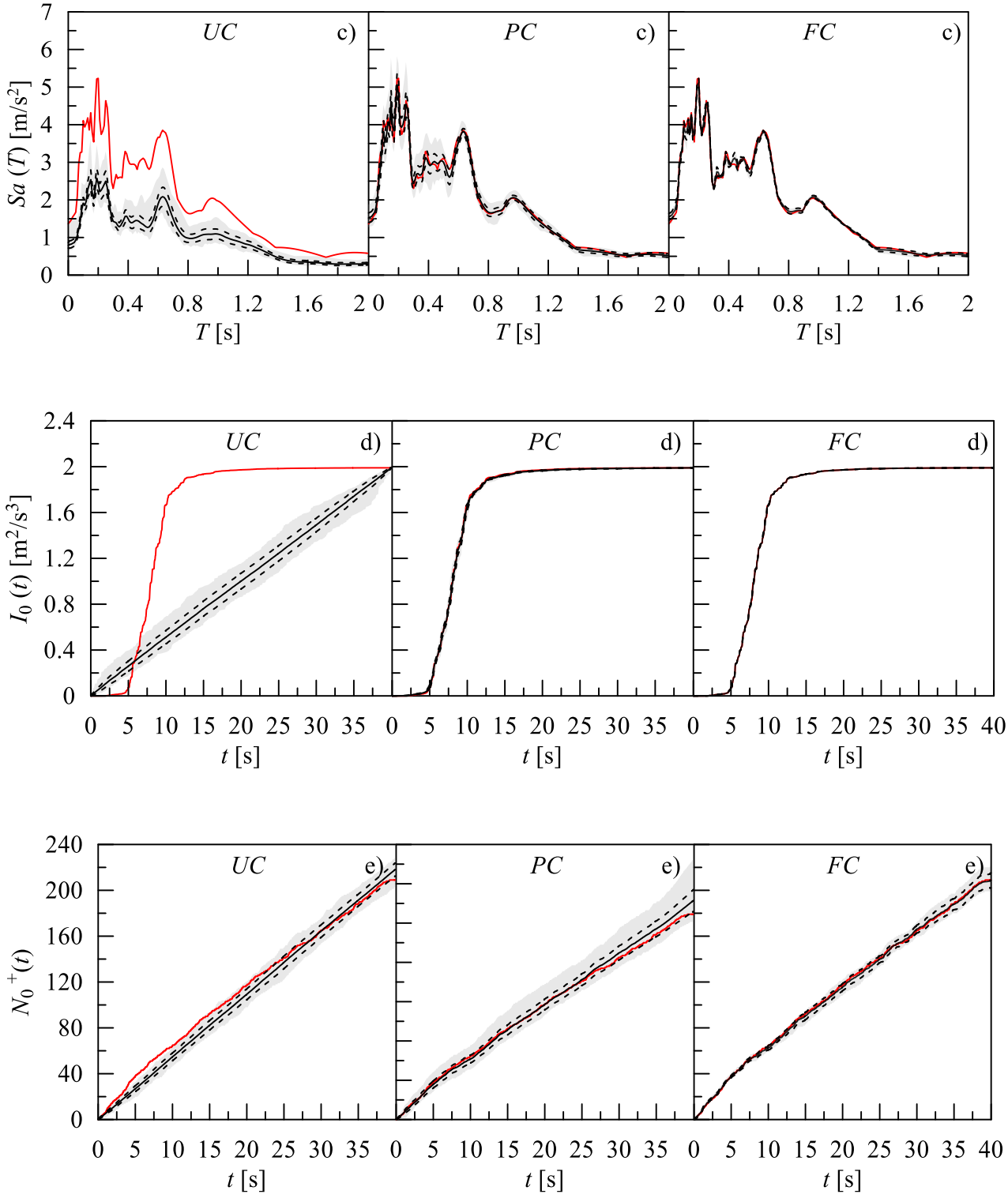

Figure 3.7 (*Continued*).

Table 3-III Main characteristics of each frequency band belonging to the *M*th partition: *M*=1,100,1000.

M	j	m_j	n_j	b_j	$\omega_{m_j} = m_j \cdot \Delta\omega$ [rad/s]	$\omega_{n_j} = n_j \cdot \Delta\omega$ [rad/s]	$\bar{\omega}_j = \left(\frac{m_j + n_j}{2} \right) \Delta\omega$ [rad/s]
1	1	0	1000	1000	0	157.158	78.5791
100	1	0	10	10	0	1.572	0.786
	2	10	20	10	1.572	3.143	2.357
	⋮	⋮	⋮	⋮	⋮	⋮	⋮
	M/2	490	500	10	77.008	78.579	77.793
	⋮	⋮	⋮	⋮	⋮	⋮	⋮
	M-1	980	990	10	154.015	155.587	154.801
	M	990	1000	10	155.587	157.158	156.372
1000	1	0	1	1	0	0.157	0.078
	2	1	2	1	0.157	0.314	0.236
	⋮	⋮	⋮	⋮	⋮	⋮	⋮
	M/2	499	500	1	78.421	78.579	78.500
	⋮	⋮	⋮	⋮	⋮	⋮	⋮
	M-1	998	999	1	156.844	157.001	156.922
	M	999	1000	1	157.001	157.158	157.08

Chapter 4

Generation of fully non-stationary random processes consistent with target seismic accelerograms

4.1 Introduction

Strong motion earthquakes are certainly the main critical actions for most *Structural and Geotechnical* (*S&G*) systems located in seismically active regions. The analysis of recorded accelerograms after earthquakes evidences that different earthquakes produce ground motions with different characteristics; that is with different intensity, duration, dominant periods and frequency content. It follows that, in order to guarantee a good performance of *S&G* systems in seismic areas, it needs to adequately characterise the ground motion acceleration [Villaverde 2009].

According to most seismic codes, the selection of proper sets of input motions for these kinds of analyses is generally carried out defining a target motion through a design elastic *pseudo-acceleration response spectrum* [Barone et al. 2019].

The characteristics of the expected ground movement at a given site are strongly affected by the possible coupling between the frequency content of the input motion and the frequencies of vibration of the soil deposit which, in turn, depend on the non-linear behaviour exhibited by soils when subjected to cyclic and dynamic loadings. About that, several recent studies have clearly pointed out the crucial role of the geotechnical properties of soils at the site of interest and the need of defining proper target energy and frequency contents instead of, or together with, target elastic *response spectra* [Genovese et al. 2021 b, Cascone et al. 2021, Genovese et al. 2019 a]. Therefore, soil mechanical properties considerably influence the site response to the motion imposed by an earthquake at the bedrock level and, thus,

should be properly accounted for in the selection of actual accelerograms [Genovese et al. 2020 a].

Different procedures for the selection of sets of recorded accelerograms have been proposed in the literature [e.g. Genovese et al. 2019 b, Cecini and Palmeri 2015, Iervolino et al 2010, Katsanos et al 2010, Pagliaroli and Lanzo 2008].

However, depending on the characteristics of the target ground motion and on the adopted compatibility criterion, it may be impossible to select an adequate number of compatible accelerograms *i*) actually reflecting the influence of the expected focal mechanism, *ii*) reliable compatible with the magnitude and site-to-source distance that dominate seismic hazard at the site of interest and, finally *iii*) without applying large acceleration scale factors which distort the actual characteristics of the un-scaled records leading to unrealistic input motions. In these situations, the use of artificial accelerograms represents a suitable alternative to realistically define the expected ground motion.

In this Chapter, after a brief overview of different numerical procedures capable to generate artificial accelerograms with energy and frequency content consistent with those of actual acceleration records proposed in the literature, a novel method for generating samples of a *fully non-stationary* zero-mean Gaussian process, in such way that a target accelerogram can be considered as one of its own samples, is presented. To this, the time duration of the selected accelerogram is divided in some contiguous time intervals in which zero-mean Gaussian *uniformly modulated* stochastic processes are adopted. Each *uniformly modulated* random process consists of the product of a positive deterministic *modulating function*, and a stationary zero-mean Gaussian sub-process, whose *power spectral density* (*PSD*) function is filtered by one high pass and one low pass Butterworth filters. It follows that the Priestley's *evolutionary power spectral density* (*EPSD*) function [Priestley 1965, Priestley 1967] is evaluated by adding the contributions of all zero-mean Gaussian *uniformly modulated* stochastic processes. In the various time intervals, a polynomial or an exponential decaying form of the *modulating function* is assumed. The order of the polynomial and their coefficients are estimated by least-square fitting, in the various time–intervals, the expected energy of the proposed model of the fully non-stationary process to the energy of the target accelerogram. Then, in each intervals the parameters of the *PSD* function of the stationary sub-process are estimated once the occurrences of maxima and the occurrences of crossings of

the time-axis with positive slope of the target accelerograms are counted. Finally, the parameters of Butterworth filter are opportunely chosen.

The analytical form of the *modulating function* has been chosen with the purpose to obtain functions that permit to evaluate closed form solutions of the *EPSD* function of the response of *S*&*G* systems in seismic areas [see e.g. Muscolino and Alderucci 2015]. This goal cannot be achieved by adopting the *modulating function* used in many models including the one proposed by Saragoni and Hart [1973].

In the last part of this Chapter, the proposed *evolutionary model*, has been modified to obtain the compatibility between the generated set of fully non-stationary artificial accelerograms and a target action. Depending on the aim to be achieved, it is possible to obtain the spectrum-compatibility in terms of *response spectrum* or *Fourier spectrum*, using two different corrective *PSD* function terms.

A numerical application shows the validity of the spectrum-compatible generation procedure and the accuracy of the proposed model in reproducing realizations with characteristics similar to those of the target motion both in time and frequency domain.

4.2 Stochastic ground motion generation procedures

To account for the uncertainties characterizing earthquake ground-motion time histories, several kinds of stochastic ground-motion models have been developed and applied over the years.

The generation of artificial accelerograms was first based upon a stationary stochastic zero-mean Gaussian process assumption. In this case, the mean value of both amplitude and frequency content of the stochastic process are time invariant. In particular, stationary white-noise ground-motion models were proposed by Housner [1947] and Bycroft [1960]. Successively, to account for the frequency content of earthquake ground motion, Gaussian filtered white noise with Kanai-Tajimi [Kanai 1957, Tajimi 1960] or Clough-Penzien [1975] spectra are frequently used in analytical random vibration analyses.

Housner and Jennings [1964] developed a method for generating filtered stationary Gaussian random processes with *power spectral density* (*PSD*) functions derived from the average of the undamped velocity spectra of recorded ground accelerations. These stationary models account for the site properties as well as for the dominant frequency in ground motion.

However, they fail since are not able to reliable reproduce the changes in amplitude and frequency content, which are observed in actual seismic records.

Moreover, it has been recognized that artificial accelerograms generated by applying stationary models have an excessive number of cycles of strong motion and consequently they possess unreasonably much higher energy content with respect to real ones [Bommer and Acevedo 2004].

It is well known that earthquake ground motions are non-stationary in both time and frequency domains. Temporal non-stationarity refers to the variation in the intensity of the ground motion in time, whereas the spectral non-stationarity refers to the time variation of the frequency content [Rezaeian and Der Kireghian 2008]. To capture variation in the intensity of accelerograms, non-stationary processes have been introduced as the product of the stationary zero-mean Gaussian random process by a suitable deterministic time-dependent function, the so-called *modulating function* [Shinozuka and Sato 1967, Amin and Ang 1968, Iyengar and Iyengar 1969, Jennings et al. 1968, Hsu and Bernard 1978, Iwan and Hou 1989, Stafford et al 2009, Marano 2019]. Due to their non-stationarity in time, these are called separable non-stationary stochastic processes or more commonly: *quasi-stationary* (or *uniformly modulated non-stationary*) random processes.

Opposite to temporal non-stationarity, which can be easily modelled by multiplying the stationary process by a *modulating function*, spectral non-stationarity is not so easy to model. The spectral non-stationarity is prevalently due to different arrival times of the body (primary, secondary) and surface waves that, propagate at different velocities through the earth crust, vary significantly in frequency content and reach the ground surface at different times. Moreover, it has been shown that the non-stationarity in frequency content can have significant effects on the response of both linear and non-linear *S&G* systems [Yeh and Wen 1990, Conte 1992, Beck and Papadimitriou 1993, Wang et al. 2002]. Non-linear *S&G* systems tend to have resonant frequencies–which decay with time as the system responds to seismic acceleration, as a consequence of non-linear effects. This trend may coincide with the variation in time of the predominant frequency of the ground motion. The stochastic processes involving both the intensity and the spectral variation in time are referred in literature as *fully non-stationary* (or *non-separable*) stochastic processes.

Several approaches have been adopted in the literature to capture the variation in both amplitude and frequency of recorded accelerograms. In particular, by solving probabilistic

energy spectra equations, Spanos [Spanos 1980, Spanos and Solomos 1982] introduced evolutionary non-separable power spectra as the product of a deterministic time-frequency dependent function by the *PSD* function of stationary zero-mean Gaussian stochastic processes. Stefanou and Tsiliopoulos [2019] applied the method of separation proposed by [Schillinger and Papadopoulos, 2010] for the estimation of the evolutionary power spectra of specific earthquakes using artificial accelerograms (generated through the algorithm of [Sabetta and Pugliese, 1996]) or actual ground motion records.

Alternative very widespread *fully non-stationary* stochastic process models based on filtered processes have also been proposed. These models, whose parameters can be identified by matching with characteristics of the target accelerogram, can be subdivided in two categories: *i*) stochastic processes obtained by passing a white noise through a filter with time dependent coefficients [Fan and Ahmadi 1990, Yeh and Wen 1990, Beck and Papadimitriou 1993, Rofooei et al 2001, Rezaeian and Der Kireghian 2008]; b) processes obtained by passing a train of Poisson pulses through a linear filter [Lin 1965, Liu. 1970, Lin 1986, Lin and Yong 1987].

A very useful approach to generate fully non-stationary zero-mean Gaussian stochastic processes is the one based on the evolutionary spectral representation, that requires the introduction of the *evolutionary power spectral density* (*EPSD*) function [Priestley 1965, Priestley 1967]. Three main models have been proposed in the literature to evaluate *EPSD* functions whose parameters are identified from recorded accelerograms. The first was the Saragoni and Hart model [1973] in which the time axis is subdivided in three contiguous intervals, each with different modulating and *PSD* functions. The *modulating function* is used to control the process intensity level, while the counting of *zero-level crossings* and *peaks* are used to characterize the *PSD* functions in the three time intervals. The second model was proposed by Der Kiureghian and Crempien [1989] in which the strength function of the process is changed at discrete points along the frequency axis. The resulting process is given by the superposition of independent processes with constant *PSD* function, and unitary variance, over their respective bands. This model, in a sense, can be considered as the complement of the Saragoni and Hart [1973] model. However, one shortcoming of this model in the identification of its parameters, is the need to perform, in each frequency segment, the *inverse Fourier transform* of the *Fourier transform* of the accelerogram.

In the third model, proposed by Conte and Peng [1997], the resulting process is evaluated as the sum of a finite number of zero-mean, independent, uniformly modulated zero-mean Gaussian sub-processes, the so-called *sigma-oscillatory processes*. Each uniformly modulated process consists of the product of a real deterministic time *modulating function* and a stationary Gaussian sub-process, having unimodal *PSD* function with unitary variance. The parameters of the resulting analytical *EPSD* function are estimated in the least-square sense by using the *short-time Thomson's multiple-window method*.

Other strategies to analyse the evolutionary frequency content of fully non-stationary stochastic processes are based on: *i*) the *short time Fourier transform* [Narasimhan and Pavanalatha 2004, Liang et al 2007]; *ii*) the *wavelet transform* [Spanos and Failla 2004, Spanos et al. 2005, Wang et al 2018]; *iii*) the *Hilbert-Huang transform* [Huang et al 2018, Garcia et al 2019].

4.3 Spectral representations of fully non-stationary zero-mean Gaussian stochastic processes

4.3.1 The Saragoni and Hart model

To generate artificial accelerograms coherent with the recorded ones, Saragoni and Hart [1973], in the framework of the *evolutionary spectral analysis*, subdivided the time duration of the accelerogram analysed in three contiguous time intervals, each with different *PSD* functions. Instead, the same modulating function is adopted for all time intervals. In particular, the *EPSD* function of this model can be defined as:

$$S_{FF}^{(SH)}(\omega,t)=a^2(t)\sum_{j=1}^{3}\mathbb{W}(t_{j-1},t_j)\,S_0^{(j)}(\omega)=\sum_{j=1}^{3}S_0^{(j)}(\omega,t) \tag{4.1}$$

where $a(t)$ is the modulating function, $\mathbb{W}(t_{j-1},t_j)=\mathbb{U}(t-t_j)-\mathbb{U}(t-t_{j-1})$ is the window function, and $\mathbb{U}(t)$ the unit step function defined, respectively, as:

$$\mathbb{W}(t_{j-1},t_j)=\begin{cases}1, & t_{j-1}<t\le t_j;\\ 0, & t\le t_{j-1},\,t>t_j;\end{cases}\qquad \mathbb{U}(t-t_j)=\begin{cases}0, & t\le t_j;\\ 1, & t>t_j.\end{cases} \tag{4.2}$$

The following *EPSD* function was proposed for each time interval of Eq.(4.1):

$$S_0^{(j)}(\omega,t) = a^2(t)\,\mathbb{W}(t_{j-1},t_j)\,S_0^{(j)}(\omega) \tag{4.3}$$

where $S_0^{(j)}(\omega)$ is the following unimodal *PSD* function:

$$S_0^{(j)}(\omega) = S_{0,j}\,|\omega|^{P_j}\,\exp\{-Q_j\,|\omega|\} \tag{4.4}$$

which satisfies the following condition:

$$\int_0^{+\infty} S_0^{(j)}(\omega)\,\mathrm{d}\omega = 1 \tag{4.5}$$

with the following constraint on

$$S_{0,j} = \frac{Q_k^{P_j+1}}{\Gamma(P_j+1)} \tag{4.6}$$

The characterization of modulating function *a*(*t*) and, of parameters P_j and Q_j, which are different for each time interval, is carried out by evaluating for the chosen recorded accelerogram: *i*) expected energy function; *ii*) the number of *zero-level up-crossings* and *peaks*. Notice that the expected energy function of a given accelerogram $\ddot{U}_g(t)$ of duration T_D, is defined as [Saragoni-Hart 1973]:

$$E_{\ddot{U}_g}(t) = \int_0^t \ddot{U}_{\mathrm{g}}^2(\tau)\,\mathrm{d}\tau \quad 0 \le t \le T_D \tag{4.7}$$

Then a complex optimization procedure is applied. Der Kiureghian and Crempien [1989] stated that the main drawback of the Saragoni-Hart [1973] model is that it exhibits discontinuity at the time points where the power spectral density is changed.

Finally, since the following relationship holds

$$\mathbb{W}(t_{j-1},t_j)\times\mathbb{W}(t_{k-1},t_k) = \begin{cases} \mathbb{W}(t_{j-1},t_j), & t_j = t_k; \\ 0, & t_j \neq t_k; \end{cases} \tag{4.8}$$

In the Saragoni and Hart (*SH*) model, the *r*-th sample of the stochastic earthquake process, $F_{SH}(t)$, having the same spectral characteristics of the analysed recorded accelerogram, can be evaluated as:

$$F_{SH}^{(r)}(t) = a(t)\sum_{j=1}^{3} \mathbb{W}(t_{j-1}, t_j) X_j^{(r)}(t) \tag{4.9}$$

where $X_j(t)$ is a stationary zero-mean Gaussian filtered white noise process defined in the time interval, $\left[t_j - t_{j-1}\right]$, possessing *PSD* function $S_0^{(j)}(\omega)$ of Eq.(4.4) .

4.3.2 The Der Kiureghian and Crempien model

Whereas in the Saragoni-Hart [1973] model the frequency content of the process was changed at discrete points in time, in Der Kiureghian and Crempien [1989] the strength function of the process is changed at discrete points along the frequency axis. This is accomplished by defining the process as a superposition of individually modulated stationary component processes, each representing the content in the motion in a distinct frequency band. The characteristics of the component processes are determined by matching the temporal moments of the process with those of a target accelerogram. The Der Kiureghian-Crempien [1989] model, in a sense, can be considered as the complement of the model by Saragoni and Hart [1973].

In this model a class of evolutionary processes is defined by simply superposing several zero-mean Gaussian stationary processes X_k (*t*), with unitary variance $\mathrm{E}\left\langle X_k^2(t)\right\rangle = 1$ and *PSD* $S_0^{(k)}(\omega)$. In the Der Kiureghian-Crempien (*DC*) model, the processes X_k (*t*), each modulated by a different modulating function a_k (*t*), were assumed to be mutually statistically independent. i.e.:

$$F_{DC}(t) = \sum_{k=1}^{M} a_k(t) X_k(t) \tag{4.10}$$

It follows that the mean value and the mean square function of this process are given respectively as:

$$\begin{aligned} &\mathrm{E}\left\langle F_{DC}(t)\right\rangle = \sum_{k=1}^{M} \mathrm{E}\left\langle X_k(t)\right\rangle = 0\,; \\ &\mathrm{E}\left\langle F_{DC}^2(t)\right\rangle = \sum_{k=1}^{M} \mathrm{E}\left\langle X_k^2(t)\right\rangle = \sum_{k=1}^{M} a_k^2(t) \end{aligned} \tag{4.11}$$

Therefore, the *EPSD* function of the process $F_{DC}(t)$ is given as:

$$S_{FF}(\omega,t)=\sum_{k=1}^{M}a_k^2(t)S_0^{(k)}(\omega) \quad \Rightarrow \quad \mathrm{E}\left\langle F_{DC}^2(t)\right\rangle=\sum_{k=1}^{M}a_k^2(t)\int_{-\infty}^{+\infty}S_0^{(k)}(\omega)\mathrm{d}\omega=\sum_{k=1}^{M}a_k^2(t) \tag{4.12}$$

since the following relationship holds:

$$\int_{-\infty}^{+\infty}S_0^{(k)}(\omega)\mathrm{d}\omega=1 \tag{4.13}$$

Dividing the frequency domain into non-overlapping interval $D_k=\left\{\omega:\ \omega_{k-1}\le|\omega|\le\omega_k\right\}$, the *PSD*s $S_0^{(k)}(\omega)$ are considered to be constant over their respective bands interval

$$S_0^{(k)}(\omega)=\begin{cases}\dfrac{1}{2(\omega_k-\omega_{k-1})}, & \omega\in D_k\\ 0, & \text{elsewhere}\end{cases} \tag{4.14}$$

The procedure adopted by Der Kiureghian-Crempien [1989] for selecting the parameters of their model is the following:

i) first to define frequency bands D_k. To do this to divide the frequency range 0 to 25 Hz of the *Fourier transform* of a recorded accelerograms $\mathcal{F}\left\{\ddot{U}_g(t)\right\}=\ddot{U}_g(\omega)$ in 32 equal bands. In each band, the total *Arias intensity* I_A is computed. If a frequency band does not contribute 10 percent or more of the *total intensity*, then that band is combined with the neighboring lower-frequency band. With this procedure, any accelerograms is decomposed into at most 9 frequency bands.

ii) to perform the *inverse Fourier transform* of the *Fourier transform* of the accelerograms in each of the at most 9 frequency bands, obtaining:

$$\ddot{U}_g^{(k)}(t)=\int_{D_k}\ddot{U}_g(\omega)\mathrm{e}^{\mathrm{i}\omega t}\,\mathrm{d}\omega \tag{4.15}$$

iii) then the parameters of the modulating function $a_{j,k}(t)$, that in the Der Kiureghian-Crempien [1989] model is assumed as a piecewise linear function depending on only two parameters $\alpha_{j,k}$ and $\beta_{j,k}$ in each frequency interval D_k, are evaluated by least-

square fitting, i.e. minimizing the following integral in 10 intervals, $[t_j, t_{j-1}]$, of equal length, Δt along the time axis:

$$\int_{t_{j-1}}^{t_j} \left[a_{j,k}^2(t) - \left(\ddot{U}_g^{(k)}(t) \right)^2 \right]^2 \mathrm{d}t \tag{4.16}$$

under the condition:

$$a_{j,k}(t) = \alpha_{j,k}(t_j - t_{j-1}) + \beta_{j,k}; \quad t_j < t < t_{j-1} \tag{4.17}$$

Furthermore, to ensure continuity of the function from one interval to the next, the following condition is also imposed

$$\beta_{j,k} = \alpha_{j-1,k}(t_j - t_{j-1}) + \beta_{j-1,k} \tag{4.18}$$

This solution is particularly simple if the piecewise linear model (4.17) for the component modulating functions is adopted.

One drawback of the model is its disregard of the physical processes involved in the generation of the ground motion, i.e., the rupture mechanism at the source and the propagation of seismic waves through the ground medium. For application in earthquake-resistant design, it is necessary to relate the parameters of the proposed model to basic variables describing the earthquake source, such as the magnitude and the distance from the source to the site. This can be done by regressing the parameters of the model against the earthquake source variables for a large number of recorded events.

4.3.3 The Conte and Peng model

In order to consider the time-frequency variation of non-stationary stochastic ground motion, Conte and Peng [1997] proposed a *sigma-oscillatory process model* in the case of mono-correlated input. This process model is evaluated as the sum of a finite number, *M*, of zero-mean, independent, uniformly modulated Gaussian sub-processes $X_k(t)$. Each uniformly modulated process consists of the product of a real deterministic time modulating function, $a_k(\omega, t)$, and a stationary Gaussian sub-process, having *PSD* function $S_k^{(CP)}(\omega)$.

In the Conte and Peng (*CP*) model, the *r*-th realization and the *EPSD* function can be expressed as [Conte and Peng 1997]:

$$F_{CP}^{(r)}(t)=\sum_{k=1}^{M} a_k(t)X_k^{(r)}(t) \quad \Rightarrow \quad S_{FF}(\omega,t)=\sum_{k=1}^{M} a_k^2(t)\,S_k^{(CP)}(\omega) \tag{4.19}$$

where:

$$a_k(t)=\varepsilon_k\,(t-t_k)^{r_k}\,e^{-\alpha_k(t-t_k)}\,\mathbb{U}(t-t_k); \qquad k=1,...,M \tag{4.20}$$

and

$$S_k^{(CP)}(\omega)=\frac{\rho_k}{2\pi}\left[\frac{1}{\rho_k^2+(\omega+\Omega_k)^2}+\frac{1}{\rho_k^2+(\omega-\Omega_k)^2}\right]; \quad k=1,...,M\,. \tag{4.21}$$

In the previous equations α_k and ε_k are positive constants; r_k is a positive integer number; t_k is the arrival time of the sub-process $X_k(t)$; ρ_k and Ω_k are two free parameters representing the frequency bandwidth and the circular mean frequency of the *k*-th stationary sub-process, respectively, whose autocorrelation function is:

$$R_{X_kX_k}(\tau)=\exp\left(-\rho_k|\tau|\right)\cos\left(\Omega_k\tau\right) \tag{4.22}$$

Since $R_{X_kX_k}(0)=\sigma_k^2=1$, it follows that:

$$\int_{-\infty}^{+\infty} S_k^{(CP)}(\omega)\,\mathrm{d}\omega\equiv\sigma_k^2=1 \tag{4.23}$$

and

$$\mathrm{E}\left\langle F_{CP}^2(t)\right\rangle=\sum_{k=1}^{M} a_k^2(t) \tag{4.24}$$

The *EPSD* function (4.19) describes simultaneously the time-varying intensity and the time-varying frequency content. It follows that the excitation $F_{CP}(t)$ is *not separable* (i.e. *fully-non stationary*) although its component processes are *individually separable* (i.e., *uniformly modulated*). Each uniformly modulated component process, $X_k(t)$, is

characterized by a unimodal *PSD* function in the frequency domain and a unimodal mean square function in the time domain [Conte and Peng 1997].

The parameters of the earthquake accelerations model defined above are estimated such that the analytical *EPSD* function best fits, in the least-square sense, the *EPSD* function of target earthquake accelerograms estimated using the *short-time Thomson's multiple window method*.

The main drawback of this very interesting model is the complexity of the identification procedure. Moreover, the *PSD* function $S_k^{(CP)}(\omega)$ of the uniformly modulated Gaussian sub-processes $X_k(t)$, defined in Eq.(4.21), presents two shortcomings: *i*) higher order moments are not convergent quantities; *ii*) since $\lim_{\omega\to 0} S_k^{(CP)}(\omega) \neq 0$, a distortion in ω=0 appears.

4.4 Proposed evolutionary model for earthquake-induced ground acceleration

A new procedure for generating a set of fully non-stationary artificial accelerograms, having the same characteristics of an earthquake induced ground motion, is detailed in the following.

In the proposed model, the *fully non-stationary* process of earthquake ground acceleration $F_0(t)$ is defined as the sum of zero-mean Gaussian *uniformly modulated stochastic processes* $F_{0,k}(t)$ each of which consists of the product of a positive deterministic *modulating function* $a(t)$ times a stationary zero-mean Gaussian filtered sub-process $X_k(t)$.

Thus, according to the philosophy of Saragoni and Hart [1973] model, the *fully non-stationary* stochastic process $F_0(t)$, of time duration T_D, is here obtained by dividing the time interval $0 \div T_D$ in n contiguous time intervals of amplitude $\Delta T_k = t_k - t_{k-1}$ $(k = 1, 2\cdots, n)$ and requiring that in each time interval the sub-process $X_k(t)$, possesses a unimodal *PSD* function, that is:

$$F_0(t) = \sum_{k=1}^{n} F_{0,k}(t) = \sum_{k=1}^{n} a(t)\, X_k(t)\, \mathbb{W}(t_{k-1}, t_k) \tag{4.25}$$

where $\mathbb{W}(t_{k-1},t_k)=\mathbb{U}(t-t_k)-\mathbb{U}(t-t_{k-1})$ is the window function, with $\mathbb{U}(t)$ the unit step function. Moreover, in the time interval $[t_{k-1},t_k)$, the sub-process $X_k(t)$ is here characterised by the following one-sided *PSD* function:

$$G_{X_k}(\omega)=\beta_k\left(\frac{\omega^2}{\omega^2+\omega_{H,k}^2}\right)\left(\frac{\omega_{L,k}^4}{\omega^4+\omega_{L,k}^4}\right)G_k^{(CP)}(\omega);\qquad k=1,...,n \tag{4.26}$$

where $\omega_{L,k}$ and $\omega_{H,k}$ are the *k*-th frequency control of the second order low pass and first order high pass Butterworth filters, respectively, $G_k^{(CP)}(\omega)=2S_k^{(CP)}$ is the unimodal one-sided *PSD* function, having unit area, of the Conte and Peng model (see Eq. (4.21)):

$$G_k^{(CP)}(\omega)=\frac{\rho_k}{\pi}\left[\frac{1}{\rho_k^2+(\omega+\Omega_k)^2}+\frac{1}{\rho_k^2+(\omega-\Omega_k)^2}\right];\qquad k=1,...,M\,. \tag{4.27}$$

Finally, in Eq.(4.26) the coefficient β_k is evaluated in such a way that the sub-process $X_k(t)$ possesses unit variance $\mathrm{E}\left\langle X_k^2(t)\right\rangle\equiv\sigma_{X_k}^2=1$. It is given in closed form solution as follows:

$$\beta_k=\frac{2\,\bar{a}_k\bar{b}_k\left(\omega_{H,k}^4+\omega_{L,k}^4\right)}{\omega_{L,k}^3\left(\bar{c}_k+\bar{d}_k+\bar{e}_k\right)} \tag{4.28}$$

where:

$$\begin{aligned}
\bar{a}_k&=\left(\rho_k^2+\Omega_k^2\right)^4+2\left(\rho_k^4-6\rho_k^2\Omega_k^2+\Omega_k^4\right)\omega_{L,k}^4+\omega_{L,k}^8;\\
\bar{b}_k&=\rho_k^4+2\rho_k^2\left(\Omega_k^2-\omega_{H,k}^2\right)+\left(\Omega_k^2+\omega_{H,k}^2\right)^2;\\
\bar{c}_k&=-2\,\bar{a}_k\,\rho_k\,\omega_{H,k}\,\omega_{L,k}\left(\rho_k^2+\Omega_k^2-\omega_{H,k}^2\right);\\
\bar{d}_k&=\left[\left(\rho_k^2+\Omega_k^2\right)^2\left(\rho_k^4-6\rho_k^2\Omega_k^2+\Omega_k^4+\omega_{L,k}^4\right)-\omega_{H,k}^2\left(\rho_k^2-\Omega_k^2\right)\left(\left(\rho_k^2+\Omega_k^2\right)^2+\omega_{L,k}^4\right)\right]\\
&\quad\times 2\omega_{L,k}\left(\omega_{H,k}^4+\omega_{L,k}^4\right);\\
\bar{e}_k&=\sqrt{2}\,\bar{b}_k\,\rho_k\left\{\omega_{L,k}^2\left(\omega_{H,k}^2-\omega_{L,k}^2\right)\left(\omega_{L,k}^4+\rho_k^4-2\rho_k^2\Omega_k^2-3\Omega_k^4\right)\right.\\
&\quad\left.+\left(\omega_{H,k}^2+\omega_{L,k}^2\right)\left[\rho_k^6+\Omega_k^6+3\Omega_k^2\rho_k^2\left(\rho_k^2+\Omega_k^2\right)+\omega_{L,k}^4\left(\rho_k^2-3\Omega_k^2\right)\right]\right\}.
\end{aligned} \tag{4.29}$$

Scaling the *PSD* function (4.26) to have unit variance allows separating, in each time interval, the time variation in amplitude from the frequency content of the various segments of the stochastic process $F_0(t)$.

It has to be emphasised that the unimodal *PSD* function $G_k^{(CP)}(\omega)$ of the Conte and Peng [1997] model behaves like ω^{-2} for ω tending to infinite and this shows that $\omega^i G_k^{(CP)}(\omega)$ for $i \geq 1$ is not integrable. So, the spectral moments of the function $G_k^{(CP)}(\omega)$ of order greater than zero are divergent quantities. Moreover, the *PSD* function $G_k^{(CP)}(\omega)$ presents frequency distortion at very low frequencies. To avoid these two drawbacks of $G_k^{(CP)}(\omega)$ function, second order low pass Butterworth filters, with *k*-th frequency control $\omega_{L,k}$, and first order high pass Butterworth filters, with *k*-th frequency control $\omega_{H,k}$, have been introduced in Eq.(4.26), to characterise the one-sided *PSD* function of the *k*-th sub-process $X_k(t)$.

Finally, the one-sided *EPSD* function for the proposed model results:

$$G_{F_0F_0}(\omega,t) = \sum_{k=1}^{n} a^2(t)\, \mathbb{W}(t_{k-1},t_k)\, G_{X_k}(\omega) \equiv \sum_{k=1}^{n} G_{X_k}(\omega,t) \tag{4.30}$$

Furthermore, since each sub-process possesses unit variance, the time-dependent variance of the *fully non-stationary* process $F_0(t)$ is given as:

$$\sigma_{F_0}^2(t) \equiv \mathrm{E}\left\langle F_0^2(t)\right\rangle = \int_0^{\infty} G_{F_0F_0}(\omega,t)\,\mathrm{d}\omega = \sum_{k=1}^{n} a^2(t)\, \mathbb{W}(t_{k-1},t_k) \tag{4.31}$$

Note that, the *EPSD* function in Eq.(4.30) describes simultaneously the time-varying intensity and the time-varying frequency content. It follows that $F_0(t)$ is *fully-non stationary*, although its component processes are individually *uniformly modulated*. Therefore, each *uniformly modulated* sub-process X_k (*t*), characterised by a *PSD* function in the frequency domain and a *modulating function* in the time domain, captures, in its time interval, a group of seismic waves possessing a specific time-frequency distribution of earthquake-induced ground motion acceleration.

4.5 Parameters estimation from target accelerograms

The purpose of this section is to define a stochastic process $F_0(t)$ such that the target accelerogram, $\ddot{U}_g(t)$, may be considered as one of its samples. To do this the *modulating function* and the frequency content of the process $F_0(t)$ can be estimated separately.

4.5.1 Estimation of modulating function

Let us consider a target accelerogram $\ddot{U}_g(t)$ of time duration T_D. To evaluate the *modulating function*, $a(t)$, the time interval $0 \div T_D$ is subdivided in n_a contiguous time intervals of amplitude $\Delta T_j = t_j - t_{j-1}$ $(j = 1, 2 \cdots, m, \cdots n_a)$. The *cumulative energy* function of the target accelerogram is evaluated as:

$$E_{\ddot{U}_g}(t) = \int_0^t \ddot{U}_g^2(\tau)\,\mathrm{d}\tau = \sum_{j=1}^{m \le n_a} \int_{t_{j-1}}^{t_j} \ddot{U}_g^2(\tau)\,\mathrm{d}\tau\,; \quad 0 \le t \le T_D \tag{4.32}$$

Moreover, $E_{\ddot{U}_g}(T_D) \equiv I_0$ is the so-called *total intensity* of the ground motion acceleration [Chang et al. 1987]. Remembering that in each time interval the sub-processes X_j (t), in Eq.(4.25), possess unitary variance as well as the definition (4.31) of the time-dependent variance of the *fully non-stationary* process, the *cumulative expected energy* function of the stochastic process $F_0(t)$ can be evaluated as [Saragoni ad Hart 1973]:

$$\mathrm{E}\left\langle E_{F_0}(t)\right\rangle = \int_0^t \mathrm{E}\left\langle F_0^2(\tau)\right\rangle \mathrm{d}\tau \equiv \int_0^t \sigma_{F_0}^2(\tau)\,\mathrm{d}\tau = \sum_{j=1}^{m \le n_a} \int_{t_{j-1}}^{t_j} a^2(\tau)\,\mathrm{d}\tau \tag{4.33}$$

To estimate $a(t)$, in the j-th time interval $[t_{j-1}, t_j)$, the *function* $\psi_j(t)$ is introduced:

$$\psi_j(t) = \int_{t_{j-1}}^{t} \left[a(t_{j-1}) + \bar{a}_j(\tau)\right]^2 \mathrm{d}\tau\,, \quad t_{j-1} \le t < t_j; \tag{4.34}$$

where the function $\bar{a}_j(t)$ is here assumed as a polynomial of p-th order:

$$\begin{cases} \bar{a}_j(t) = \sum_{i=1}^{p} \alpha_i \, (t - t_{j-1})^i, & t_{j-1} \le t < t_j; \\ \bar{a}_j(t) = 0, & t < t_{j-1}, \quad t \ge t_j. \end{cases} \tag{4.35}$$

The polynomial coefficients α_i can be evaluated by least-square fitting $\psi_j(t)$ to the accelerogram *cumulative energy* $E_{\ddot{U}_g}(t)$. That is, in the *j*-th time interval $[t_{j-1}, t_j)$, the following optimization problems have to be solved:

$$\begin{cases} \text{find } \alpha_1, \ \alpha_2, \cdots \ \alpha_p; \\ \text{minimising} \quad \int_{t_{j-1}}^{t_j - \Delta t} \left[E_{\ddot{U}_g}(t) - \psi_j(t) \right]^2 \mathrm{d}t; & j = 1, 2, \cdots, n_a - 1. \\ \text{such that} \quad \bar{a}_j(t) \ge 0, \quad \bar{a}_j(t) = \sum_{i=1}^{p} \alpha_i \, (t - t_{j-1})^i, \quad t_{j-1} \le t < t_j; \end{cases} \tag{4.36}$$

being Δt the sampling interval of the target accelerogram. Note that the upper limit of the integral, in the optimization problem, avoids the overlap between the values of the *cumulative energy* function at the extremes of chosen time intervals. This guarantees the continuity of modulating functions too.

In the last (n_a-th) time interval with $t \in [t_{n_a-1}, t_{n_a} \equiv T_D]$, the *modulating function* is approximated by an exponential decaying function whose coefficients are evaluated by imposing the continuity with the previous one and its decaying down to the absolute value, $\left|\ddot{U}_{\mathrm{g}}(T_D)\right|$, at the end of the target accelerogram:

$$a(t) = a(t_{n_a-1}) \exp\left[\frac{t - t_{n_a-1}}{T_D - t_{n_a-1}} \ln\left(\frac{\left|\ddot{U}_{\mathrm{g}}(T_D)\right|}{a(t_{n_a-1})} \right) \right], \quad t_{n_a-1} \le t \le T_D. \tag{4.37}$$

Finally, once the functions $\bar{a}_j(t)$ are evaluated, the *modulating function* in the time interval $[0, T_D]$ can be written as:

$$a(t) = \sum_{j=1}^{n_a-1} \bar{a}_j(t) \, \mathbb{W}(t_{j-1}, t_j) + a(t_{n_a-1}) \exp\left[\frac{t - t_{n_a-1}}{T_D - t_{n_a-1}} \ln\left(\frac{\left|\ddot{U}_{\mathrm{g}}(T_D)\right|}{a(t_{n_a-1})} \right) \right] \mathbb{W}(t_{n_a-1}, T_D). \tag{4.38}$$

It should be emphasised that for the estimation of the *modulating function*, in each generic time interval, only the evaluation of the energy of the target accelerogram in the same time-interval is required.

Notice that in the proposed procedure it could be also assumed $n_a \neq n$, n being the number of contiguous time intervals in which the *EPSD* function Eq.(4.30) of the stochastic process $F_0(t)$ is subdivided. Obviously, the assumption $n_a=n$ simplifies the procedure from a computational point of view.

4.5.2 Estimation of PSD function parameters

Since analysing the expected *cumulative energy* function of the fully non-stationary stochastic process $F_0(t)$, it is possible only to estimate the amplitude variation of the target accelerogram $\ddot{U}_g(t)$, another criterion to estimate the variation of the frequency content of $F_0(t)$ must be established, such that $\ddot{U}_g(t)$ may be considered as one of its samples. Once the time interval $0 \div T_D$ is divided in n contiguous time intervals, this purpose is here achieved by capturing in the generic k-th time interval a group of seismic waves possessing the specific frequency distribution of the target accelerogram in the same time interval. To do this the spectral parameters, Ω_k, ρ_k, $\omega_{H,k}$ and $\omega_{L,k}$, appearing in Eq.(4.26), of the one-sided *PSD* function $G_{X_k}(\omega)$ of the stationary sub-process $X_k(t)$ must be appropriately estimated.

It is well known that the frequency content of a recorded accelerogram $\ddot{U}_g(t)$ can be related to the frequency of occurrences of certain events. The most useful are: a) occurrences of both positive and negative maxima, here simply called *peaks*; b) occurrences of crossings of the time-axis with positive slope, commonly called *zero-level up-crossings*.

For theoretical narrow-band zero-mean stationary stochastic process, the *zero-level up-crossings* frequency and *peaks* frequency are exactly the same and are coincident with the *mean frequency* of the process. For wider bandwidths, more than one peak occurs between two *zero-level up-crossings*. It follows that the ratio of the *zero-level up-crossings* frequency to the *peak* frequency, the so-called *irregularity factor* [Lutes and Sarkani 2004], gives a measure of the bandwidth of the process, i.e. how much the examined stochastic process differs from the narrow band one. To account for the irregularity of zero-mean stationary stochastic processes, Cartwright and Longuet-Higgins [1956] introduced the *bandwidth parameter*, which can be evaluated as [Wirshing et al. 1995, Solnes 1997]:

$$\varepsilon = \sqrt{1 - \left(\frac{N_0^+}{P_0} \right)^2} \tag{4.39}$$

where N_0^+ and P_0 are the total number of *zero-level up-crossings* and the total number of *peaks* of target accelerogram. It follows that, having evaluated the *mean circular frequency*, $2\pi N_0^+ / T_D$, a measure of the dispersion width of the *energy spectrum* of the target accelerogram $\ddot{U}_g(t)$ can be approximately evaluated by the following spectral parameter:

$$\delta = \frac{2\pi N_0^+}{T_D} \sqrt{1 - \left(\frac{N_0^+}{P_0} \right)^2} \tag{4.40}$$

To capture the frequency content of the target accelerogram in the n contiguous time intervals in which T_D is divided, the number of *peaks*, P_k, and the number of *zero-level up-crossings*, $N_{0,k}^+$, in all time intervals, $[t_{k-1}, t_k)$, are evaluated.

Since in the k-th time interval the stochastic process is assumed uniformly modulated, with *EPSD* function $a(t)\, G_{X_k}(\omega)$, the *zero-level up-crossing* frequency of target accelerogram, $N_{0,k}^+ / \Delta T_k$, is very close to the *mean frequency* of the process and it can be reasonably assumed equal to the predominant circular frequency, Ω_k, of the k-th stationary sub-process. That is, the following relationship is written:

$$\Omega_k \cong \frac{2\pi N_{0,k}^+}{\Delta T_k} \tag{4.41}$$

In order to evaluate the circular frequency bandwidth parameter, ρ_k, of the unimodal one-sided *PSD* function $G_k^{(CP)}(\omega)$, it needs to evaluate the convergent part of the second $\tilde{\lambda}_{1,X_k}^{(CP)}$ and third $\tilde{\lambda}_{2,X_k}^{(CP)}$ spectral moments as [Di Paola and Muscolino 1986]:

$$\tilde{\lambda}_{1,X_k}^{(CP)} = \frac{\Omega_k^2 + \rho_k^2}{\Omega_k} \left[1 + \frac{\Omega_k^2 - \rho_k^2}{\pi \left(\Omega_k^2 + \rho_k^2 \right)} \right] \arctan\left(\frac{\Omega_k}{\rho_k} \right); \quad \tilde{\lambda}_{2,X_k}^{(CP)} = \Omega_k^2 - \rho_k^2; \tag{4.42}$$

Relating, for every time interval $[t_{k-1},t_k)$, the spectral parameter given in Eq.(4.40) to the radius of gyration, with respect to the centre of gravity, of the unimodal one-sided *PSD* function $G_k^{(CP)}(\omega)$, the following relationship can be written:

$$\delta_{X_k}^{(CP)} = \sqrt{\tilde{\lambda}_{2,X_k}^{(CP)} - \left(\lambda_{1,X_k}^{(CP)}\right)^2} \cong \frac{2\pi N_{0,k}^+}{\Delta T_k}\sqrt{1-\left(\frac{N_{0,k}^+}{P_k}\right)^2} \tag{4.43}$$

After some algebra, it can be proved that the frequency bandwidth ρ_k of the function $G_k^{(CP)}(\omega)$ can be approximated as:

$$\rho_k \simeq \frac{\pi N_{0,k}^+}{2\Delta T_k}\left[\pi - 2\frac{N_{0,k}^+}{P_k}\right] \tag{4.44}$$

To complete the characterization of the one-sided *PSD* function $G_{X_k}(\omega)$, given in Eq.(4.26), the circular frequency control of two Butterworth filters $\omega_{H,k}$ and $\omega_{L,k}$ in all time intervals, $[t_{k-1},t_k)$, have to be estimated. In particular, the *k*-th high pass filter was introduced only to avoid very low frequency distortion of the *PSD* function $G_k^{(CP)}(\omega)$. On the contrary the *k*-th low pass filter was introduced for both to ensure the convergence of spectral moments until fourth order of the one-sided *PSD* function $G_{X_k}(\omega)$, and to reduce the gap between the number of *zero-level up-crossings* $N_{0,k}^+$ of target accelerogram and the expected number of *zero-level up-crossings* of the *fully non-stationary* process $F_0(t)$.

4.6 Numerical examples

In the previous sections the *fully-non stationary* zero-mean Gaussian process $F_0(t)$, was defined as the sum of zero-mean Gaussian *uniformly modulated* processes, defined in contiguous time intervals (see Eq.(4.30)). Then, a method for generating samples of a *fully non-stationary* zero-mean Gaussian process, in such a way that a given target accelerogram $\ddot{U}_g(t)$ can be considered as one of its own samples, was proposed.

In this section, in order to verify the accuracy of the proposed method, some statistics of a set of *fully non-stationary* Gaussian zero-mean artificial accelerograms having on average the

cumulative energy functions and the *cumulative zero-level up-crossings* functions of the target ones, are evaluated. The temporal variation of the amplitude is obtained through an appropriate estimate of the *modulating function* $a(t)$, while the variation in the frequency content of the generated samples is obtained by appropriately estimating the *PSD* functions of stationary sub-processes having unit variances. Since the sub-processes have unit variances, the *modulating function* and the main parameters characterizing the *PSD* functions, in the various time intervals, can be estimated separately.

The proposed procedure is applied to both the horizontal components of four seismic acceleration records, namely: Kern County (California, USA) 1952, Kobe (Japan) 1995, Friuli (Italy) 1976, Kocaeli (Turkey) 1999, downloaded from PEER database [Ancheta et al. 2013].

Table 4-I lists the main characteristics of the analysed accelerograms: event name, station name and event date, moment magnitude M_w, site-source distance R_{JB} [Joyner and Boore 1981], *peak ground acceleration* a_{max} (i.e. the largest absolute value of the target accelerogram), average value of propagation velocity of *S* waves in the upper 30 m of the soil profile at the recording station v_{s30}, time duration of the analysed accelerogram T_D, significant strong motion duration *SMD* (i.e. interval of time elapsed between the 5% and 95% of the I_0), *total intensity* I_0, *Arias intensity* I_A [Arias 1970], total number of *zero-level up-crossings* N_0^+ and total number of *peaks* P_0.

Table 4-I Main characteristics of the selected accelerograms.

n°	Earthquake Name	Station and Event Date	M_w	R_{JB} [km]	a_{max} [m/s^2]	$v_{s,30}$ [m/s]	T_D [s]	*SMD* [s]	I_0 [m^2/s^3]	I_A [m/s]	N_0^+	P_0
1	Kern County	Taft Lincoln School-21 21/07/1952	7.4	38.4	1.55	385.4	54.3	30.3	3.4	0.55	163	289
2	Kern County	Taft Lincoln School-111 21/07/1952	7.4	38.4	1.76	385.4	54.3	28.8	3.7	0.59	167	295
3	Kobe Japan	Kakogawa-0 16/01/1995	6.9	22.5	2.35	312.0	40.9	13.2	6.4	1.03	154	259
4	Kobe Japan	Kakogawa-90 16/01/1995	6.9	22.5	3.18	312.0	40.9	12.9	10.5	1.68	134	264
5	Friuli Italy-02	Forgaria Cornino-0 15/09/1976	5.9	14.6	2.56	412.4	21.9	4.5	1.8	0.29	116	196
6	Friuli Italy-02	Forgaria Cornino-270 15/09/1976	5.9	14.6	2.07	412.4	21.9	4.6	2.3	0.37	99	204
7	Kocaeli, Turkey	Yarimca-60 17/08/1999	7.5	1.4	2.22	297.0	28.9	15.0	8.3	1.32	60	112
8	Kocaeli, Turkey	Yarimca-150 17/08/1999	7.5	1.4	3.15	297.0	28.9	15.0	8.3	1.32	71	260

4.6.1 Estimation of the modulating function parameters

To evaluate the *modulating function a*(*t*) of the uniformly modulated sub-processes, the time duration of the analysed accelerogram $0 \div T_D$, must be divided in n_a time intervals. Two strategies can be adopted to obtain a good match between the expected *cumulative energy* function of artificial and target accelerograms: *i*) subdivide the target accelerogram in several time intervals, e.g. Der Kiureghian and Crempien [1989] suggested at most nine frequency bands); *ii*) subdivide the time duration in only three time intervals n_a=3, also optimizing the choice of instants of passage from one time interval to adjacent ones.

The second strategy is here adopted. Moreover, according to the models by Amin and Ang [1968] and by Jennings et al. [1968], the *modulating function* in the first time interval, $0 \le t < t_1$, is here assumed parabolically increasing from zero; while in the third time interval, $t_2 \le t \le T_D$, it is assumed exponentially decreasing, consistently with Eq.(4.38).

In the second time interval, $t_1 \le t < t_2$, the assumption of constant *modulating function*, as proposed by Amin and Ang [1968] and by Jennings et al. [1968], leads to very unsatisfactory results for both energy and frequency content of the *fully non-stationary* process $F_0(t)$. Therefore, in the proposed approach, a polynomial of *p*-th order to model the *modulating function* in the second interval is adopted. It has been also observed that the choice of time instants t_1 and t_2 strongly influences both the energy and frequency content of the process $F_0(t)$. Hence, the proposed method requires an optimal choice of time instants t_1 and t_2, as well as of the order *p* of the polynomial *modulating function*. As a measure of the accuracy, the *root-mean-square* (*rms*) difference D_p between the estimated *modulating function*, given in Eq.(4.38), and the target accelerogram absolute values, is defined as follows:

$$D_p = \sqrt{\frac{\Delta t}{T_D} \sum_{j=0}^{T_D/\Delta t} \left[a(j\ \Delta t) - |\ddot{U}_g(j\ \Delta t)| \right]^2} \tag{4.45}$$

where Δt is the sampling interval of the target accelerogram and the subscript *p* denotes the order of the polynomial considered in the second time interval.

Specifically, for the estimation of the *modulating function* the following steps are required:

i) in the first time interval, the *modulating function a*(*t*), is assumed as a polynomial of second order; then the optimization problem described with reference to Eq. (4.36) for five values of

$t_1 = t_{1\%}, t_{2\%}, \cdots, t_{5\%}$ ($t_{k\%}$ time instant in which the *cumulative energy* function of the accelerogram assumes the *k*% of its *total intensity*: $E_{\ddot{U}_g}(t_{k\%}) \equiv k\,\% \times I_0$), is solved;

ii) in the second time interval it is assumed that the *modulating function* is a polynomial, the order of which, *p*, varies from one to ten; furthermore, different values of both time instant of passage from the first to the second interval, $t_1 = t_{1\%}, t_{2\%}, \cdots, t_{5\%}$, and from the second to the third interval, $t_2 = t_{90\%}, t_{91\%}, \cdots, t_{99\%}$ are chosen;

iii) in the third time interval [t_2, T_D], according to Eq.(4.38), an exponential decay form for the *modulating function* is assumed; its initial value, $a(t_2)$ depends on the various combinations adopted for the *modulating function* in the second time interval.

Finally, among the various *modulating function*s obtained by applying the previously described procedure (varying the instants t_1 and t_2), the one characterised by the lowest *rms* D_p, is selected.

The parameters which characterise the selected *modulating functions* $a(t)$ are listed in Table 4-II, for all the selected accelerograms, together with the values of the time instants, t_1 and t_2, corresponding to the passage from one interval to another, the corresponding percentages of *total intensity*, k_1% and k_2%, the order *p* of the polynomial in the second time interval, the *rms* difference D_p, and the absolute value $\left|\ddot{U}_g(T_D)\right|$ at the end of the target accelerogram.

For the first two time intervals, the polynomial coefficients α_i, obtained through the optimization procedure, are listed in Table 4-III.

In Figure 4.1, for the eight analysed accelerograms, the absolute value of each accelerogram together with the four *modulating function*s having the smaller *rms* difference D_p are plotted. This figure shows that small *rms* differences D_p can be obtained with different choices of the polynomial order and that often the highest order of the polynomial does not provide the smallest D_p. Furthermore, choosing the same polynomial order for all target accelerograms could give in many cases inaccurate results. For coherence in the following the polynomial order which gives the lowest D_p is adopted.

Finally, Figure 4.2 shows that the moduli of *Fourier transforms* of the eight modulating functions of Figure 4.1 are mainly concentrated in the region of zero frequency. This is in accord with Priestley's definition of a slowly varying function of time [Priestly 1967].

Table 4-II Parameters of the modulating function selected for the accelerograms listed in Table 4-I.

$n°$	t_1 [s]	t_2 [s]	k_1%	k_2%	p	D_p [m/s^2]	$\lvert\ddot{U}_g(T_D)\rvert$ [m/s^2]
1	3.13	40.58	1	98	7	0.167	0.00275
2	3.45	25.82	3	91	7	0.171	0.00758
3	2.55	14.22	1	91	10	0.247	0.00210
4	2.63	26.47	1	99	9	0.308	0.00084
5	2.51	6.84	2	90	5	0.192	0.00134
6	3.33	7.55	4	94	9	0.191	0.00114
7	2.55	14.10	1	91	8	0.285	0.02539
8	3.31	14.55	3	91	10	0.310	0.01282

Table 4-III Polynomial coefficients [m/s^{i+2}] in the first two time intervals of the modulating functions of the selected accelerograms.

	$0 \le t < t_1$		$t_1 \le t < t_2$									
$n°$	α_1	α_2	α_1	α_2	α_3	α_4	α_5	α_6	α_7	α_8	α_9	α_{10}
1	$8.6\cdot10^{-3}$	0.02	0.226	-0.054	$5.6\cdot10^{-3}$	$-3.3\cdot10^{-4}$	$1.2\cdot10^{-5}$	-1.9	$1.4\cdot10^{-9}$	-	-	-
2	$3.7\cdot10^{-4}$	0.03	0.513	-0.247	0.1	-0.005	$3.2\cdot10^{-4}$	$-9.6\cdot10^{-6}$	$1.18\cdot10^{-7}$	-	-	-
3	$1.5\cdot10^{-3}$	0.05	1.679	-3.106	2.6	-1.101	0.3	-0.05	$4.5\cdot10^{-3}$	$-2.7\cdot10^{-4}$	$8.9\cdot10^{-6}$	$-1.2\cdot10^{-7}$
4	$1.9\cdot10^{-4}$	0.06	1.246	-0.857	0.3	-0.054	$5.8\cdot10^{-3}$	$-3.8\cdot10^{-4}$	$1.5\cdot10^{-5}$	$-3.1\cdot10^{-7}$	$2.7\cdot10^{-9}$	-
5	0.07	$5.1\cdot10^{-4}$	0.309	1.251	-1.2	0.358	-0.03	-	-	-	-	-
6	0.07	$4.6\cdot10^{-3}$	6.505	-22.109	34.2	-27.535	12.1	-2.8	0.3	$2.6\cdot10^{-4}$	$-1.7\cdot10^{-3}$	-
7	0.1	$6.8\cdot10^{-5}$	1.680	-1.725	0.9	-0.283	0.05	-0.005	$2.9\cdot10^{-4}$	$-6.6\cdot10^{-6}$	-	-
8	0.1	$1.3\cdot10^{-4}$	5.799	-11.743	10.4	-5.114	1.5	-0.3	0.03	$2.5\cdot10^{-3}$	$1.0\cdot10^{-4}$	$1.8\cdot10^{-6}$

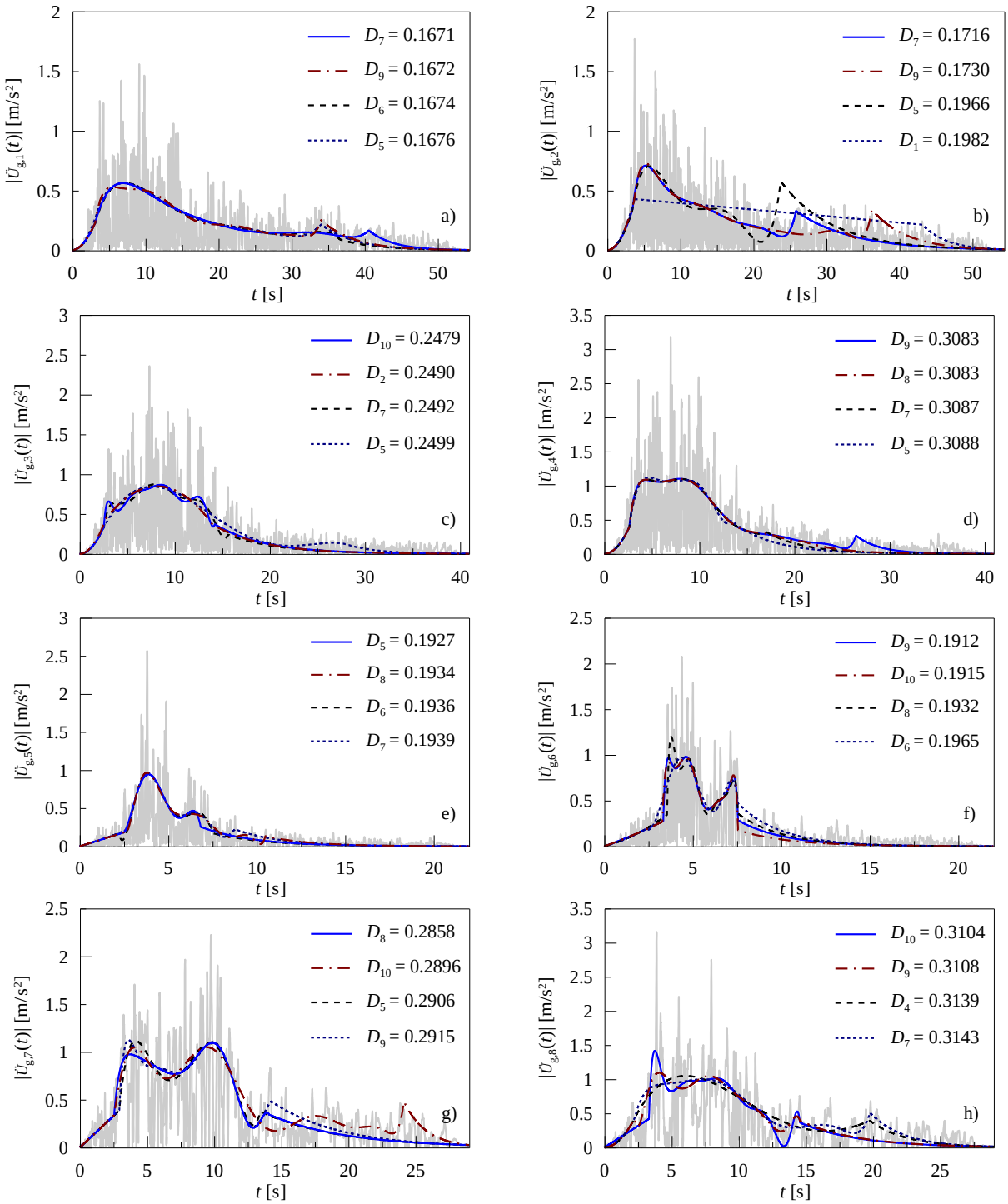

Figure 4.1 Absolute value of the analysed accelerograms and selected *modulating functions* $a(t)$, having the smaller *rms* difference D_p: a) Taft Lincoln School-21; b) Taft Lincoln School-111; c) Kakogawa-0; d) Kakogawa-90; e) Forgaria Cornino-0; f) Forgaria Cornino-270; g) Yarimca-60; h) Yarimca-270.

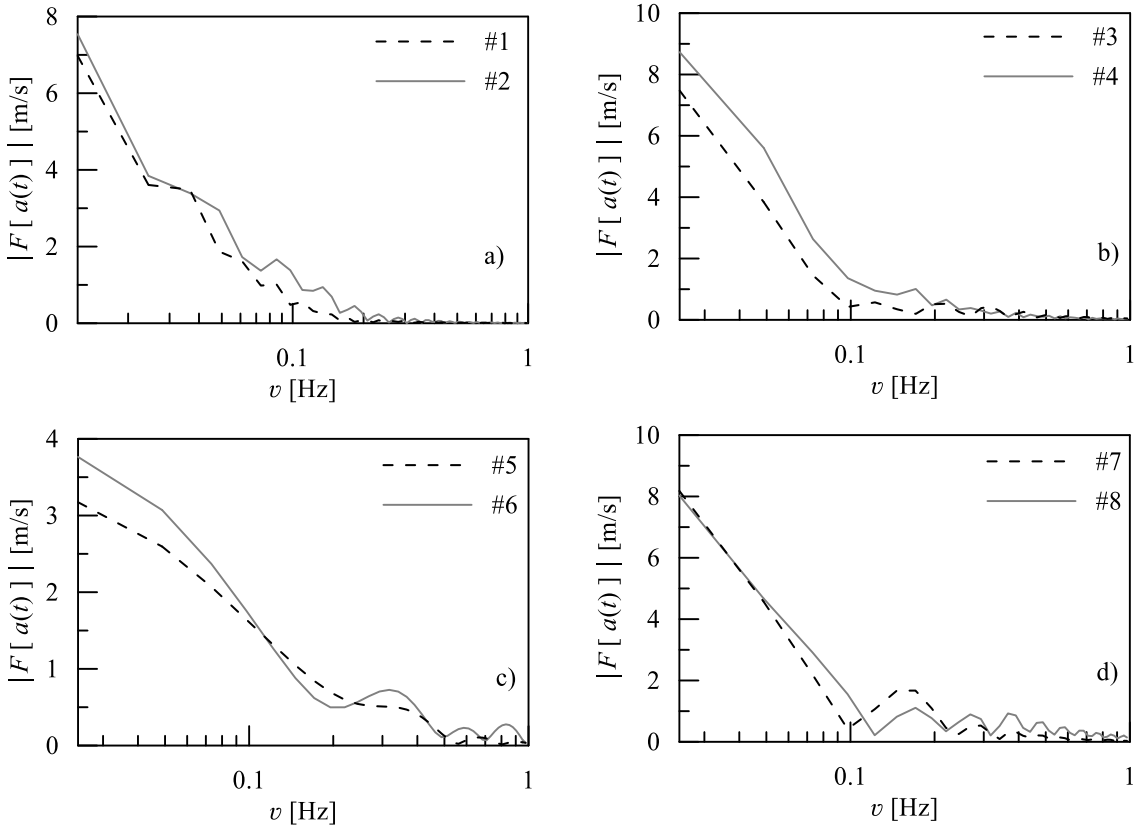

Figure 4.2 Moduli of *Fourier transforms* of the eight modulating functions evaluated by applying the proposed procedure: a) Taft Lincoln School; b) Kakogawa; c) Forgaria Cornino; d) Yarimca.

4.6.2 Estimation of the sub-processes PSD function parameters

The characterization of the *fully-non stationary* zero-mean Gaussian process $F_0(t)$ must be completed by estimating the parameters of the one-sided *PSD* function $G_{X_k}(\omega)$ of the stationary sub-process $X_k(t)$, appearing in Eq.(4.26). To do this, for the three time intervals of each of the eight analysed accelerograms $\ddot{U}_{g,\ell}(t)$, the predominant circular frequency Ω_k, and the bandwidth frequency parameters ρ_k, have to be evaluated. According to Eqs.(4.41) and (4.44), the evaluation of these parameters requires the counting of the number of *zero-level up-crossings* $N_{0,k}^{+}$, and the number of *peaks* P_k in the time intervals ΔT_k, of each accelerogram. The parameters useful to the characterisation of the one-sided *PSD* function $G_{X_k}(\omega)$ are reported in Table 4-IV.

Finally, through several numerical tests it was verified that the control frequencies of two Butterworth filters $\omega_{H,k}$ and $\omega_{L,k}$ can be assumed equal to:

$$\omega_{H,k} = 0.1\,\Omega_k \tag{4.46}$$

$$\omega_{L,k} = \Omega_k + 0.8\,\rho_k \tag{4.47}$$

Table 4-IV Main parameters of the one-sided *PSD* functions in the three time intervals analysed for each of the selected accelerograms.

	$0 \le t < t_1$						$t_1 \le t < t_2$						$t_2 \le t \le T_D$					
$n°$	$N_{0,1}^+$	P_1	ΔT_1 [s]	Ω_1 [rad/s]	ρ_1 [rad/s]	β_1^2	$N_{0,2}^+$	P_2	ΔT_2 [s]	Ω_2 [rad/s]	ρ_2 [rad/s]	β_2^2	$N_{0,3}^+$	P_3	ΔT_3 [s]	Ω_3 [rad/s]	ρ_3 [rad/s]	β_3^2
1	12	23	3.1	24.16	12.67	7.14	128	204	37.4	21.48	10.13	5.68	23	65	14.7	10.50	6.39	3.62
2	13	30	3.7	21.60	12.28	6.95	79	127	22.3	22.54	10.69	6.00	75	142	28.5	16.51	8.60	4.84
3	18	24	2.5	44.52	18.27	10.21	52	77	11.6	28.02	12.54	7.02	84	166	26.7	19.74	10.51	5.92
4	14	29	2.6	33.57	18.26	10.31	89	151	23.8	23.46	11.51	6.47	31	91	14.4	13.45	8.27	4.70
5	21	30	2.5	52.56	22.88	12.80	26	33	4.3	37.81	14.80	8.26	69	138	15.1	28.62	15.32	8.64
6	26	40	3.3	49.05	22.58	12.66	20	26	4.2	29.81	11.94	6.67	53	140	14.4	23.07	13.75	7.80
7	15	39	2.5	36.95	21.92	12.43	21	82	11.5	11.42	7.51	4.28	24	99	14.8	10.12	6.72	3.84
8	23	55	3.3	43.72	25.19	14.26	18	103	11.2	10.06	7.02	4.02	30	110	14.4	13.05	8.47	4.83

In Figure 4.3, for the eight analysed accelerograms $\ddot{U}_{g,\ell}(t)$, the one-sided *PSD* functions, $G_{X_k,\ell}(\omega)$ of the stationary sub-processes $X_{k,\ell}(t)$ are depicted. Curves in Figure 4.3 represent the variation of the three *PSD* functions in the three contiguous time intervals, pointing out the time variation of the frequency content of target accelerograms. Analysing the results in Figure 4.3, and the predominant circular frequencies listed in Table 4-IV, it is apparent that the predominant frequencies Ω_k usually decrease with increasing time. However, in some cases, this condition is not completely satisfied.

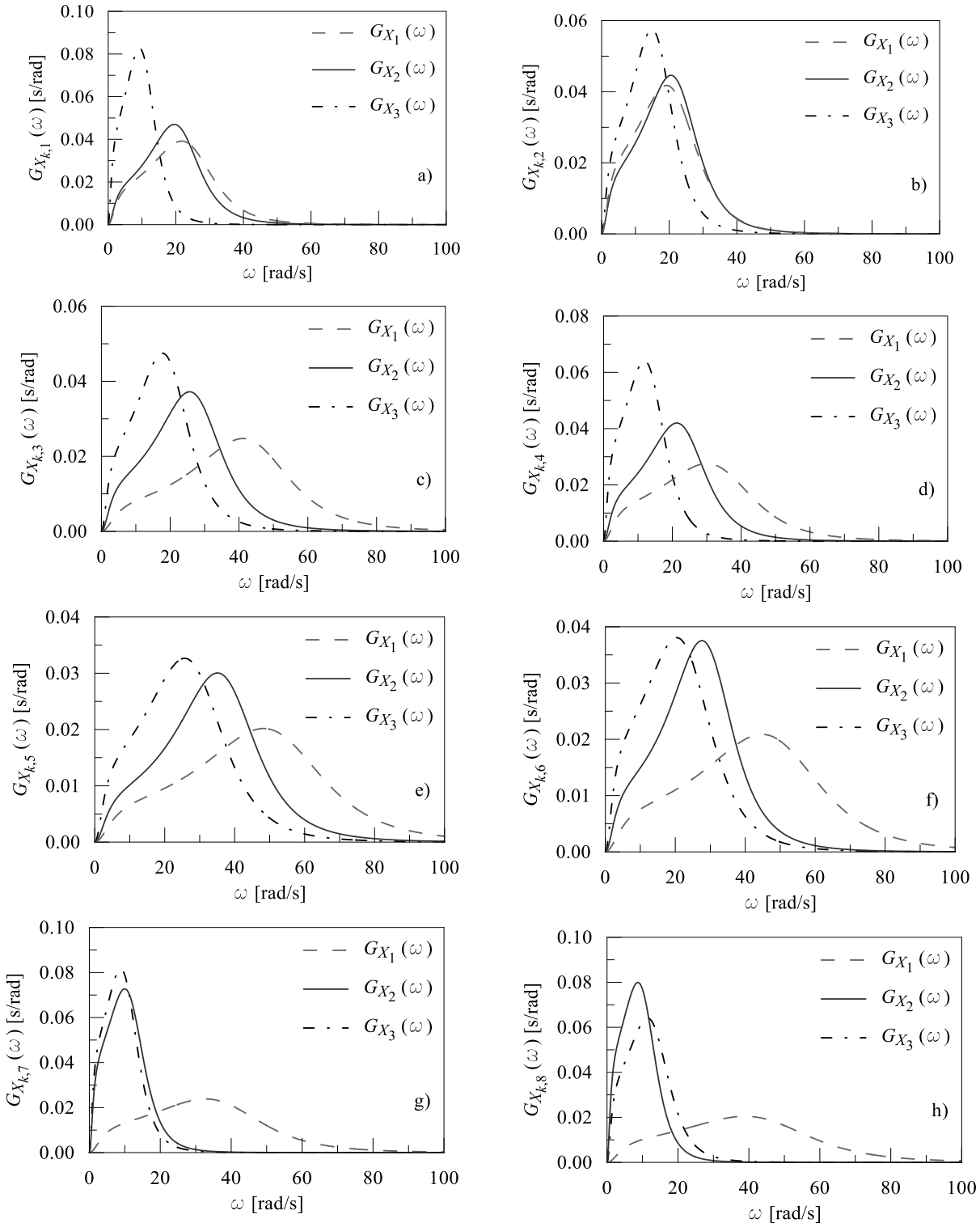

Figure 4.3 One-sided *PSD* functions in the three contiguous time intervals, of the selected accelerograms: a) Taft Lincoln School-21; b) Taft Lincoln School-111; c) Kakogawa-0; d) Kakogawa-90; e) Forgaria Cornino-0; f) Forgaria Cornino-270; g) Yarimca-60; h) Yarimca-270.

4.6.3 Generation of artificial accelerograms

Once the parameters characterizing the *fully-non-stationary* zero-mean Gaussian process, $F_0(t)$, are estimated, it is easy to generate its samples in such a way that the selected target accelerogram can be considered as one of its own samples. Indeed, the *i*-th sample of the real part of the $F_0(t)$, containing in its set the target accelerogram $\ddot{U}_g(t)$, can be evaluated as:

$$\bar{F}_0^{(i)}(t) = a(t)\sqrt{2\Delta\omega}\left[\sum_{k=1}^{n} \mathbb{W}(t_{k-1},t_k)\sum_{r=1}^{m_N}\cos\left(r\,\Delta\omega t + \theta_r^{(i)}\right)\sqrt{G_{X_k}\left(r\,\Delta\omega\right)}\right] \qquad (4.48)$$

assuming a frequency increment $\Delta\omega = \omega_N / m_N = 0.1\,\text{rad/s}$, an upper cut-off circular frequency $\omega_N = 100\ \text{rad/s}$, $m_N = 1000$ and $\Delta t = \pi/(4\omega_N)$. Note that the random phase angles, $\theta_r^{(i)}$, uniformly distributed over the interval $[-\pi,\pi)$, must be the same for all segments of the *i*-th sample.

Using this approach, a set of one hundred samples is evaluated for each of the selected accelerogram. In Figure 4.4 the time-history of the eight analysed records, numbered in Table 4-I, is compared with one sample of the corresponding stochastic process Eq.(4.48) and a good similarity of the sample to the target accelerogram can be observed.

A more complete comparison can be performed by evaluating for the eight analysed accelerograms the *cumulative energy* functions $E_{\ddot{U}_{g,\ell}}(t)$ and cumulative *zero-level up-crossing* functions $N_{0,\ell}^{+}(t)$, which count the number of *zero-level up-crossing* until the time *t*. These two functions are compared, for each of the analysed accelerogram, with the corresponding mean value functions obtained by calculating the average of the results of the sets of artificial accelerogram samples.

In particular, in Figure 4.5 the *cumulative energy* functions of the eight analysed target accelerograms are compared to those obtained as the mean value of the hundred samples. In the Figure 4.5 the *cumulative energy* function confidence intervals, evaluated as the mean values plus/minus the corresponding standard deviation, are also plotted. In Figure 4.6 the cumulative *zero-level up-crossing* functions of target accelerograms are compared with the mean value functions of the one hundred samples and the cumulative *zero-level up-crossing* function confidence intervals. In Figures 4.5 and 4.6, the shaded areas represent the envelope

of the maximum and minimum values of the *cumulative energy* function and cumulative *zero-level up-crossing* of the 100 generated samples, respectively.

Figures 4.5 and 4.6 evidence the accuracy of the proposed procedure. Note that the choice of the simple decreasing exponential function in the third time interval is paid for with a small difference in terms of *zero-level up-crossings* in the last time interval.

Note that although the generated accelerograms are samples of a zero-mean Gaussian process, the corresponding *cumulative energy* function and the cumulative *zero-level up-crossing* function are not zero-mean Gaussian processes. To evidence this, the mean values $\mu_{I_0}, \mu_{N_0^+}$, the standard deviations $\sigma_{I_0}, \sigma_{N_0^+}$, and the coefficients of variation $\sigma_{I_0}/\mu_{I_0}, \sigma_{N_0^+}/\mu_{N_0^+}$ of *total intensity* I_0 and of the total number of *zero-level up-crossing* N_0^+ are reported in Table 4-V for the eight analyzed accelerograms.

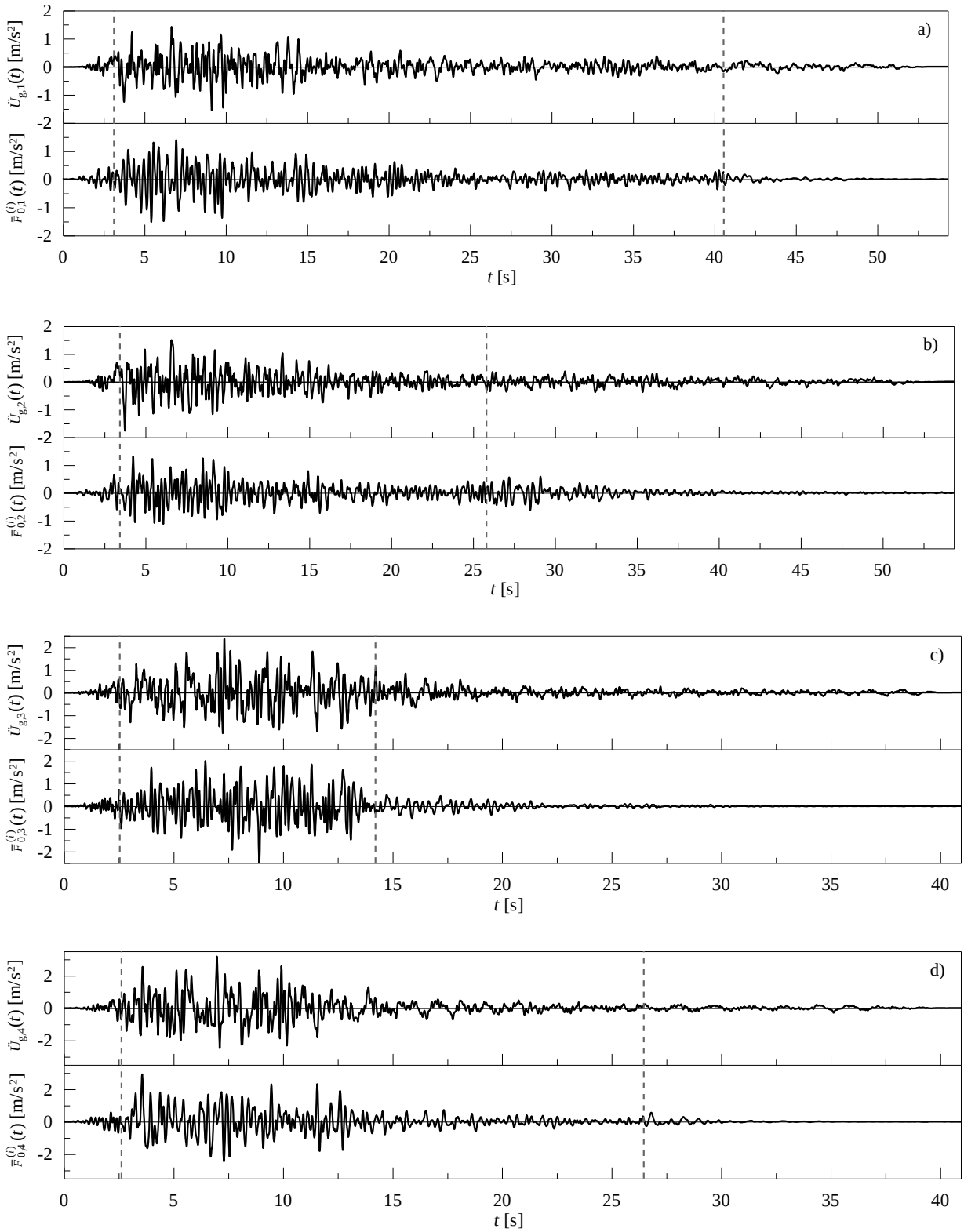

Figure 4.4 Comparison between the selected horizontal and the corresponding *i*-th generated samples $\bar{F}_{0,\ell}^{(i)}$. The vertical dashed lines delimit the three time intervals: a) Taft Lincoln School-21; b) Taft Lincoln School-111; c) Kakogawa-0; d) Kakogawa-90; e) Forgaria Cornino-0; f) Forgaria Cornino-270; g) Yarimca-60; h) Yarimca-270.

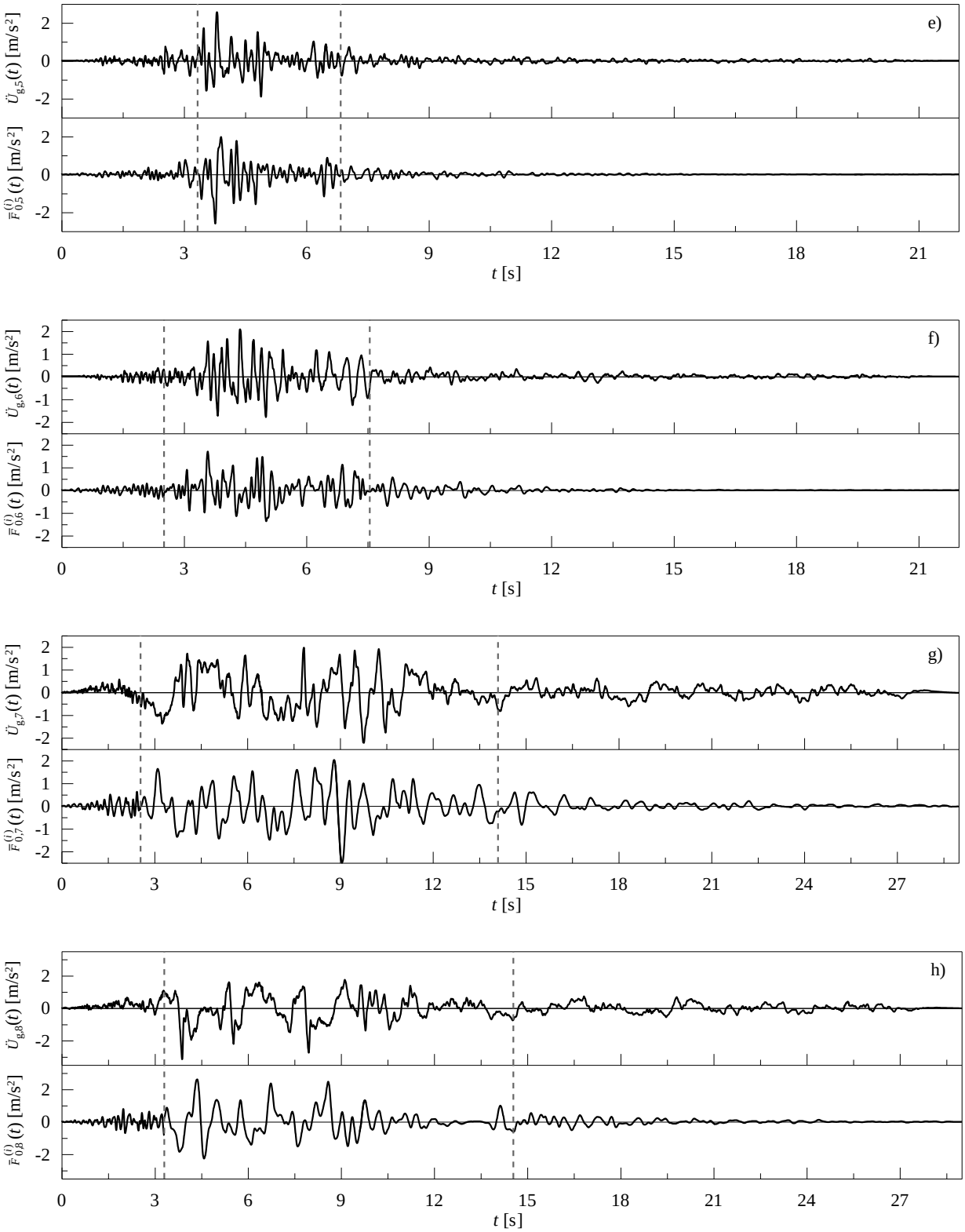

Figure 4.4 **(***Continued*).

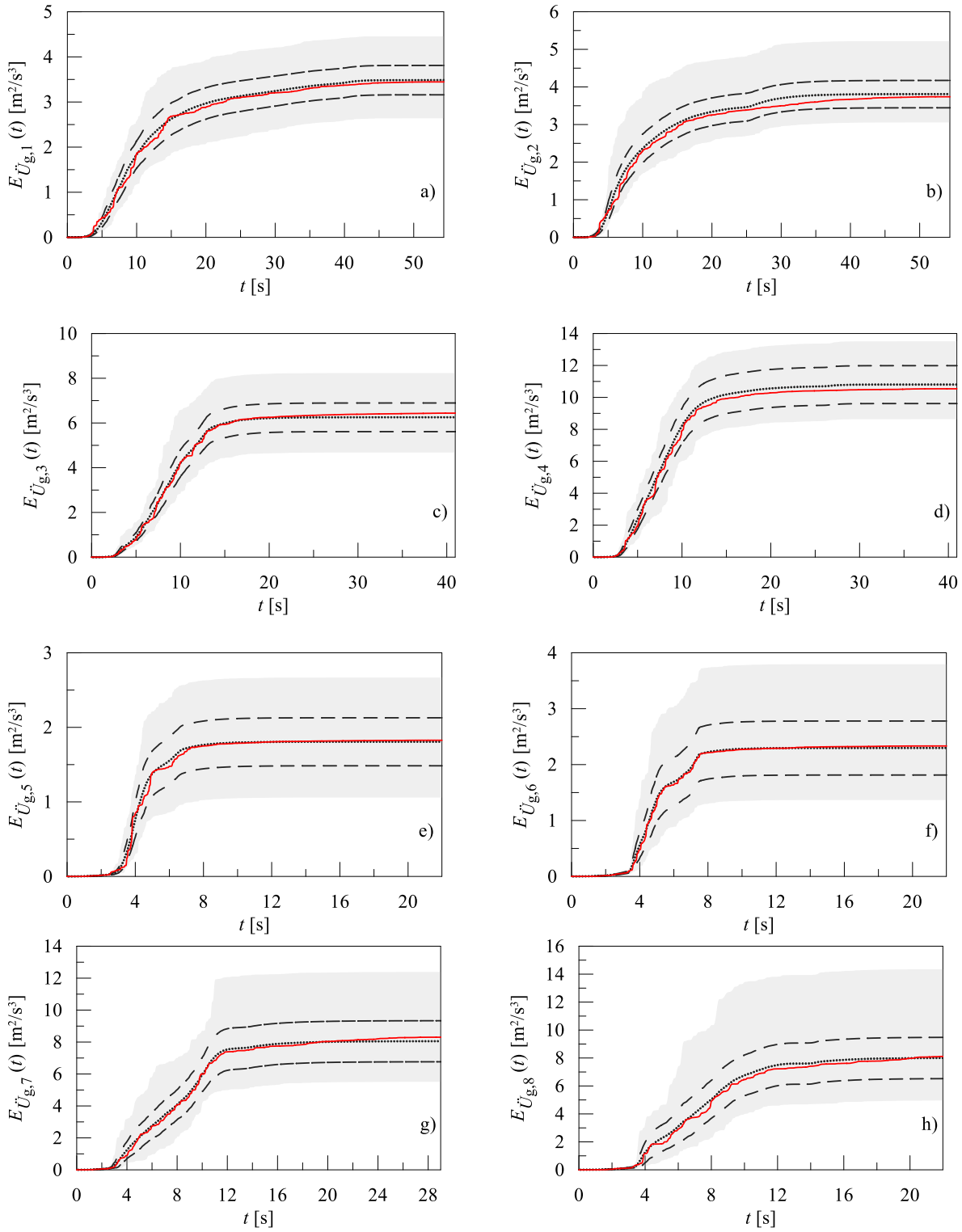

Figure 4.5 Comparison among the energy functions of the selected accelerograms with statistics of the artificial ones: a) Taft Lincoln School-21; b) Taft Lincoln School-111; c) Kakogawa-0; d) Kakogawa-90; e) Forgaria Cornino-0; f) Forgaria Cornino-270; g) Yarimca-60; h) Yarimca-270. Target accelerogram (red solid line); mean value function (black dotted line); mean value plus/minus standard deviation functions (black dashed lines); envelope of the maximum and minimum values of all samples (shaded area).

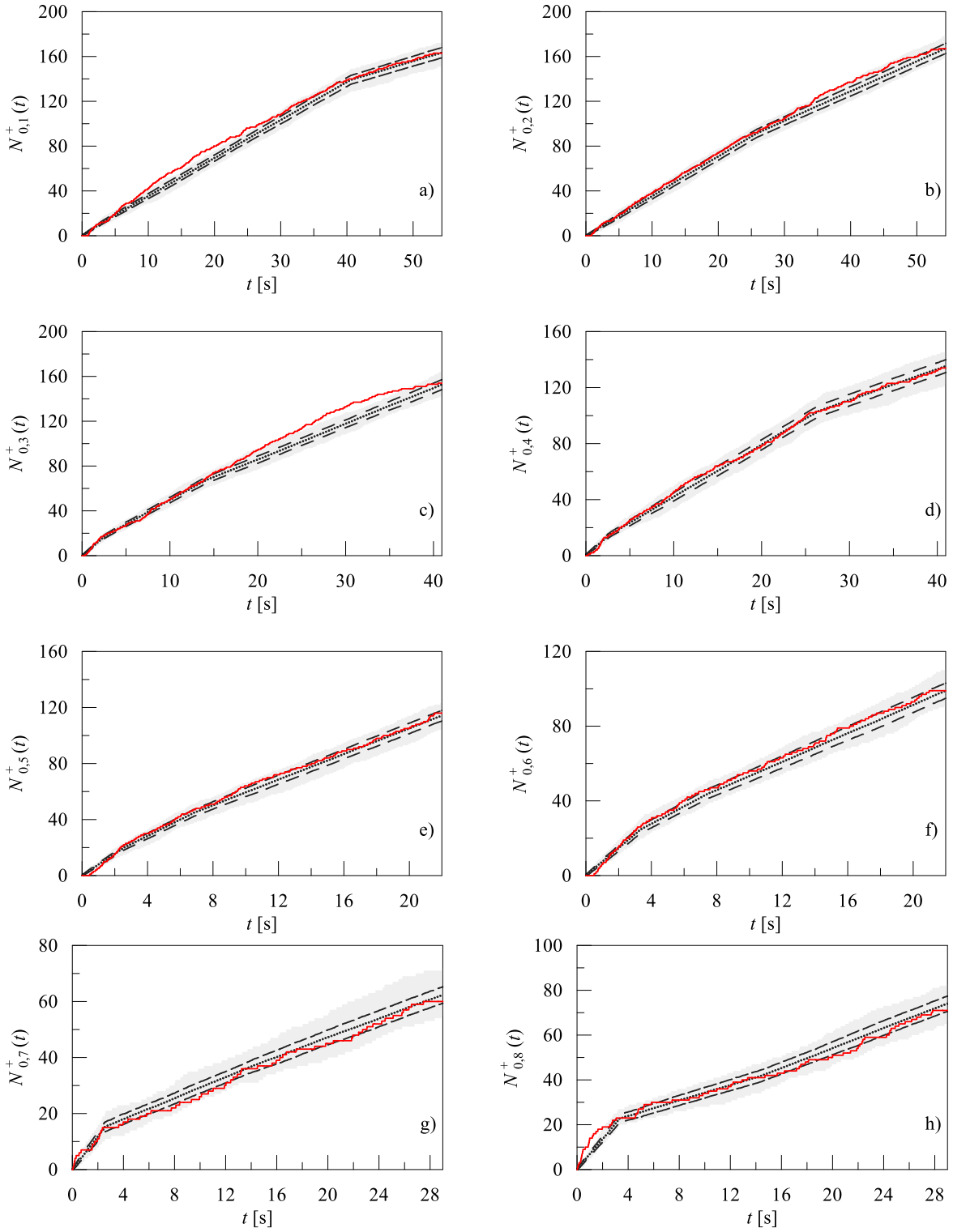

Figure 4.6 Comparison among the *zero-level up-crossings* of the selected accelerograms with statistics of the artificial ones: a) Taft Lincoln School-21; b) Taft Lincoln School-111; c) Kakogawa-0; d) Kakogawa-90; e) Forgaria Cornino-0; f) Forgaria Cornino-270; g) Yarimca-60; h) Yarimca-270. Target accelerogram (red solid line); mean value function (black dotted line); mean value plus/minus standard deviation functions (black dashed lines); envelope of the maximum and minimum values of all samples (shaded area).

Table 4-V Mean values $\mu_{I_0}, \mu_{N_0^+}$, standard deviations $\sigma_{I_0}, \sigma_{N_0^+}$, and coefficients of variation $\sigma_{I_0}/\mu_{I_0}, \sigma_{N_0^+}/\mu_{N_0^+}$, of *total intensity* I_0, and of the total number of *zero-level up-crossing* N_0^+, for the eight analyzed accelerograms.

n°	μ_{I_0} [m²/s³]	σ_{I_0} [m²/s³]	σ_{I_0}/μ_{I_0}	$\mu_{N_0^+}$	$\sigma_{N_0^+}$	$\sigma_{N_0^+}/\mu_{N_0^+}$
1	3.48	0.32	0.093	163.34	4.65	0.028
2	3.80	0.36	0.095	167.17	4.59	0.027
3	6.25	0.64	0.102	152.62	4.44	0.029
4	10.80	1.18	0.109	135.26	4.58	0.033
5	1.80	0.32	0.178	114.16	3.75	0.032
6	2.29	0.48	0.210	98.98	4.06	0.041
7	8.04	1.28	0.159	62.32	2.92	0.046
8	8.00	1.47	0.184	74.02	3.37	0.045

4.7 Generation of fully non-stationary spectrum compatible artificial accelerograms

In this section the *EPSD* of the fully non-stationary process is modified to guaranty the spectrum compatibility of the sets of artificial accelerograms. Specifically, to reduce the gap between the mean spectrum of generated samples and a target spectrum, an iterative procedure has been implemented and the *EPSD* function is rewritten as:

$$\begin{aligned} &\bar{G}_{F_0F_0}^{(j)}(\omega,t) = a^2(t)\,\bar{G}^{(j)}(\omega)\sum_{k=1}^{n} W(t_{k-1},t_k)\,G_{X_k}(\omega); \\ &\bar{G}_{F_0F_0}^{(0)}(\omega,t) \equiv G_{F_0F_0}(\omega,t) \end{aligned} \tag{4.49}$$

where $\bar{G}^{(j)}(\omega)$ is a corrective *PSD* function at the *j*-th iteration evaluated as follows [Vanmarcke and Gasparini 1977]:

$$\bar{G}_X^{(j)}(\omega) = \bar{G}_X^{(j-1)}(\omega)\; R_S^{(j-1)}(\omega,\zeta_0) \tag{4.50}$$

where $R_S^{(j-1)}(\omega,\zeta_0)$ is the ratio between the square values of the mean spectrum of the generated samples $\bar{S}^{(j-1)}(\omega,\zeta_0)$ and the target spectrum $S^{(T)}(\omega,\zeta_0)$:

$$R_S^{(j-1)}(\omega,\zeta_0)=\frac{S^{(T)}(\omega,\zeta_0)^2}{\bar{S}^{(j-1)}(\omega,\zeta_0)^2} \tag{4.51}$$

being ζ_0 the viscous damping ratio.

Notice that at first iteration it is assumed $\bar{G}^{(0)}(\omega)=1$ [Vanmarcke and Gasparini 1977]. Once the corrective *PSD* function $\bar{G}^{(j)}(\omega)$ is introduced, by using the original set of random phase angles, $\theta_r^{(i)}$, a new set of spectrum-compatible samples $\bar{F}_0^{(i)}(t)$ can be generated as:

$$\bar{F}_0^{(i)}(t)=a(t)\sqrt{2\Delta\omega}\left[\sum_{k=1}^{n}\mathbb{W}(t_{k-1},t_k)\sum_{r=1}^{m_N}\cos\left(r\,\Delta\omega t+\theta_r^{(i)}\right)\sqrt{\bar{G}^{(j)}(r\,\Delta\omega)G_{X_k}\left(r\,\Delta\omega\right)}\right] \tag{4.52}$$

It has to be emphasized that the procedure should not be expected to be convergent at all selected control frequencies.

4.7.1 Types of spectrum-compatibility

Depending on the purposes of the accelerogram generation procedure, the spectrum compatibility can be checked against:

i) the *pseudo acceleration response spectrum* $Sa^{(T)}(\omega,\zeta_0)$ of the target accelerogram;

ii) the *Fourier spectrum* $S_F^{(T)}(\omega)$ of the target accelerogram;

iii) the code-prescribed *elastic response spectrum* $S_R^{(T)}(\omega,\zeta_0)$.

Notice that to achieve the *Fourier-spectrum compatibility* $S^{(T)}(\omega,\zeta_0)=S_F^{(T)}(\omega,\zeta_0)$, the corrective iterative *PSD* function $\bar{G}^{(j)}(\omega)$ term can be particularized as follows:

$$\bar{G}^{(j)}(\omega)=\bar{G}^{(j-1)}(\omega)\,\frac{S_V^{(T)}(\omega,0)^2}{\bar{S}_V^{(j-1)}(\omega,0)^2} \tag{4.53}$$

being $S_V^{(T)}(\omega,0)$ and $\bar{S}_V^{(j-1)}(\omega,0)$ the *velocity response spectra* for ζ_0=0.

4.8 Numerical application

In this section, in order to verify the accuracy of the proposed method, two different sets of one hundred artificial accelerograms, spectrum-compatible with the *pseudo acceleration response spectrum* and the *Fourier spectrum* of the target accelerogram, have been generated.

The same accelerogram used in Chapter 3 that is, the "090" component of the time history recorded at Vasquez Rocks Park during the Northridge earthquake, has been used as target in the following.

For the application of the proposed method, the target accelerogram has been purged of its initial and final parts having energy I_0 less than 1% and higher than 99% respectively. In this way the initial and final parts containing a lot of zero crossings have been removed and the duration of the signal changes from T_D=39.98 s to T_D=36.60 s.

4.8.1 Set of fully non-stationary accelerograms

A set of one-hundred artificial accelerograms is generated by the use of appropriate modulating and power spectral density functions which allowed to preserve the amplitude and the frequency content of the target motion.

To evaluate the *modulating function* $a(t)$ of Eq. (4.38), the time duration of the analysed accelerogram $0 \div T_D$, is divided in three-time intervals, optimizing the choice of instants of passage from one time interval to adjacent ones.

Figure 4.7 shows the absolute value of the target accelerogram together with the *modulating function* $a(t)$. The vertical dashed lines in Figure 4.7 denote the portions in which the target accelerograms has been subdivided to evaluate $a(t)$.

The parameters which characterise $a(t)$ are listed in Table 4-VI, together with the values of the time instants t_1 and t_2, corresponding to the passage from one interval to another, the corresponding percentages of *total intensity* k_1% and k_2%, the order p of the polynomial in the second time interval and the absolute value $|\ddot{U}_g(T_D)|$ at the end of the target accelerogram.

For the first two time-intervals, the polynomial coefficient α_i, obtained through the optimization procedure, are listed in Table 4-VII.

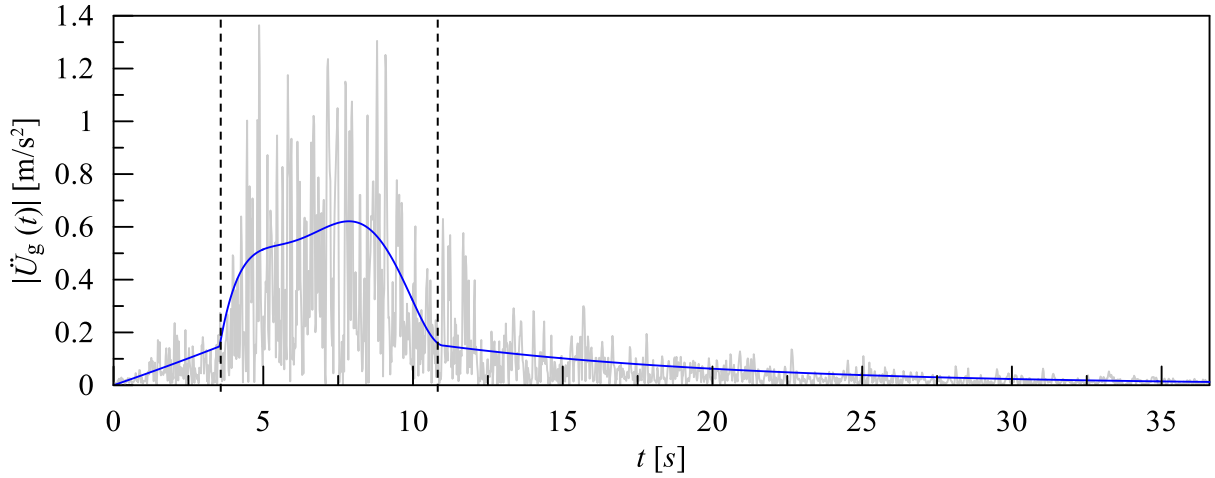

Figure 4.7 Absolute value of the analysed accelerogram (grey line) with the *modulating functions* $a(t)$ (blue line).

Table 4-VI Parameters of the modulating function selected for the target accelerogram.

t_1 [s]	t_2 [s]	k_1%	k_2%	p	$\lvert\ddot{U}_g(T_D)\rvert$ [m/s^2]
3.54	11.02	1	92	5	0.0123

Table 4-VII Polynomial coefficients [m/s^{i+2}] in the first two time-intervals of the modulating function.

$0 \le t < t_1$		$t_1 \le t < t_2$				
α_1	α_2	α_1	α_2	α_3	α_4	α_5
0.039	$6.998 \cdot 10^{-4}$	0.641	-0.429	0.138	-0.020	$1.042 \cdot 10^{-3}$

The characterization of the *fully-non stationary* zero-mean Gaussian process $F_0(t)$ must be completed by estimating the predominant circular frequency Ω_k, and the bandwidth circular frequency ρ_k of the one-sided *PSD* function $G_{X_k}(\omega)$ of the stationary sub-process $X_k(t)$, that depend exclusively from the number of *zero level up crossings* $N_{0,k}^{+}$ and peaks P_0, according to Eqs. (4.41) and (4.44). The two control frequencies of two Butterworth filters $\omega_{H,k}$ and $\omega_{L,k}$ have been assumed equal to $\omega_{H,k} = 0.1\,\Omega_k$ and $\omega_{L,k} = \Omega_k + 0.8\,\rho_k$, respectively (see Eqs. (4.46) and (4.47)).

To evaluate the spectral parameters, the target accelerogram is preliminary divided into *n* time intervals. Notice that, the subdivision made for the evaluation of the modulating function *a*(*t*) could be different from that made for the characterization of the one-sided *PSD* function $G_{X_k}(\omega)$.

As highlighted in [Genovese et al. 2020 b], to obtain accurate results, the analysed accelerogram is subdivided into $n>3$ time intervals $\ddot{U}_{g,k}(t)$. Each time interval must contain a number of *zero level up crossings* $N_{0,k}^{+}$ at least equal to one. Consequently, in this section the selected accelerogram is subdivided in 73-time intervals with a constant time step of Δt=0.5s. Since the total duration of the accelerogram is not a multiple of the time step Δt, the last time interval of the signal has a duration of 0.6 s.

The parameters useful for the characterisation of the one-sided *PSD* function $G_{X_k}(\omega)$ are summarized in Table 4-VIII. The representation of the target accelerogram subdivided in 73 time intervals is reported in Figure 4.8.

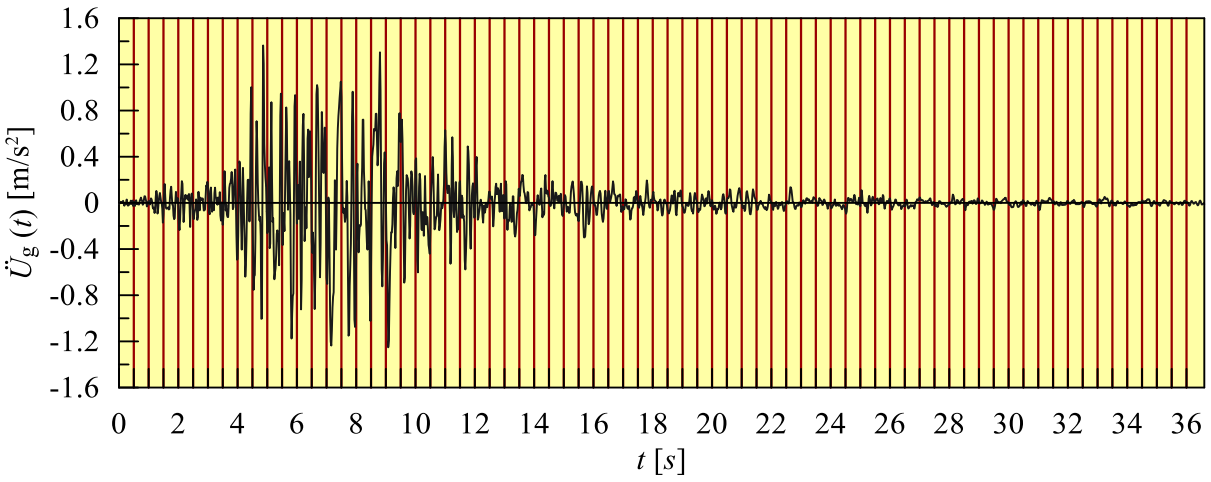

Figure 4.8 Selected accelerogram (Northridge earthquake) subdivided in 73-time intervals with a constant time step of 0.5 s.

Table 4-VIII Main parameters of the one-sided *PSD* functions in the time intervals analysed.

#	N_0^+	P_0	Ω_k [rad/s]	ρ_k [rad/s]	ω_H [rad/s]	ω_L [rad/s]	β	#	N_0^+	P_0	Ω_k [rad/s]	ρ_k [rad/s]	ω_H [rad/s]	ω_L [rad/s]	β
1	4	6	52.3	23.8	5.2	71.3	13.3	**38**	3	5	39.3	19.1	3.9	54.5	10.7
2	4	5	52.3	20.2	5.2	68.5	11.3	**39**	2	4	26.2	14.0	2.6	37.4	7.9
3	3	4	39.3	16.1	3.9	52.2	9.0	**40**	4	5	52.4	20.2	5.2	68.5	11.3
4	3	5	39.3	19.1	3.9	54.5	10.7	**41**	3	5	39.3	19.1	3.9	54.5	10.7
5	3	6	39.3	21.0	3.9	56.1	11.9	**42**	1	3	13.1	8.1	1.3	19.6	4.6
6	4	5	52.4	20.2	5.2	68.5	11.3	**43**	3	4	39.3	16.1	3.9	52.2	9.0
7	6	7	78.6	28.0	7.9	100.9	15.6	**44**	2	4	26.2	14.0	2.	37.4	7.9
8	3	3	39.3	11.2	3.9	48.2	6.7	**45**	3	6	39.3	21.0	3.93	56.1	11.9
9	4	4	52.4	14.9	5.2	64.3	8.3	**46**	2	4	26.2	14.0	2.6	37.4	7.9
10	3	3	39.3	11.2	3.9	48.2	6.3	**47**	2	5	26.2	15.3	2.6	38.4	8.7
11	3	4	39.3	16.1	3.9	52.2	9.01	**48**	2	4	26.2	14.0	2.6	37.4	7.9
12	3	4	39.3	16.1	3.9	52.2	9.0	**49**	2	5	26.2	15.3	2.6	38.4	8.7
13	4	6	52.4	23.7	5.2	71.3	13.3	**50**	3	6	39.3	21.0	3.9	56.2	11.9
14	2	5	26.2	15.3	2.6	38.4	8.7	**51**	3	4	39.3	16.1	3.9	52.3	9.0
15	3	3	39.3	11.2	3.9	48.2	6.3	**52**	3	5	39.3	19.1	3.9	54.5	10.7
16	2	4	26.2	14.0	2.6	37.4	7.9	**53**	1	4	13.1	8.6	1.3	20.0	4.9
17	3	3	39.3	11.2	3.9	48.2	6.3	**54**	2	5	26.2	15.3	2.6	38.4	8.7
18	2	3	26.2	11.8	2.6	35.7	6.6	**55**	1	5	13.1	8.9	1.3	20.3	5.1
19	2	4	26.2	14.0	2.6	37.4	7.9	**56**	1	5	13.1	8.9	1.3	20.3	5.1
20	3	4	39.3	16.1	3.9	52.2	9.0	**57**	3	3	39.3	11.2	3.9	48.2	6.3
21	2	4	26.2	14.0	2.6	37.4	7.9	**58**	4	6	52.4	23.7	5.2	71.3	13.3
22	2	4	26.2	14.02	2.6	37.39	7.9	**59**	3	4	39.3	16.1	3.9	52.2	9.0
23	3	5	39.3	19.06	3.9	54.52	10.7	**60**	2	3	26.2	11.8	2.6	35.7	6.6
24	4	4	52.4	14.94	5.2	64.31	8.3	**61**	3	5	39.3	19.1	3.9	54.5	10.7
25	3	5	39.3	19.06	3.9	54.52	10.7	**62**	3	4	39.3	16.1	3.9	52.2	9.0
26	3	5	39.3	19.06	3.9	54.52	10.71	**63**	1	4	13.1	8.6	1.3	20.0	4.9
27	3	4	39.3	16.12	3.9	52.16	9.0	**64**	3	5	39.3	19.1	3.9	54.5	10.7
28	1	3	13.1	8.10	1.3	19.57	4.6	**65**	2	4	26.2	14.0	2.6	37.4	7.9
29	3	5	39.3	19.06	3.9	54.52	10.7	**66**	1	4	13.09	8.6	1.3	20.0	4.9
30	3	6	39.3	21.03	3.9	56.09	11.9	**67**	2	4	26.18	14.0	2.6	37.4	7.9
31	2	4	26.2	14.02	2.6	37.39	7.9	**68**	5	5	65.45	18.68	6.5	80.4	10.4
32	3	3	39.3	11.21	3.9	48.24	6.3	**69**	2	6	26.18	16.20	2.6	39.1	9.2
33	3	4	39.3	16.12	3.9	52.16	9.01	**70**	2	4	26.18	14.02	2.6	37.4	7.9
34	1	4	13.1	8.64	1.3	20.01	4.9	**71**	2	3	26.18	11.84	2.6	35.7	6.6
35	3	4	39.3	16.12	3.9	52.16	9.0	**72**	3	4	39.27	16.12	3.9	52.2	9.0
36	3	4	39.3	16.12	3.9	52.16	9.0	**73**	3	5	31.42	15.25	3.1	43.6	8.6
37	3	3	39.3	11.21	3.9	48.24	6.3								

Once the parameters characterizing the *fully-non stationary* zero-mean Gaussian process, $F_0(t)$, are estimated, through the application of Eq.(4.48), a set of one-hundred samples has been generated in such a way that the selected target accelerogram can be considered as one of its own samples. The *cumulative energy* function and the cumulative *zero-level up-crossing* function of the analysed accelerogram are compared with the corresponding mean value functions obtained by calculating the average of the results of the set of artificial accelerograms samples.

In particular, in Figure 4.9 a) the *cumulative energy* function of the analysed target accelerogram (solid red line) is compared to that obtained as the mean value of 100 samples (dotted black line). In the Figure 4.9 a) the *cumulative energy* function confidence interval, evaluated as the mean values plus/minus the corresponding standard deviation, are also plotted (dashed black lines). In Figure 4.9 b) the cumulative *zero-level up-crossing* function of target accelerogram (red line) is compared with the mean value function of 100 samples (dotted black line) and the *zero-level up-crossing* function confidence intervals (dashed lines).

In Figures 4.9 a) and 4.9 b), the shaded areas represent the envelope of the maximum and minimum values of the *cumulative energy* function and the cumulative *zero-level up-crossing* function of the 100 generated samples, respectively.

It can be observed that the mean *energy function* and *zero level up crossing* function are in a perfect agreement with the corresponding target functions.

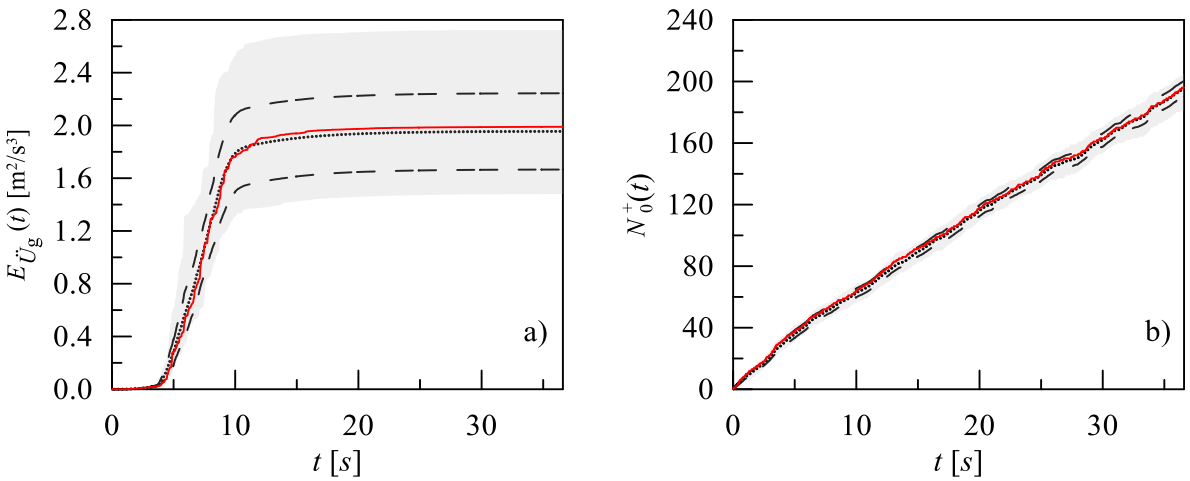

Figure 4.9 Comparison among the *cumulative energy* function a) and the *cumulative zero-level up-crossing* function b) of the selected accelerogram with statistics of the artificial ones: target function (red line); mean value function (black dotted line); mean value plus/minus standard deviation functions (black dashed lines); envelope of the maximum and minimum values of all samples (shaded area).

4.8.2 Spectrum compatibility

Then, to satisfy the spectrum compatibility in terms of *pseudo acceleration response spectrum* (*RSC*) or *Fourier Spectrum* (*FSC*), the iterative procedure has been applied four times and two different sets of one hundred accelerograms, have been obtained by Eq. (4.52).

Figure 4.10 illustrates the change assumed by different functions, as the *j* iterations vary, for the case in which the spectrum compatibility in terms of *pseudo acceleration response spectrum* (*RSC*) has been sought. Specifically, for the *4-iterations* (*RSC* model), in Figure 4.10 are reported the trends of: a) *total intensities*; b) *zero level up crossings*; c) *pseudo-acceleration response spectra*; d) percentage deviations between the target spectrum and those obtain as the mean values of the generated samples (*err* %); e) ratio between the mean squares values of the mean spectrum of the generated samples $\bar{S}^{(j-1)}(\omega,\zeta_0)$ and the target one $S^{(T)}(\omega,\zeta_0)$; f) *corrective power spectral density* functions.

Figure 4.11 shows a comparison between the time history of the target accelerogram and the *i*-th generated sample $\bar{F}_0^{(i)}(t)$, after 4 iterations, using the *pseudo acceleration response spectrum* compatibility (*RSC*) model and the *Fourier spectrum*-compatibility (*FSC*) model. In both cases the variation in amplitude of the generated samples appears to be preserved in the time domain.

In Figure 4.12, the mean value of the *cumulative energy* function $I_0(t)$ and the cumulative *zero level up crossing* function $N_0^+(t)$ of the generated samples, applying the *pseudo acceleration response spectrum* compatibility (*RSC*) model or the *Fourier spectrum* compatibility (*FSC*) model, after *4*-th iterations, have been compared with the trend of the target functions.

In Figures 4.13 and 4.14 the average *acceleration response spectrum Sa*(*T*) and the average *Fourier spectrum module* $|\mathbb{F}[\ddot{U}_g(t)]|$ of the two sets of artificial accelerograms, generated after 4 iterations by the *RSC* and *FSC* model, are compared with the corresponding target spectrum, respectively.

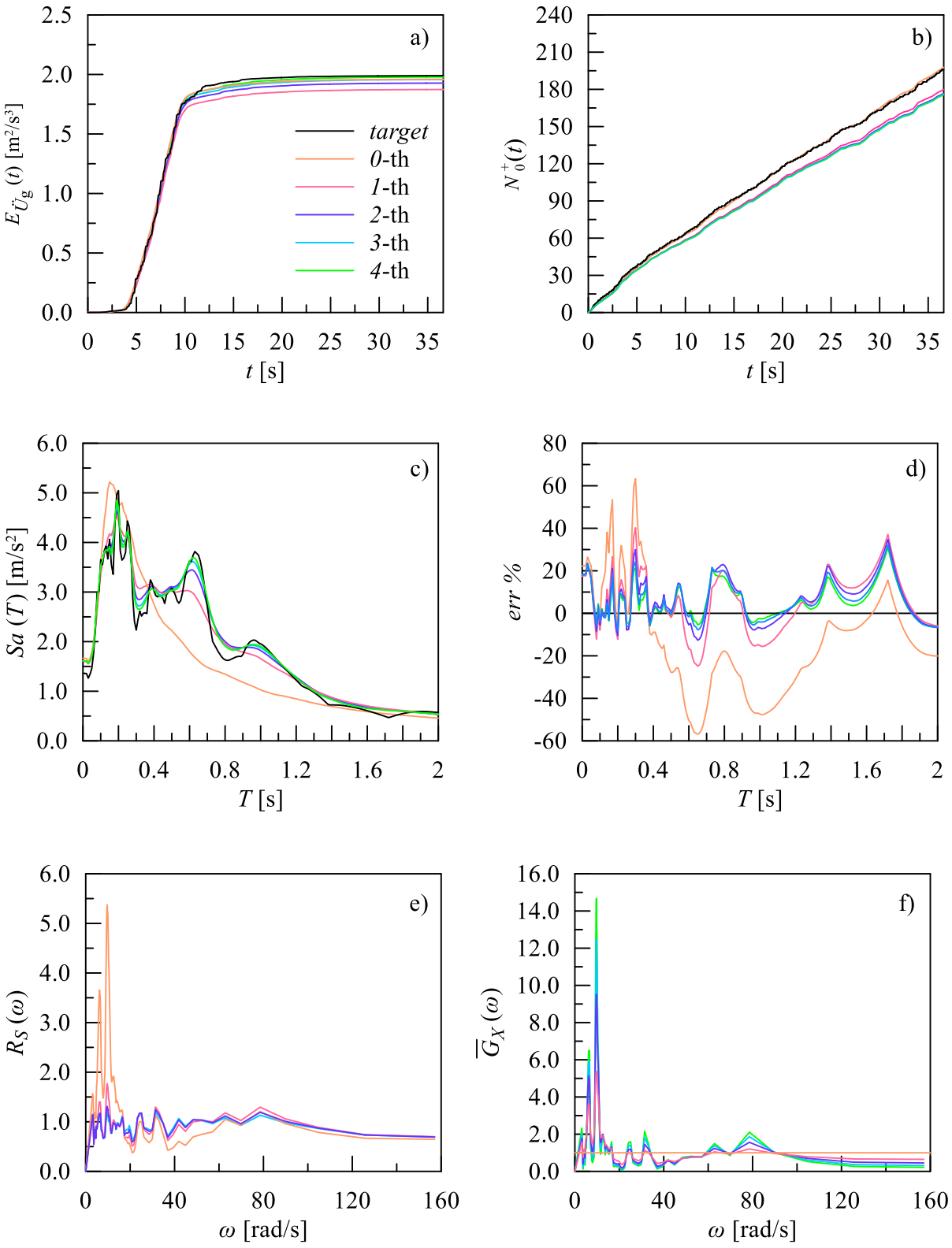

Figure 4.10 Comparison among: a) the target and the mean *cumulative energy* functions; b) *cumulative zero level up crossing functions*; c) *pseudo acceleration response spectra*; d) spectra deviations; e) spectra ratio; f) *corrective power spectral density functions*, for the *4-th* iterations (*RSC* model).

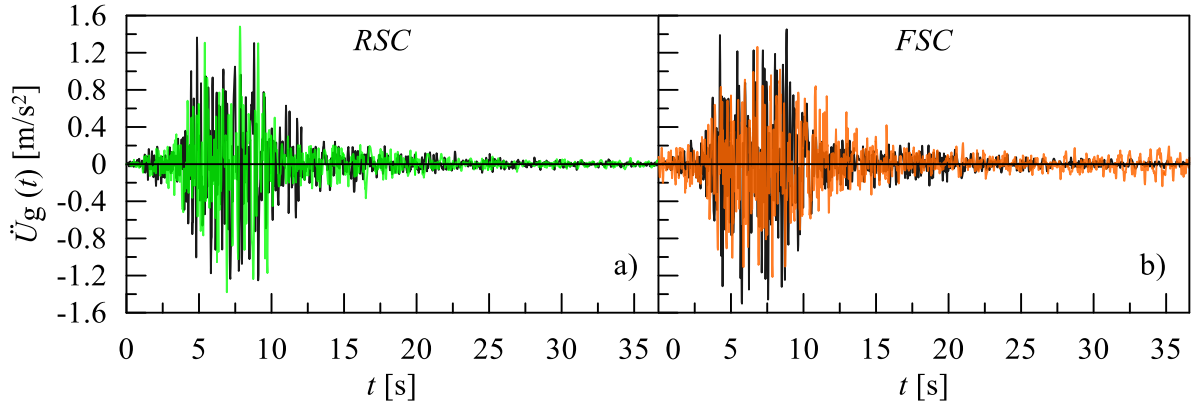

Figure 4.11: Comparison among the selected accelerogram (black line) and the corresponding *i*-th generated sample by the proposed fully non-stationary spectrum-compatible model, after 4 iterations: a) *pseudo acceleration response spectrum*-compatibility (*RSC*) model; b) *Fourier spectrum*-compatibility (*FSC*) model.

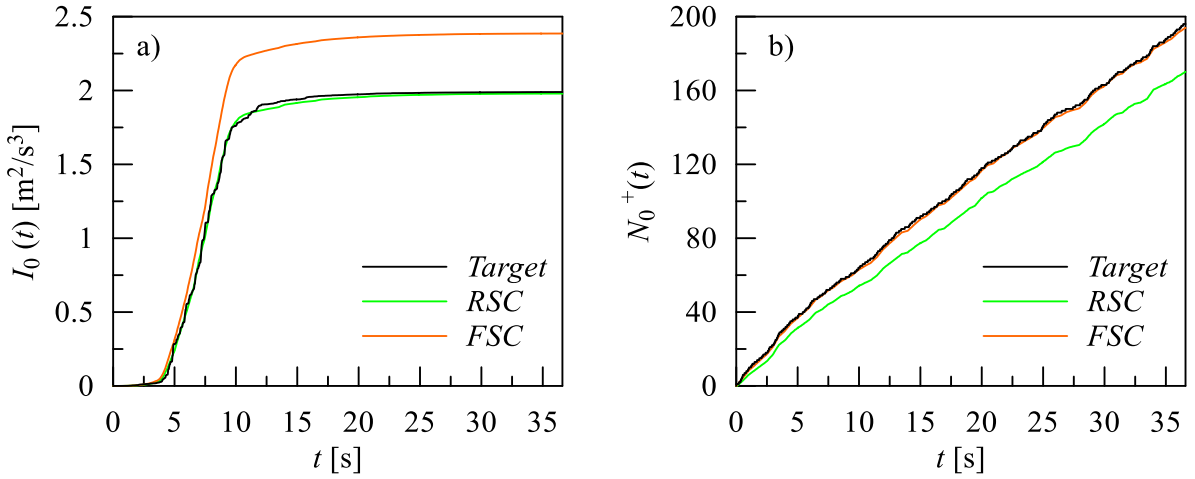

Figure 4.12 Comparison among the *cumulative energy* function a) or cumulative *zero level up crossing* function b) between the *target* accelerogram and the corresponding mean cumulative functions of the 100 samples, evaluated using *RSC* model and the *FSC* model, after *4*-th iterations.

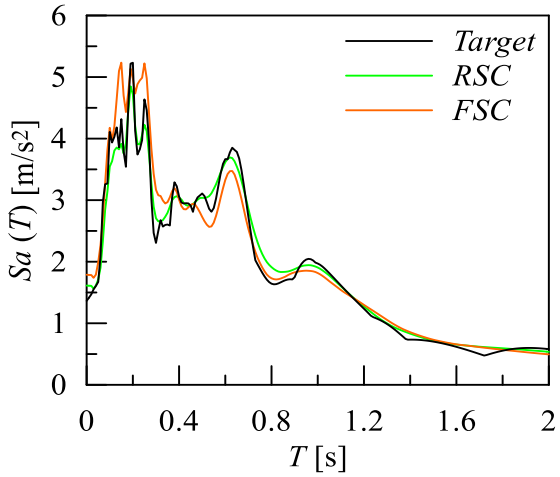

Figure 4.13 Comparison between the *pseudo acceleration response spectrum* and the mean *response spectra* of the 100 samples, evaluated using the *RSC* model and *FSC* model after *4*-th iterations.

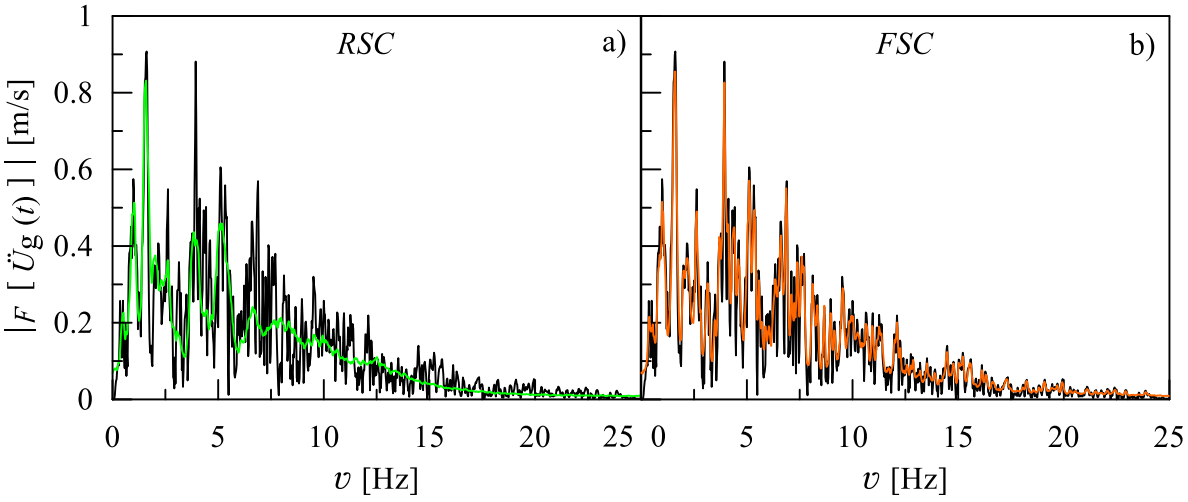

Figure 4.14 Comparison among the Fourier spectrum module of the selected accelerogram and the mean Fourier spectrum module of the generated sample, evaluated after 4 iterations by the: a) *RSC* model, b) *FSC* model.

From the observation of the results obtained in the time and frequency domain, it emerges that:

- the use of the *pseudo acceleration response spectrum*-compatibility (*RSC*) model leads to outcomes statistically closer to those of the target one in terms of *cumulative energy* function $E_{\ddot{U}_g}(t)$ and *pseudo-acceleration response spectrum Sa*(*T*) respect to the trends obtained by the application of the *FSC* model;
- the application of the Fourier-compatibility (*FSC*) model allows to obtain samples having an average *zero level up crossing function* $N_0^+(t)$ and Fourier spectrum closer to target one trend respect to those evaluated though the *RSC* model.

Chapter 5

Imprecise power spectral density function characterizing the strong motion of recorded accelerograms on rigid soil deposits

5.1 Introduction

In the framework of earthquake engineering, the recorded accelerograms must be critically analysed to predict the seismic behaviour of structures under future earthquakes. Recent studies have highlighted that, besides the amplitude, the spectral content of accelerograms also plays a key role in the seismic analysis of structural systems. The spectral content varies significantly from one accelerogram to another even for records belonging to the same soil category. It follows that to account for uncertainty about future seismic events, it is necessary to analyse an ensemble of recorded accelerograms and to perform statistical calculations. Although various authors recommend certain values of the parameters characterizing the above described models of the *power spectral density* (*PSD)* function (see sections 4.1-3), it has been shown that the parameters characterizing the *PSD* function are strongly influenced by the geotechnical characteristics of the soil deposits on which the seismic accelerograms are recorded [Genovese et al. 2019 a]. Consequently, different parameters such as Magnitude M_w, site-to-source distance R_{JB}, event depth z_{ip}, *Arias intensity* I_A [Arias 1970], *strong-motion duration* $t_{5\text{-}95}$ [Trifunac and Brady, 1975], *peak ground acceleration* (*PGA*), average shear wave velocity in the upper 30 meters $V_{S,30}$, etc., which are very often vaguely considered, must be taken into account for a correct modelling of the *PSD* function.

In 1977, Vanmarcke stated “In reality, of course, neither the seismic load effect nor the seismic resistance are perfectly predictable. Therefore, it makes sense to express structural performance under earthquake excitation of known intensity in probabilistic terms”. The uncertainties that affect the main parameters of strong ground motions have been highlighted

in two concomitant studies by Vanmarcke and Lai [1980 a,b], and Luco [1980]. After these pioneering studies, Lai [1982] computed the histograms of the main parameters of the Kanai-Tajimi *PSD* function by analysing 140 accelerograms recorded in western Unites States. Then, he fitted the histograms with analytical probability density functions. More recently, Zhang et al. [2017] developed an analytical approach for quantifying the uncertainty in stochastic process power spectrum estimates based on samples with missing data. There is a general consensus that, when available information on the various sources of uncertainty is incomplete or fragmentary, the use of non-probabilistic approaches [see e.g., Elishakoff 2000, Elishakoff and Ohsaki 2010] is more appropriate to retrieve reliable predictions of the safety level [see e.g., Sofi et al. 2020]. Thus, besides the inherently random nature of seismic excitation, epistemic uncertainties affecting the relevant *PSD* function should be taken into account resorting to non-probabilistic models. In this framework, recently, Faes et al. [2020] evaluated the bounds of the first excursion probability of linear structures subjected to imprecise seismic actions by using the *Directional Importance Sampling* method.

In this Chapter, in order to characterize epistemic uncertainties affecting the power spectrum of seismic acceleration, the spectral content in the *strong-motion time duration* of a large set of accelerograms, recorded on rigid soil deposits, is first analysed. The set of analysed accelerograms, downloaded from the Engineering Strong Motion database (ESM) [Luzi et al. 2020], is subdivided into two subsets following the international seismic code EC8 [2004] which recommends the use of two categories of spectra: Type 1 for areas of high and moderate seismicity (surface-wave magnitude $M_s > 5.5$), and Type 2 for areas of low seismicity ($M_s \leq 5.5$). All the selected accelerograms present an almost linear variation of the cumulative number of *zero-level up-crossings* within the *strong-motion time region*. This means that they do not exhibit sensible variation in time of the frequency content and can be reasonably regarded as samples of a zero-mean stationary Gaussian random process fully characterized by a suitable *PSD* function. Indeed, for a stationary random process the expected number of *zero-level up-crossings* is constant [see e.g., Lutes and Sarkani 2004]. The power spectrum model introduced in Chapter 4, that is able to catch the frequency content of recorded accelerograms, is herein adopted. This *PSD* function depends on the following parameters: the total number of both *zero-level up-crossing* and *peaks*, and the *total energy* in the *strong-motion time region*, which are different from one accelerogram to another [Muscolino et al. 2021]. In order to estimate the aforementioned parameters and

quantify the uncertainty affecting ground motion representation, the associated histograms are defined by analysing the spectral content of the selected accelerograms in the *strong-motion time region*. The *Chauvenet Criterion* [Chauvenet 1863, Barbato et al. 2011] is iteratively applied [Maples et al. 2018] to discard outliers from the set of accelerograms. As a final outcome of the statistical analysis of the selected accelerograms, the ranges of variability of the main parameters of the *PSD* function are determined. Thus, it is shown that a *PSD* function, representative of accelerograms recorded on soils with specific geotechnical characteristics, should be more appropriately modelled as a function of interval parameters [Moore 1966, Moore et al. 2009] whose ranges reflect the main properties of the excitation. A notable feature of the proposed model of the *imprecise PSD* function is that it depends on three interval parameters only.

In the context of structural safety assessment, the response level which has a specified probability, *p*, of not being exceeded during a given time interval should be evaluated. This quantity is referred to as fractile of order *p* of the structural response. Due to the imprecision of the assumed *PSD* function, both the *CDF* and the fractile of order *p* of the response have an interval nature [Muscolino et al. 2016]. Their lower bound (*LB*) and upper bound (*UB*) can be readily evaluated taking into account that the assumed model of the imprecise earthquake spectrum depends on three interval parameters only. Numerical results concerning a single-degree-of-freedom (*SDOF*) system under imprecise seismic excitation are presented.

5.2 Selected power spectral density function

It is well known that the seismic ground motion acceleration can be modelled as a sample of a *fully non-stationary* zero-mean Gaussian random process, evaluated as the product of a sample of a zero-mean stationary Gaussian process by a suitable time-frequency dependent modulating function. By analysing the frequency content of accelerograms recorded on rock soil, it can be observed that they exhibit almost constant *zero-level up-crossings* especially in the *strong motion duration*. It follows that the pertinent modulating function can be assumed as frequency independent unlike the one used for accelerograms recorded on soft soils. Moreover, in the *strong-motion time region* the modulating function can be reasonably assumed constant [Jennings et al. 1968, Iyengar and Iyengar 1969]. Since accelerograms recorded on rock soil are characterized by an almost constant frequency content and

amplitude, they can be modelled as samples of zero-mean stationary Gaussian processes. In this Chapter the unimodal one-sided *PSD* function, has been assumed proportional to the unimodal one-sided *PSD* function introduced in Chapter 4 (see Eq.(4.26)):

$$G_{\ddot{U}_g}(\omega)=\sigma_{\ddot{U}_g}^2\beta_0\left(\frac{\omega^2}{\omega^2+\omega_H^2}\right)\left(\frac{\omega_L^4}{\omega^4+\omega_L^4}\right)G_0^{(CP)}(\omega) \tag{5.1}$$

where ω_L and ω_H are the control frequencies of the second-order low pass and first-order high pass Butterworth filters, respectively, $G_0^{(CP)}(\omega)$ is a unimodal one-sided *PSD* function, which can be viewed as the linear combination of the displacement and velocity responses of a second-order oscillator subjected to two statistically independent Gaussian white noise processes [Conte and Peng 1997]:

$$G_0^{(CP)}(\omega)=\frac{\rho_0}{\pi}\left[\frac{1}{\rho_0^2+(\omega+\Omega_0)^2}+\frac{1}{\rho_0^2+(\omega-\Omega_0)^2}\right]. \tag{5.2}$$

In the previous equation, ρ_0 and Ω_0 are two free parameters. The first one is a circular frequency bandwidth, the second one is close enough to the predominant circular frequency of the filtered stationary process [Conte and Peng 1997]. In Eq. (5.1) $\omega_L=\Omega_0+0.8\rho_0$ is the frequency control, of a second-order low pass Butterworth filters, while $\omega_H=0.1\Omega_0$ is the frequency control of the first-order high pass Butterworth filters, [Muscolino et al. 2021]. Finally, in Eq.(5.1) the coefficient β_0:

$$\beta_0=\frac{2a_0b_0\left(\omega_H^4+\omega_L^4\right)}{\omega_L^3\left(c_0+d_0+e_0\right)} \tag{5.3}$$

depends on five parameters (a_0, b_0, c_0, d_0 and e_0), evaluated in closed form (see Eq.(4.29)) in such a way that the process $\ddot{U}_g(t)$ possesses variance $\mathrm{E}\left\langle\ddot{U}_g^2(t)\right\rangle=\sigma_{\ddot{U}_g}^2$ (where $\mathrm{E}\langle\cdot\rangle$ denoting the stochastic average operator). Notice that the variance, $\sigma_{\ddot{U}_g}^2$, of the zero-mean Gaussian stationary process characterized by the unimodal *PSD* function of Eq.(5.1), defines the *spectral intensity* of the process $\ddot{U}_g(t)$. Indeed, if I_0 is the *total intensity* of a recorded accelerogram, assumed as a generic sample of the stochastic process, the *cumulative expected energy* function of the process can be evaluated as [Saragoni and Hart 1973]:

$$E_{\ddot{U}_g}(t) = \int_0^t \mathrm{E}\left\langle \ddot{U}_g^2(\tau) \right\rangle \mathrm{d}\tau \equiv \int_0^t \sigma_{\ddot{U}_g}^2 \, \mathrm{d}\tau = \sigma_{\ddot{U}_g}^2 \, t. \tag{5.4}$$

It follows that the *total intensity* of a recorded accelerogram is given as:

$$I_0 \equiv E_{\ddot{U}_g}(T_D) = \int_0^{T_D} \sigma_{\ddot{U}_g}^2 \, \mathrm{d}\tau = \sigma_{\ddot{U}_g}^2 T_D \quad \Rightarrow \quad \sigma_{\ddot{U}_g}^2 = \frac{I_0}{T_D}. \tag{5.5}$$

The previous relationship shows that the variance, $\sigma_{\ddot{U}_g}^2$, of the zero-mean Gaussian stationary process, strictly related to the power spectrum intensity of the process, can be defined as a function of the *total intensity* of a recorded accelerogram, I_0, if the latter is considered as a sample of the stationary process itself.

5.3 Statistical analysis of accelerograms recorded on rigid soil deposits

5.3.1 Preliminary selection of recorded accelerograms

In order to estimate the parameters of the *PSD* function introduced in the previous section, a set of 270 corrected accelerograms is downloaded from the Engineering Strong Motion (*ESM*) database [Luzi et al. 2020]. All the selected accelerograms pertain to events mainly recorded in the European-Mediterranean regions and the Middle East, with *reference magnitude* $M_R \geq 4.0$, *epicentral distances* R_{epi}<100 km, *PGA*>0.05 g, *hypocentral depths* z_{ip}<49 km, *strong-motion time duration* $t_{5\text{-}95}$ [Trifunac and Brady 1975] and *Arias intensity* I_A<6 m/s [Arias 1970]. The value of the reference magnitude M_R is taken equal to the moment magnitude M_W if this information is provided by the *ESM* database otherwise, M_R equal to the local Magnitude M_L is assumed.

All the accelerograms used in this work are recorded at stations located on rock subsoil (grounds type A, according to EC8 [2004] classification), belonging mainly to the topographic class T_1 (flat surfaces, isolated slopes, or relief with inclination $i \leq 15^o$), with plane, slope or "not classified" morphological conditions.

The metadata of recording stations are stored in three main thematic levels based on the topographic features (*T*), geological features (*G*) and geophysical measurements (*S*). In most

cases the velocity profiles, used for calculation of the average share-wave velocity in the uppermost 30 meters $V_{S,30}$, are derived from a variety of surveys (*S*) such as down-hole, cross-hole and surface wave methods. When geophysical measures are not available, proxy relationships based on various descriptor or quantitative metrics of site conditions (surface geology, topographic slope, and geotechnical or geomorphic categories) have been used to estimate $V_{S,30}$ [Felicetta et al. 2016]. Among all the available recorded accelerograms present in the *ESM* database, only 270 horizontal acceleration time-histories, recorded by 66 stations in the frame 1979 - 2019, respect the required conditions.

Table 5-I lists the main characteristics of the recording stations: network and station code and descriptive metadata related to the soil characterization of the recording stations such as type of measurement to estimate the shear-wave velocity and $V_{S,30}$ value. The number of the components #c recorded by each station is also reported in Table 5-I.

The number of recording stations, divided according to the method used to estimate the shear-wave velocity $V_{S,30}$, is collected in the dark grey histogram of Figure 5.1 a). The corresponding number of components, recorded by the stations, are shown in the light grey histogram of Figure 5.1 a). Notice that in the *ESM* database, the $V_{S,30}$ values are available only when the metadata of recording stations are inferred from Topography (*T*) or Geophysical survey (*S*). For these two cases (*T* and *S*), the corresponding distribution of the $V_{S,30}$ values are reported in Figure 5.1 b).

Figure 5.2 shows the histograms of the distribution of the number of components as a function of a) reference magnitude M_R, b) focal mechanism, c) focal depth z_{ip} and d) epicentral distance R_{epi}. Most of the accelerograms (62.6 %) are characterised by a *normal* focal mechanism (*N*), while the events with *strike-slip* (*SS*) and *thrust* (*Th*) fault mechanisms are the 11.5 % and 7.8% of the total data, respectively. The focal mechanism information is not available (*n.a.*) for 49 (18.1 %) time histories.

In Table 5-II are summarized the main characteristics of the selected accelerograms, having $M_R > 5.5$, recorded by the stations listed in Table 5-I: date time, ground-motion component channel code (HNN/HNE or HGN/HGE: North-South/East-West components; HN2/HN3: orthogonal components but non-traditional orientations), *focal mechanism* F_P, *reference magnitude* M_R, *epicentral distance* R_{epi}, *site-source distance* R_{JB} [Jooner and Boore 1981] and d*epth* z_{ip}. The same above quantities, for the accelerograms having $M_R \leq 5.5$, are collected in Table 5-III.

Table 5-I Main characteristics of the recording stations. In the $V_{S,30}$ column the used symbols refer to: surface geology (*G*), topography (*T*) and geophysical survey (*S*).

#c	Network and Station Code	$V_{S,30}$ Estimation	$V_{S,30}$ [m/s]
1	4A.MI05	*G*	-
2	A.C1060	*T*	822
3	A.C1061	*T*	820
4	A.C1062	*T*	838
5	A.STBO	*G*	-
6	A.STRS	*G*	-
7	AC.SRN	*S*	1512
8	CL.AGRP	*G*	-
9	CL.ROD3	*G*	-
10	CR.A3062	*G*	-
11	ES.SADR	*G*	-
12	EU.ULA	*G*	-
13	GE.KARP	*T*	932
14	HI.ATH4	*S*	1020
15	HI.KRN1	*T*	850
16	HI.PAL1	*T*	803
17	HL.KARP	*T*	925
18	HL.KYPA	*S*	822
19	IT.0EQT	*G*	-
20	IT.0LAI	*G*	-
21	IT.ACC	*G*	-
22	IT.ANT	*S*	912
23	IT.ATN	*G*	-
24	IT.CESM	*G*	-
25	IT.FCC	*G*	-
26	IT.FORC	*G*	-
27	IT.GVD	*G*	-
28	IT.LPR	*G*	-
29	IT.MRM	*S*	1906
30	IT.MZZ	*G*	-
31	IT.NOT	*G*	-
32	IT.ORT	*G*	-
33	IT.RQT	*S*	805

#c	Network and Station Code	$V_{S,30}$ Estimation	$V_{S,30}$ [m/s]
34	IT.SPT1	*G*	-
35	IT.SRT	*S*	871
36	IT.SVN	*G*	-
37	IT.UST	*G*	-
38	IT.VGG	*G*	-
39	IT.VGL	*G*	-
40	IV.EMCN	*G*	-
41	IV.EVRN	*G*	-
42	IV.FEMA	*G*	-
43	IV.ILLI	*G*	-
44	IV.MDAR	*G*	-
45	IV.MMUR	*G*	-
46	IV.POFI	*G*	-
47	IV.RM03	*G*	-
48	IV.RM13	*G*	-
49	IV.T0912	*G*	-
50	IV.T1211	*G*	-
51	IV.T1212	*G*	-
52	IV.T1213	*G*	-
53	IV.T1215	*G*	-
54	IV.T1218	*G*	-
55	IV.T1242	*G*	-
56	IV.T1245	*G*	-
57	IV.T1256	*G*	-
58	KO.GMLD	*T*	816
59	KO.MASR	*T*	942
60	KO.SHAP	*T*	841
61	RA.PYAD	*G*	-
62	RA.PYBB	*S*	894
63	SI.CEY	*G*	-
64	SI.DRZN	*G*	-
65	TK.4101	*S*	827
66	YP.AC01	*T*	874

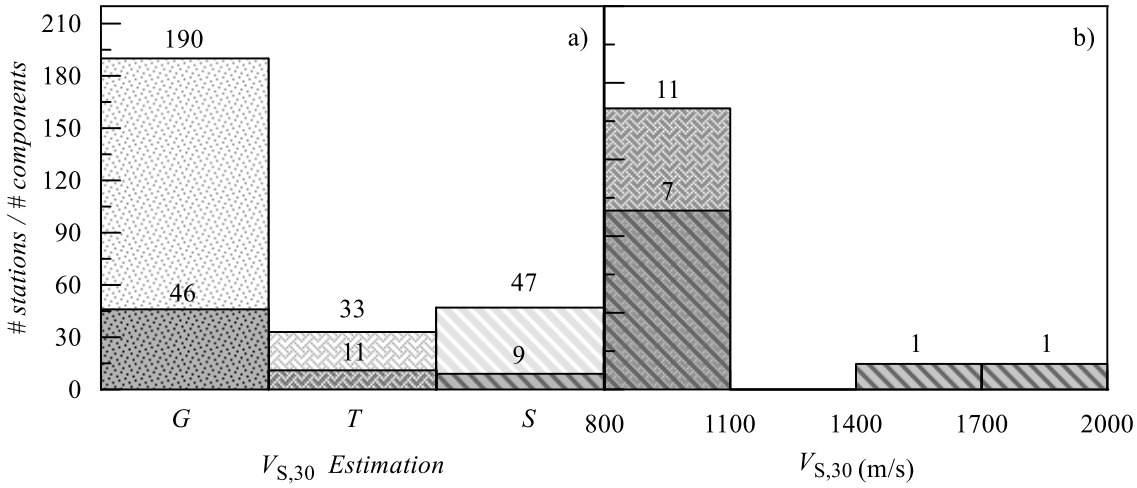

Figure 5.1 a) Distribution of: number of stations (dark grey histogram) and time histories (light grey histogram) as a function of site classification methodology; b) $V_{S,30}$ values inferred from topography (*T*) or a variety of surveys (*S*).

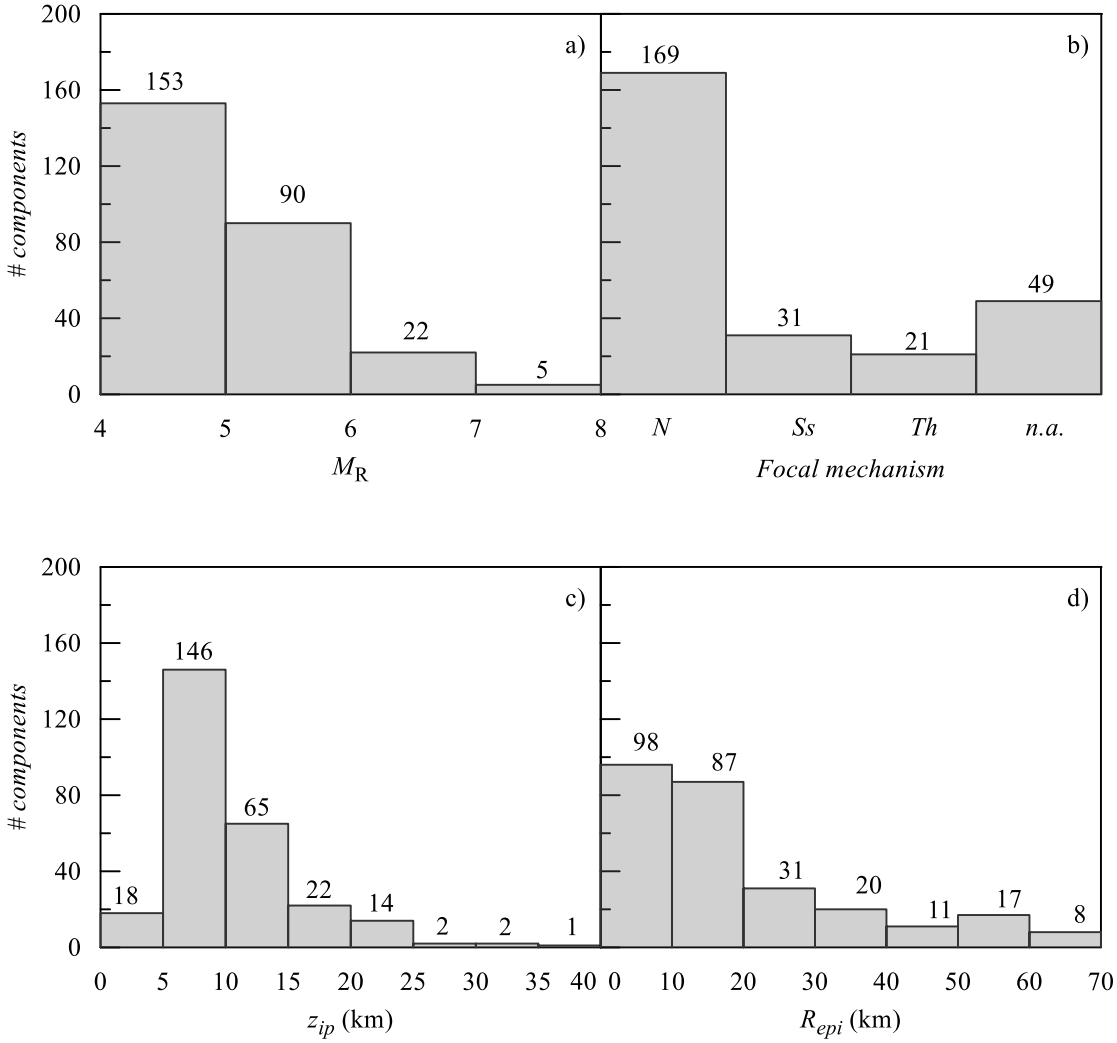

Figure 5.2 Distributions of: number of time histories versus a) reference magnitude; b) focal mechanism; c) focal depth and d) epicentral distance.

The values of the reference magnitude M_R versus the epicentral distance R_{epi} of the 270 horizontal acceleration time-histories are plotted in Figure 5.3 a). The black points provide the limits of near-field motions to far-field ones, according to [Vanmarcke 1979], while the black solid line is the interpolation of the aforementioned points. A particularization of the Figure 5.3 a) has been done in Figures 5.3 (b-d) considering only the horizontal acceleration time-histories recorded by station characterized by: b) geological features, c) topographic features or d) by geophysical surveys.

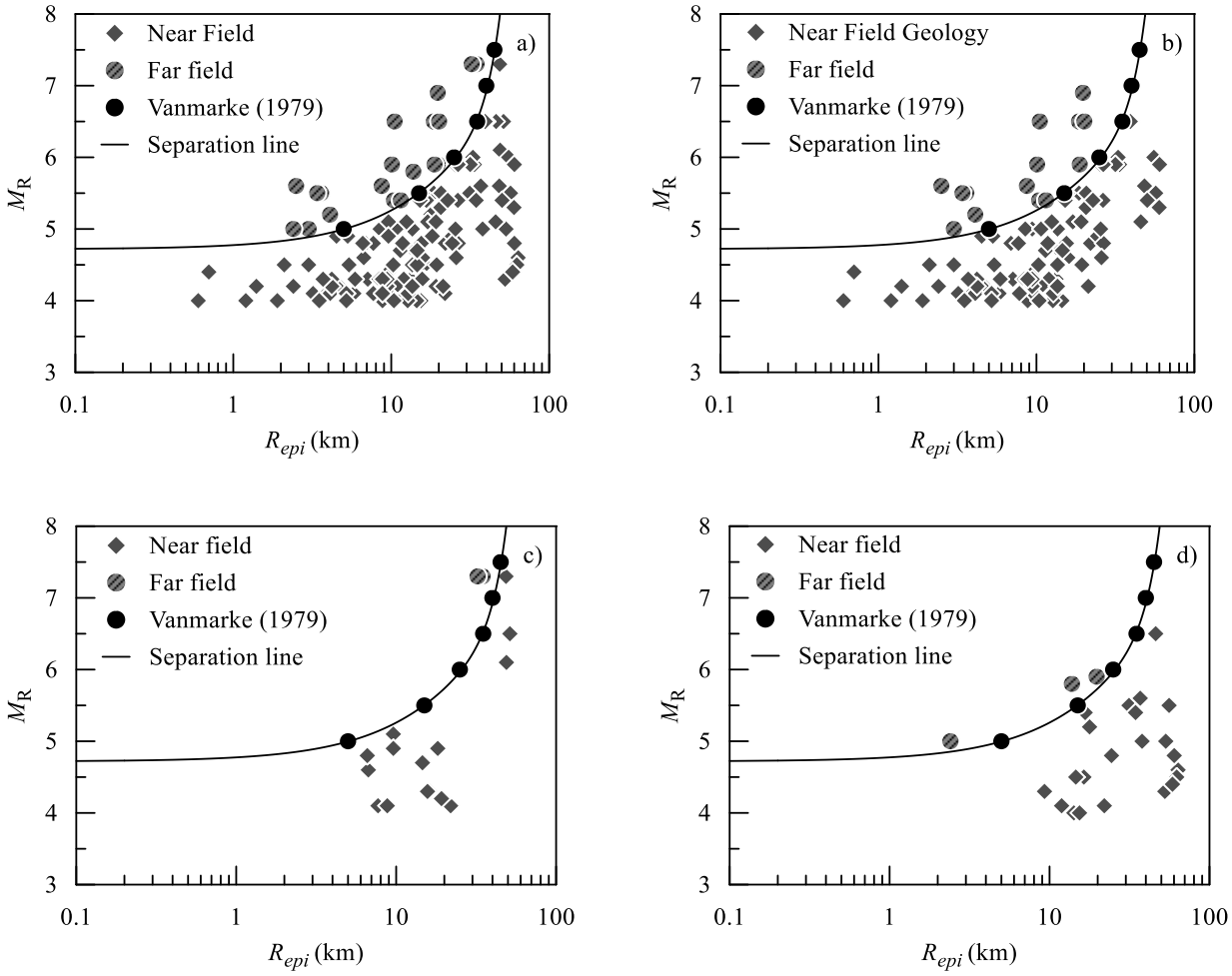

Figure 5.3 Reference magnitude versus epicentral distance for the selected acceleration time-histories: a) all the recording stations; b-d) recording stations classified by: b) geology, c) surface topography and d) geophysical measurements.

Table 5-II Main characteristics of the accelerograms having $M_R > 5.5$.

#	Station Code	date time	comp.	F_P	M_R	R_{epi} [km]	R_{JB} [km]	z_{ip} [km]
1	A.C1060	1999/11/12 16.57.19	HNE	*Ss*	7.3	48.6	21.12	10.4
2	A.C1061	1999/11/12 16.57.19	HNE/HNN	*Ss*	7.3	34.7	6.01	10.4
3	A.C1062	1999/11/12 16.57.19	HNE	*Ss*	7.3	32.3	3.62	10.4
4	EU.ULA	1979/04/15 06.19.41	HNE/HNN	*Th*	6.9	19.7	5.56	3.8
5	GE.KARP	2015/04/16 18.07.45	HNE/HNN	*Ss*	6.1	48.9	-	22.6
6	HI.ATH4	1999/09/07 11.56.49	HN2/HN3	*N*	5.9	19.7	14.03	9.4
7	HI.KRN1	1997/10/13 13.39.36	HN2/HN3	*Th*	6.5	51.4	-	13.3
8	HL.KARP	2015/04/16 18.07.45	HNE/HNN	*Ss*	6.1	48.9	-	22.6
9	IT.ACC	2016/10/26 19.18.06	HGE/HGN	*N*	5.9	25.4	18.05	7.5
		2016/10/30 06.40.18	HGE/HGN	*N*	6.5	18.6	2.19	9.2
10	IT.ANT	2016/10/30 06.40.18	HGN	*N*	6.5	46.1	2.19	9.2
11	IT.ATN	1984/05/07 17.49.43	HNE	*N*	5.9	10.1	12.28	20.5
12	IT.CESM	1997/10/14 15.23.09	HNE/HNN	*N*	5.6	8.7	6.2	6
13	IT.ORT	1984/05/07 17.49.43	HNE/HNN	*N*	5.9	33.6	32.79	20.5
14	IT.SRT	1990/12/13 00.24.26	HNE	*Ss*	5.6	36.9	24.59	5
15	IV.FEMA	2016/08/24 01.36.32	HNE/HNN	*N*	6	32.9	13.92	8.1
16	IV.MDAR	2016/10/30 06.40.18	HNE/HNN	*N*	6.5	40.1	27.05	9.2
		2016/10/26 19.18.06	HNE/HNN	*N*	5.9	31.6	20.08	7.5
		2016/08/24 01.36.32	HNN	*N*	6	55.4	35.47	8.1
17	IV.MMUR	2016/10/26 19.18.06	HNE/HNN	*N*	5.9	60.2	48.95	7.5
18	IV.T1211	2016/10/30 06.40.18	HNE/HNN	*N*	6.5	39.3	34.29	9.2
19	IV.T1212	2016/10/26 19.18.06	HNE/HNN	*N*	5.9	18.8	12.06	7.5
		2016/10/30 06.40.18	HNE/HNN	*N*	6.5	10.5	8.77	9.2
20	IV.T1215	2016/10/30 06.40.18	HNE/HNN	*N*	6.5	20.1	18.61	9.2
21	IV.T1218	2016/10/26 19.18.06	HNE/HNN	*N*	5.9	26.5	18.83	7.5

Table 5-III Main characteristics of the accelerograms having $M_R \leq 5.5$.

#	Station Code	date time	comp.	F_P	M_R	R_{epi} [km]	R_{JB} [km]	z_{ip} [km]
1	4A.MI05	2009/04/07 17.47.37	HNE/HNN	*N*	5.5	3.6	1.89	17.1
		2009/04/09 00.52.59	HNE/HNN	*N*	5.4	26.4	23.43	11
		2009/04/23 15.14.08	HNE	*N*	4.1	5.8	-	10.3
2	A.STBO	2002/04/25 17.41.22	HN2/HN3	-	4.8	6.9	-	10
3	A.STRS	1990/12/16 15.45.40	HNE	*Ss*	5.4	50.4	-	28.3
4	AC.SRN	2016/10/16 00.48.19	HNE/HNN	-	4.6	63.6	-	10
		2016/10/19 21.23.57	HNE/HNN	-	4.3	52.6	-	10
		2016/10/16 00.09.59	HNE/HNN	-	4.5	62.4	-	10
		2016/10/15 20.14.48	HNE/HNN	*Th*	5.5	55.9	-	22
		2016/10/16 02.21.02	HNE/HNN	*Th*	5	53.3	-	19.4
		2016/10/16 03.40.20	HNE/HNN	*Th*	4.8	60.2	-	20.4
5	CL.AGRP	2016/10/11 11.48.30	HNE	*N*	4.3	7.1	-	10.9
6	CL.ROD3	2016/10/11 11.48.30	HNE/HNN	*N*	4.3	13.3	-	10.9
7	CR.A3062	1990/04/03 22.02.37	HNN	-	4.8	22	-	10
		1990/11/27 04.37.57	HNE/HNN	*Th*	5.5	56.9	-	10
		1990/11/27 04.51.36	HNE/HNN	-	5.3	59.9	-	10
8	ES.SADR	1994/01/04 08.03.15	HNN	-	4.9	24.4	-	16
9	EU.ULA	1979/04/09 02.10.21	HNE	*Th*	5.4	10.4	-	7.1
10	HI.PAL1	1994/04/10 19.46.20	HN3	-	4.6	6.7	-	18
11	HL.KYPA	1993/03/05 06.55.08	HN3	*Th*	5.2	17.8	-	38.8

		1996/10/09 09.46.27	HN2/HN3	-	4.4	58.7	-	5
12	IT.0EQT	2013/06/30 14.40.08	HGE/HGN	*N*	4.5	3	2.09	6.1
13	IT.0LAI	2012/10/25 23.05.24	HGE	*N*	5	9.4	-	9.7
14	IT.ACC	2016/08/24 17.46.09	HGE	*N*	4.2	4.7	-	10.3
		2016/10/26 17.10.36	HGE/HGN	*N*	5.4	22.1	19.17	8.1
		2016/10/30 07.13.06	HGN	-	4.2	1.4	-	10.6
		2016/11/12 14.43.33	HGE/HGN	*N*	4.1	3.9	-	9.8
		2017/01/18 09.25.42	HGN	*N*	5.1	17	14.6	10
		2017/01/18 10.14.12	HGN	*N*	5.5	18.6	5.45	9.6
15	IT.CESM	1997/10/14 23.23.28	HNE/HNN	-	4.2	4.5	-	5.1
		1998/03/21 16.45.09	HNN	*N*	5	3	0.65	5
16	IT.FCC	2016/09/03 10.18.51	HGE/HGN	*Ss*	4.3	12	-	8.3
		2016/10/30 12.07.00	HGE/HGN	*N*	4.5	13.7	12.29	9.7
		2016/10/31 03.27.40	HGN	*N*	4	8.8	-	10.6
		2016/11/01 07.56.39	HGN	*N*	4.8	26.6	25.28	8.3
		2016/11/12 14.43.33	HGE/HGN	*N*	4.1	4.1	-	9.8
17	IT.FORC	1997/10/12 11.08.35	HNE/HNN	*N*	5.2	4.1	1.53	4.8
18	IT.GVD	2004/11/24 22.59.38	HNN	*T*	5	13.6	11.92	5.4
19	IT.LPR	2010/08/16 12.54.47	HNN	*Ss*	4.7	14	12.9	13.5
20	IT.MZZ	2006/02/27 04.34.01	HNN	*N*	4.4	9.6	-	9.2
21	IT.RQT	2016/09/03 10.18.51	HGE/HGN	*Ss*	4.3	9.3	-	8.3
		2016/10/26 17.10.36	HGE/HGN	*N*	5.4	16.7	12.82	8.1
		2016/10/26 21.42.01	HGE/HGN	*N*	4.5	16.4	14.88	9.9
		2016/10/27 03.19.27	HGE/HGN	*N*	4	14.2	-	9.2
		2016/10/30 13.34.54	HGE/HGN	*N*	4.1	11.9	-	9.6
		2016/10/31 07.05.45	HGE	*N*	4	15.4	-	9.5
		2016/11/01 07.56.39	HGE/HGN	*N*	4.8	24.4	-	8.3
		2017/01/18 10.14.12	HGE/HGN	*N*	5.5	31.4	16.55	9.6
		2017/01/18 10.25.26	HGE/HGN	*N*	5.4	34.5	24.59	9.4
		2017/01/18 11.07.39	HGE/HGN	*N*	4.1	22	22.8	10.7
		2017/01/18 13.33.37	HGE/HGN	*N*	5	37.9	-	9.5
22	IT.SPT1	2013/12/29 17.08.43	HGE/HGN	*N*	5	8.5	-	20.4
		2014/01/20 07.12.40	HGE	*N*	4.2	10.7	-	17.2
23	IT.SVN	2018/12/26 02.19.17	HGE/HGN	*Ss*	4.9	4.5	-	1
24	IT.UST	2016/12/11 12.54.52	HGE/HGN	-	4.3	4.2	-	8.5
		2017/01/18 09.25.42	HGN	*N*	5.1	45.8	-	10
		2017/01/18 10.25.26	HGN	*N*	5.4	50.3	24.59	9.4
		2018/04/10 03.11.31	HGE/HGN	*N*	4.6	15.8	14.86	8.1
25	IT.VGL	1980/06/07 18.35.01	HNE/HNN	*N*	4.6	25.8	-	30
		2013/06/21 10.33.56	HGE/HGN	*N*	5.1	12.5	10.55	7
		2013/06/23 15.01.33	HGN	*N*	4.4	9.6	-	9.2
26	IV.EMCN	2018/12/24 16.50.12	HNE	-	4.3	8.4	-	2.2
27	IV.EVRN	2018/12/26 02.19.17	HNN	*Ss*	4.9	5.3	-	1
28	IV.FEMA	2017/04/27 21.19.43	HNN	*N*	4	1.2	-	7.9
		2017/04/27 21.16.59	HNN	*N*	4	0.6	-	7.9
		2017/02/03 04.10.05	HNN	*N*	4.2	4.2	-	7.1
		2016/12/11 12.54.52	HNE	-	4.3	8.4	-	8.5
		2016/10/30 12.07.00	HNE/HNN	*N*	4.5	13.5	12.46	9.7
		2016/10/26 17.10.36	HNE/HNN	*N*	5.4	11.5	8.49	8.1
		2016/08/24 02.33.29	HNE/HNN	*N*	5.3	20.6	17.54	8
29	IV.ILLI	2010/08/16 12.54.47	HNN	*Ss*	4.7	11.4	10.32	13.5
30	IV.POFI	2013/02/16 21.16.09	HNE	*N*	4.8	11.8	9.97	17.1
31	IV.RM03	2009/04/07 17.47.37	HNE/HNN	*N*	5.5	3.4	0.26	17.1
32	IV.RM13	2009/04/07 17.47.37	HNE/HNN	*N*	5.5	15.6	12.29	17.1
33	IV.T0912	2013/06/23 15.01.33	HNE/HNN	*N*	4.4	0.7	-	9.2

		2013/06/30 14.40.08	HNE/HNN	*N*	4.5	2.1	0.8	6.1
34	IV.T1212	2016/10/26 17.10.36	HNN	*N*	5.4	15.2	12.27	8.1
		2016/10/26 21.42.01	HNE	*N*	4.5	14	12.95	9.9
		2016/10/30 11.58.17	HNE/HNN	*N*	4	10.4	-	9.8
		2016/10/31 03.27.40	HNE/HNN	*N*	4	3.5	-	10.6
35	IV.T1213	2016/08/25 03.17.16	HNE/HNN	*N*	4.3	5.9	-	9
		2016/10/30 07.07.54	HNE/HNN	-	4.1	5.2	-	10.2
		2016/10/30 11.58.17	HNE/HNN	*N*	4	14.5	-	9.8
		2016/10/30 12.07.00	HNE/HNN	*N*	4.5	13.6	12.77	9.7
		2016/10/30 13.34.54	HNE/HNN	*N*	4.1	9.6	-	9.6
		2016/10/31 03.27.40	HNE/HNN	*N*	4	5.2	-	10.6
		2016/10/31 07.05.45	HNN	*N*	4	12.7	-	9.5
36	IV.T1218	2017/01/18 19.32.32	HNE/HNN	*N*	4.2	13.8	-	10.9
		2017/01/18 13.33.37	HNN	*N*	5	25.5	23.5	9.5
		2017/01/18 11.07.39	HNN	*N*	4.1	12.8	-	10.7
		2017/01/18 10.14.12	HNE/HNN	*N*	5.5	20.7	8.5	9.6
		2017/01/18 09.25.42	HNE/HNN	*N*	5.1	19.2	17.1	10
		2016/10/31 03.27.40	HNE	*N*	4	10.4	-	10.6
		2016/10/30 12.07.00	HNE	*N*	4.5	19.4	-	9.7
		2016/10/30 07.13.06	HNE	-	4.2	9.4	-	10.6
		2016/10/30 07.07.54	HNE/HNN	-	4.1	7.8	-	10.2
		2016/10/26 17.10.36	HNE/HNN	*N*	5.4	22.8	19.66	8.1
37	IV.T1242	20160825.031716	HNN	*N*	4.3	9.4	-	9
		20160903.101851	HNN	*Ss*	4.3	3.7	-	8.3
38	IV.T1245	2016/10/26 21.42.01	HNE	*N*	4.5	5.4	3.8	9.9
		2016/11/01 07.56.39	HNN	*N*	4.8	15.5	14.22	8.3
39	IV.T1256	2016/11/01 07.56.39	HNN	*N*	4.8	7.7	6.07	8.3
		2016/11/03 00.35.01	HNN	*N*	4.7	14.6	12.42	8.1
40	KO.GMLD	2019/08/08 08.39.09	HNN	-	4.8	6.6	-	10
41	KO.MASR	2014/09/04 03.53.00	HNE/HNN	*Th*	4.1	7.7	-	12.7
42	KO.SHAP	2014/07/15 12.25.52	HNE/HNN	-	4.1	21.9	-	9.3
		2015/09/22 06.25.04	HNE/HNN	-	4.3	16.2	-	11.9
		2015/09/22 07.11.11	HNE/HNN	-	4.3	15.7	-	9
		2015/10/13 23.18.10	HNE/HNN	*N*	4.2	19.2	-	10.2
43	RA.PYAD	2008/07/16 20.33.31	HNE/HNN	-	4.2	13.6	-	4.2
44	RA.PYBB	2006/11/17 18.19.50	HNE/HNN	-	4.5	14.6	-	0.9
45	SI.CEY	1995/05/22 11.16.54	HNE/HNN	-	4.2	21.3	-	19.9
46	SI.DRZN	1998/05/06 02.52.59	HNE	-	4.3	8.8	-	5.6
47	YP.AC01	2014/11/08 23.15.43	HNE/HNN	*Ss*	5.1	9.6	7.57	18
		2014/11/07 07.41.35	HNE/HNN	*Th*	4.9	9.6	-	18
		2014/02/21 15.18.25	HNE	*N*	4.1	8.8	-	15.9
		2014/02/15 07.31.16	HNE	*Th*	4.9	18.2	-	25.3
		2014/02/06 19.20.59	HNE	*Th*	4.7	14.6	13.67	16.4

Among all the 270 accelerograms that fulfil the required conditions, only those that present an almost linear variation of the cumulative number of *zero-level up-crossings* $N_0^+(t)$ into the *strong-motion time region* $t_{5\text{-}95}$, are considered. This means that in such time region the selected accelerograms do not present a sensible variation in time of the frequency content and can be satisfactorily assumed as samples of a zero-mean stationary Gaussian process. Figure 5.4 a) displays the normalized *zero-level up crossing functions* of the 270

accelerograms, $N_0^+(t)/N_0^+(t_{5-95,i})$, into the *strong-motion time region* versus the normalized time $t/t_{5-95,i}$, with $t_{5-95,i}$ denoting the *strong-motion time duration* of the *i*-th record, together with the bisector of the graph. Figure 5.4 b) shows the absolute maximum residual values of the *i*-th accelerogram, $|e_i|$, (symbols) calculated as the difference between the absolute maximum values of the *zero-level up-crossing functions* $N_{0,i}^+(t)$, of the *i*-th accelerogram, and the bisector of the graph. The mean-value $\mu_{|e_i|}$ of $|e_i|$ (solid line), together with the mean-value plus the standard deviation $\mu_{|e_i|}+\sigma_{|e_i|}$ (dashed line), are also reported in Figure 5.4 b). All the accelerograms having absolute maximum residual values $|e_i|$ that exceed the confidence interval given by the mean-value plus the standard deviation (dashed grey line in Figure 5.4 b) are discarded. Consequently, the number of accelerograms considered in the analysis changes from 270 to 229.

According to [EC8 2004], which suggests the use of the Type 1 spectrum for areas with high-medium seismicity (M_R>5.5) and the Type 2 spectrum for areas with low seismicity (M_R≤5.5), the set of 229 accelerograms is subdivided into two subsets composed by 44 and 185 time-histories, respectively.

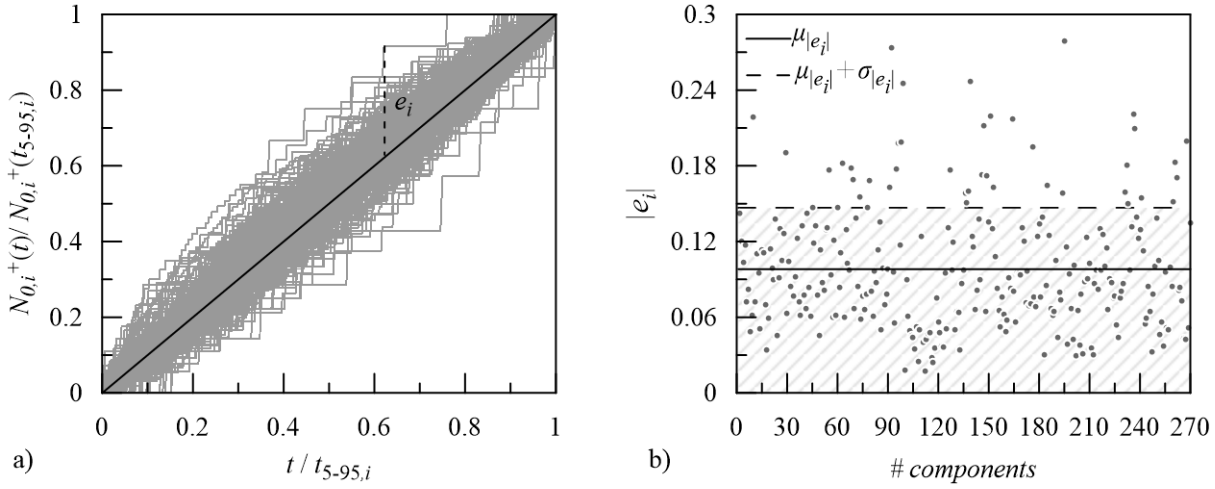

Figure 5.4 a) Normalized zero level up-crossing functions of the selected accelerograms with respect to the strong motion time duration (grey lines) together with the bisector of the graph (black line); b) Absolute maximum residual values together with its mean value (solid line) and the mean value plus standard deviation (dashed line)**.**

5.3.2 Statistical analysis of the main parameters of the PSD function

Then, a further selection of the accelerograms is performed by analysing the light grey histograms in Figures 5.5 and 5.6 , associated with the following parameters: *i*) *strong-motion time duration* $t_{5\text{-}95}$; *ii*) frequency of *zero-level up-crossings* $\upsilon_N = N_0^+ / t_{5\text{-}95}$; *iii*) frequency of the *peaks* $\upsilon_P = P_0 / t_{5\text{-}95}$; *iv*) variance $\sigma_{\ddot{U}_g}^2 = I_0 / t_{5-95}$; *v*) predominant circular frequency Ω_0, *vi*) circular frequency bandwidth ρ_0.

Afterwards, the *Chauvenet's Criterion* [Chauvenet 1863, Barbato et al. 2011] is iteratively applied [Maples et al. 2018] to the selected parameters. So operating, the outliers from both subsets of accelerograms are discarded.

The *Chauvenet's Criterion* works by creating an acceptable band of data around the mean, specifying any values that fall outside that band should be eliminated. The application of the *Chauvenet's Criterion* requires the following steps:

1) calculate the mean μ and standard deviation σ of the observed set of data;

2) evaluate the absolute value of the difference between each data x_i and the mean divided by the standard deviation:

$$\tau_i = \frac{x_i - \mu}{\sigma} \tag{5.6}$$

3) if $n \cdot \left(2 \int_{\mu+\tau_i}^{\infty} p(x)\,\mathrm{d}x \right) < 0.5$ then reject x_i and repeat the step 1 and 2, being n the number of data and $p(x)$ the probability density function of a normal distribuited set of data with expected value μ and variance σ^2:

$$p(x) = \frac{1}{\sigma\sqrt{2\pi}} \mathrm{e}^{\left(-\frac{1}{2} \frac{(x-\mu)^2}{\sigma^2} \right)} \tag{5.7}$$

4) repeat steps 1 and 2 until the number of complying accelerograms remain stable.

The histograms of the analysed quantities after the iterative application of the *Chauvenet's Criterion* are also plotted in Figures 5.5 and 5.6 for the two subsets of accelerograms (dark grey histograms).

After the iterative application of the *Chauvenet's Criterion*, the number of the remaining accelerograms for the Type 1 and Type 2 subsets reduces to 20 and 107. The station code,

date time, and the ground-motion component channel code (HNN/HNE or HGN/HGE: North-South/East-West components; HN2/HN3: orthogonal components but non-traditional orientations) of the remaining accelerograms are reported Tables 5-IV and 5-V.

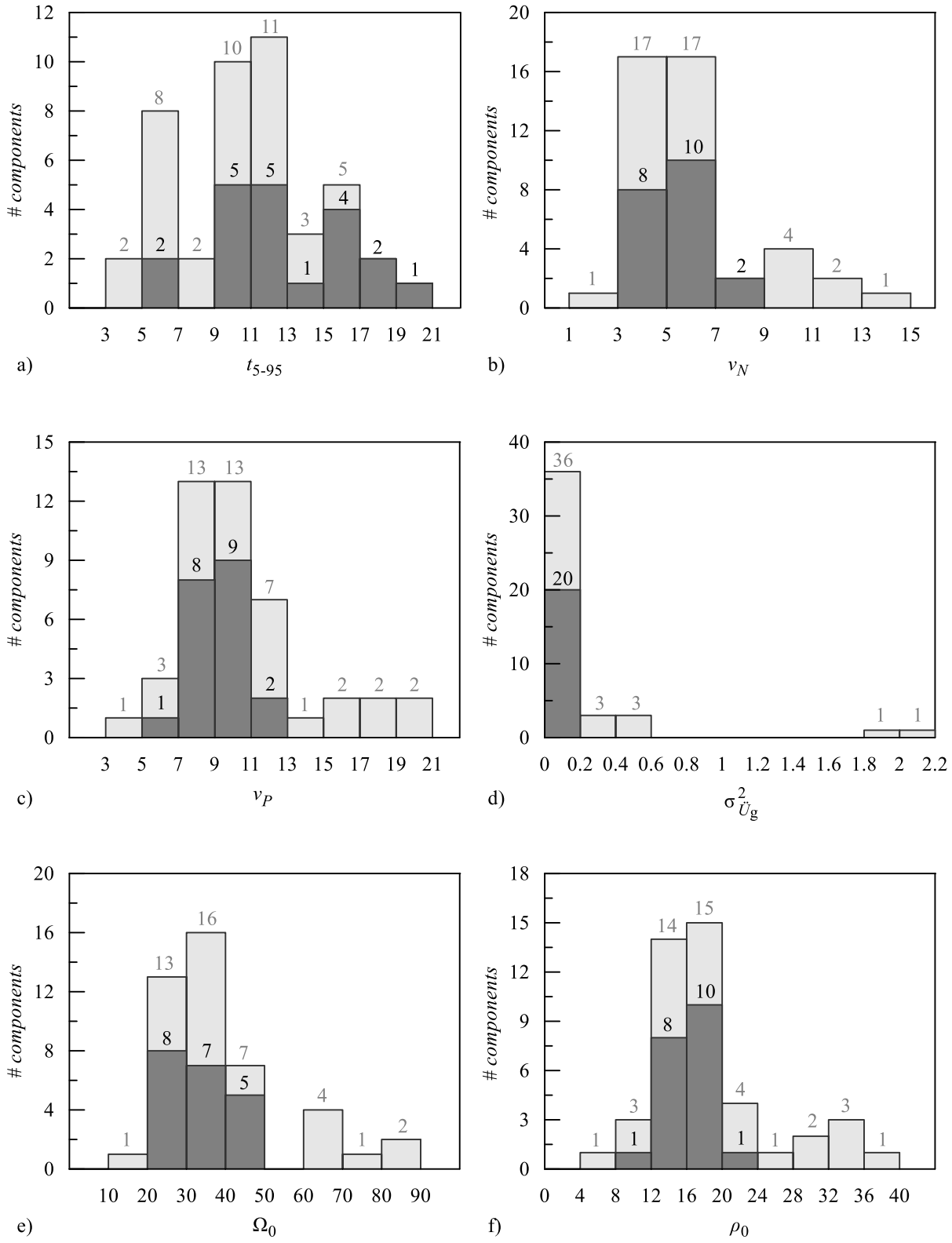

Figure 5.5 Distribution of the main characteristics of the accelerograms with M_R>5.5 (Type 1) before (*light grey histogram*) and after (*dark grey histogram*) the iterative application of the *Chauvenet's Criterion* in terms of: a) *strong-motion time duration*; b) frequency of *zero-level up-crossings*; c) frequency of the *peaks*; d) variance; e) predominant circular frequency; and f) circular frequency bandwidth.

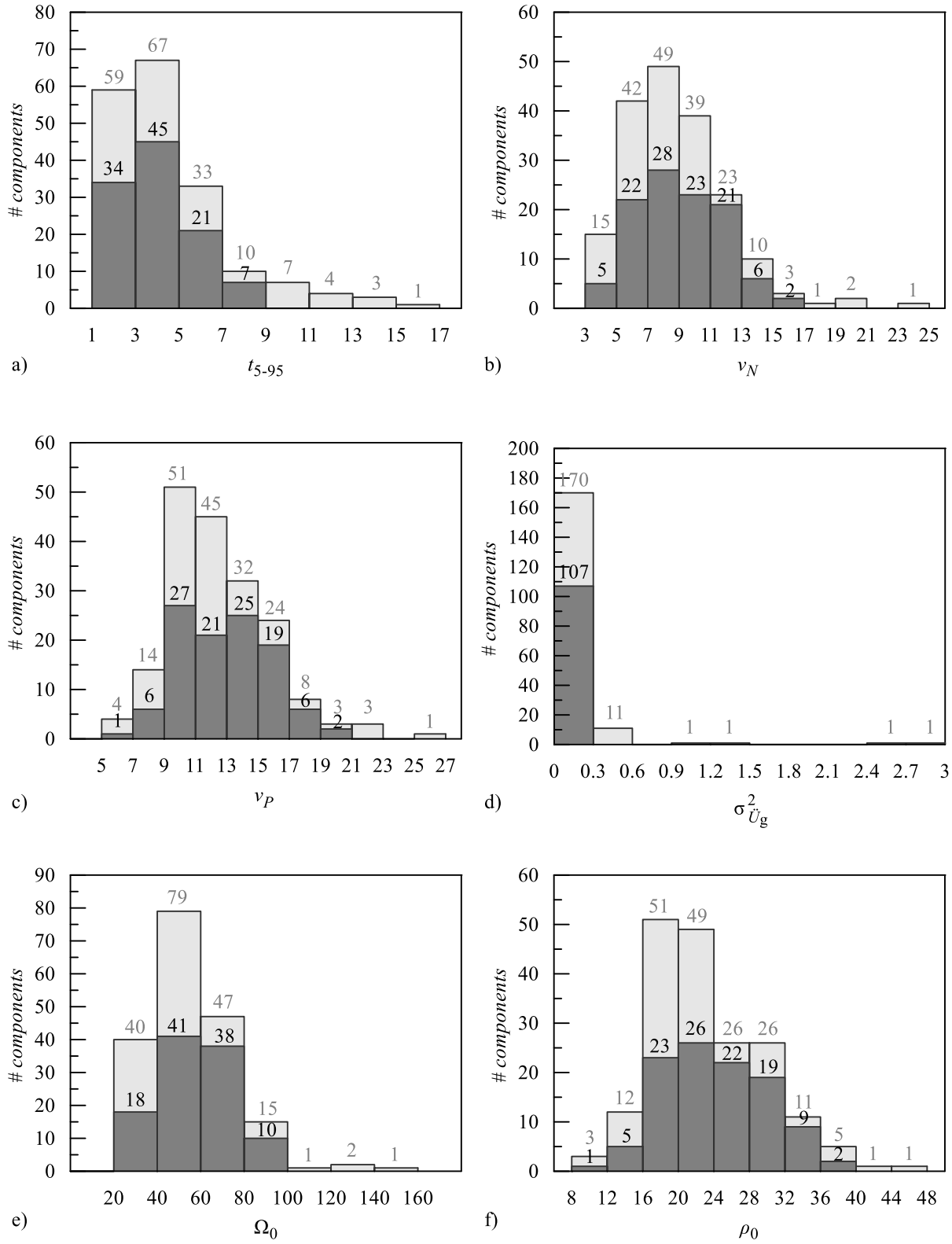

Figure 5.6 Distribution of the main characteristics of the accelerograms with $M_R \leq 5.5$ (Type 2) before (*light grey histogram*) and after (*dark grey histogram*) the iterative application of the *Chauvenet's Criterion* in terms of: a) *strong-motion time duration*; b) frequency of *zero-level up-crossings*; c) frequency of the *peaks*; d) normalized *total intensity*; e) predominant circular frequency; and f) frequency bandwidth.

Table 5-IV Main recording information of the remaining accelerograms with M_R>5.5 (Type 1) after the application of the *Chauvenet's Criterion*.

#	station code	date time	comp.	#	station code	date time	comp.
1	A.C1060	1999/11/12 16.57.19	HNE	**7**	IT.ACC	2016/10/26 19.18.06	HGE/HGN
2	A.C1061	1999/11/12 16.57.19	HNE	**8**	IT.ORT	1984/05/07 17.49.43	HNE/HNN
3	GE.KARP	2015/04/16 18.07.45	HNE/HNN	**9**	IV.T1211	2016/10/30 06.40.18	HNE/HNN
4	HI.ATH4	1999/09/07 11.56.49	HN2/HN3	**10**	IV.T1212	2016/10/26 19.18.06	HNE/HNN
5	HI.KRN1	1997/10/13 13.39.36	HN2/HN3	**11**	IV.T1218	2016/10/26 19.18.06	HNE/HNN
6	HL.KARP	2015/04/16 18.07.45	HNE/HNN				

Table 5-V Main recording information of the remaining accelerograms with M_R≤5.5 (Type 2) after the application of the *Chauvenet's Criterion*.

#	station code	date time	comp.	#	station code	date time	comp.
1	4A.MI05	2009/04/09 00.52.59	HNE/HNN	**21**	IT.VGL	1980/06/07 18.35.01	HNE
		2009/04/23 15.14.08	HNE	**22**	IV.FEMA	2017/02/03 04.10.05	HNN
2	A.STBO	2002/04/25 17.41.22	HN2/HN3			2016/12/11 12.54.52	HNE
3	A.STRS	1990/12/16 15.45.40	HNE			2016/10/30 12.07.00	HNE/HNN
4	CL.AGRP	2016/10/11 11.48.30	HNE	**23**	IV.RM03	2009/04/07 17.47.37	HNE/HNN
5	CL.ROD3	2016/10/11 11.48.30	HNE	**24**	IV.RM13	2009/04/07 17.47.37	HNE/HNN
6	CR.A3062	1990/11/27 04.51.36	HNE/HNN	**25**	IV.T1212	2016/10/30 11.58.17	HNE/HNN
7	ES.SADR	1994/01/04 08.03.15	HNN			2016/10/31 03.27.40	HNE/HNN
8	EU.ULA	1979/04/09 02.10.21	HNE	**26**	IV.T1213	2016/08/25 03.17.16	HNE/HNN
9	HL.KYPA	1996/10/09 09.46.27	HN2/HN3			2016/10/30 07.07.54	HNE/HNN
10	IT.0LAI	2012/10/25 23.05.24	HGE			2016/10/30 11.58.17	HNE/HNN
11	IT.ACC	2016/08/24 17.46.09	HGE			2016/10/30 13.34.54	HNE/HNN
		2016/10/26 17.10.36	HGE/HGN			2016/10/31 07.05.45	HNN
		2017/01/18 10.14.12	HGN	**27**	IV.T1218	2017/01/18 19.32.32	HNE/HNN
12	IT.CESM	1997/10/14 23.23.28	HNE/HNN			2017/01/18 13.33.37	HNN
		1998/03/21 16.45.09	HNN			2017/01/18 11.07.39	HNN
13	IT.FCC	2016/10/30 12.07.00	HGE/HGN			2017/01/18 10.14.12	HNE/HNN
		2016/10/31 03.27.40	HGN			2017/01/18 09.25.42	HNE
		2016/11/01 07.56.39	HGN			2016/10/30 12.07.00	HNE
		2016/11/12 14.43.33	HGE/HGN			2016/10/30 07.13.06	HNE
14	IT.FORC	1997/10/12 11.08.35	HNE/HNN			2016/10/30 07.07.54	HNE/HNN
15	IT.GVD	2004/11/24 22.59.38	HNN			2016/10/26 17.10.36	HNE/HNN
16	IT.LPR	2010/08/16 12.54.47	HNN	**28**	IV.T1242	2016/08/25 03.17.16	HNN
17	IT.MZZ	2006/02/27 04.34.01	HNN			2016/09/03 10.18.51	HNN
18	IT.RQT	2016/09/03 10.18.51	HGE	**29**	IV.T1256	2016/11/01 07.56.39	HNN
		2016/10/26 21.42.01	HGN			2016/11/03 00.35.01	HNN
		2016/10/27 03.19.27	HGE/HGN	**30**	KO.MASR	2014/09/04 03.53.00	HNN
		2016/10/30 13.34.54	HGE	**31**	KO.SHAP	2014/07/15 12.25.52	HNE/HNN
		2016/11/01 07.56.39	HGE/HGN			2015/09/22 06.25.04	HNE/HNN
		2017/01/18 10.14.12	HGE/HGN			2015/09/22 07.11.11	HNE
		2017/01/18 10.25.26	HGE/HGN	**32**	SI.CEY	1995/05/22 11.16.54	HNN
		2017/01/18 11.07.39	HGE/HGN	**33**	SI.DRZN	1998/05/06 02.52.59	HNE
		2017/01/18 13.33.37	HGE/HGN	**34**	YP.AC01	2014/11/08 23.15.43	HNE/HNN
19	IT.SPT1	2013/12/29 17.08.43	HGE/HGN			2014/11/07 07.41.35	HNE/HNN
20	IT.UST	2016/12/11 12.54.52	HGN			2014/02/21 15.18.25	HNE
		2017/01/18 09.25.42	HGN			2014/02/15 07.31.16	HNE
		2018/04/10 03.11.31	HGN			2014/02/06 19.20.59	HNE

A statistical analysis of the data represented in the histograms of Figures 5.5 and 5.6, for Type 1 and Type 2 areas, before and after the application of the *Chauvenet's Criterion,* have been performed.

Specifically, the following quantities have been evaluated in the strong motion time region $t_{5\text{-}95}$ of the downloaded accelerograms: lower bound (*LB*), upper bound (*UB*), midpoint (*mid*), normalized deviation amplitude (*dev/mid*), defined as (*UB*-*LB*)/(*UB*+*LB*) [Moore 1966]; mean value (*MV*); standard deviation (*SD*); skewness (skew); and kurtosis (*kurt*) [Lutes and Sarkani 2004].

The values of statistical parameters have been collected in: Tables 5-VI (Type I) and 5-VII (Type II) before the application of the *Chauvenet's Criterion*, and in Tables 5-VIII (Type I) and 5-IX (Type II) after the application of the *Chauvenet's Criterion*.

Tables 5-VI and 5-VII clearly show a remarkable variation of the selected parameters which would entail a huge change of the associated *PSD* function of ground motion acceleration.

Comparing Tables 5-VI and 5-VII with Tables 5-VIII and 5-IX as expected, it is observed that the application of *Chauvenet's Criterion* leads to a significantly smaller scatter of the selected parameters.

By inspection of Tables 5-VI and 5-VII, it appears that the main parameters characterizing the one sided *PSD* function in Eq.(5.1) should be more appropriately modelled as non-deterministic quantities. Notice that, based on the statistical analysis of the selected accelerograms, the parameters pertaining to low seismicity regions (Type 2, Table 5-IX) exhibit larger fluctuations around the midpoint value, as can be readily inferred by comparing the normalized deviation amplitudes listed in Table 5-VII and Table 5-IX. Furthermore, it is worth emphasizing that, for both Type 1 and Type 2 regions, the variance $\sigma^2_{\ddot{U}_g}$ is affected by a very high degree of uncertainty. Alternative methods for the statistical analysis of the recorded data could be applied to obtain tighter ranges of variability.

Table 5-VI Main characteristics of selected accelerograms for Type 1 regions.

	LB	***UB***	***mid***	***dev/mid***	***MV***	***SD***	***skew***	***kurt***
t_{5-95} [s]	3.690	19.470	11.580	0.681	10.894	3.850	0.144	2.426
ν_N [Hz]	1.704	13.980	7.842	0.783	6.268	2.651	1.329	4.287
ν_P [Hz]	4.158	20.858	12.508	0.668	10.370	3.664	1.077	3.879
$\sigma^2_{\ddot{U}_g}$ [m^2/s^4]	0.010	2.062	1.036	0.990	0.181	0.420	3.741	16.392
Ω_0 [rad/s]	10.708	87.838	49.273	0.783	39.380	16.654	1.329	4.287
ρ_0 [rad/s]	6.216	36.583	21.399	0.709	18.644	6.788	1.147	3.897

Table 5-VII Main characteristics of selected accelerograms Type 2 regions.

	LB	***UB***	***mid***	***dev/mid***	***MV***	***SD***	***skew***	***kurt***
t_{5-95} [s]	0.805	15.355	8.080	0.900	4.576	2.788	1.564	5.729
ν_N [Hz]	3.598	23.022	13.310	0.729	8.921	3.234	1.145	5.398
ν_P [Hz]	5.021	25.036	15.028	0.666	12.439	3.195	0.768	4.105
$\sigma^2_{\ddot{U}_g}$ [m^2/s^4]	0.005	2.791	1.398	0.996	0.114	0.309	6.688	52.669
Ω_0 [rad/s]	22.606	144.649	83.628	0.729	56.053	20.320	1.145	5.398
ρ_0 [rad/s]	9.710	47.102	28.406	0.658	23.202	6.281	0.740	3.682

Table 5-VIII Main characteristics of selected accelerograms for Type 1 regions evaluated through the iterative application of the *Chauvenet's Criterion*.

	LB	***UB***	***mid***	***dev/mid***	***MV***	***SD***	***skew***	***kurt***
t_{5-95} [s]	5.025	19.470	12.248	0.598	12.523	3.883	-0.004	2.252
ν_N [Hz]	3.746	7.802	5.774	0.351	5.591	1.166	0.192	2.031
ν_P [Hz]	6.006	11.406	8.706	0.310	8.955	1.629	-0.132	1.672
$\sigma^2_{\ddot{U}_g}$ [m^2/s^4]	0.010	0.092	0.051	0.804	0.036	0.028	0.958	2.457
Ω_0 [rad/s]	23.534	49.024	36.279	0.351	35.127	7.327	0.192	2.031
ρ_0 [rad/s]	11.145	20.899	16.022	0.304	16.442	2.897	-0.240	1.582

Table 5-IX Main characteristics of selected accelerograms for Type 2 regions evaluated through the iterative application of the *Chauvenet's Criterion*.

	LB	***UB***	***mid***	***dev/mid***	***MV***	***SD***	***skew***	***kurt***
t_{5-95} [s]	1.040	8.215	4.628	0.775	4.084	1.713	0.482	2.553
ν_N [Hz]	3.766	15.505	9.636	0.609	9.212	2.750	0.164	2.343
ν_P [Hz]	5.021	20.444	12.733	0.606	12.825	2.869	0.158	2.728
$\sigma^2_{\ddot{U}_g}$ [m^2/s^4]	0.005	0.104	0.054	0.908	0.037	0.025	0.928	2.991
Ω_0 [rad/s]	23.661	97.423	60.542	0.609	57.881	17.278	0.164	2.343
ρ_0 [rad/s]	9.710	38.062	23.886	0.593	24.065	5.718	0.186	2.514

5.4 Imprecise power spectral density function

5.4.1 The interval model

The probabilistic approaches require a wealth of data, often unavailable, to define the probability distribution density of the uncertain parameters. It has recently been recognized that when crucial information on a variability is missing, it is not good practice to model it as a probabilistic quantity [Moens and Vandepitte 2005]. In this section the above described uncertainties affecting the *PSD* function of ground motion acceleration are modelled via *interval analysis* [Moore 1966, Moore et al. 2009], which may be viewed as the most popular among non-probabilistic approaches for uncertainty treatment. According to this model, the generic parameter characterizing the *PSD* function in Eq.(5.1) is described as an interval variable defined by its *LB* and *UB* or, alternatively, by the *midpoint* and *deviation amplitude*, whose values are determined by statistically analysing the set of recorded accelerograms (see Tables 5-VIII and 5-IX). In the framework of the so-called *Improved Interval Analysis* via *Extra Unitary Interval* (*IIA* via *EUI*) [Muscolino and Sofi 2012], an interval variable x_i^I can be defined as follows:

$$x_i^I = \left[\underline{x}_i \, , \overline{x}_i \right] \equiv x_{\text{mid},i}(1+\alpha_i^I) = x_{\text{mid},i}(1+\Delta\alpha_i \hat{e}_i^I) \tag{5.8}$$

where the symbols $\underline{x}_i$ and $\overline{x}_i$ denote the *LB* and *UB* of the interval, respectively; the apex *I* characterizes the interval variables; $\hat{e}_i^I = [-1,1]$ is the so-called *EUI*, associated with the *i*-th interval variable [Muscolino and Sofi 2012]. In Eq.(5.8), $x_{\text{mid},i}$ and $\Delta\alpha_i$ are the *midpoint value* (or mean) and the normalized *deviation amplitude* (or radius) of x_i^I, given, respectively, by:

$$x_{\text{mid},i} = \frac{\underline{x}_i + \overline{x}_i}{2}; \tag{5.9}$$

$$\Delta\alpha_i = \frac{\Delta x_i}{x_{\text{mid},i}} = \frac{\overline{\alpha}_i - \underline{\alpha}_i}{2} > 0 \tag{5.10}$$

where $\Delta x_i = (\overline{x}_i - \underline{x}_i)/2$ is the *deviation amplitude* of x_i^I. Notice that $\Delta\alpha_i$ represents the *deviation amplitude* (or radius) of the dimensionless interval fluctuation $\alpha_i^I = \Delta\alpha_i \hat{e}_i^I$ around $x_{\text{mid},i}$ such that $\Delta\alpha_i < 1$.

In the framework of interval symbolism, a generic interval-valued function *f* and a generic interval-valued matrix function **A** of the interval variables α_i^I, $(i = 1,2,...)$ or β_j^I $(j = 1,2,...)$ and of classical, not interval, quantities b_k $(k = 1,2,...)$ and c_ℓ $(\ell = 1,2,...)$ will be denoted in equivalent form, respectively, as:

$$f^I(b_1, b_2, \cdots) \equiv f(b_1, b_2, \cdots \alpha_1^I, \alpha_2^I, \cdots); \quad \mathbf{A}^I(c_1, c_2, \cdots) \equiv \mathbf{A}(c_1, c_2, \cdots \beta_1^I, \beta_2^I, \cdots). \tag{5.11}$$

5.4.2 Interval PSD function

The *PSD* function introduced in Eq.(5.1) depends on three parameters: the predominant circular frequency, Ω_0; the circular frequency bandwidth ρ_0; and the variance, $\sigma_{\ddot{U}_g}^2$. In this section, according to the results reported in Tables 5-VIII and 5-IX, these parameters are treated as interval variables in the framework of the *IIA* via *EUI* [Muscolino and Sofi 2012]:

$$\begin{aligned}
\Omega_0^I &= \left[\underline{\Omega}_0, \overline{\Omega}_0\right] = \Omega_{0,\text{mid}}(1 + \alpha_{\Omega_0}^I) = \Omega_{0,\text{mid}}(1 + \Delta\alpha_{\Omega_0}\, \hat{e}_{\Omega_0}^I); \\
\rho_0^I &= \left[\underline{\rho}_0, \overline{\rho}_0\right] = \rho_{0,\text{mid}}(1 + \alpha_{\rho_0}^I) = \rho_{0,\text{mid}}(1 + \Delta\alpha_{\rho_0}\hat{e}_{\rho_0}^I); \\
\left(\sigma_{\ddot{U}_g}^2\right)^I &= \left[\underline{\sigma}_{\ddot{U}_g}^2, \overline{\sigma}_{\ddot{U}_g}^2\right] = \sigma_{\ddot{U}_g,\text{mid}}^2(1 + \alpha_{\sigma_{\ddot{U}_g}^2}^I) = \sigma_{\ddot{U}_g,\text{mid}}^2(1 + \Delta\alpha_{\sigma_{\ddot{U}_g}^2}\, \hat{e}_{\sigma_{\ddot{U}_g}^2}^I).
\end{aligned} \tag{5.12}$$

The midpoints, $\Omega_{0,\text{mid}}$, $\rho_{0,\text{mid}}$ and $\sigma_{\ddot{U}_g,\text{mid}}^2$, and the normalized deviation amplitudes, $\Delta\alpha_{\Omega_0}$, $\Delta\alpha_{\rho_0}$, and $\Delta\alpha_{\sigma_{\ddot{U}_g}^2}$, are herein assumed equal to those listed in the fourth and fifth columns of Tables 5-VIII and 5-IX for Type 1 and Type 2 regions, respectively. Under this assumption, the *PSD* function representative of accelerograms recorded in soils with specific geotechnical characteristics is consistently modelled as an interval function. This entails that the well-established seismic spectra, with deterministic parameters proposed in literature, provide only

indicative models of recorded accelerograms in seismic areas which may differ from the actual ones. Note that, since the *PSD* function in Eq. (5.1) depends linearly on $(\sigma^2_{\ddot{U}_g})^I$, this parameter could be set a posteriori as a function of site seismic hazard or as a function of the expected *peak ground acceleration* (*PGA*). Relying on this observation, the following expression of the interval extension of the *PSD* function given in Eq.(5.1) is assumed:

$$G_{\ddot{U}_g}\left(\omega;\Omega_0^I,\rho_0^I,(\sigma^2_{\ddot{U}_g})^I\right)\equiv(\sigma^2_{\ddot{U}_g})^I\,\tilde{G}^I_{\ddot{U}_g}(\omega) \tag{5.13}$$

with

$$\tilde{G}^I_{\ddot{U}_g}(\omega)\equiv\tilde{G}_{\ddot{U}_g}\left(\omega;\Omega_0^I,\rho_0^I\right)=\beta_0^I\left(\frac{\omega^2}{\omega^2+\left(\omega_H^I\right)^2}\right)\left(\frac{\left(\omega_L^I\right)^4}{\omega^4+\left(\omega_L^I\right)^4}\right)G_0^{(CP)}\left(\omega,\Omega_0^I,\rho_0^I\right) \tag{5.14}$$

denoting the interval *PSD* function of the unit variance process $\ddot{\ddot{U}}^I_g(t)\equiv\ddot{\ddot{U}}_g(t;\Omega_0^I,\rho_0^I)=\ddot{U}_g(t;\Omega_0^I,\rho_0^I,\sigma^I_{\ddot{U}_g})/\sigma^I_{\ddot{U}_g}$. The interval quantities appearing in Eq. (5.14) are defined as follows:

$$\beta_0^I\equiv\beta_0\left(\Omega_0^I,\rho_0^I\right);\quad \omega_H^I\equiv\omega_H(\Omega_0^I)=0.1\,\Omega_0^I;\quad \omega_L^I\equiv\omega_L(\Omega_0^I,\rho_0^I)=\Omega_0^I+0.8\rho_0^I. \tag{5.15}$$

For illustration purposes, Figures 5.7 (a,b) show the realizations of the *imprecise PSD* function $\tilde{G}^I_{\ddot{U}_g}(\omega)$ (see Eq.(5.14)) pertaining to the extreme values of the interval parameters Ω_0^I and ρ_0^I along with the nominal spectrum for Type 1 and Type 2 seismic actions, respectively. The nominal *PSD* function is evaluated by assuming the three parameters of Eqs. (5.13) and (5.14) simultaneously equal to their mid-point value.

Notice that imprecision causes a significant variation of the *PSD* function. In particular, for Type 2 areas, the degree of uncertainty affecting the predominant circular frequency, Ω_0^I, and the circular frequency bandwidth, ρ_0^I, is much larger than the one pertaining to Type 1 spectrum. This entails that seismic excitation may have the highest power content over quite different ranges of frequencies depending on the value of the uncertain parameters.

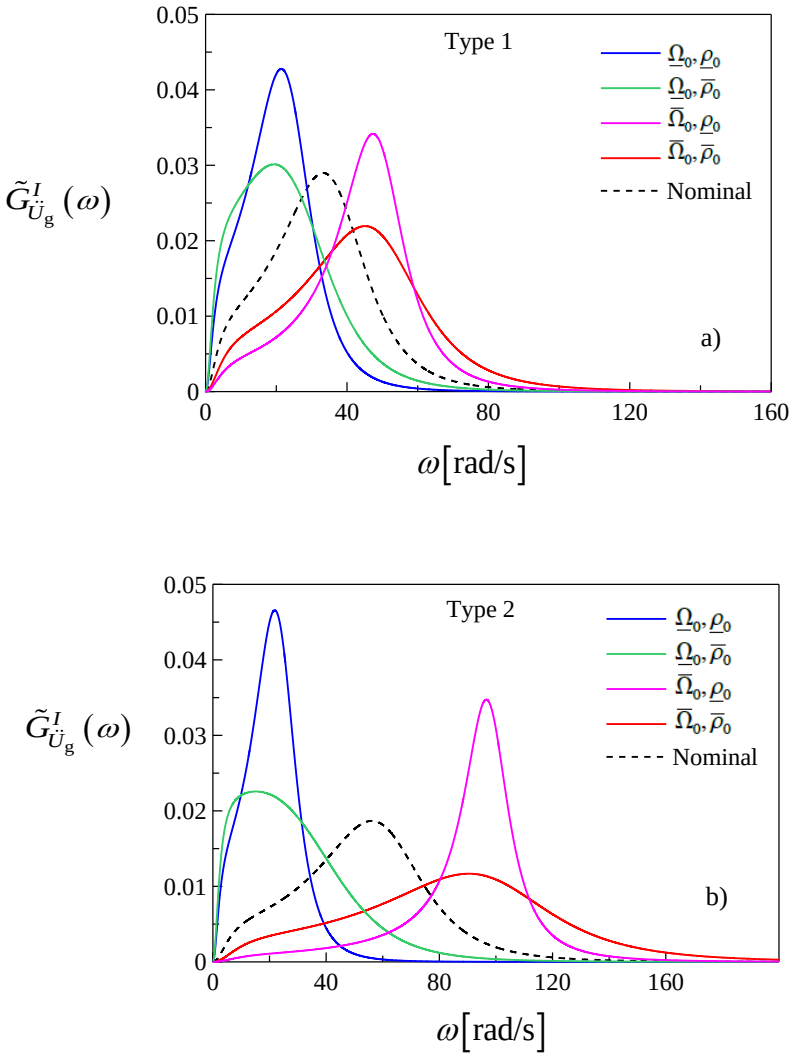

Figure 5.7 Realizations of the *imprecise PSD* function $\tilde{G}^I_{\ddot{U}_g}(\omega)$ of ground motion acceleration (see Eq. (5.14)) for different values of the uncertain predominant circular frequency Ω_0 and circular frequency bandwidth ρ_0: a) Type 1 regions (see Table 5-VIII); b) Type 2 regions (see Table 5-IX).

5.5 Bounds of interval fractiles

In the context of structural safety assessment, a very meaningful quantity, able to provide a direct design provision, is the so-called *fractile* of order *p*, i.e. the response level which has a specified probability, *p*, of not being exceeded during the observation time.

To do this, let us introduce a generic response quantity of interest, $Y^I_h(t)$ (e.g., displacement, strain or stress at a critical point). Since the *PSD* function is imprecise and

modelled as an interval function, the *extreme value* random process, over the time interval [0,*T*], has an interval nature and is mathematically defined as:

$$Y_{\max,h}^{I}(T) \equiv Y_{\max,h}\left(T;\Omega_0^I,\rho_0^I,\sigma_{\ddot{U}_g}^I\right) = \max_{0\le t\le T}\left|Y_h\left(t;\Omega_0^I,\rho_0^I,\sigma_{\ddot{U}_g}^I\right)\right| \tag{5.16}$$

where the symbol |·| denotes absolute value.

In the framework of stochastic dynamics, the *interval fractile* of order *p* can be directly estimated by the interval extension of the approximate analytical expression which holds in the context of the Vanmarcke [1975 and 1972] assumption of out-crossings in clump i.e. [Muscolino et al. 2016]:

$$Z_{Y_{h,\max}}^{I}(p,T) = \psi_{Y_h}^{I}(p,T)\sqrt{(\sigma_{\ddot{U}_g}^2)^I\,\tilde{\lambda}_{0,Y_h}^I} = \sqrt{(\sigma_{\ddot{U}_g}^2)^I}\,\tilde{Z}_{Y_{h,\max}}^{I}(p,T) \tag{5.17}$$

where $\tilde{Z}_{Y_{h,\max}}^{I}(p,T)$ is the *interval fractile* of order *p*, purged of $\sqrt{(\sigma_{\ddot{U}_g}^2)^I}$, and $\psi_{Y_h}^{I}(p,T)$ is the so-called *interval peak factor*, which can be defined, according to Vanmarcke [1975 and 1972], as:

$$\begin{aligned}\psi_{Y_h}^{I}(p,T) &\equiv \psi_{Y_h}\left(p,T;\Omega_0^I,\rho_0^I,(\sigma_{\ddot{U}_g}^2)^I\right) = \\ &= \sqrt{2\ln\left\{\frac{T}{-\pi\ln(p)}\sqrt{\frac{\tilde{\lambda}_{2,Y_h}^I}{\tilde{\lambda}_{0,Y_h}^I}}\left[1-\exp\left(-\left(\tilde{\delta}_{Y_h}^I\right)^{1.2}\sqrt{\pi\ln\left[\frac{T}{-\pi\ln(p)}\sqrt{\frac{\tilde{\lambda}_{2,Y_h}^I}{\tilde{\lambda}_{0,Y_h}^I}}\right]}\right)\right]\right\}}\end{aligned} \tag{5.18}$$

In the previous equations, $\tilde{\lambda}_{0,Y_h}^I \equiv \tilde{\lambda}_{0,Y_h}\left(\Omega_0^I,\rho_0^I\right)$, $\tilde{\lambda}_{1,Y_h}^I \equiv \tilde{\lambda}_{1,Y_h}\left(\Omega_0^I,\rho_0^I\right)$ and $\tilde{\lambda}_{2,Y_h}^I \equiv \tilde{\lambda}_{2,Y_h}\left(\Omega_0^I,\rho_0^I\right)$ are the interval spectral moments [Muscolino and Sofi 2012] of zero-, first- and second-order, respectively, of the normalized random process $\tilde{Y}_h^I(t) = Y_h^I(t)/\sigma_{\ddot{U}_g}^I$, given by:

$$\tilde{\lambda}_{\ell,Y_h}^I \equiv \tilde{\lambda}_{\ell,Y_h}\left(\Omega_0^I,\rho_0^I\right) = \int_0^\infty \omega^\ell\,\tilde{G}_{Y_hY_h}^I(\omega)\,\mathrm{d}\omega, \quad \ell = 0,1,2 \tag{5.19}$$

where $\tilde{G}_{Y_hY_h}^I(\omega)$ is the one-sided interval *PSD* function of the normalized response process $\tilde{Y}_h^I(t) = Y_h^I(t)/\sigma_{\ddot{U}_g}^I$, whose *PSD* function can be defined as follows:

$$\tilde{G}^I_{Y_h Y_h}(\omega) \equiv \frac{1}{(\sigma^2_{\ddot{U}_g})^I} G^I_{Y_h Y_h}(\omega,) \tag{5.20}$$

In Eq.(5.18) $\tilde{\delta}^I_{Y_h}$ is the so-called *interval bandwidth parameter* of the stationary process $\tilde{Y}^I_h(t) = Y^I_h(t) / \sigma^I_{\ddot{U}_g}$ defined as:

$$\tilde{\delta}^I_{Y_h} \equiv \tilde{\delta}_{Y_h}\left(\Omega^I_0, \rho^I_0\right) = \sqrt{1 - \frac{\mathrm{Re}\left\{\tilde{\lambda}^I_{1,Y_h}\right\}^2}{\tilde{\lambda}^I_{0,Y_h}\ \tilde{\lambda}^I_{2,Y_h}}}. \tag{5.21}$$

Since the interval spectral moments, in general, are not monotonic functions of the interval parameters affecting the *imprecise PSD* function, the lower and upper bounds of $\tilde{Z}^I_{Y_{h,\max}}(p,T)$ can be evaluated by solving numerically the following constrained minimum and maximum problems [Muscolino et al. 2016]:

$$\underline{\tilde{Z}}_{Y_{h,\max}}(p,T) \equiv \min_{\Omega_0 \in \Omega^I_0,\ \rho_0 \in \rho^I_0} \left\{\tilde{Z}_{Y_{h,\max}}\left(b,T;\Omega_0,\rho_0\right)\right\}; \tag{5.22}$$

$$\overline{\tilde{Z}}_{Y_{h,\max}}(p,T) \equiv \max_{\Omega_0 \in \Omega^I_0,\ \rho_0 \in \rho^I_0} \left\{\tilde{Z}_{Y_{h,\max}}\left(b,T;\Omega_0,\rho_0\right)\right\} \tag{5.23}$$

Notice that only two uncertain parameters appear in Eqs. (5.22) and (5.23) i.e. $\rho_0 \in \rho^I_0$ and $\Omega_0 \in \Omega^I_0$.

Finally, taking into account Eq.(5.17), the bounds of the *interval fractile* of order *p* can be derived as follows:

$$\underline{Z}_{Y_{h,\max}}(p,T) = \sqrt{\underline{\sigma}^2_{\ddot{U}_g}}\,\underline{\tilde{Z}}_{Y_{h,\max}}(p,T); \tag{5.24}$$

$$\overline{Z}_{Y_{h,\max}}(p,T) = \sqrt{\overline{\sigma}^2_{\ddot{U}_g}}\,\overline{\tilde{Z}}_{Y_{h,\max}}(p,T). \tag{5.25}$$

It is worth remarking that the quantity of interest for design purpose is the *UB* of the *interval fractile* of order *p* , which describes the worst case scenario. In fact, for the *UB* of the *fractile* of order *p*, a higher value of the maximum of the response of interest is exceeded, with the same probability, than that in the *LB*.

5.6 Numerical example

The presented procedure is applied to a *single-degree-of-freedom (SDOF)* system under seismic excitation characterized by the proposed *imprecise PSD* function (see Eq.(5.14)) with interval parameters defined in Table 5-VIII for moderate and high seismicity areas. Under this assumption, the normalized one-sided *PSD* function matrix of the response in terms of displacement, $U^I(t)$, can be written as:

$$\tilde{G}^I_{UU}(\omega) = \left|H_0(\omega)\right|^2 \tilde{G}^I_{\ddot{U}_g}(\omega) \tag{5.26}$$

where $H_0(\omega)$ is the *frequency response function FRF* function of the *SDOF* system:

$$H_0(\omega) = \frac{1}{\omega_0^2 - \omega^2 + 2\mathrm{i}\,\xi_0\,\omega_0\,\omega} \tag{5.27}$$

with ω_0 denoting the natural circular frequency of the *SDOF* system, ξ_0 its damping ratio herein assumed equal to ξ_0=0.05 and $i = \sqrt{-1}$ is the imaginary unity.

Figure 5.8 a) shows the bounds of the *interval fractiles* $\tilde{Z}^I_{U_{\max}}(p,T)$ of order p=0.50 (the median) and p=0.95, purged of $\sqrt{(\sigma^2_{\ddot{U}_g})^I}$, versus the natural vibration period T_0 of the seismically excited *SDOF* system for a given value of the modal damping ratio ξ_0=0.05.

Finally, in Figure 5.8 b), the *interval fractile* $\tilde{Z}^I_{U_{\max}}(p,T)$ multiplied by the square of the natural frequency ω_0^2 of the *SDOF* system versus T_0 is plotted. The nominal values of the aforementioned quantities are also reported. It is recalled that the quantities plotted in Figures 5.8 (a,b) play a crucial role in the framework of seismic structural analysis.

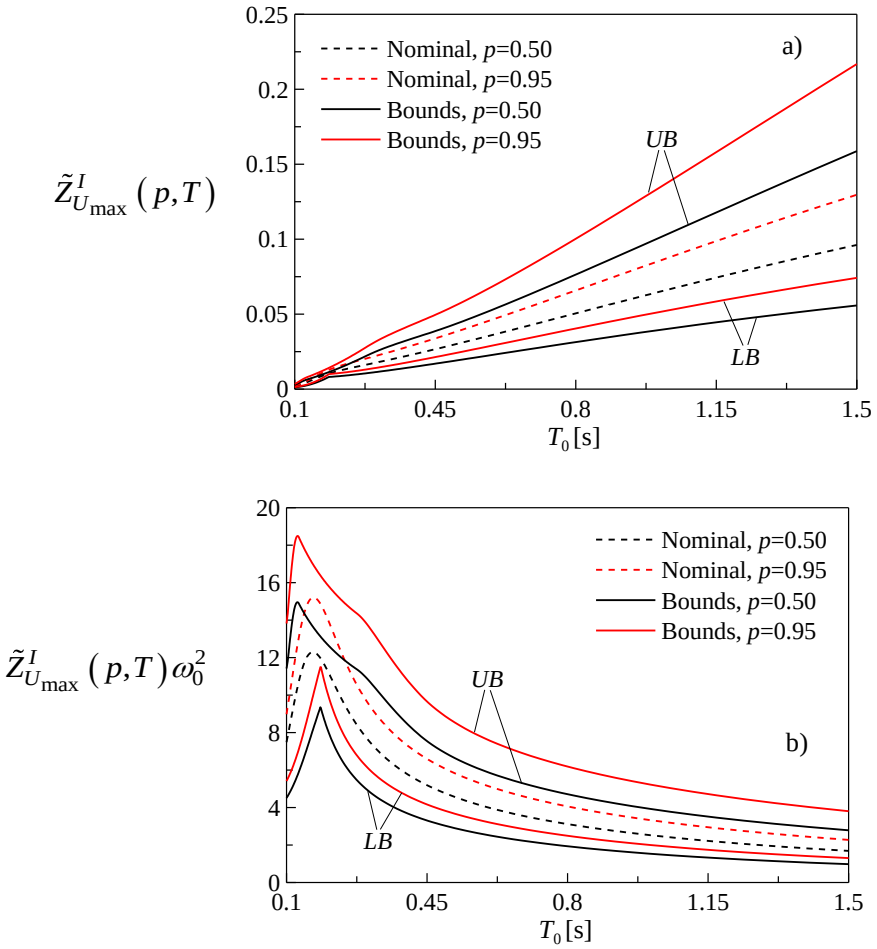

Figure 5.8 a) Interval fractile $\tilde{Z}^I_{U_{\max}}(p,T)$ and b) $\tilde{Z}^I_{U_{\max}}(p,T)\omega_0^2$ of order p=0.5 and p=0.95 versus the natural period of vibration T_0.

By inspection of Figure 5.8 a), it is observed that, as expected, the bounds of the interval fractiles of order $p=0.95$ are larger than the ones of order $p=0.5$. Furthermore, the region enclosed by the *LB* and *UB* becomes wider as the natural period of vibration increases. The comparison with the nominal values clearly shows the remarkable influence of imprecision of the excitation on safety assessment of structures subjected to earthquake ground motion. These results show that the structural performance under imprecise excitation might range from very low to very high safety levels. In this regard, it is worth mentioning that the region of the interval fractiles $Z^I_{U_{\max}}(p,T)$ (see Eqs. (5.24) and (5.25)), herein not plotted, would be much larger due to the high degree of uncertainty affecting the variance of the excitation

process $(\sigma^2_{\ddot{U}_g})^I$. It follows that, further statistical analyses of recorded accelerograms are needed to obtain tighter bounds of the interval variance.

Conclusions

Earthquake-resistant design of new structures and evaluation of safety of existing ones requires the analysis of their response to the expected seismic excitation. The level of shaking produced by an earthquake, for which satisfactory performance is expected, is often referred to as a *design level* of shaking and is described by a *design ground motion.*

Seismic ground motions, usually expressed in the form of acceleration time histories, provide the basic data for earthquake engineering as they contain information regarding both the nature of the wave propagation and the soil characteristics.

Despite the increasing availability of recorded accelerograms, due to mechanical properties and non-linear behaviour of soils, there are situations in which it is not possible to obtain the minimum number of spectrum-compatible accelerograms required by seismic codes to carry out fully dynamic analysis without applying large scale factors to each record of the set, which may distort the recorded accelerogram, leading to unrealistic input motions. In these situations, the generation of artificial accelerograms could represent a possible alternative to realistically reproduce the seismic excitations.

Since stationary artificial accelerograms are usually characterized by an excessive number of strong motion cycles and a high energy content, it becomes necessary to develop procedures to generate artificial accelerograms which suitably incorporate the large variability of the seismological parameters observed in real-life time-histories (i.e. magnitude, site to source distance, local site characteristics, etc).

For conventional earthquake resistant systems, intensity measures such as *Arias intensity*, *peak ground acceleration* and *pseudo-acceleration response spectrum* provide important information to carry out the seismic analysis and design checks. A brief overview of the main information carried by the different engineering measures of the strong ground motions has been reported in Chapter 1.

From the analysis of recorded accelerograms it can be observed that the acceleration amplitudes and the frequency content of actual ground motions changes over the duration of

shaking. Thus, because of the inherent non-stationarity of the signals encountered in earthquake engineering there is a need for methods implementing joint time-frequency analysis algorithms.

After an introduction to *wavelet analysis*, that was originally designed as a tool that could eliminate the disadvantages of both traditional *Fourier analysis* and *short time Fourier analysis*, Chapter 2 focused on the properties of the circular harmonic wavelets through which it is possible to exactly reproduce the non-stationary characteristics of a given signal.

In Chapter 3, the properties of the circular wavelets have been exploited to propose a novel wavelet-based method for the generation of fully non-stationary random accelerograms. The proposed discrete circular-wavelet transform method, consisting of a phase angle rotation of the circular wavelets, allows the generation of the required number of fully non-stationary samples without the need of defying the *evolutionary power spectral density* function of the ground acceleration. Because of the inherent uncertain nature of the earthquake, the correct choice of the number of bands in which to divide the frequency domain is an important step to generate samples with the desired time-variation of amplitude and frequency content.

A second method for generating samples of a fully non-stationary zero-mean Gaussian process, in such a way that the chosen target accelerogram can be considered as one of its own samples, has been proposed in Chapter 4. The main advantage of the procedure proposed in this Chapter, which is based on the use of the evolutionary spectral model, is that requires only the knowledge of the total intensity, number of *peaks* and *zero level up crossings* of the design earthquake. Specifically, the *evolutionary power spectral density* (*EPSD*) function of the proposed fully non-stationary model is evaluated as the sum of uniformly modulated processes. The *EPSD* function is defined in each time interval in which the target signal is subdivided, as the product of deterministic modulating functions times stationary zero-mean Gaussian sub-processes, whose unimodal *power spectral density* (*PSD*) functions are filtered by high pass and low pass Butterworth filters. In each time interval the parameters of modulating functions are estimated by least-square fitting the expected energy of the proposed model to the energy of the target accelerogram, while the parameters of *PSD* functions of stationary sub-processes are estimated once both occurrences of *peaks* and of *zero-level up-crossings* of the target accelerogram, in the various intervals, are counted. Therefore, unlike the wide variety of methods based on non-stationary random process theory, for the application of the proposed method there is no need for sophisticated processing of the

recorded motion. It is important to notice that, despite the proposed procedure was presented and described with reference to a single target accelerogram, it can be extended to account for the variability of the expected ground motion considering the uncertainties inherent to the values of the seismic parameters assumed as targets in the generation procedure. In the last part of Chapter 4, the evolutionary spectral model has been modified to obtain the compatibility between the generated fully non-stationary accelerograms and a target spectrum. Specifically, the reduction of the gap between the mean spectrum of the generated samples and the target one has been done through the introduction of a corrective iterative *PSD* function. Depending on the aim to be achieved, the target spectrum can be a *response spectrum* or a *Fourier spectrum* therefore, to achieve the desired spectrum-compatibility, the procedure is particularized using two different corrective *PSD* function terms.

The examination of the characteristics of recorded accelerograms plays a key role in the field of earthquake engineering. In the Chapter 5, the analysis of a large number of accelerograms recorded on rigid soil deposits has shown that: *i*) within the *strong-motion duration*, the number of *zero level up-crossings* is almost constant, so that the records can be reasonably considered as samples of zero-mean stationary Gaussian processes, fully characterized by a *PSD* function; *ii*) the accelerograms exhibit different spectral contents even if they are recorded in the same soil category, so that the main parameters of the pertinent *PSD* function vary from one accelerogram to another. As a consequence, in order to provide a reliable characterization of future seismic events on rigid soil deposits, the spectral parameters should be more appropriately treated as uncertain quantities leading to an *imprecise PSD* function of seismic excitation. Based on these results, an imprecise model of the *PSD* function of ground motion acceleration has been derived relying on the spectrum able to catch the frequency content of recorded accelerograms proposed in Chapter 4. Specifically, the three main parameters characterizing the novel spectral model i.e. the *predominant circular frequency*, the *circular frequency bandwidth* and the *variance of the process*, have been modelled as interval variables whose bounds have been estimated by analysing a large set of accelerograms recorded on rigid soil deposits. Such analysis has shown that the power spectrum representative of accelerograms recorded in soils with specific geotechnical characteristics is more appropriately described by an interval function.

The well-established seismic spectra with deterministic parameters turn out to provide only indicative models of recorded accelerograms in seismic areas which may differ to a large extent from the actual spectra.

References

Alguacil, G., Havskov, J. (2014). Recording Seismic Signals. *Encyclopedia of Earthquake Engineering*, Springer-Verlag, Berlin, Heidelberg.

Ambraseys, N.N., Sarma, S.K. (1967). The response of earth dams to strong earthquakes. *Geotechnique*, *17*(3), 181-213.

Amin, M., Ang, A.H.S. (1968). Nonstationary stochastic models of earthquake motions. *Journal of the Engineering Mechanics Division*, *94*(2), 559-584.

Ancheta, T.D., Darragh, R.B., Stewart, J.P., Seyhan, E., Silva, W.J., Chiou, B.S.J., K.E. Wooddell, Graves, R.W., Kottke, A.R., Boore, D.M., Kishi, T., Donahue J. L. (2013). *PEER NGA-West2 database*. Pacific Earthquake Engineering Research Center/03; California.

Ang, A.H.S. (1990). Reliability bases for seismic safety assessment and design, *Proceedings, Fourth U.S. National Conference on Earthquake Engineering*, Earthquake Engineering Research Institute, Palm Springs,.*1* (pp. 29-45).

Arias, A. (1970). Measure of earthquake intensity, Massachusetts Institute of Technology, *Cambridge. University of Chile, Santiago de Chile*.

Barbato, G., Barini, E. M., Genta, G., Levi, R. (2011). Features and performance of some outlier detection methods. *Journal of Applied Statistics*, *38*(10), 2133-2149.

Barone, G., Iacono, F.L., Navarra, G., Palmeri, A. (2019). Closed-form stochastic response of linear building structures to spectrum-consistent seismic excitations. *Soil Dynamics and Earthquake Engineering*, *125*, 105724.

Basu, B., Gupta, V.K. (1997). Non-stationary seismic response of MDOF systems by wavelet transform. *Earthquake engineering and Structural Dynamics*, *26*(12), 1243-1258.

Basu, B., Gupta, V.K. (1998). Seismic response of SDOF systems by wavelet modeling of nonstationary processes. *Journal of Engineering Mechanics*, *124*(10), 1142-1150.

Basu, B., Gupta, V.K. (2000). Stochastic seismic response of single-degree-of-freedom systems through wavelets. *Engineering Structures*, *22*(12), 1714-1722.

Beck, J.L., Papadimitriou, C. (1993). Moving resonance in nonlinear response to fully nonstationary stochastic ground motion. *Probabilistic Engineering Mechanics*, *8*(3-4), 157-167.

Bycroft, G. N. (1960). White noise representation of earthquakes. *Journal of the Engineering Mechanics Division*, *86*(2), 1-16.

Bolt, B.A. (1973). Duration of strong ground motion. In *5th World Conference on Earthquake Engineering* (pp. 25-29).

Bommer, J.J., Martinez-Pereira, A. (1999). The effective duration of earthquake strong motion. *Journal of Earthquake Engineering*, *3*(02), 127-172.

Bommer, J.J., Acevedo, A.B. (2004). The use of real earthquake accelerograms as input to dynamic analysis. *Journal of Earthquake Engineering*, *8*(01), 43-91.

Boore, D.M. (1999). *Effect of baseline corrections on response spectra for two recordings of the 1999 Chi-Chi, Taiwan, earthquake* (p. 37). US Department of the Interior, US Geological Survey.

Boore, D.M. (2001). Effect of baseline corrections on displacements and response spectra for several recordings of the 1999 Chi-Chi, Taiwan, earthquake. *Bulletin of the Seismological Society of America*, *91*(5), 1199-1211.

Boore, D.M., Stephens, C.D., Joyner, W.B. (2002). Comments on baseline correction of digital strong-motion data: Examples from the 1999 Hector Mine, California, earthquake. *Bulletin of the Seismological Society of America*, *92*(4), 1543-1560.

Boore, D.M., Bommer, J.J. (2005). Processing of strong-motion accelerograms: needs, options and consequences. *Soil Dynamics and Earthquake Engineering*, *25*(2), 93-115.

Carmona, R., Hwang, W.J., Torresani, B. (1998). *Practical time–frequency analysis*, Academic, New York.

Cartwright, D.E., Longuet-Higgins, M.S. (1956). The statistical distribution of the maxima of a random function. *Proceedings of the royal society of London. series a. mathematical and physical sciences*, *237*(1209), 212-232.

Cascone, E., Biondi, G., Aliberti, D., Rampello, S. (2021). Effect of vertical input motion and excess pore pressures on the seismic performance of a zoned dam. *Soil Dynamics and Earthquake Engineering*, *142*, 106566.

Cecini, D., Palmeri, A. (2015). Spectrum-compatible accelerograms with harmonic wavelets. *Computers and Structures*, *147*, 26-35.

Chang, F.K., Franklin, A.G. (1987). PGA, RMSA, PSDF, Duration, and MMI. In *Developments in Geotechnical Engineering* , *44* (pp. 449-466). Elsevier, Amsterdam .

Chauvenet, W. (1863). *A Manual of Spherical and Practical Astronomy, vol. 2: Theory and Use of Astronomical Instruments.* J.B. Lippincott Company, Philadelphia:

Cohen, L. (1995). *Time-Frequency Analysis*. Prentice Hall PTR, Upper Saddle River, New Jersey 07458.

Chiu, H. C. (1997). Stable baseline correction of digital strong-motion data. *Bulletin of the Seismological Society of America*, *87*(4), 932-944.

Clough, R. W., Penzien, J. (1975). *Dynamics of Structures*. McGraw-Hill.

Cohen-Tannoudji, C., Dupont-Roc, J., Grynberg, G. (1997). *Photons and Atoms-Introduction to Quantum Electrodynamics* , EDP Sciences; Les Ulis, France.

Conte, J.P. (1992). Effects of earthquake frequency nonstationarity on inelastic structural response. In *Proc. of the 10th World Conference on Earthquake Engineering* (pp. 3645-3651).

Conte, J.P., Peng, B.F. (1997). Fully nonstationary analytical earthquake ground-motion model. *Journal of Engineering Mechanics*, *123*(1), 15-24.

Decai, W. Xianguo, Y. (2011). Baseline correction of the near-fault records and its uncertainty analysis [J] *World Earthquake Engineering*, *02*: 63-69.

Der Kiureghian, A., Crempien, J. (1989). An evolutionary model for earthquake ground motion. *Structural Safety*, *6*(2-4), 235-246.

Di Paola, M., Muscolino, G. (1986). On the convergent parts of high order spectral moments of stationary structural responses. *Journal of Sound Vibration*, *110*(2), 233-245.

EC8 (2004). European Committee for Standardization, Eurocode 8: Design of structures for earthquakes resistance-Part 1: General rules, seismic actions and rules for buildings. EN 1998-1.

Elishakoff, I. (2000). Possible limitations of probabilistic methods in engineering. *Applied Mechanics Reviews, 53* (2), 19–36.

Elishakoff, I. Ohsaki, M. (2010). *Optimization and Anti-Optimization of Structures under* Uncertainty. Imperial College Press, London.

Faes, M. G., Valdebenito, M. A., Moens, D., Beer, M. (2020). Bounding the first excursion probability of linear structures subjected to imprecise stochastic loading. *Computers and Structures, 239*, 106320.

Fan, F. G., Ahmadi, G. (1990). Nonstationary Kanai-Tajimi models for El Centro 1940 and Mexico City 1985 earthquakes. *Probabilistic Engineering Mechanics*, *5*(4), 171-181.

Felicetta, C., D'Amico, M., Lanzano, G., Puglia, R., Russo, E., Luzi L. (2016). Site characterization of Italian accelerometric stations. *Bulletin of Earthquake Engineering 15(6), 2329-2348.*

Gabor, D. (1946). Theory of communication. Part 1: The analysis of information. *Journal of the Institution of Electrical Engineers-Part III: Radio and Communication Engineering*, *93*(26), 429-441.

Garcia, S. R., Romo, M. P., Alcántara, L. (2019). Analysis of non-linear and non-stationary seismic recordings of Mexico city. *Soil Dynamics and Earthquake Engineering*, *127*, 105859.

Genovese, F. (2021). Influence of soil non-linear behaviour on the selection of input motion for dynamic geotechnical analysis. In *International Conference of the International Association for Computer Methods and Advances in Geomechanics* , Springer, Cham (pp. 588-596).

Genovese, F., Aliberti, D., Biondi, G., Cascone, E. (2019 a). Geotechnical aspects affecting the selection of input motion for seismic site response analysis. *Proceedings of the 7th COMPDYN* (pp 24-26).

Genovese, F., Aliberti, D., Biondi, G., Cascone, E. (2019 b). A procedure for the selection of input ground motion for 1D seismic response analysis. *Proceedings of 7ICEGE*, pp 2591-2598.

Genovese, F., Aliberti, D., Biondi, G., Cascone, E. (2020 a). Influence of Soil Heterogeneity on the Selection of Input Motion for 1D Seismic Response Analysis. In *National Conference of the Researchers of Geotechnical Engineering* (pp. 694-704), Springer, Cham.

Genovese, F., Muscolino, G., Biondi, G., Cascone, E. (2020 b). Generation of artificial accelerograms consistent with earthquake-induced ground motions. In *Proceedings of the 11th International Conference on Structural Dynamic* (pp. 3027-3042).

Genovese, F., Muscolino, G., Palmeri, A. (2021, a). Influence of different fully non-stationary artificial time histories generation methods on the seismic response of frequency-dependent structures, In *Proceedings of the 4th International Conference on Uncertainty Quantification in Computational Sciences and Engineering* (pp 15-25).

Genovese, F., Muscolino, G., Biondi, G., Cascone, E. (2021 b). A novel method for the generation of fully non-stationary spectrum compatible artificial accelerograms, *Proceedings of 8th International Conference on Computational Methods in Structural Dynamics and Earthquake Engineering* (pp 1437,1444).

Giaralis, A., Spanos, P.D. (2009). Wavelet-based response spectrum compatible synthesis of accelerograms—Eurocode application (EC8). *Soil Dynamics and Earthquake Engineering*, *29*(1), 219-235.

Goupillaud, P., Grossmann, A., Morlet, J. (1984). Cycle-octave and related transforms in seismic signal analysis. *Geoexploration*, *23*(1), 85-102.

Guorui, H., Tao, L. (2015). Review on baseline correction of strong-motion accelerogram. *International Journal of Environmental Science and Technology*, *3*, 309-314.

Haiying, Y., Wenxiang, J., Quancai, X. (2009). Baseline correction of digital strong-motion records in near-field. [J]. *Earthquake Engineering and Engineering Vibration*, *6*, 1-12.

Housner, G.W. (1947). Characteristics of strong-motion earthquakes. *Bulletin of the Seismological Society of America*, *37*(1), 19-31.

Housner, G.W. (1959). Behavior of structures during earthquakes, *Journal of the Engineering Mechanics Division,* ASCE, Vol. 85, No. EM14, 109-129.

Housner, G. W., Jennings, P. C. (1964). Generation of artificial earthquakes. *Journal of the Engineering Mechanics Division, 90*(1), 113-150.

Hsu, T.I., Bernard, M. C. (1978). A random process for earthquake simulation. *Earthquake Engineering, Structural Dynamics, 6*(4), 347-362.

Huang, T.L., Lou, M.L., Chen, H.P., Wang, N.B. (2018). An orthogonal Hilbert-Huang transform and its application in the spectral representation of earthquake accelerograms. *Soil Dynamics and Earthquake Engineering, 104*, 378-389.

Iervolino, I., Galasso, C., Cosenza, E. (2010). REXEL: computer aided record selection for code-based seismic structural analysis. *Bulletin of Earthquake Engineering, 8*(2), 339-362.

Iyama, J., Kuwamura, H. (1999). Application of wavelets to analysis and simulation of earthquake motions. *Earthquake Engineering, Structural Dynamics, 28*(3), 255-272.

Iyengar, R.N., Iyengar, K. T. (1969). A nonstationary random process model for earthquake accelerograms. *Bulletin of the Seismological Society of America, 59*(3), 1163-1188.

Iwan, W. D., Moser, M. A., Peng, C. Y. (1985). Some observations on strong-motion earthquake measurement using a digital accelerograph. *Bulletin of the Seismological Society of America, 75*(5), 1225-1246.

Iwan, W. D., Hou, Z. K. (1989). Explicit solutions for the response of simple systems subjected to nonstationary random excitation. *Structural Safety, 6*(2-4), 77-86.

Jennings P.C., Housner G.W., Tsai N.C. (1968). Simulated earthquake motions. *Earthquake Engineering Research Laboratory,* California Institute of Technology. Technical report.

Joyner, W.B., Boore D.M. (1981). Peak horizontal acceleration and velocity from strong motion records including records from the 1979 Imperial Valley, California, earthquake. *Bulletin of the Seismological Society of America 1981,* 71: 2011–2038.

Kay, S., Sudhaker, R. (1986). A zero crossing-based spectrum analyzer. *IEEE Transactions on Acoustics, Speech, and Signal Processing, 34*(1), 96-104.

Kanai, K. (1957). Semi-empirical formula for the seismic characteristics of the ground. *Bulletin of the Earthquake Research Institute, University of Tokyo, 35*(2), 309-325.

Katsanos, E. I., Sextos, A. G., Manolis, G. D. (2010). Selection of earthquake ground motion records: A state-of-the-art review from a structural engineering perspective. *Soil dynamics and earthquake engineering, 30*(4), 157-169.

Kedem, B. (1986). Spectral analysis and discrimination by zero-crossings. *Proceedings of the IEEE, 74*(11), 1477-1493.

Kramer, S.L. (1996). *Geotechnical earthquake engineering*. Prentice Hall, Upper Saddle River, New Jersey.

Lai, S. S. P. (1982). Statistical characterization of strong ground motions using power spectral density function. *Bulletin of the Seismological Society of America*, *72*(1), 259-274.

Liang, J., Chaudhuri, S. R., Shinozuka, M. (2007). Simulation of nonstationary stochastic processes by spectral representation. *Journal of Engineering Mechanics*, *133*(6), 616-627.

Lin, Y.K. (1965). Nonstationary excitation and response in linear systems treated as sequences of random pulses. *The Journal of the Acoustical Society of America*, *38*(3), 453-460.

Lin, Y.K. (1986). On random pulse train and its evolutionary spectral representation. *Probabilistic Engineering Mechanics*, *1*(4), 219-223.

Lin, Y.K., Yong, Y. (1987). Evolutionary kanai-tajimi earthquake models. *Journal of Engineering Mechanics*, *113*(8), 1119-1137.

Liu, S.C. (1970). Synthesis of stochastic representations of ground motions. *The Bell System Technical Journal*, *49*(4), 521-541.

Luco, J.E. (1980). Lower bounds for peak horizontal strong-motion amplitudes. *Bulletin of the Seismological Society of America*, *70* (4): 1309–1320.

Lutes, L. D., Sarkani, S. (2004). *Random vibrations: analysis of structural and mechanical systems*. Elsevier, Butterworth-Heinemann, Burlington.

Luzi, L., Lanzano, G., Felicetta, C., D'Amico, M.C., Russo, E., Sgobba, S., Pacor, F., ORFEUS Working Group 5. 2020. Engineering Strong Motion Database (ESM) (Version 2.0). Istituto Nazionale di Geofisica e Vulcanologia (INGV).

Mallat, S. (1999). *A wavelet tour of signal processing*. Elsevier, Burlington.

Maples, M.P., Reichart, D.E., Konz, N.C., Berger, T.A., Trotter, A.S., Martin, J. R., Dutton, D.A., Paggen M.L., Joyner, R.E., Salem, C.P. (2018). Robust Chauvenet Outlier Rejection. *The Astrophysical Journal Supplement Series*, *238*(1):1-49.

Marano, G. C. (2019). Non-stationary stochastic modulation function definition based on process energy release. *Physica A: Statistical Mechanics and its Applications*, *517*, 280-289.

Michaelov, G., Sarkani, S., Lutes, L.D. (1999). Spectral characteristics of nonstationary random processes—a critical review. *Structural Safety*, *21*(3), 223-244.

Moens, D., Vandepitte, D. (2005). A survey of non-probabilistic uncertainty treatment in finite element analysis. *Computer Methods in Applied Mechanics and Engineering*, *194*(12-16), 1527-1555.

Moore R.E. (1966). *Interval Analysis*. Prentice-Hall, Englewood Cliffs.

Moore, R. E., Kearfott, R.B., Cloud, M. J. (2009). *Introduction to interval analysis*. Society for Industrial and Applied Mathematics., SIAM, Philadelphia.

Muscolino, G., Sofi, A. (2012). Stochastic analysis of structures with uncertain-but-bounded parameters via improved interval analysis. *Probabilistic Engineering Mechanics*, *28*, 152-163.

Muscolino, G., Alderucci, T. (2015). Closed-form solutions for the evolutionary frequency response function of linear systems subjected to separable or non-separable non-stationary stochastic excitations. *Probabilistic Engineering Mechanics*, *40*, 75-89.

Muscolino, G., Santoro, R., Sofi, A. (2016). Interval Fractile Levels for Stationary Stochastic Response of Linear Structures With Uncertainties. *Journal of Risk and Uncertainty in Engineering Systems Part B*, *2*(1), 011004.

Muscolino, G., Genovese, F., Biondi, G., Cascone, E. (2021). Generation of fully non-stationary random processes consistent with target seismic accelerograms. *Soil Dynamics and Earthquake Engineering*, *141*, 106467.

Narasimhan, S.V., Pavanalatha, S. (2004). Estimation of evolutionary spectrum based on short time Fourier transform and modified group delay. *Signal Processing*, *84*(11), 2139-2152.

Newland, D.E. (1975). *An introduction to random vibrations and spectral analysis.* Longman Scientific and Technical; New York

Newland, D.E. (1993). Harmonic wavelet analysis. *Proceedings of the Royal Society of London. Series A: Mathematical and Physical Sciences*, *443*(1917), 203-225.

Newland, D.E. (1994). Harmonic and musical wavelets. *Proceedings of the Royal Society of London. Series A: Mathematical and Physical Sciences*, *444*(1922), 605-620.

Pacor, F., Luzi L. (2014). Engineering characterization of earthquake Ground Motions. *Encyclopedia of Earthquake Engineering*, Springer-Verlag, Berlin, Heidelberg.

Pagliaroli, A., Lanzo, G. (2008). Selection of real accelerograms for the seismic response analysis of the historical town of Nicastro (Southern Italy) during the March 1638 Calabria earthquake. *Engineering Structures*, *30*(8), 2211-2222.

Peizhen, Z. (2008). GPS measurement of 2008 wenchuan Ms8.0 earthquake coseismic displacement field. *Science in China press*, *10*: 1195-1206.

Plancherel, M., Leffler, M. (1910). Contribution à l'étude de la représentation d'une fonction arbitraire par des intégrales définies. *Rendiconti del Circolo Matematico di Palermo (1884-1940)*, *30*(1), 289-335.

Priestley, M. B. (1965). Evolutionary spectra and non-stationary processes. *Journal of the Royal Statistical Society: Series B (Methodological)*, *27*(2), 204-229.

Priestley, M. B. (1967). Power spectral analysis of non-stationary random processes. *Journal of Sound and Vibration*, *6*(1), 86-97.

Priestley, M.B. (1981). *Spectral analysis and time series: probability and mathematical statistics*. Academic Press, New York.

Sabetta, F., Pugliese, A. (1996). Estimation of response spectra and simulation of nonstationary earthquake ground motions. *Bulletin of the Seismological Society of America*, *86*(2), 337-352.

Sarma, S. K., Yang, K. S. (1987). An evaluation of strong motion records and a new parameter A95. *Earthquake Engineering and Structural Dynamics*, *15*(1), 119-132.

Schillinger, D., Papadopoulos, V. (2010). Accurate estimation of evolutionary power spectra for strongly narrow-band random fields. *Computer Methods in Applied Mechanics and Engineering*, *199*(17-20), 947-960.

Skolnik, M. I. (1980). *Introduction to Radar Systems*. McGraw Hill Book Co., Singapore.

Rezaeian, S., Der Kiureghian, A. (2008). A stochastic ground motion model with separable temporal and spectral nonstationarities. *Earthquake Engineering and Structural Dynamics*, *37*(13), 1565-1584.

Rofooei, F. R., Mobarake, A., Ahmadi, G. (2001). Generation of artificial earthquake records with a nonstationary Kanai–Tajimi model. *Engineering Structures*, *23*(7), 827-837.

Saragoni, R.G., Hart, G.C. (1973). Simulation of artificial earthquakes. *Earthquake Engineering and Structural Dynamics*, *2*(3), 249-267.

Saragoni, G.R., Díaz, H. (1999). Seismic power for earthquake design. In *Proceedings of the International Post-SmiRT Conference Seminar on Seismic Isolation, Passive Energy Dissipation and Active Control of Vibrations of Structures, Korea*.

Shinozuka, M., Sato, Y. (1967). Simulation of nonstationary random process. *Journal of the Engineering Mechanics Division*, *93*(1), 11-40.

Shinozuka, M., Deodatis, G. (1988). Stochastic process models for earthquake ground motion. *Probabilistic Engineering Mechanics, 3,* (3): 114-123.

Shinozuka, M., Deodatis, G. (1991). Simulation of Stochastic Processes by Spectral Representation. *Applied Mechanics Reviews,* 44(4):191-204.

Spanos, P.D. (1980). Probabilistic earthquake energy spectra equations. *Journal of the Engineering Mechanics Division*, *106*(1), 147-159.

Spanos, P.T., Solomos, G.P. (1983). Markov approximation to transient vibration. *Journal of Engineering Mechanics*, *109*(4), 1134-1150.

Spanos, P.D., Failla, G. (2004). Evolutionary spectra estimation using wavelets. *Journal of Engineering Mechanics*, *130*(8), 952-960.

Spanos. P.D., Failla. G., Politis N.P. (2005). *Wavelets: Concepts and Applications*, in De Silva C.W., Vibration and Shock Handbook. CRC Press, Boca Raton (USA).

Spanos, P. D., Tezcan, J., Tratskas, P. (2005). Stochastic processes evolutionary spectrum estimation via harmonic wavelets. *Computer Methods in Applied Mechanics and Engineering*, *194*(12-16), 1367-1383.

Spanos, P.D., Kougioumtzoglou, I.A. (2012). Harmonic wavelets based statistical linearization for response evolutionary power spectrum determination. *Probabilistic Engineering Mechanics*, *27*(1), 57-68.

Sreenivas, T.V., Niederjohn, R.J. (1992). Zero-crossing based spectral analysis and SVD spectral analysis for formant frequency estimation in noise. *IEEE transactions on Signal Processing*, *40*(2), 282-293.

Sofi, A., Muscolino, G., Giunta, F. (2020). A Sensitivity-Based Approach for Reliability Analysis of Randomly Excited Structures With Interval Axial Stiffness. *ASCE-ASME Journal of Risk and Uncertainty in Engineering Systems, Part B: Mechanical Engineering*, *6*(4), 041008.

Sólnes, J. (1997). *Stochastic processes and random vibrations: theory and practice*. Wiley, Chichester.

Stafford, P. J., Sgobba, S., Marano, G. C. (2009). An energy-based envelope function for the stochastic simulation of earthquake accelerograms. *Soil Dynamics and Earthquake Engineering*, *29*(7), 1123-1133.

Stefanou, G., Tsiliopoulos, S. (2019). Estimation of evolutionary power spectra of seismic accelerograms. M. Papadrakakis, M. Fragiadakis eds, *7th International Conference on Computational Methods in Structural Dynamics and Earthquake Engineering*, *3* (pp. 5880–5888).

Tajimi, H. (1960). A statistical method of determing the maximum response of a building structure during an earthquake. In *Proceedings of the Second World Conference on Earthquake Engineering* (pp. 781-797).

Trifunac, M. D., Brady, A. G. (1975). A study on the duration of strong earthquake ground motion. *Bulletin of the Seismological Society of America*, *65*(3), 581-626.

Trifunac, M. D. (2009). 75th anniversary of strong motion observation—a historical review. *Soil Dynamics and Earthquake Engineering*, *29*(4), 591-606.

Vanmarcke, E. H. (1972). Properties of spectral moments with applications to random vibration. *Journal of the Engineering Mechanics Division*, *98*(2), 425-446.

Vanmarcke, E.H. (1975). On the distribution of the first-passage time for normal stationary random processes. *Journal of Applied Mechanics*, *42* (1), 215–220.

Vanmarcke, E.H. (1976). Structural response to earthquakes. In *Developments in geotechnical engineering*, Elsevier , *15* (pp. 287-337).

Vanmarcke, E. H. (1977). Seismic Safety Assessment. *In: Parkus H. (eds) Random Excitation of Structures by Earthquakes and Atmospheric Turbulence.* International Centre for Mechanical Sciences (Courses and Lectures), 225, Springer, Vienna:

Vanmarcke, E. H. (1979). *State-of-the-Art for Assessing Earthquake Hazards in the United States. Report 14. Representation of Earthquake Ground Motion: Scaled Accelerograms and Equivalent Response Spectra*. Massachusetts Institute of Technology. Cambridge, Department of Civil Engineering.

Vanmarcke, E.H., Gasparini D.A. (1977). Simulated earthquake ground motions. K - *Seismic Response Analysis of Nuclear Power Plant Systems K1 - Ground Motion and Design Criteria SMiRT 4*, San Francisco, USA.

Vanmarcke, E.H. Lai, S.-S. P. (1980a). Strong-motion duration and RMS amplitude of earthquake records. *Bull Seism. Soc. Am*. 70 (4), 1293-1307.

Vanmarcke, E.H., Lai, S.S.P. (1980 b). A measure of duration of strong ground motion. In *Proceedings of the 7th World Conference on Earthquake Engineering, Turkey*, 2 (pp. 537-544).

Villaverde, R. (2009). *Fundamental concepts of earthquake engineering*. CRC press, Boca Raton.

Wang, J., Fan, L., Qian, S., Zhou, J. (2002). Simulations of non-stationary frequency content and its importance to seismic assessment of structures. *Earthquake Engineering and Structural dynamics*, *31*(4), 993-1005.

Wang, G.Q., Boore, D.M., Igel, H., Zhou, X.Y. (2003). Some observations on colocated and closely spaced strong ground-motion records of the 1999 Chi-Chi, Taiwan, earthquake. *Bulletin of the Seismological Society of America*, *93*(2), 674-693.

Wang, X.Y., Zhouu, X.Y. (2004). Baseline correction of near fault ground motion recordings of the 1999 Chi-Chi, Taiwan earthquake [J]. *Seismology and Geology*, *26*(1),1-14.

Wang, D., Fan, Z., Hao, S., Zhao, D. (2018). An evolutionary power spectrum model of fully nonstationary seismic ground motion. *Soil Dynamics and Earthquake Engineering*, *105*, 1-10.

Xiaojun, L., Zhenghua, Z., Haiying, Y., Ruizhi, W., Dawei, L., Moh, H., Yongnian, Z., Jianwen, C. (2008). Strong motion observations and recordings from the great Wenchuan Earthquake. *Earthquake Engineering and Engineering Vibration*, *7*(3), 235-246.

Xie, W.C., Ni, S.H., Liu, W.,Jiang, W. (2019). *Seismic risk analysis of nuclear power plants*. Cambridge University Press.

Yeh, C.H., Wen, Y.K. (1990). Modeling of nonstationary ground motion and analysis of inelastic structural response. *Structural Safety*, *8*(1-4), 281-298.

Zhang, Z.M., Chen, S., Liang, Y.Z. (2010). Baseline correction using adaptive iteratively reweighted penalized least squares. *Analyst*, *135*(5), 1138-1146.

Zhang, Y., Comerford, L., Kougioumtzoglou, I. A., Patelli, E., Beer, M. (2017). Uncertainty quantification of power spectrum and spectral moments estimates subject to missing data. *ASCE-ASME Journal of Risk and Uncertainty in Engineering Systems, Part A: Civil Engineering*, *3*(4), 04017020.